LA-UR-20-28783
Approved for public release; distribution is unlimited.

Title: Analytic Modeling of a Deep Shielding Problem

Author(s): Remedes, Tyler Joseph

Intended for: PhD Dissertation

Issued: 2020-10-29

ANALYTIC MODELING OF A DEEP SHIELDING PROBLEM
LA-UR-20-XXXXX

By

TYLER J. REMEDES

A DISSERTATION PRESENTED TO THE GRADUATE SCHOOL
OF THE UNIVERSITY OF FLORIDA IN PARTIAL FULFILLMENT
OF THE REQUIREMENTS FOR THE DEGREE OF
DOCTOR OF PHILOSOPHY

UNIVERSITY OF FLORIDA

2020

ACKNOWLEDGMENTS

I would like to thank Dr. CJ Solomon, Dr. Mike Rising, Dr. Joel Kulesza, and Dr. Jeff Favorite for help with developing MCNP. These colleagues were irreplaceable in answering my questions and helping me understand some of the troubles I was having in developing the MCNP models, especially Dr. Kulesza. I would also like to Dr. Jeremy Conlin and Dr. Wim Haeck who thought a class on NJOY and Dr. Tom Saller who helped me parse the NJOY ACE files to generate the cross section data I needed. I would also like to acknowledge Dr. Cory Ahrens who Introduced me to my mentors who where imperative in completing this dissertation.

I would like to specially thank Dr. Scott Ramsey and Mr. Joe Schmidt for providing me the opportunity to complete my dissertation with Los Alamos National Laboratory, mentor and guide me through the process, and provide knowledge and "pick me ups" when I needed them. Thank you Scott and Joe.

Finally, I would like to thank my friend Dr. Kelsey Stadnikia. She kept me going through the process when I was ready to acknowledge defeat. Without her encouragement, this document would not exist.

This work was supported by the US Department of Energy through the Los Alamos National Laboratory. Los Alamos National Laboratory is operated by Triad National Security, LLC, for the National Nuclear Security Administration of the U.S. Department of Energy (Contract No. 89233218CNA000001).

TABLE OF CONTENTS

LIST OF TABLES

LIST OF FIGURES

Abstract of Dissertation Presented to the Graduate School
of the University of Florida in Partial Fulfillment of the
Requirements for the Degree of Doctor of Philosophy

ANALYTIC MODELING OF A DEEP SHIELDING PROBLEM
LA-UR-20-XXXXX

By

Tyler J. Remedes

December 2020

Chair: James Baciak
Major: Nuclear Engineering Sciences - Department of Material Science

Previous generations of scientists would make tremendous efforts to simplify non-tractable problems and generate simpler models that preserved the fundamental physics. This process involved applying assumptions and simplifications to reduce the complexity of the problem until it reached a solvable form. Each assumption and simplification was chosen and applied with the intent to preserve the essential physics of the problem, since, if the core physics of the problem were eliminated, the simplified model served no purpose. Moreover, if done correctly, solutions to the reduced model would serve as useful approximations to the original problem. In a sense, solving the simple models laid the ground-work for and provided insight into the more complex problem. Today, however, the affordability of high performance computing has essentially replaced the process for analyzing complex problems. Rather than "building up" a problem by understanding smaller, simpler models, a user generally relies on powerful computational tools to directly arrive at solutions to complex problems. As computational resources grow, users continue trying to simulate new, more complex, or more detailed problems, resulting in continual stress on both the code and computational resources. When these resources are limited, the user will have to make concessions by simplifying the problem while trying to preserve important details. In the context of the Monte Carlo N-Particle radiation transport simulation tool, simplifications typically come as reductions in geometry, or by using variance reduction techniques. Both approaches can influence the

physics of the problem, leading to potentially inaccurate or non-physical results. Errors can also be introduced as a result of faulty input into a computational tool: something as simple as transposing numbers in a tally input can result in incorrect answers.

In this paradigm, reduced complexity computational and analytical models still have an important purpose. The explicit form of an analytic solution is arguably the best way to understand the qualitative properties of simple models [1]. In contrast to "building up" a complex problem through understanding simpler problems, results from detailed computational scenarios can be better explained by "building down" the complex model through simple models rooted in the fundamental or essential phenomenology. Simplified analytic and computational models can be used to 1) increase a user's confidence in the computational solution of a complex model, 2) confirm there are no user input errors, and 3) ensure essential assumptions of the simulation tool are preserved.

This process of using analytic models to develop a more valuable analysis of simulation results is named the results assessment methodology. The utility of the results assessment methodology and a complimentary sensitivity analysis is exemplified through the analysis of the neutron flux in a dry used fuel storage cask. This application was chosen due to current scientific interest in used nuclear fuel storage.

CHAPTER 1
INTRODUCTION AND MOTIVATION

1.1 Motivation

America is the largest producer of nuclear power in the world, with 98 reactors producing approximately 805 billion killowatt-hours of power in 2017 [2]. Despite being the largest producer of nuclear energy, the United States has not established a permanent used nuclear fuel storage facility. Instead, nuclear power plants store used fuel on site, many using storage casks or canisters. A Savanah River National Laboratory report states nearly 100,000 fuel assemblies are stored in more than 2,000 casks at 75 storage sites [3].

Fuel casks are designed to store and protect spent nuclear fuel while shielding power plant workers and others from harmful radiation generated by unstable radioisotopes created through the fission process. There does not exist a singular design of a spent fuel cask due to multiple companies designing fuel casks and various types of spent nuclear fuel which need to be stored. While each design is varied, there exist certain components which are found across many spent fuel cask designs. Spent fuel casks typically have a right cylindrical shape with layers of high atomic number and low atomic number materials, such as steel alloys and concrete respectively. Layering materials with different compositions and atomic numbers provides radiation shielding for both gamma rays and neutrons, which are the two most penetrating types of radiation emitted by radioisotopes present in the fuel (e.g., O-17, Cm-242, and Sr-90). High atomic number materials are used to mainly shield gamma rays, whereas low atomic number materials are used to mainly shield neutrons. For this reason, most spent fuel casks have an inner region where spent fuel is stored, an outer region made of low atomic number materials (i.e., concrete) and high atomic number materials (e.g., steel alloys). Layered materials are also utilized in baseplates and lids.

Materials in a spent fuel cask are specifically chosen to be multi-functional. Spent fuel casks must conduct heat away from spent fuel rods, protect fuel from damage, prevent

proliferation of radioactive materials, as well as shield radiation. Heat conduction is achieved by using materials with high thermal conductivities to draw heat away from spent fuel rods to the environment. Thick layers of materials, such as steel and concrete, protect the cask contents from environmental or other sources of damage (e.g., a hurricane or a cask being dropped during transportation). Casks are also designed to prevent proliferation by, for example, featuring welded lids or the addition of security tags to discourage unauthorized access to spent fuel. Finally, spent fuel casks are designed to shield employees and the public from the harmful radiation produced by decaying radioisotopes created in the fuel during the power making process.

If a cask inadequately performs any of the above functions, it may become necessary to open the cask for a visual inspection. This is a costly and time consuming endeavor. Greulich et. al. state the cost to re-open a cask could be in the millions of dollars and require man-months of time [4]. The process of opening a cask to visually inspect the contents also carries an increased risk of exposing workers to radiation. The high costs associated with opening a cask would certainly make visual inspection an unappealing option. Simulation based and experimental research has been motivated by the desire to develop a non-destructive assay techniques to verify cask contents.

Analyzing the capabilities of technology to ensure the contents of a spent fuel cask has motivated many scientific investigations, with a large reliance on computational simulations [4–6]. Simulation results can then be correlated to experimental observations in order to identify promising techniques to inspect the interior of a cask without opening the cask. Neutron flux and dose are common measurable quantities sought after in the simulation and experimental works surrounding radiation shielding investigations of spent fuel casks. In reality, these two quantities are the same with the latter being a scalar multiple of the former. These works tend to be concerned with the neutron flux at or beyond the surface of the cask, since the radiation environment exterior to the spent fuel cask is potentially harmful to worker safety. Understanding the interior neutron flux

is useful in any simulation studying the exterior neutron flux. The neutron flux at the surface of the spent fuel cask is directly dependent on the physics occurring interior to the spent fuel cask. Ultimately, the behavior of the interior neutron flux is controlled by the configuration and choice of materials inside the fuel cask. The relationship between interior structure and exterior neutron flux has prompted many simulation investigations using radiation transport codes. Further, simulation tools are not only used to design non-destructive assay techniques, but are also used to validate radiation transport codes as applied to spent fuel casks.

Ideally, simulation results should be compared to a series of identical or similar experiments *and* numerous results from other computational and numerical tools, and analogous analytical models. Computational, numerical and analytical tools act complimentary to experiments, in that the former tend not to be limited by physical restraints such as, but not limited to, detector placement, experimental design challenges, personnel safety, and costs. Nonetheless, experimental data is highly sought after since analytical models only provide exact solutions for the most simplistic non-physical problems and computational and numerical tools only approximate solutions, albeit these approximations can be quite accurate. Unfortunately, limited amounts of experimental data result in an increased reliance on computational and numerical tools. To further exacerbate the issue, it is of utmost importance that conclusions can be confidently drawn from simulation results. In the case of spent fuel casks, human lives and livelihood depend on the correctness of simulation results.

A discussion motivating the use of analogs is, therefore, useful. Fickett describes analogs as a qualitative representation of the original, constructed, not derived, in order to maximize simplicity while minimizing loss important properties [7]. Further, analogs have the following benefits 1) exact solutions are simpler to find and more likely to exist, 2) mathematical rigor in determining analytical solutions is reduced, and 3) salient physics is more readily observable after the removal of extraneous features. The

simplified computational and analytical models used in this work are developed as analogs. Before further description of the analytical models acting as analogs in this work, it is important to discuss the processes of validation, verification, uncertainty quantification and sensitivity analysis as applied to general computational tools and to simulations of used fuel casks.

1.2 Practices for Code Reliability, Confidence, and Predictive Capability

The behavior of physical systems is commonly described using complex mathematical expressions, typically consisting of differential equations. Exact solutions of these equations (also variously known as analytical or closed-form solutions) tend to be limited to only the simplest scenarios. Indeed, the cost of exactly solving these equations often involves the extensive use of simplifying assumptions to reduce the complexity of an equation to a form where an analytical solution is possible. Approximating a differential equation as a series of coupled linear equations has become an alternative to finding direct analytical solutions as access to high performance computing has become more widespread. Unfortunately, discretizing spatial, direction, energy or other continuous variables introduces a degree of error into the solution proportional to the fidelity to which a problem was discretized. Further, discretization requires a high degree of computational rigor and, therefore, was not a realistic technique for solving differential equations until adequate advancements in computation had occurred. However, the modern-day advancement of computational power has motivated the development of tools which approximate the solutions of complex differential equations in broad sets of circumstances via approximation techniques, as opposed to simplifying assumption techniques that may yield closed-form solutions only in special cases.

These simulation tools, or simulation codes, often rely on algebraic calculations to approximate solutions of the complex differential equations which describe real-world physics. The accuracy of these codes needs to be investigated since approximate solutions introduce error. The processes of verification and validation, shown in Fig. 1-1 generate

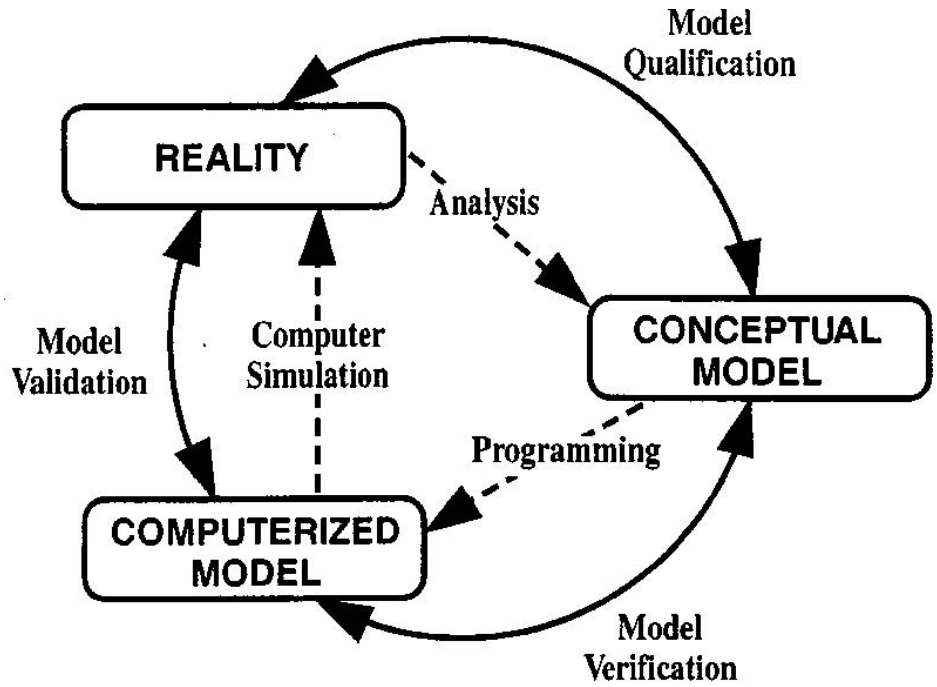

Figure 1-1. A flow chart showing the processes of verification and validation [10].

evidence "that computer [codes] have adequate accuracy and level of detail for their intended use" [8]. Verification assesses "the numerical accuracy of the solution to a computational model," and validation "addresses the physical modeling accuracy of a computational simulation by comparing the computational results with experimental data" [9]. For the scope of this effort, model qualification will not be discussed. Stated another way, verification studies if a code solves equations correctly, and validation investigates the utility of a code through comparison with experimental data.

Like verification and validation, uncertainty quantification evaluates the adequacy of models. However, uncertainty quantification does not "tell you that your model is 'right' ..., but only that, *if* you accept the validity of the model ..., *then* you must logically accept the validity of certain conclusion (to some quantified degree)" [11]. Further, sensitivity analysis can be considered a type of uncertainty quantification which stratifies input parameters based on degree of impact to the error of simulation results. A short description of verification, validation, and sensitivity analysis is discussed below.

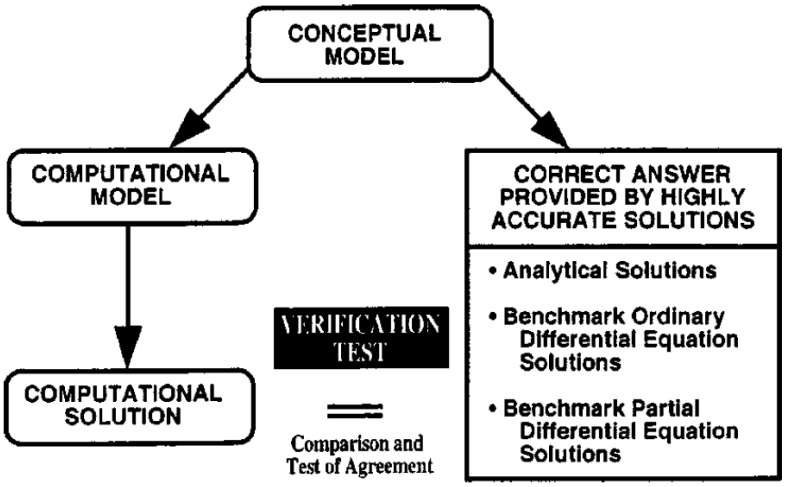

Figure 1-2. A flow chart showing the process of verification [10]. Verification compares the results of computation solutions with exact analytic and benchmarking solutions to quantify the accuracy of the computational solutions.

Verification is aimed to quantitatively demonstrate that the approximate equations in the code are being solved in a manner consistent with known solutions of its governing equations [12]. Figure 1-2 is a graphical representation of the process of verifying computational solutions. There are two general types of verification activities in computational modeling: 1) code verification and 2) solution verification [10]. Code verification consists of numerical algorithm verification and software quality assurance. Numerical algorithm verification focuses on the correctness with which algorithms are programed into the code, as well as, the accuracy and reliability of implemented algorithms. Software quality assurance treats the computational software as a product and ensures that computational results are repeatable. Solution verification ensures the numerical algorithms converge to a solution. Then, solution verification is concerned with quantifying the errors of numerical approximation techniques.

In contrast to verification, validation ensures a simulation tool approximately solves a representative set of equations consistent with the applications of the code. Validation relies on comparing experimental, analytical or numerical results against simulation results

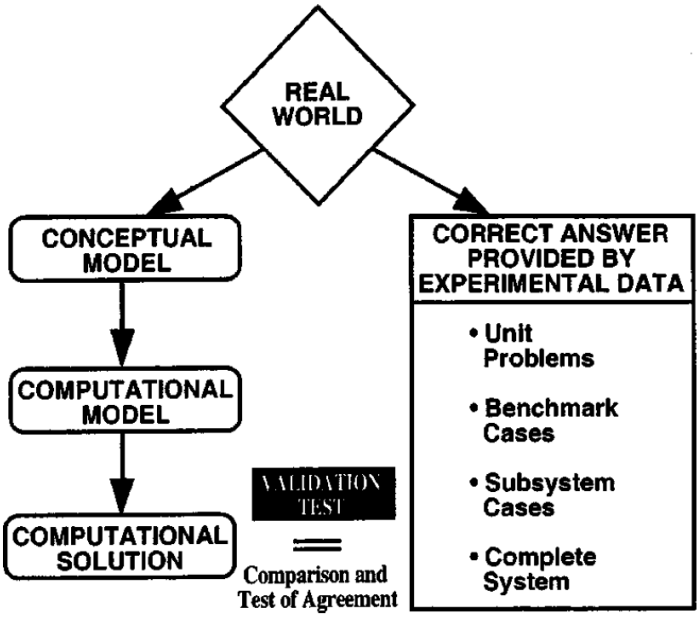

Figure 1-3. A flow chart showing the process of validation [10]. The computational solution is compared against experimental data based on the application of the intended computational tool

and is conducted on an application specific situations. Fig. 1-3 is a flowchart showing how validation compares computational results with experimental data. Simulation tools are validated for different applications on a case-by-case basis. Validation commonly requires experimental data for a given application. Unfortunately, sometimes experimental data is limited or non-existent since experiments can be financially burdensome, potentially risky to public and worker health, or difficult to conduct due to proprietary reasons. Difficulties in obtaining experimental data necessitate alternative methods for validation.

Uncertainty quantification and sensitivity analysis aid in determining the error of computational tools and the importance of input parameters respectively. However, instead of investigating the numerical methods and equations which are used to develop computational tools (as in verification and validation methods), uncertainty quantification and sensitivity analysis investigate the effects error in parameter data has on numerical solutions. Simulation tools require parameters, or data provided by the user, such as

physical properties measured through experiments (e.g., cross section data, viscosity, or thermal conductivity. These values have associated error; measurement error is an example. Uncertainty quantification is concerned with quantifying the error in the simulation output due to the error of input parameters.

Sensitivity analysis act complementarily to uncertainty quantification by identifying which parameters most influence the result. A typical approach to computational sensitivity analysis requires performing many simulations where a change is made in each computation - an approach called the direct method [13]. Running many simulations where a single change in make in each computation is s process that requires extensive computational resources.

The history of sensitivity analysis as applied to differential equations is broad and extensive, therefore, only previous research that pertains to this work will be discussed. The first methodology for sensitivity analysis was developed on linear electrical circuits by Bode in 1945 [14]. At that time, sensitivity analysis motivated the use of feedback in circuit design. From its origins in circuit control, sensitivity analysis permeated many others fields of science, including nuclear engineering, and many methods were developed. McKay provides an introduction into basic definitions and concepts related to sensitivity analysis [15]. Cacuci unified and generalized the direct method and the perturbation methods of sensitivity analysis in 1980 based on Frechet-derivatives [13]. A year later, Cacuci further generalized his methodology to analyze systems of response along arbitrary directions using the Gâteaux-derivative (G-derivative). This linear operator determines system responses to multiple perturbations in input parameters simultaneously. In doing so, Cacuci developed the Forward Sensitivity Analysis Procedure (FSAP) and Adjoint Sensitivity Analysis Procedure. The FSAP is used to find sensitivities of the linear differential equations in this work.

The overall purpose of performing verification, validation, uncertainty quantification, and sensitivity analysis procedures is to identify the accuracy, credibility, and predictive

capabilities of a particular code for given scenarios. Ultimately, a code user must decide if a code adequately simulates the problem and if the user can have confidence that the simulated results are an accurate portrayal of the real-world problem. While the processes of verification, validation, uncertainty quantification, and sensitivity analysis have been and continue to be extensively developed, there exists a limitation - how can a code be validated if there is no experimental data for comparison? The purpose of this document is to introduce a methodology aimed at answering this question.

1.3 State of Current Used Fuel Cask Research

Interest in experimental and simulation work stems from the need to ensure the safety and security of spent fuel casks; since there is currently no long term, national storage plan. Even though there is motivation for investigating radiation transport in spent fuel casks, the breadth of experimental data publicly available is limited. In the limited body of experimental work measuring the radiation dose at or near the surface of various used fuel casks, experimental data on the HI-STORM 100 spent fuel casks is not available. Hence, discussion of past experiments will include radiation measurements performed on any spent fuel cask, including but not limited to experiments compared to any radiation transport code.

Thiele et. al. provide a comparison between experimental results and the results from two radiation transport simulation tools (comparing Monaco/MARVIC with SAS4/MORSE) [16]. Both simulation tools are developed as part of the Standardized Computer Analysis for Licensing Evaluation (SCALE) packages by Oak Ridge National Laboratory [17]. Since these radiation transport codes are not used in this work, no further explanation of the codes will be given. Thiele et. al. conclude that simulation tools can be applied for the assessment of dry storage casks. While experimental validation of simulation results is arguably the best way to corroborate simulation results, it is still important to not treat experimental data as sacrosanct, as experimental results still include sources of error [18].

Experiments still include measurement and procedural errors, and without the validation of multiple experiments of the same cask, the result of a lone experiment should not be considered to validate or invalidate simulation results. Ziock et. al. measure the thermal neutron and gamma ray radiation signatures from six different spent fuel cask designs; the HI-STORM 100 was not one of the six. Ziock et. al. posit the radiation signature can be used as an identifier for individual casks. Their experiments proved inconclusive resulting from limitations of the imaging devices used. That is, the measurement tools introduce error into the thermal neutron and gamma ray measurements which prevent using the radiation spectra as an identification tool.

Wharton et. al. use the Monte Carlo N-Particle (MCNP) radiation transport code to determine the fraction of gamma rays which would be detected by a high purity germanium detector placed at the top surface of two spent fuel cask designs [19]. These simulations are used to determine the feasibility of a system designed to use passive gamma radiation to determine if a fuel bundle was present or absent from a spent fuel cask. The authors conclude that the thick shielding of the spent fuel casks sufficiently scattered radiation and the system is not capable of resolving discrete gamma ray peaks. This resulted in the measurements being stopped without fully testing the capabilities of the system. It should be noted, the MCNP results suggest the system was capable of performing the measurements and distinguishing between empty and filled fuel storage positions. This work serves as an example for the importance of corroborating simulation results with further investigations.

Simulation studies of the HI-STORM 100 spent fuel cask using MCNP are more numerous than experimental studies. Before further discussing how simulations have been used to study spent fuel casks, it is important to take an aside and discuss the verification and validation of a commonly used radiation transport simulation code, the MCNP simulation code [20].

MCNP has been extensively verified and includes a series of benchmark problems. Further, Mosteller compiled a list of documents which discuss verification efforts on MCNP [21]. Analytical models have also been used in validation efforts [22, 23]. analytical models provide an exact solutions against which simulation tools can be compared. However, exact analytical solutions are often only available for heavily simplified problems which do not represent physical systems. Nonetheless, excellent agreement has been achieved between simple MCNP models and analytical solutions. Verification is considered an activity in mathematics where a successful test demonstrates that the governing equations of a simulation tool are solved correctly [18]. Further, validation of a simulation code is undertaken after verification.

MCNP has also undergone general validation in multiple disciplines within nuclear science and engineering; including but not limited to radiation shielding [24], criticality [25], and intermediate and high-energy physics [26] where MCNP results are compared to simple experiments. In order to validate computational tools as applied to spent fuel casks, scientists have turned to a comparative method where results from other radiation transport codes are compared with MCNP [27, 28]. However, discrepancies between results from different simulation tools are attributed to different physics being included in each tool. While this may be the driving factor leading to the apparent disagreement, this conclusion would benefit from identifying the physics seen in one simulation tool and neglected in the other. Comparison with experiments and other simulation tools is a valid, imperative, and important technique for validating simulation results, but more analysis should be done in order to increase confidence that simulation results can be trusted. After discussing the verification and validation of MCNP, it is beneficial to summarize the extent of computational research pertaining to the radiation transport in spent fuel casks using MCNP.

Priest conducted an in-depth investigation of neutron and gamma flux and dose rates interior to a HI-STORM 100 spent fuel cask with the purpose of identifying an imaging

system capable of withstanding the harsh environment inside the multi-purpose canister (MPC) [29]. Priest performed simulations using multiple MPC configurations with used nuclear fuel from both pressurized water and boiling water reactors.

Harkness et. al. used MCNP to investigate the validity using helium-4 fast neutron detectors to determine if fuel had been removed from a HI-STORM 100 spent fuel cask [6]. This work describes a methodology to generate a source definition for MCNP based on data provided in the Next Generation Safeguards Initiative. This fuel rod composition data was aged using ORIGEN-S, a material irradiation and decay calculation code, to create an MCNP compatible source definition. A further description of this process will be provided later in this work. The neutron flux and energy spectrum at the surface of the cask were tallied as part of this investigation. From the results of MCNP simulations, the authors concluded that neutron spectroscopy was feasible using helium-4 detectors, however, confidently determining if all fuel was present in a sealed spent fuel cask required further investigation.

Kelly et. al. performed an uncertainty analysis in radiation dose exterior to a HI-STORM 100S (a variant of the HI-STORM 100 cask) spent fuel cask based on variabilities in concrete composition and density using MCNP [30]. The authors state that density variations in the concrete have the largest effect on radiation shielding capabilities. Varying concrete composition mostly affected neutron and associated capture gamma ray dose rates. These simulation results motivated the design requirements of a robotic camera system to perform visual inspection of the fuel elements in the MPC.

Because of the interest in modeling radiation transport in spent fuel casks, research is not limited to using MCNP as a simulation tool nor is it limited to a single cask design. Gao et. al. use the radiation transport code MAVRIC (a radiation transport code developed by Oak Ridge National Laboratory and distributed in with the SCALE code package) to simulate neutron and gamma transport through a TN-32 spent fuel cask [31]. In this work, Gao et. al. explore the effect of two geometries and two sets of

cross section data on the neutron and gamma fluxes at the surface of the cask. Gao et. al. use a detailed model, which include details of individual fuel rods, and a homogenous model, where a homogenous fuel definition is determined and the model uses a simplified geometry in each fuel cell. The authors also use two sets of cross section data. The first set is continuous energy cross section data and the second set is of multigroup cross sections. The authors conclude that changes to the geometry of the problem have a larger effect on the result that changing how the cross section data is handled.

Interest in verifying cask contents has led to simulations investigating methods for tomographic imaging. These investigations rely on simulation tools as a proof of concept and to aid experimental design. Liao and Yang use cosmic-ray muon simulations to aid in experimental design choices for a spent fuel cask tomography system [32, 33]. The authors use Geant4 (another radiation transport code) and MCNP to simulate cosmic-ray muon transport through a spent fuel cask, as well as through a test setup to guide experimental design [34]. The authors then conduct experiments using the prototype muon imaging systems. Liao and Yang concluded they are able to detect a quarter of a missing fuel bundle located anywhere in the cask.

Greulich et. al. also investigate the possibly of tomographic imaging techniques in verifying the contents of a spent fuel cask [4]. Greulich et. al. simulate neutron transport through a TN-32 spent fuel cask using MCNP. Using a beam source of neutrons incident at the surface of the cask, the uncollided flux of neutrons leaving the cask provides information which can be used to reconstruct an image of the interior of the cask.

Miller et. al. determine the feasibility of using a monoenergetic photon source to verify the contents of a sealed HI-STORM 100 spent fuel cask using MCNP [35]. Miller et. al. simulate photon transport through the spent fuel cask and found a 1000-fold reduction in the transmitted flux when a fuel assembly is present as compared to a reduction of two in the transmitted flux when there is no assembly present. Miller et. al. further corroborate their work using analytical calculations to predict the scale of the uncollided

flux for when a fuel assembly is present and when there is no fuel assembly. The results from their analytical modeling agree with corresponding MCNP simulations. The results from Miller et. al. motivate using analytic modeling as a tool to guide MCNP simulation development.

The previously described works are all interested in either radiation dose or radiation flux values at the surface or exterior to the surface of the cask. Since dose is directly proportional to flux, and since the exterior neutron flux is a direct result of how interior cask structure affects the interior flux, the aim of this work is to investigate the interior neutron flux, so as to have the most general relevance to existing work. The neutron flux is chosen over other types of radiation as gamma ray shielding on the casks is generally more effective than neutron shielding, motivating further investigation of the neutron flux.

The body of work focusing on simulations of spent fuel cask is quite large, which demonstrates scientific interest in simulating spent fuel casks. However, experimental data to validate simulated results is limited. Further, the final safety analysis report delivered by Holtec when licensing the HI-STROM 100 spent fuel canister system did not include any experimental data pertaining to the radiation shielding capabilities of this design [36]. Instead, MCNP is used to demonstrate the cask design is capable of attenuating radiation to an adequate level. Maintaining a safe environment for power plant workers and members of the public is of utmost importance and an alternate method for validating the accuracy of simulation results is needed if simulation results are to be relied upon in the absence of experimental data. The discrepancy between the amount of simulated results and experimental data identifies the need to validate or otherwise reinforce confidence in simulation results without relying on experimental data.

1.4 General Description of the Work

This work includes high-fidelity MNCP simulations of the interior neutron flux from a Holtec Hi-STORM 100 spent fuel cask, and the attendant analytical analysis of the simulation results in the absence of significant experimental validation data. A detailed

model of the HI-STORM 100 spent fuel cask is simulated in MCNP to investigate the neutron flux interior to the fuel cask. Owing to a lack of validation data against which to compare these simulation results, an analytical analysis framework called "simulation results assessment" (or, henceforth, "results assessment") is developed and applied to provide an alternative (but not replacement) means for enhancing confidence in the computational model. The accuracy of the model is assessed by first developing simplified analytical and MCNP computational models. The design of these analogous models is made to retain essential physics while reducing geometric complexities. Since the essential physics is preserved, the neutron flux found using the analogous models will approximate the neutron flux interior to the cask of the detailed model. Developing analogous models is an iterative process where the initial simplified models are overly simplified and lose essential physics. Essential physics is identified from locations where disagreements between the results of the detailed model and the analogous models occur. More detailed analogs are developed in order to rectify differences observed between the two sets of results until a final set of analogous models are found. This process identified physical details that must be preserved in the detailed model in order for the detailed model to accurately simulate reality. A sensitivity analysis is also conducted on the final analogous model in each material region as well as on the detailed model as an extension of the results assessment methodology through sensitivity analysis. The results assessment and sensitivity analysis methods presented in this work act complimentary to existing techniques - verification, validation, uncertainty analysis, and sensitivity analysis- in order to develop a more valuable analysis.

1.4.1 Results Assessment

The results assessment methodology provides a way to ensure the appropriateness and inerrancy of computational and numerical tools. This methodology formulates analogs which are designed to share phenomenological physics with its more detailed counterpart. The purpose of using tractable analytic models is develop closed form solutions, as the

salient physics is more readily available in closed form solutions. Figure 1-4 shows how the results assessment methodology is developed to act in the absence of experimental data, and complimentary to existing validation techniques, to enhance analysis, identify salient physics, and further ensure a computational model is appropriately constructed. To exemplify the process, a detailed model of this cask is developed in the MCNP code to predict the neutron flux in its interior. In an attempt to isolate essential physics, 1) five other MCNP simulations are developed to model various analogous problems, and 2) analytical models are developed to explain key characteristics of the flux seen in these analogous problems. The results of the simplified calculations are then used to reveal the fundamental physics controlling the shape and other characteristics of the flux distribution resulting from the complex model. This procedure is phenomenological in nature, and is thus intended to capture elemental physical processes that are occurring within sub-regions of the full-scale system. Therefore, while no single analytical solution is expected to be available for the full-scale system, any understanding gained in the sub-regions reinforces confidence that the integrated scales are being simulated in accordance with physical intuition. This outcome is valuable in cases where experimental data is sparse or nonexistent. A complimentary investigation of sensitivity structures produces a quantitative basis for comparison of analytical and computational models.

1.4.2 Sensitivity Analysis

The procedure of quantifying comparisons between analytical models, reduced geometry computational models, and the full model is demonstrated through the inclusion of sensitivity analysis procedures. The previously developed models used in the results assessment methodology lend themselves to analytic sensitivity analysis. Through the use of an analytic sensitivity analysis, the results assessment methodology can compare sensitivity information between the computational and analytic models. Forward modeling of sensitivity structures is conceptually simple but computationally expensive for large problems, as it involves sampling a space of possible parameter values and executing a new

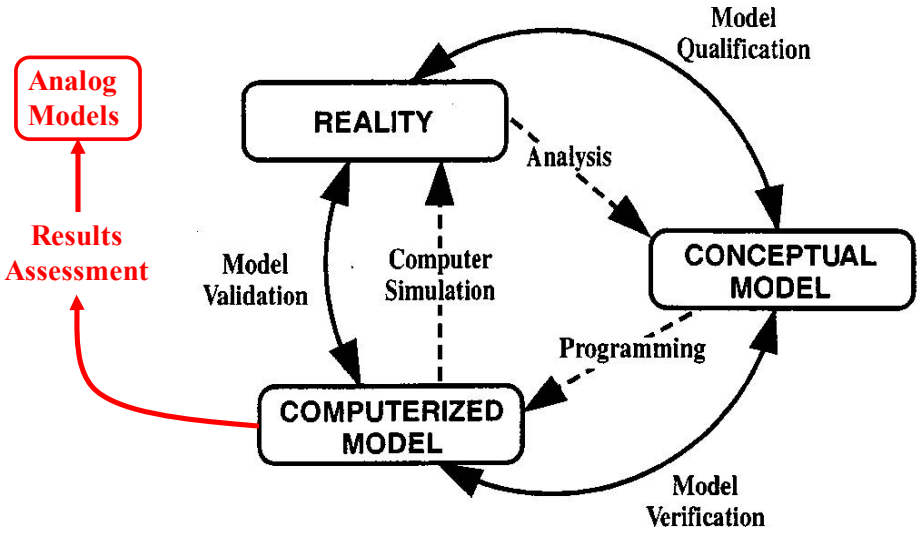

Figure 1-4. A flow chart showing the complimentary addition of the results assessment methodology. The purpose of results assessment is not to replace validation, but to act complimentary to existing validation techniques.

simulation for each value. Applying sensitivity analysis techniques to analytical models allows for the identification of sensitivities without requiring as much computational resources, a strength of analytical sensitivity analysis. Further, if an equation yields an analytical solution, the sensitivities of an equation to its parameters can be found with minimal computational resources and requires solving sensitivity equations only once. Sensitivity structures can be computed in closed-form using a generalized notion of the directional derivative. The comparison of these two methods forms the final component of this work. In addition to basic physics phenomenology, the sensitivity structure arising from analytical models can be compared to that found from forward sensitivity modeling of full-scale simulations. When these structures compare favorably, confidence in the full-scale simulations is once again reinforced.

1.5 General Overview of Chapters

This document discusses the rigorous analysis of a HI-STORM 100 used fuel cask using the results assessment methodology and a sensitivity analysis procedure. The results assessment methodology is discussed in chapters 2, 3, and 4, and chapters 5, 6 and 7 describe the process of adding a complimentary sensitivity analysis.

The second chapter of this document introduces the detailed MCNP model of the HI-STORM 100 used fuel cask. This model is used to demonstrate the results analysis methodology. The results of the simulated interior neutron flux are shown and features are identified in this chapter. A feature is defined in more depth in chapter 2.

Chapter 3 introduces the various analytical models used in this work. The neutron transport equation is derived and then reduced through application of assumptions and simplifications. From a reduced form of the neutron transport equation, the multigroup discrete ordinates equation and diffusion approximation are developed. The two equations form the basis of the analytical modeling used in this work.

The results assessment methodology is demonstrated in chapter 4. This chapter discusses why each analytical model is chosen as well as how each reduced complexity computational model is developed. After describing how the models are determined, each previously identified feature of the interior neutron flux is analyzed using the results assessment methodology.

Chapter 5 introduces the method for conducting a sensitivity study using MCNP. Further, this chapter provides the results of the sensitivity analysis on the detailed MCNP model of the HI-STORM 100 spent fuel cask. Finally, the results of the sensitivity analysis of the detailed HI-STORM 100 cask are discussed.

Chapter 6 provides foundational theory of sensitivity analysis of the analytic models using Cacuci's FSAP [13]. In this chapter, the process of the FSAP is applied to both the analytic representation of the neutron flux, as well as a set of governing ordinary differential equations with corresponding boundary conditions. This chapter also discusses the method for determining sensitivity values from the analytic models which can be compared to the sensitivity results from the detailed MCNP model of the HI-STORM 100 cask.

Chpt. 7 discusses the results of the sensitivity analysis as applied to the analytic models. Further, comparisons between the FSAP analysis on analytical models and

MCNP results are discussed, introducing the results assessment methodology through sensitivity analysis. Discussions comparing the two model's sensitivity coefficients also include identifying the physical and mathematical reasons for any discrepancies.

The last chapter includes final thoughts and conclusion regarding the work. Recommendations for future work are also provided in chapter 8.

CHAPTER 2
DISCUSSION OF MAIN PROBLEM

Dry storage casks provide protection, shielding, security, and cooling for used nuclear fuel which has spent at least one year in a spent fuel pool [37]. Shielding is especially important as used nuclear fuel is highly radioactive after being removed from a reactor and shielding is required to protect civilians, radiation plant workers, and the environment. The storage of used nuclear fuel has become a challenge in the United States since there is no long-term storage location. Instead, used nuclear fuel is stored in dry storage casks at the facility where it was generated. These casks are designed to 1) shield harmful radiation generated by the used nuclear fuel, 2) conduct decay heat away from fuel rods to prevent damage to the fuel and cladding, 3) protect spent nuclear fuel from environmental damage and other hazards, and 4) prevent proliferation of nuclear materials. Large efforts have been made in studying and designing casks to accomplish these challenges. While each function is imperative in analyzing the efficacy of a spent fuel cask, this work is only concerned with the radiation shielding capabilities of a Holtec International HI-STORM 100 spent fuel canister system [36].

Figure 2-1 is a diagram of the HI-STORM 100 spent fuel canister system partially loaded into an overpack of the same name. These two components together, the canister and overpack, will be referred to as a spent fuel cask. The HI-STORM 100 canister system is chosen as it is the most common used fuel storage system in the United States (750 canisters have been loaded before 2017) [3]. The overpack consists of two parts: a cylindrical dual material structure welded to a baseplate and a dual material removable lid. Both parts of the overpack use a combination of concrete and carbon steel to shield radiation, protect fuel, and prevent proliferation of nuclear material. Four vents are located at both the top and bottom of the overpack. These vents allow air to circulate between the overpack and MPC, removing heat caused by decaying isotopes in the spent fuel. Spent fuel rods are stored in the MPC, the central cylinder in Fig. 2-1. Figure 2-2 is

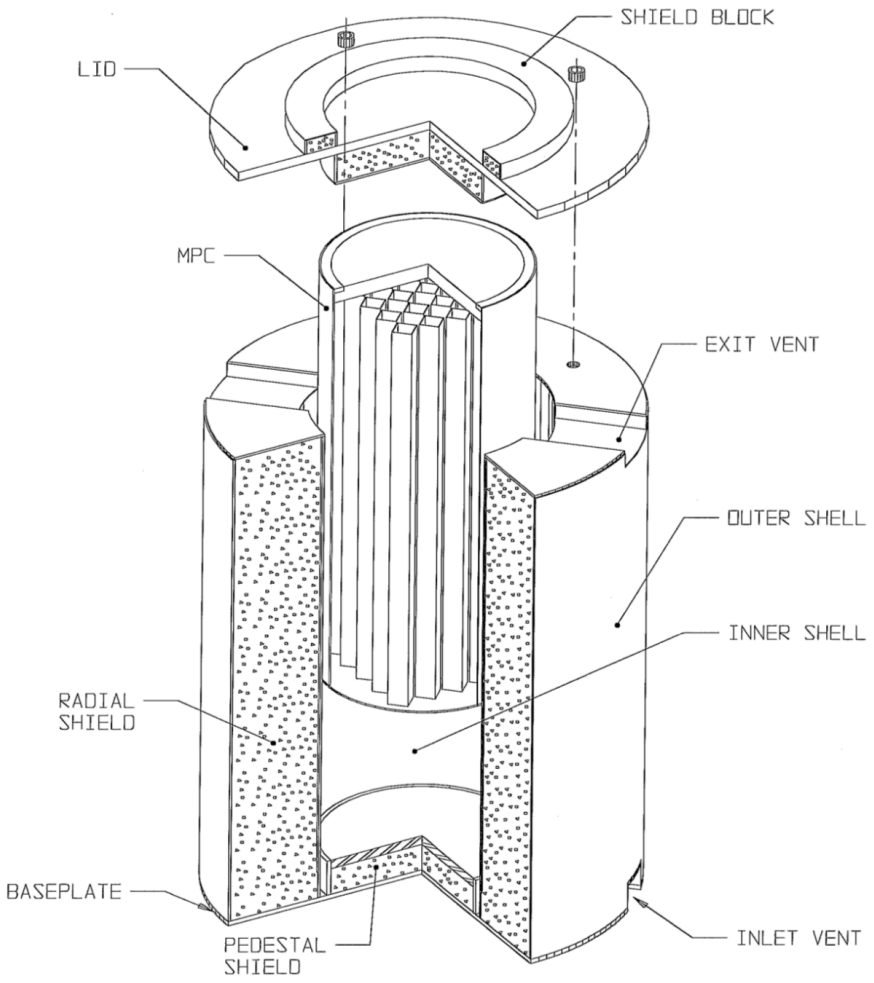

Figure 2-1. The Holtec HI-STORM 100 spent fuel cask system is designed to protect fuel, transfer decay heat to the environment, prevent proliferation of nuclear material, and attenuate radiation [36]. The MPC is seen partially inserted into the steel and concrete overpack. Current designs of the HI-STORM 100 do not use the inner shell and, therefore, the inner shield is not modeled in MCNP.

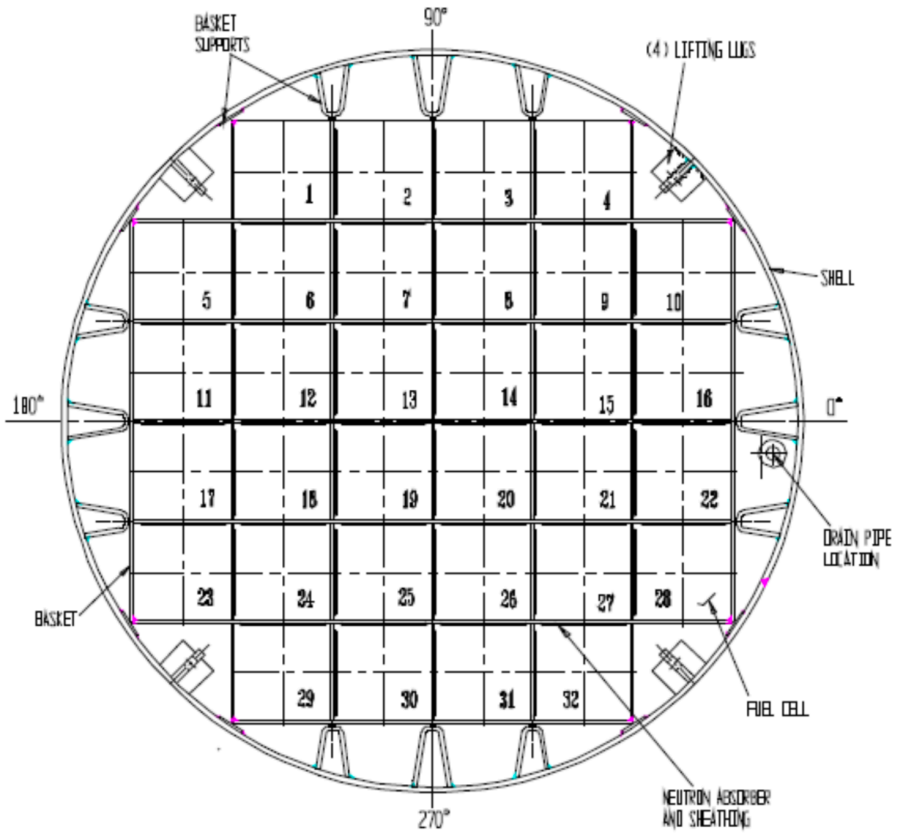

Figure 2-2. A cross section view of the multi-purpose canister. While there are multiple designs which accommodate different amounts of fuel, the MPC-32 is chosen for this work [36]. The MPC-32 is capable of holding 32 fuel bundles, one bundle in each square lattice element. The fuel basket and cylindrical wall of the MPC are made using stainless steel 304 and the canister is sealed by welding a baseplate to the bottom and a lid and closure ring to the top of the cylinder respectively.

the top-down cross section view of the MPC. Each cell in the honeycomb structure houses a single fuel bundle.

Power plant workers must be protected from the radiation produced by spent nuclear fuel rods, hence opening a sealed MPC is an expensive and potentially dangerous task. Therefore, alternative methods are being explored to ensure the content and integrity of fuel components which do not require opening a cask. A sample of these techniques includes neutron spectroscopy, deduction of interior structure based on exterior dose rates, and neutron based computer tomography which were previously discussed in detail

in Section 1.3. Each of these techniques relies on simulations using various radiation source definitions, virtual detectors, and simulated cask designs to determine specific quantities related to the neutron flux within the spent fuel cask. The key metric of this work is the interior neutron flux spatial distribution of the HI-STORM 100 spent fuel cask, as this quantity is shared among research in spent fuel casks. Clearly, simulation tools have become an important part of investigating the efficacy of a nondestructive evaluation technique, and ensuring the accuracy of these results is even more important since experimental data associated with the techniques is limited.

2.1 Description of Detailed Model

The MPC and overpack are modeled using the MCNP simulation code to determine the simulated interior neutron flux spatial distribution as a function of radial distance from the centerline, averaged over the height of the cask. Figures 2-3 and 2-4 show, respectively, a side view and cross section of the cask geometry simulated in MCNP. This model is called the "detailed model" throughout this work and models the geometry of the cask down to the individual fuel rod level. Each fuel rod acts as a source term for neutrons produced from spontaneous fission and (α, n) reactions.

Figure 2-5 shows a single fuel cell cross section from the detailed model. The fuel cell contains two neutron absorbing pads composed of boron-carbide and aluminum, 264 fuel rods with zircalloy cladding and 25 water rods representing instrumentation. Fuel rod composition is determined using data from the Next Generation Safeguards Initiative which analyzed the composition of Westinghouse 17x17 fuel bundles with various degrees of initial ^{235}U enrichment and burn-up values [38]. This work investigates fuel with an initial enrichment of 3% ^{235}U and a burn-up value of 30 GWd/MTU. The composition of each individual fuel rod is unique, since fission fragment distribution is probabilistic, which introduces variance in the local neutron flux. Each fuel bundle is assumed to have the same fuel burn-up and composition. These variations in fuel rod composition could influence the flux and potentially hide salient physics. Identifying and explaining salient

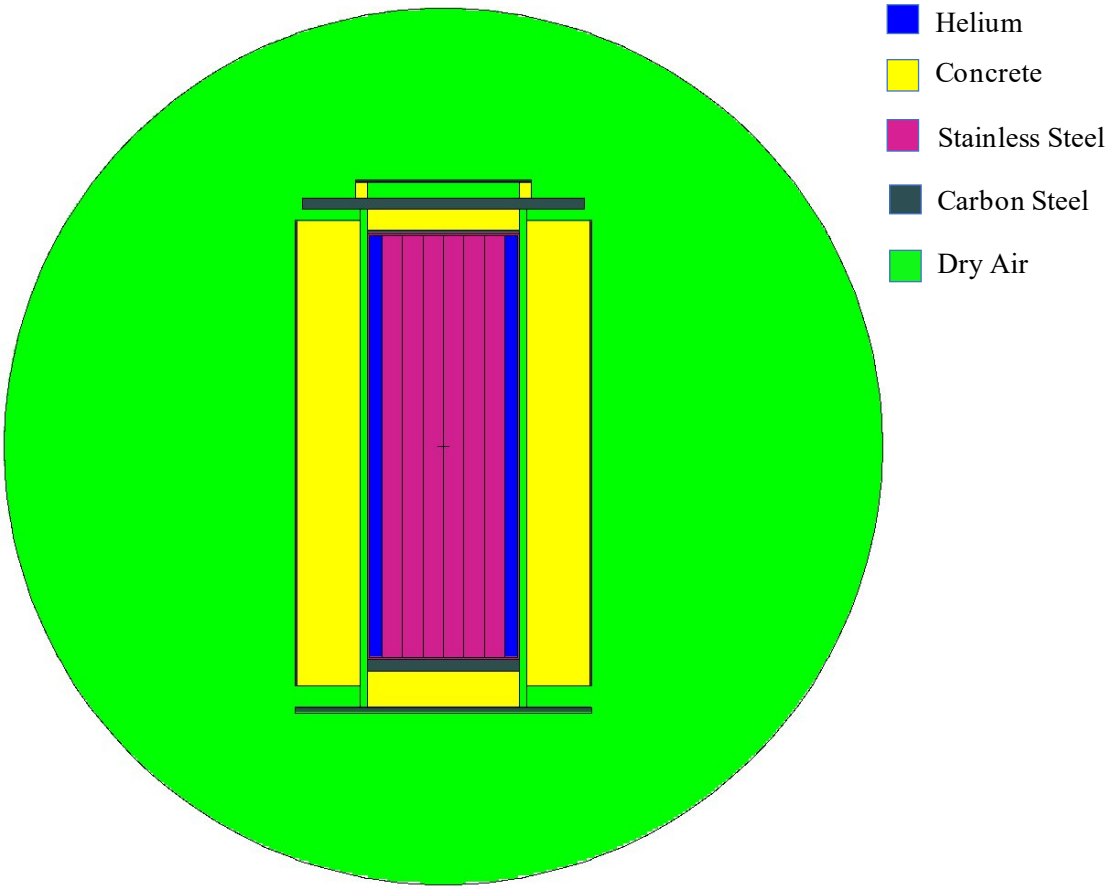

Figure 2-3. The side view of the HI-STORM 100 spent fuel cask (canister and overpack) modeled in MCNP. This is referred to as the detailed model.

physics is a goal of this work. Therefore, an average fuel rod composition is determined based on the mass of each isotope present in a single spent fuel bundle in order to more clearly investigate the effects of geometry, detail, and non-fuel materials without influence from loading patterns of specific fuel rods. Table 2-1 and Tab. 2-2 provide a summary of the isotpes, source strengths, and weight fractions of neutron producing isotopes in the fuel.

The associated intrinsic neutron source is included via an MCNP neutron source definition. This definition is found using the ORIGEN-S 0-dimensional irradiation and decay code supplied with the SCALE package from Oak Ridge National Laboratory [17]. The neutron energy spectrum associated with the intrinsic source is shown in Fig. 2-6. The source spectrum results from spontaneous fission of isotopes in the fuel (such as ^{252}Cf)

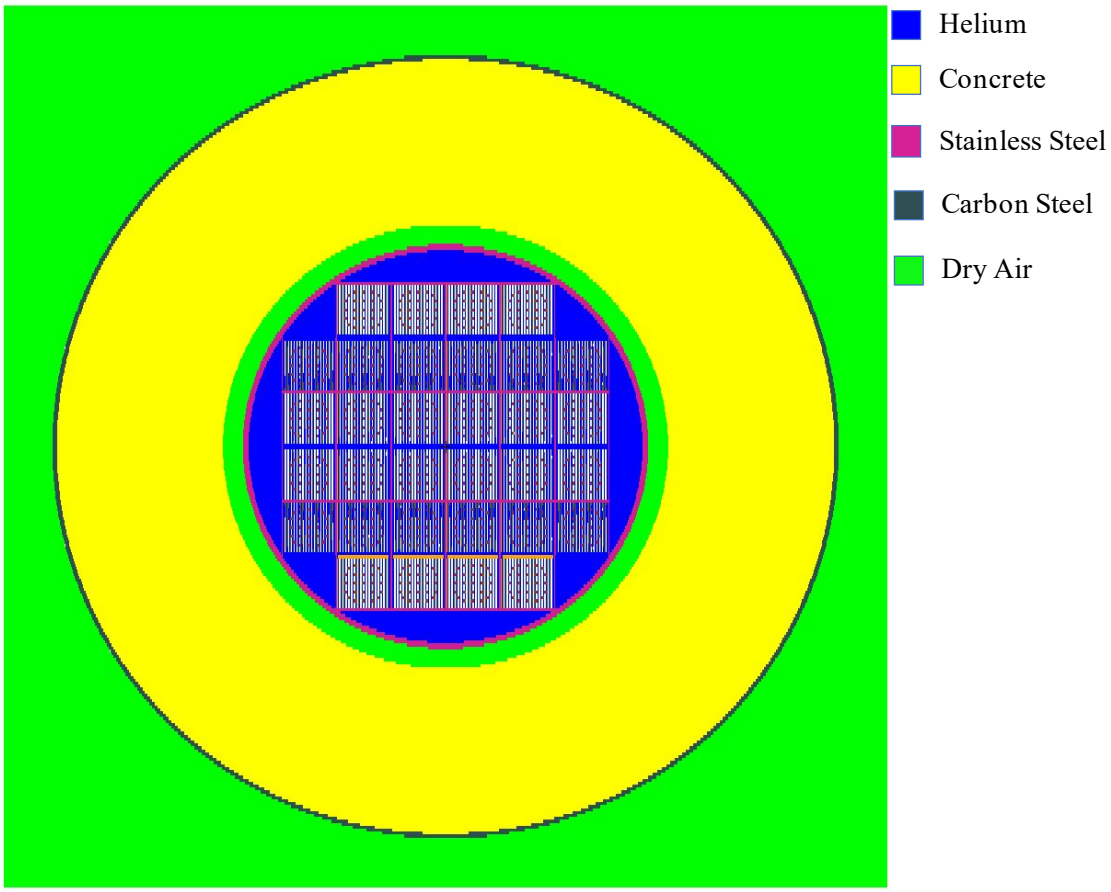

Figure 2-4. The top view of the HI-STORM 100 spent fuel cask modeled in MCNP. This view shows the fuel arrangement of the detailed model. This image shows the extent of geometric details which range from millimeters to meters.

Table 2-1. Summary of fuel source materials caused by (α, n) reactions.

Isotope	**Source strength** $\frac{neutrons}{cm^3 s}$	**Weight Fraction**
^{234}U	5.307E-05	1.087E-03
^{238}Pu	1.743E-01	8.338E-05
^{239}Pu	2.512E-02	0.004
^{240}Pu	4.072E-02	0.002
^{241}Pu	1.222E-04	0.001
^{242}Pu	1.201E-04	3.829E-03
^{241}Am	1.797E-01	2.081E-05
^{243}Am	1.400E-03	6.823E-05
^{242}Cm	1.671E-07	7.585E-06
^{243}Cm	7.315E-04	1.281E-07
^{244}Cm	1.350E-01	1.738E-05

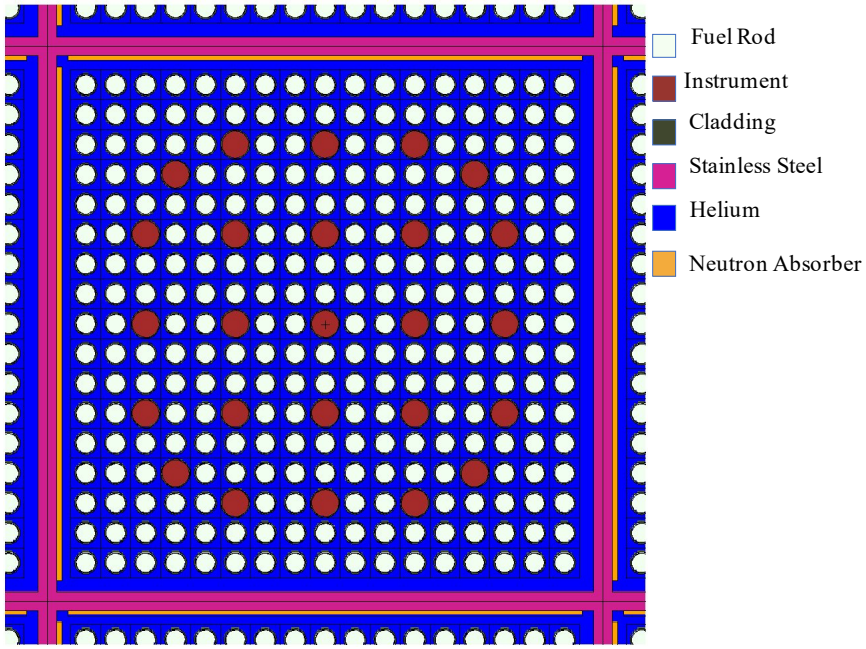

Figure 2-5. The zoomed in image of a single fuel cell cross section in the detailed model. There are neutron absorbing pads (orange rectangles) placed along the interior left and upper faces of the fuel basket (pink regions). Fuel rods (small white circles) include a fuel region, helium gap, and cladding, the helium gap and cladding are not visible in the figure. The larger red circles are the cross sectional view of water cylinders which represent instruments used for monitoring the safety of the HI-STORM 100 spent fuel cask system.

and (α,n) reactions occurring in the irradiated fuel. The maximum neutron intensity occurs at 2.71 MeV. The flux intensity has reduced to nearly 1% of the maximum intensity by 51.4 keV.

Fig. 2-7 depicts the height-averaged scalar neutron flux as a function of radial position within the HI-STORM 100 spent fuel cask predicted using MCNP. The color of the line is related to the material through which the neutron flux is being simulated: fuel is green (the entire area interior to the MPC is considered the fuel region), MPC is blue, air is yellow, concrete is red, and carbon steel is black. The vertical lines designate interfaces between material boundaries; green is the interface between the fuel region and MPC, blue is the interface between the MPC and dry air, yellow is the interface between air and the concrete annulus, red is the interface between concrete and carbon steel,

Table 2-2. Summary of fuel source materials featuring spontaneous fission reactions.

Isotope	**Source strength** $\frac{neutrons}{cm^3 s}$	**Weight Fraction**
^{233}U	1.623E-13	1.791E-09
^{234}U	1.201E-07	1.087E-03
^{235}U	1.123E-08	0.007
^{236}U	2.040E-06	0.003
^{238}U	1.687E-03	0.819
^{237}Np	5.239E-09	2.961E-03
^{238}Pu	3.326E-02	8.338E-05
^{239}Pu	9.692E-06	0.004
^{240}Pu	2.985E-01	0.002
^{241}Pu	1.882E-07	0.001
^{242}Pu	1.005E-01	3.829E-03
^{241}Am	8.223E-05	2.081E-05
^{243}Am	6.827E-06	6.823E-05
^{242}Cm	8.743E-07	7.585E-06
^{243}Cm	3.961E-06	1.281E-07
^{244}Cm	1.906E+01	1.738E-05
^{245}Cm	1.430E-05	8.515E-07
^{246}Cm	9.711E-02	6.809E-08

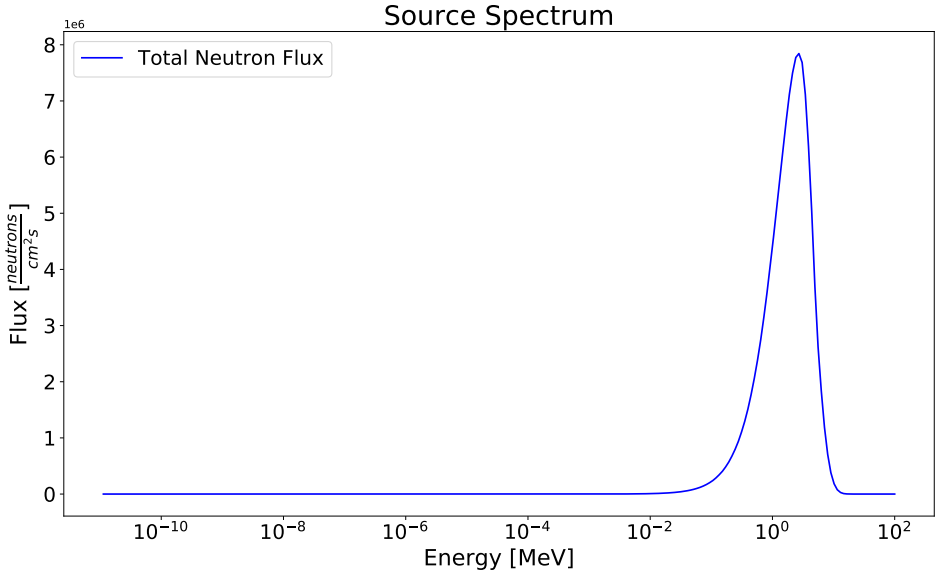

Figure 2-6. The source spectrum used in MCNP simulations. The spectrum is a result of spontaneous fission and (α, n) reactions.

and black is exterior face of the cast. Figure 2-7 shows about half (54%) of the neutron flux is attenuated in the fuel region, and the concrete further reduces the flux by 39%. This result is intuitively sensible: the fuel region is comparatively dense and contains neutron-absorbing materials (e.g., boron), while the thick concrete overpack region is composed principally of highly thermalizing isotopes (e.g., hydrogen). Together, these processes are indicative of the observed dramatic reduction in neutron flux throughout the cask. However, advancing beyond intuition requires definitive answers to a variety of additional questions, namely:

- Are the results correct?
- Could a mistake have been made in the simulation input?
- Was an assumption made that neglected important physics?
- Does the problem include physics or exist in a physical regime outside the viability of the simulated tool used?

While corroborating simulation results with intuition is qualitatively valuable, quantitative or semi-quantitative assessments and their associated effects on confidence in simulation results demands that the preceding questions be comprehensively addressed. The purpose of this work is to answer these questions by 1) identifying key features of the neutron flux spatial distribution as simulated in the detailed model, 2) developing simple physical models to determine the cause of each feature, and 3) gain confidence in the accuracy of the solution and inerrancy of the simulation process. In order to identify features in the neutron flux, each material region in the spent fuel cask is analyzed briefly.

2.2 Analysis of the Detailed Model

2.2.1 Fuel Region

The fuel region of the HI-STORM 100 spent fuel cask features various materials including spent UO_2 nuclear fuel, a stainless steel basket, boron-containing neutron absorbing pads, and helium backfill. The geometric configuration of these materials is highly complex, as depicted in Fig. 2-1. Unfortunately, a single mathematical

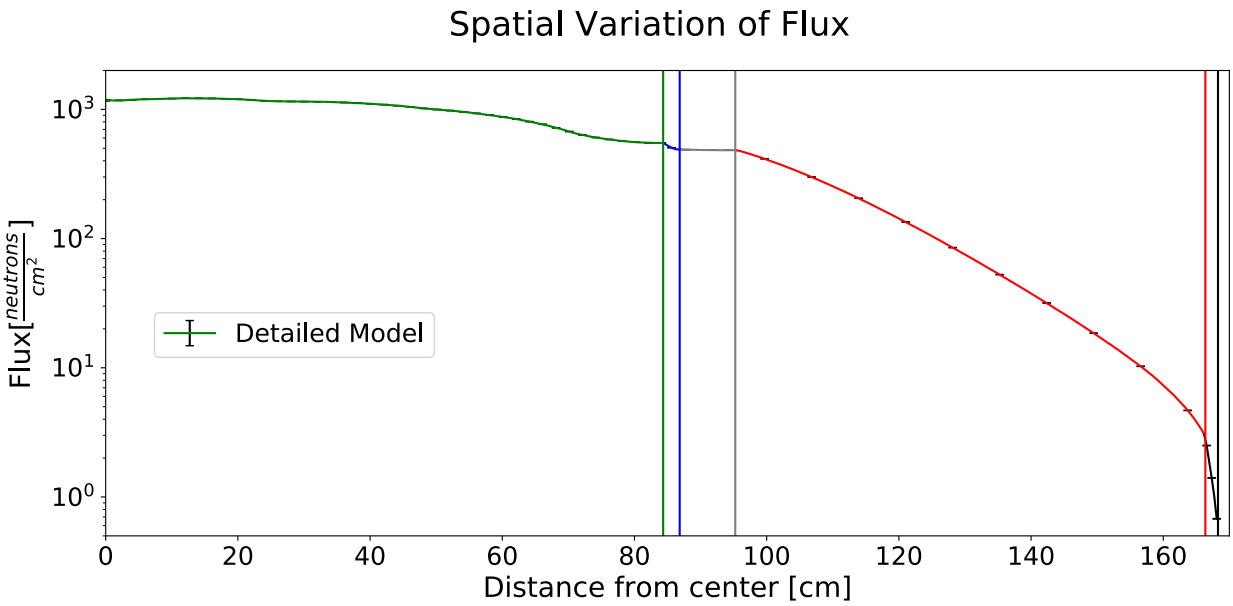

Figure 2-7. The interior neutron flux spatial distribution of the simulated HI-STORM 100 spent fuel cask. The vertical lines represent interfaces between material regions. Error bars are shown along the curve. However, error is converged to less than 1%.

model capable of describing the neutron flux in the fuel region is not analytically tractable. Therefore, a simplified model must be developed using assumptions and approximations derived from physics occurring in the model. In order to identify appropriate simplification, the energy spectrum and angular distribution of the neutron flux and cross section data of various materials are analyzed at various locations in the fuel region.

Figure 2-8 shows the energy spectrum of the neutron flux throughout the spent fuel cask. These plots show the neutron flux has little variation throughout the fuel region. This is a result of evenly distributing fuel rods through the fuel region. Further, the lack of thermalizing materials in the fuel region means there is little change in the energy spectrum. Therefore, it can be assumed that energy dependence of the neutrons can be handled uniformly throughout the fuel region. This is a very helpful assumption that allows for uniform treatment of material properties throughout the fuel region with respect to energy. Unfortunately, there have been no assumptions concerning how to handle

neutron energy-dependence at this point, (e.g., is a monoenergetic method appropriate, or will a different model be required?).

Analysis of the energy spectrum will determine how to best handle energy-dependence. The percent of neutrons above 1 keV varies between approximately 88% at inner radius values to ∼81% at the edge of the fuel region as shown in Figs. 2-8a-2-8h. A monoenergetic handling of the energy-dependence can be assumed since the majority of neutrons have energies between 1 keV and 10 MeV, using an appropriate group weighting spectrum described by Bell and Glasstone [39]. After choosing a method for handing energy-dependence, it becomes necessary to determine a method for handling directional-dependence of the neutron flux.

Figure 2-9 shows the angular distribution of the flux 0.5 cm from the centerline (Fig. 2-9a) and at the edge of the fuel region (Fig. 2-9b). The angular distribution was tallied at these locations to capture the two extents of the angular flux. A perfectly isotropic flux would be a horizontal line with zero slope. If half of the neutron population is traveling in either direction (inward and outward), then the neutron flux can be approximated as isotropic with the understanding that deviations from isotropy will lead to errors in the results. Figure 2-9a shows the neutron flux is slightly inward-peaked 0.5 cm from the centerline with 50.278% of all neutrons traveling toward the centerline. This indicates the flux can be approximated as isotropic near the centerline, a perfectly isotropic flux would have 50% of neutrons scattering toward the center of the fuel region. The flux at the outer edge has an outward peaked flux as shown in Fig. 2-9b. This is because the neutron population density is high in the fuel region, since the source of neutrons is in the fuel region, and neutrons are diffusing, or leaking, out of the fuel region where the neutron population density is lower. The percent of neutrons traveling outward from the fuel region 57.290% at the surface of the fuel region. While, the angular distribution in Fig. 2-9b shows the neutrons are slightly forward peaked, the angular distribution of the neutron flux deviates from isotropic by only ∼7%, thus, can be approximated as isotropic

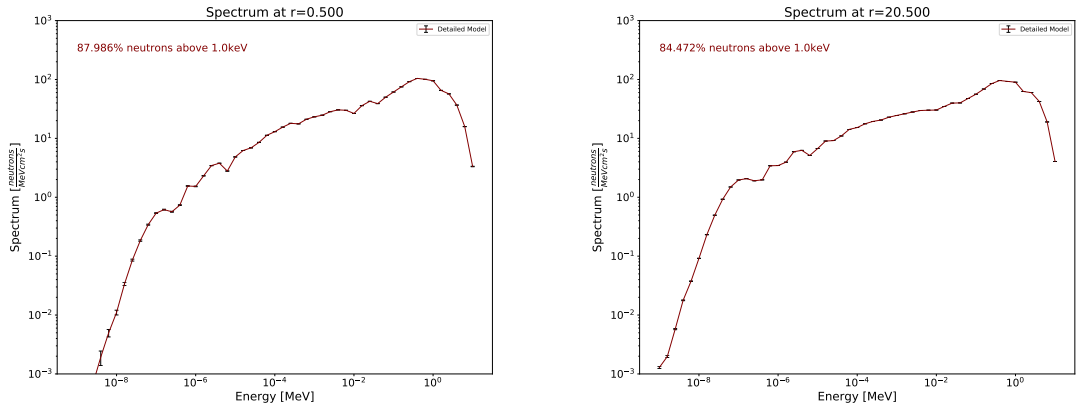

(a)

(b)

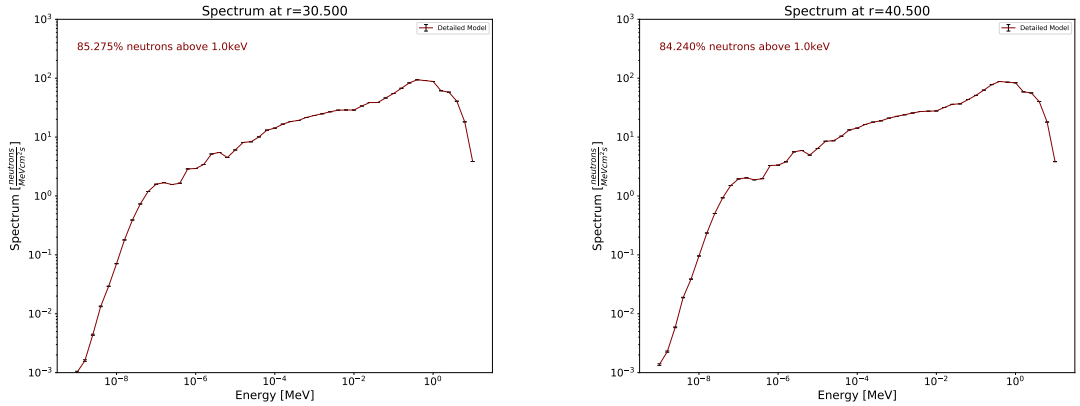

(c)

(d)

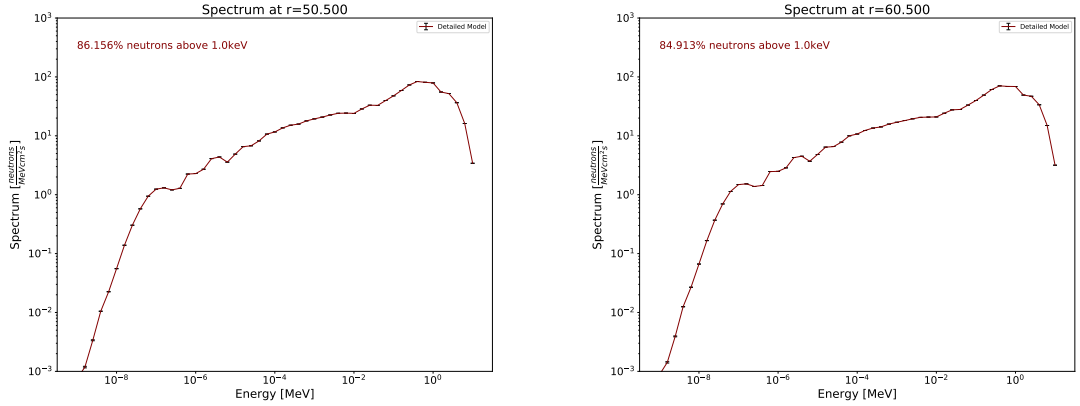

(e)

(f)

Figure 2-8. Energy spectrum of the neutron flux at various locations in the MPC where fuel rods are stored.

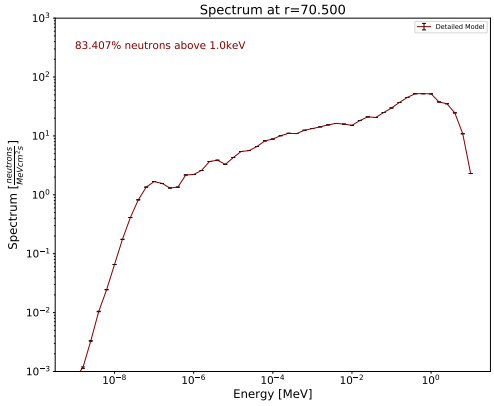

(g)

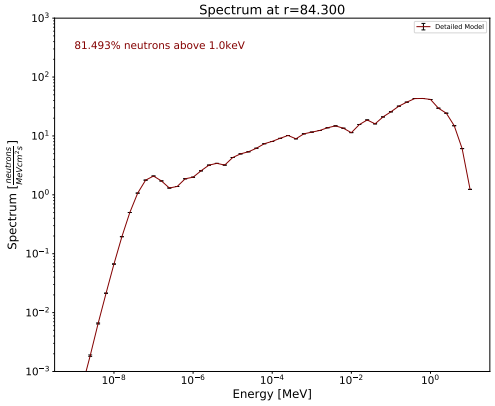

(h)

Figure 2-8. Continued.

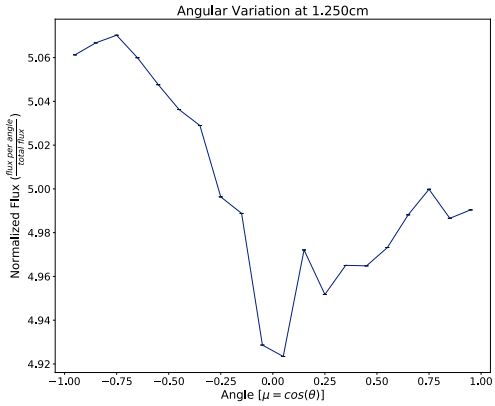

(a)

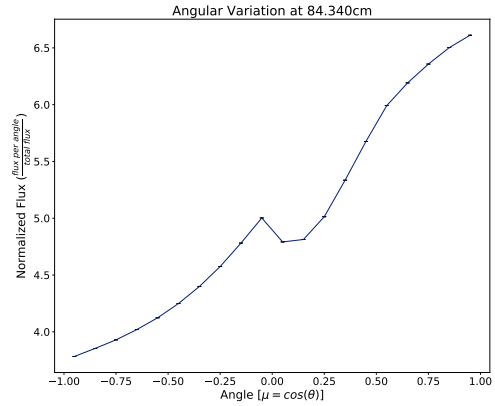

(b)

Figure 2-9. Angular distribution of the neutron flux at 2-9a 0.50 cm and at 2-9b the inner surface of the MPC (84.34 cm) from the centerline of the fuel cask.

with the understanding that this approximation may lead to some disagreement between analytic and computational results.

Figure 2-10 shows the mean-free-path (MFP) of each of the materials in the fuel region. The MFP is the average distance between neutron interactions in a material. Figure 2-10 shows the MFP in the fuel (blue), cladding (orange), helium (green), stainless steel (red), and neutron absorbing material (purple). The source flux is also shown in grey to identify which energy regions are most important (i.e., energy regions where the

source flux is higher are more important). Assessing the MFP of each material helps to identify other assumptions and approximations that aid in determining the appropriate mathematical model to represent the neutron flux. The MFP of helium is about 1 km where the source flux is most intense near 1 MeV. The thickest region of helium occurs between the fuel cells and edge of the fuel region and is on the order of 10 cm thick. The MFP is approximately two orders of magnitude larger, meaning there will be a negligible number of neutrons interacting in helium. The first material assumption is that helium outside of the fuel cells can be neglected.

The remaining materials have a MFP of approximately 1 cm at 1 MeV. These materials show up in the fuel region on the same order, therefore, the remaining materials cannot be neglected. However, since these materials are evenly distributed (i.e., the materials exist throughout the fuel region and not just at a single location) and since the remaining materials have similar MFP's, a homogenization technique can be used to approximated the geometry in the fuel region.

A cylinder shaped homogenous fuel material is made based on the weight ratio of each material in the fuel region. The volume of the homogenous cylinder of fuel material is determined to preserve the volume from the 32 original fuel cells, and the radius of the cylinder is approximately 75 cm. The volume around the cylinder of homogenous fuel is treated as a vacuum in the mathematical model. The radius of the homogenized fuel is about two orders of magnitude greater than the MFP of the materials used in the fuel region (e.g., $\sim$100 cm radius of fuel $>>$ $\sim$1 cm MFP). Hence, the diffusion equation is an appropriate model since the fuel material is much thicker than the neutron's MFP. Therefore, the monoenergetic diffusion equation is an appropriate mathematical model to represent the neutron flux in the fuel region, given the previous identified assumptions and approximations derived from physical properties of materials in the fuel region.

A monoenergetic diffusion approximation is an appropriate choice of an analytic model for the fuel region, however, that may not be the case for other materials in the

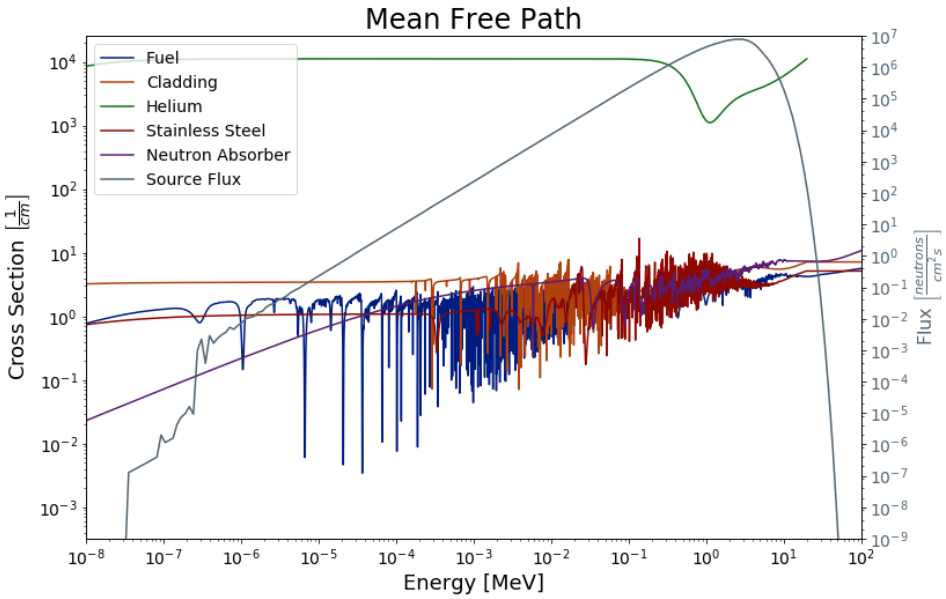

Figure 2-10. The mean-free-path, or distance between interactions, of the materials in the fuel region. The source flux is provided in order to identify energy ranges of greater importance.

cask. It is important to identify how the flux behaves in the remaining materials of the fuel cask and to identify appropriate models.

2.2.2 Stainless Steel MPC

The MPC encompasses the fuel area in a 2.5 cm thick stainless steel 304 cylindrical container. Figure 2-11 shows the MFP in stainless steel 304, where MFP implies the neutron MFP. The most important thing to notice from the figure is that the MFP is on a similar order of magnitude as the thickness of the MPC. The diffusion equation is not an appropriate model when a material's thickness is fewer than a couple MFP's thick. Therefore, the diffusion approximation is unlikely to be an appropriate mathematical model within the MPC. Instead, the multigroup discrete ordinates equation is a better approximation in this situation.

The number of energy groups and angles required to adequately model neutron transport in the stainless steel is still needed. Analyzing the energy spectrum at the interior and exterior surface of the MPC aids in finding an appropriate number of energy

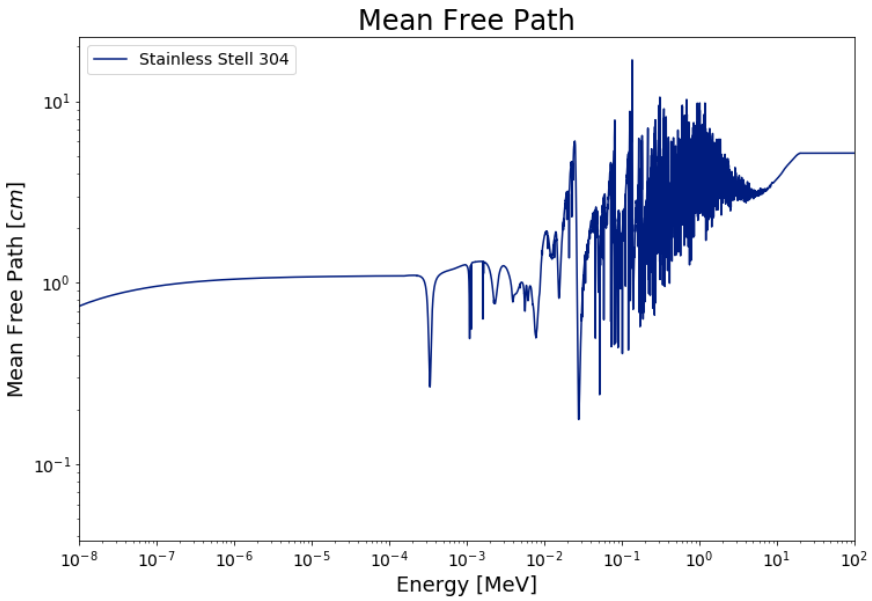

Figure 2-11. The mean-free-path of neutrons in stainless steel 304.

groups. Figure 2-12 shows the neutron energy spectrum at the interior surface (Fig. 2-12a) and exterior surface (Fig. 2-12b) of the MPC. At the interior surface of the MPC, the neutron flux is ∼81% above 1 keV and a single energy model would be appropriate. This would be preferable since the group structure in the MPC would match the energy group boundaries in the fuel region. However, the number of slow neutrons increases throughout the thickness of the MPC, and Fig. 2-12b shows that ∼70% of neutrons are above 1 keV. Hence, a two group analytic model is preferable.

Analysis of the angular distribution (Fig. 2-13) helps to determine the number of angles to use in the multigroup discrete ordinates approximation. Figure 2-13a is the angular distribution of the flux at the interior surface of the MPC. Approximately 57% of the neutrons are forward scattering at this point in the MPC. In the fuel region, the flux is considered isotropic even though over half of the neutrons are traveling away from the centerline near the outer surface of the cask. This is an acceptable approximation since there exist locations in the fuel region that feature near-isotropic neutron flux distributions. However, the neutron flux in the stainless steel is only forward-pointed,

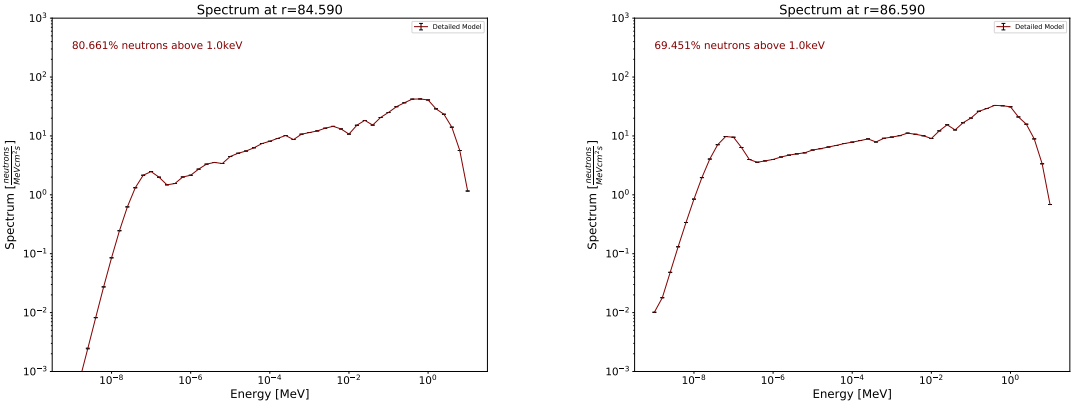

(a) (b)

Figure 2-12. The neutron energy spectrum at a) 84.590 cm and b) 86.590 cm in the stainless steel MPC.

which alludes to using two angles to approximate the neutron flux. Finally, the multigroup discrete ordinates approximation with two energy groups and two angles is chosen to model neutron transport within the stainless steel.

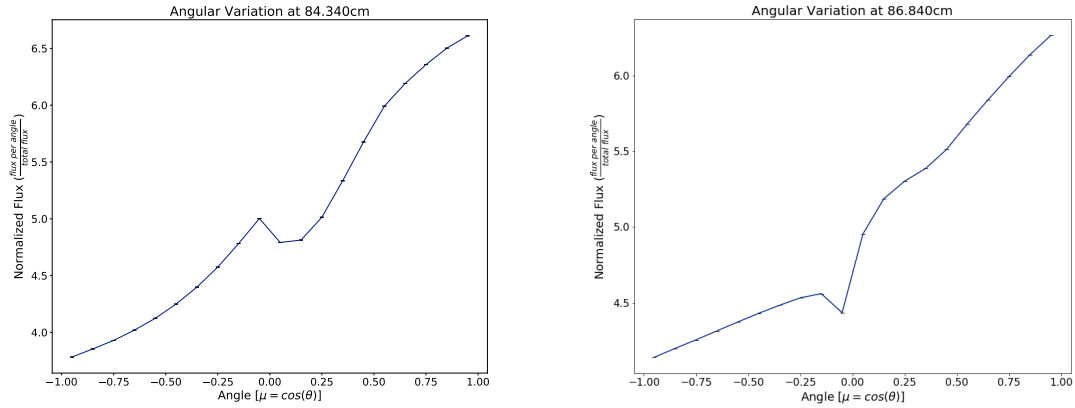

(a) (b)

Figure 2-13. The neutron angular distribution at the a) inner surface and b) outer surface of the MPC.

2.2.3 Dry Air Gap

Surrounding the MPC is a gap of dry air for heat removal from the fuel. Figure 2-14 shows the mean-free-path of neutrons in dry air. The MFP is two orders of magnitude

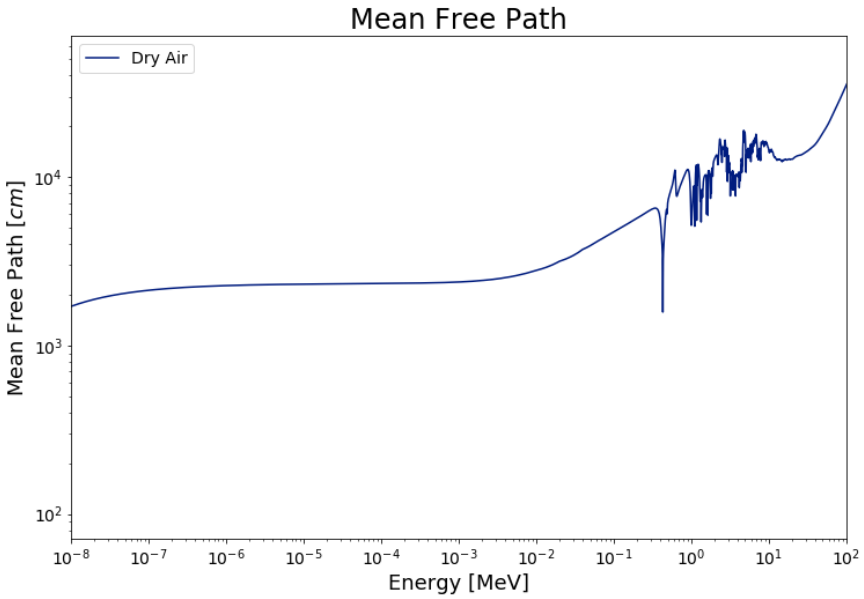

Figure 2-14. The mean-free-path of neutrons in the air gap. The low density of gaseous air leads to a high MFP. The air gap can be treated as a streaming region since the MFP is much larger than the thickness of the air gap.

larger than the thickness of the air gap (∼10 cm). Meaning, the air gap can be treated as a vacuum and there is no need for a mathematical model in this region when modeled in a planar geometry. The air region is treated in a planar geometry as the thickness of the air region is small as compared to the distance which the air region is located from the centerline (approximately $\frac{1}{9}$). The MCNP results confirm this assumption as 97.653% of the flux is preserved through the air gap, meaning the flux is left relatively unchanged. Further discussion concerning geometric coordinate systems is provided in Sec. 3.2.

2.2.4 Concrete Annulus

The 71.120 cm thick concrete annulus provides nearly half the neutron shielding capabilities in the spent fuel cask due to scattering on hydrogen. Following a similar method as before, the MFP of neutrons in concrete are investigated. Concrete, being a thermalizing material, is expected to change the neutron energy spectrum through down-scattering neutrons, so both fast and thermal energies need to be taken into account when analyzing Fig. 2-15. At higher energies, 1 MeV, the concrete is about 7 MFP's

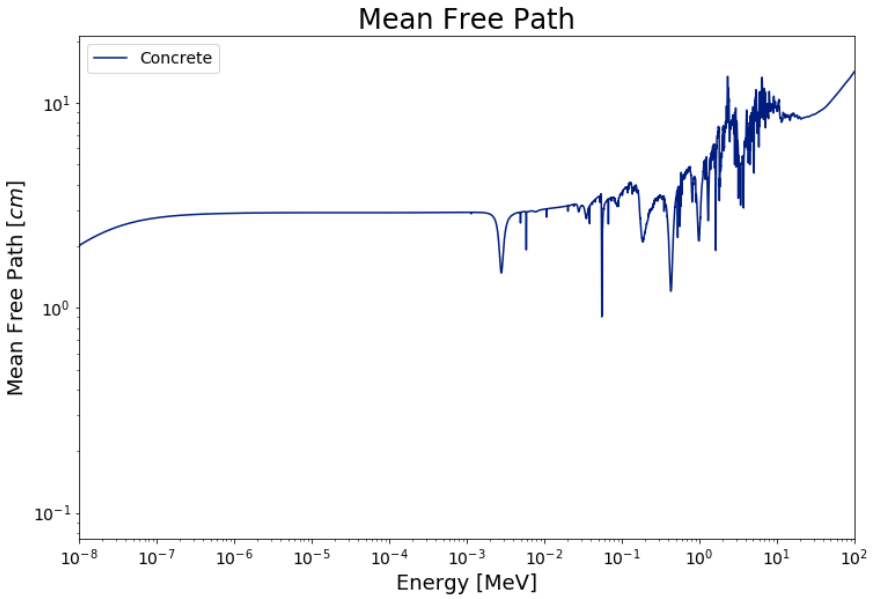

Figure 2-15. The mean-free-path of neutrons in the concrete annulus.

thick. Therefore, diffusion may not be an appropriate model for these energies of neutrons. However, at lower energies, 1 eV, the concrete is about 35 MFP's thick. At lower energies, the diffusion approximation is an appropriate model. Overall, analysis of Fig. 2-15 would indicate that a multigroup discrete ordinates approximation would be better suited as an analytic model in the entire concrete. Further investigation of the neutron energy spectrum and angular distribution will aid in solidifying a model choice.

The energy spectrum does change significantly over the thickness of the concrete annulus. Figure 2-16a shows the neutron energy spectrum at the inside surface of the concrete annulus. The neutron flux is ∼63% above 1 keV at the innermost surface of the concrete. The neutron flux is quickly thermalized and approximately a third of the neutron flux is above 1 keV after the neutrons have traveled ten centimeters into the concrete (Fig. 2-16b). At the exiting surface, less than 8% of the neutrons remain above 1 keV as shown in Fig. 2-16h. The large change in neutron energies means more than one energy group will be required to model transport in concrete. The shape of the flux shows the presence of two local maxima in the neutron energy spectrum that occur throughout

the concrete region, one near 1 MeV and the other near 0.1 eV. Therefore, a two energy group model is expected to be adequate. Analysis of the angular distribution will indicate the number of angles necessary for the multigroup discrete ordinates model.

Figure 2-17 show the angular distribution at the entering and exiting surfaces of the concrete annulus. Analysis of the angular distribution shows the neutron flux is forward-peaked with ∼55% of the neutrons traveling outward at the inner surface of the concrete annulus. At the exiting surface, ∼68% of the neutrons are traveling outward. At the interior surface, the flux deviates from isotropic by 5%. Therefore two angles are assumed to be adequate for capturing the neutron flux with the expectation that the analytic model may show higher disagreement at the exiting surface of the concrete.

2.2.5 Carbon Steel Outer Shell

The 1.905 cm thick carbon steel shell is the final material being analyzed in the spent fuel cask. Using a similar analysis as with previous materials, the MFP is compared to the thickness of the steel shell to aid in determining a mathematical model. Figure 2-18 shows the MFP of neutrons in carbon steel. The most probable energy of neutrons leaving entering the carbon steel shell is about 0.1 MeV, shown in Fig. 2-16h. Using this information, the most probable MFP of neutrons in the carbon steel shell is ∼1 cm. This is on the order of the magnitude of the carbon steel shell thickness. Therefore, the diffusion equation is likely a poor choice of mathematical model and the multigroup discrete ordinates equation is likely a better choice.

Figure 2-19 shows the energy spectrum at the inner surface (Fig. 2-19a) and outer surface (Fig. 2-19b). The percentage of fast neutrons increases in the carbon steel, further discussion of this effect is provided in Sec. 7.1.4. For this reason, two energy groups should be used to model the neutron flux in the carbon steel.

Finally, the angular distribution graphs of the neutron flux entering the carbon steel (Fig. 2-20a) and leaving the carbon steel shell (Fig. 2-20b) show the neutron flux is forward peaked. In fact, at the inner carbon steel surface ∼68% of the flux is traveling

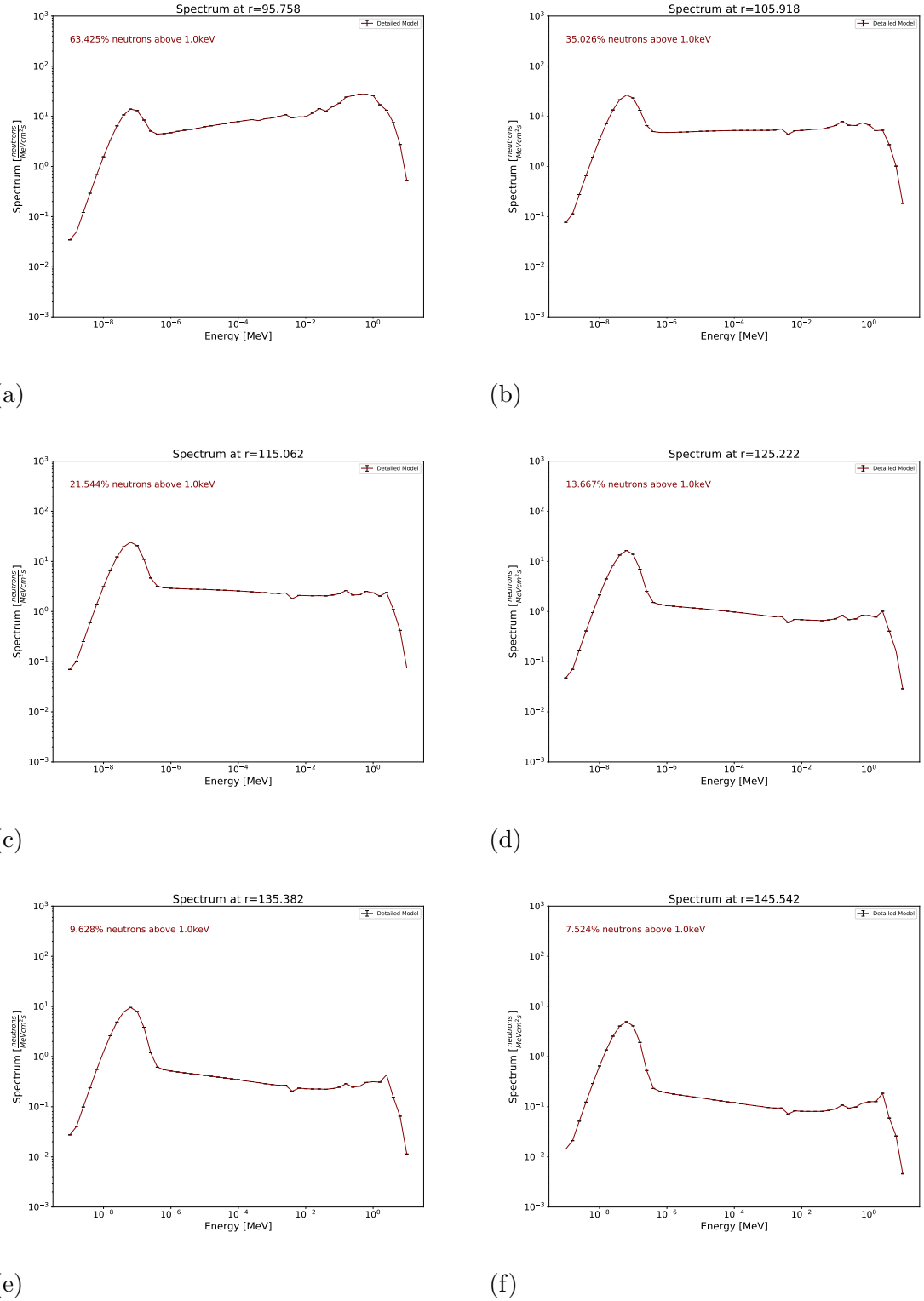

Figure 2-16. Energy spectrum of neutrons throughout the concrete annulus.

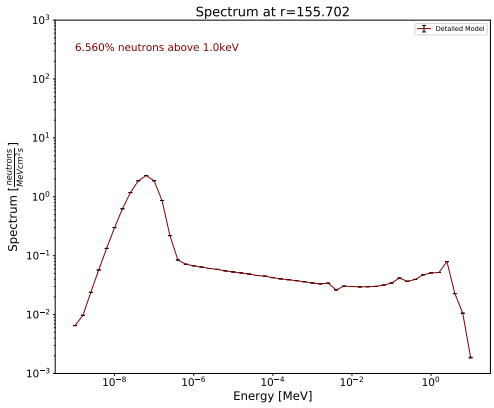

(g)

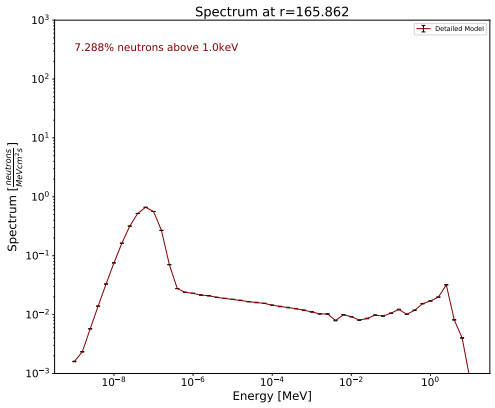

(h)

Figure 2-16. Continued.

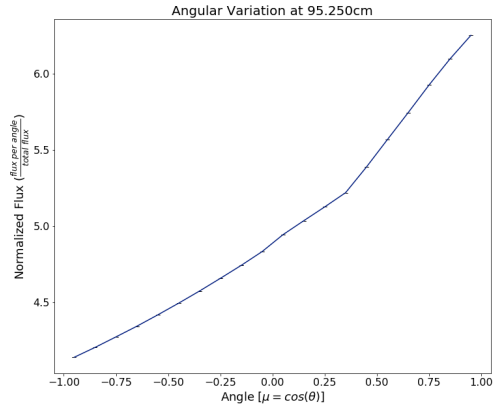

(a)

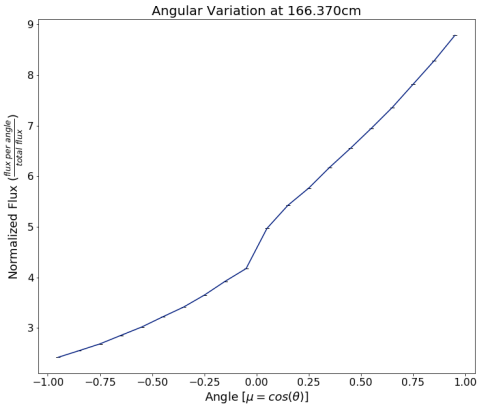

(b)

Figure 2-17. The angular distribution of the neutron flux at a) the inner surface (95.250 cm) and the b) outer surface (166.370 cm) of the concrete annulus.

outward and that fraction increases to ∼97% of neutrons traveling outward at the exiting surface of the cask. Nearly all of the neutrons are traveling away from the cask because the cask is placed in dry air. As shown previously, the MFP of neutrons in dry air is large, greater than 1 km, resulting in a small number of neutrons returning to the cask after leaving. The small number of returning neutrons provides boundary condition information for the final model. Therefore, the outermost boundary of the spent fuel cask can be treated as non-reentrant. The most simplistic analytic models are revealing of salient

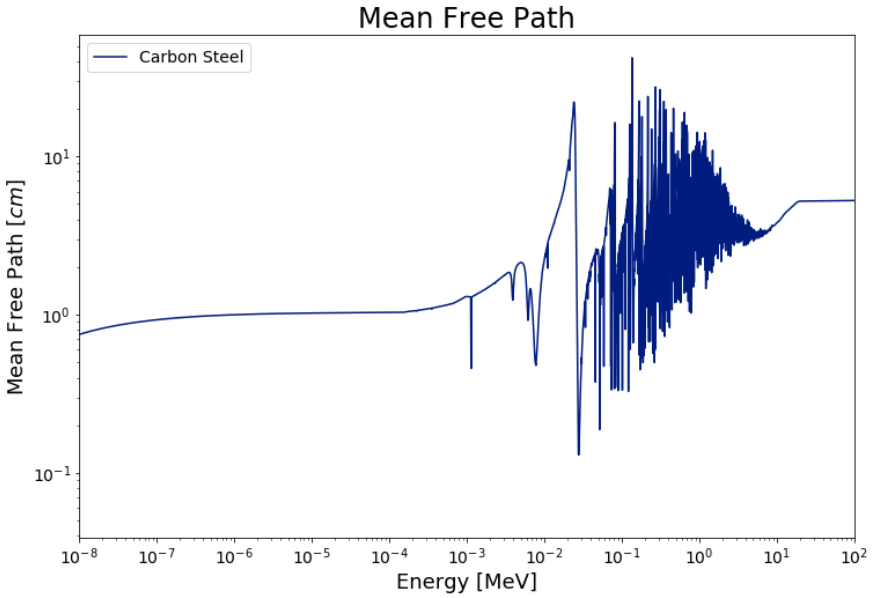

Figure 2-18. The mean-free-path of neutrons in carbon steel.

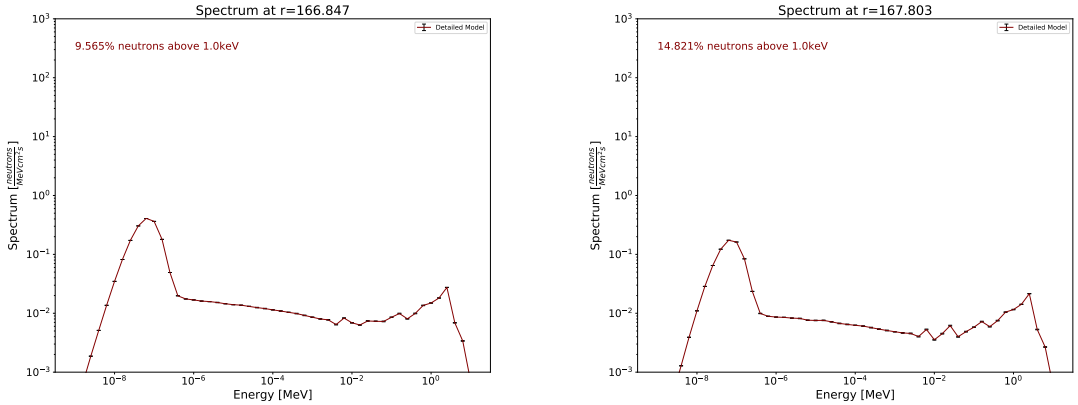

(a) (b)

Figure 2-19. The neutron energy spectrum near the a) inner surface (166.847 cm) and the b) outer surface (167.803 cm) of the carbon steel shell. The two peaks in each figure allude to a two energy group model.

physics. As using two angles are chosen for the other materials, a two angle model is also chosen for the stainless steel.

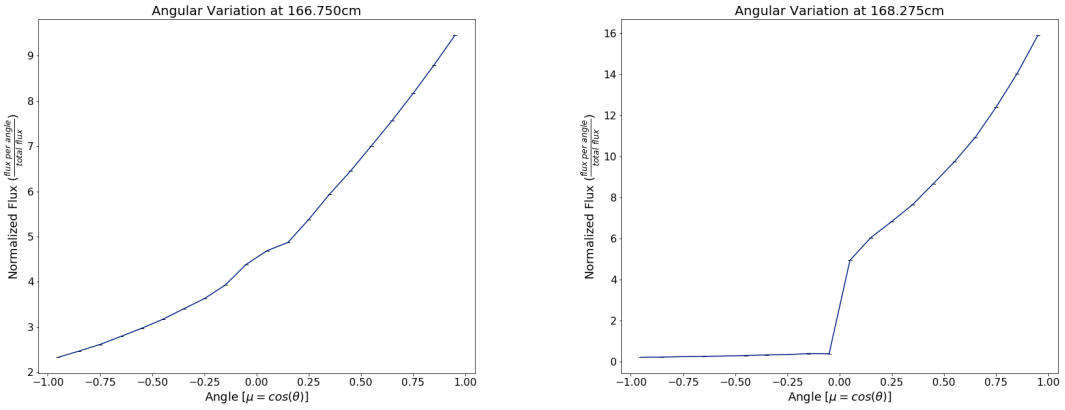

(a) (b)

Figure 2-20. The angular distribution of the neutron flux at the a) inner surface and b) outer surface of the carbon steel shell. Since the flux is heavily forward-pointed, two directions can be used to model the flux.

By no means are the previous choices in analytic models meant to be the most exhaustive means of describing the neutron flux in each material. Rather, choices were made in order to keep the models as simplistic as possible while capturing the physics of the spent fuel cask in an attempt to highlight inherent phenomena in the problem. As will be seen during the sensitivity analysis portion of the work, even these simplistic models yield complex sensitivity results. Therefore, identifying any physical meaning using the analytic models becomes challenging, if possible, even when using very simple models. Chapter 4 compares the results of the analytic models (derived in Chp. 3), reduced-fidelity models, and the detailed model.

2.3 Identification of Features

"Features" are locations in the simulated neutron flux spatial distribution shown in Fig. 2-7 which appear to be the result of a physical process. Using a reduced complexity analytic or computational model to reproduce a feature yields two benefits: 1) the physical process that generates the feature in question is identified and, 2) confidence is gained in

the accuracy of the simulation result. Confidence in the simulation result is gained when a feature is determined to be a result of an understood physical process. That is, the feature should exist in the problem, is being modeled correctly in the code, and is not a computational artifact. Ensuring agreement between simplified and complex models also corroborates the accuracy of the simulation input itself. Something as simple as inputing an incorrect area or volume would not result in a fatal error message in MCNP, but would lead to incorrect neutron flux results. The process of reproducing features using simplified analytic and computational models provides an opportunity to identify errors in the simulation input and addressing these errors leads to increased confidence in the accuracy of a simulation.

There are five features discussed in this effort which are identified as:

1. The "flat" flux region (highlighted in Fig. 2-21): The flux in this region smoothly decreases by approximately 36% even though intuition suggests the flux should increase in the fuel pins and decrease in the space between fuel pins.
2. The abrupt level-off region (highlighted in Fig. 2-22): The flux only decreases ∼3 % over the region 65.000 cm $\leq r \leq$ 84.100 cm from the cask centerline.
3. Periodic depressions (highlighted in Fig. 2-23): There is a ∼2% reduction in the flux near 25 cm, 50 cm, and 75 cm from the cask centerline.
4. The asymmetric flux: Figure 2-24 is a density plot of the neutron flux when looking at a center slice of the cask from above. Figure 2-25 is a contrast plot to better illustrate the neutron flux asymmetry present in Fig. 2-24. The neutron flux in the upper left section (above the diagonal line) of the plot is less than the neutron flux in the lower right section (below the diagonal line) of the image. This asymmetry is most obvious at the outer edge of the fuel region.
5. The concrete flux (Fig. 2-26): The concrete region provides the second-most significant reduction in the neutron flux within the cask. Identifying the processes

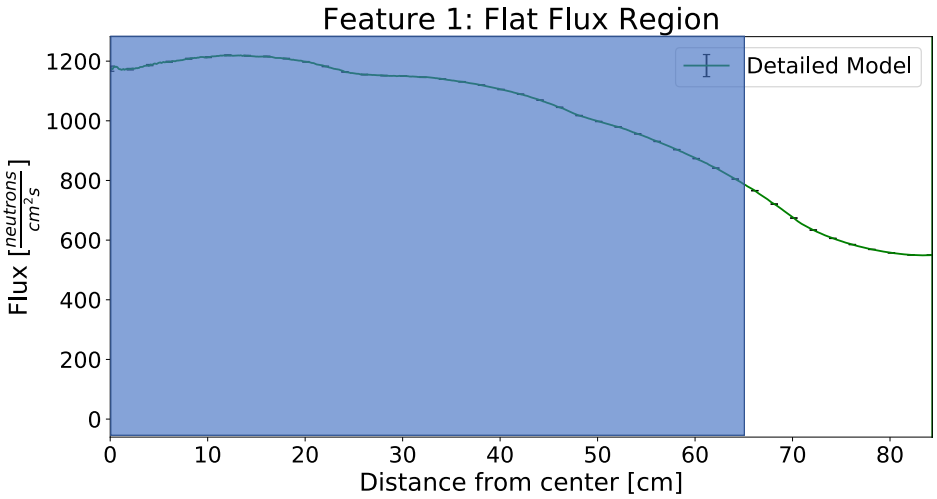

Figure 2-21. The neutron flux spatial distribution between the cask centerline and inner face of the MPC. The highlighted region is considered the flat flux region. This neutron flux is relatively flat and does not vary on the same order as the physical dimensions of materials in this region.

which attenuate radiation in this region provides evidence the overpack was modeled correctly.

Beyond investigating these features, the neutron flux in the MPC and carbon steel shell are also investigated.

The remaining chapters will discuss how the results assessment methodology is used to identify the salient physics in each of the previously identified features, as well as, how confidence is gained in the simulation results of the detailed model through sensitivity analysis. However, the next chapter will provide an in-depth background on neutron transport theory and the development of the analytic models which will be used in the analysis provided in Chpt. 4.

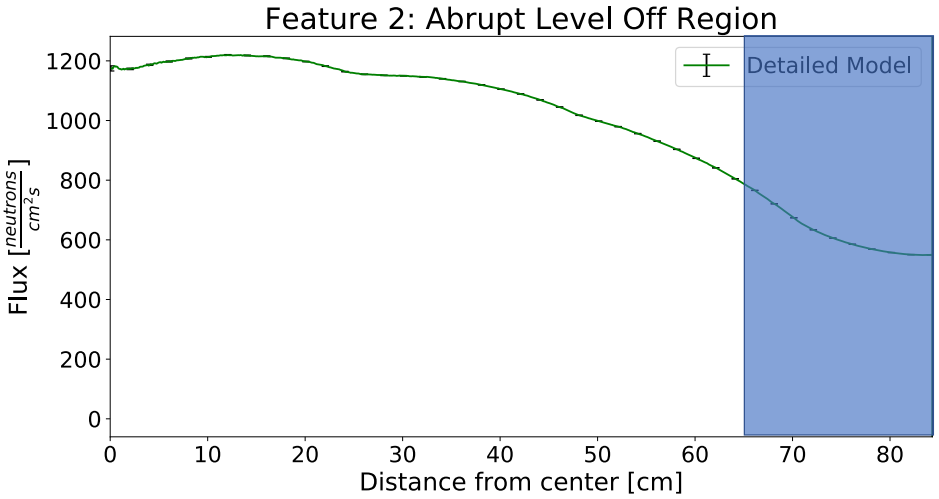

Figure 2-22. The flux stops decreasing and instead levels-off in the abrupt level-off region. The flux decreases less than 3% over the last ten centimeters before the interface between the fuel region and MPC.

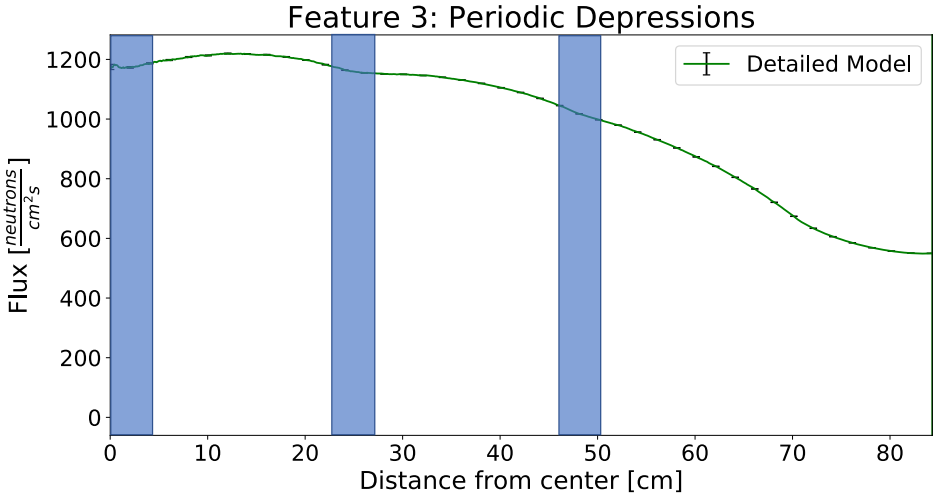

Figure 2-23. There are three depressions in the neutron flux spatial distribution located approximately 22 cm apart. The flux decreases about 2% at each depression.

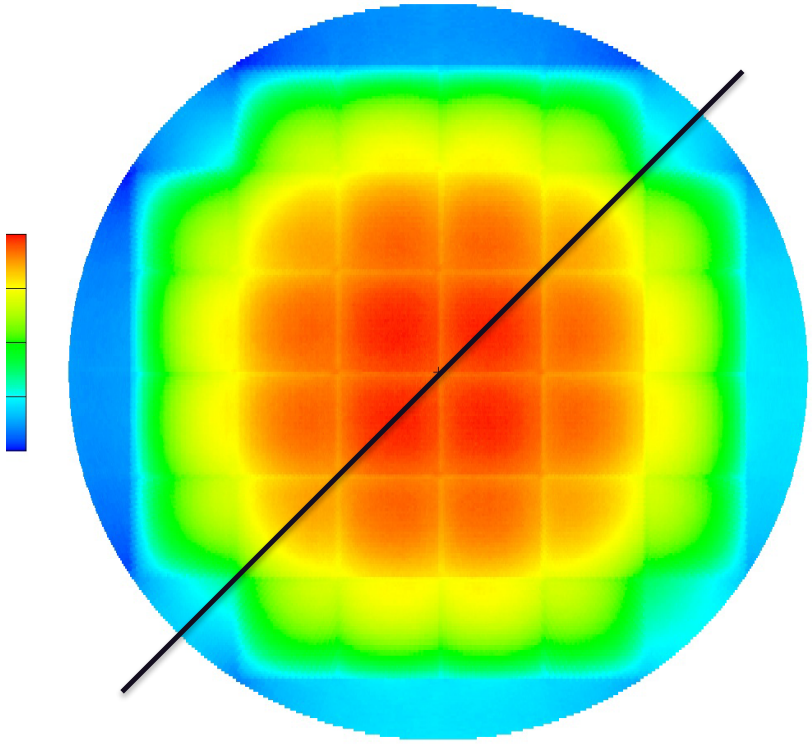

Figure 2-24. A density plot of the neutron flux at a "central slice" of the fuel cask as viewed from above. This plot shows the neutron flux is less in the upper left section than in the lower right section. The asymmetry is most evident in the blue and light blue sections at the outer radius of the figure.

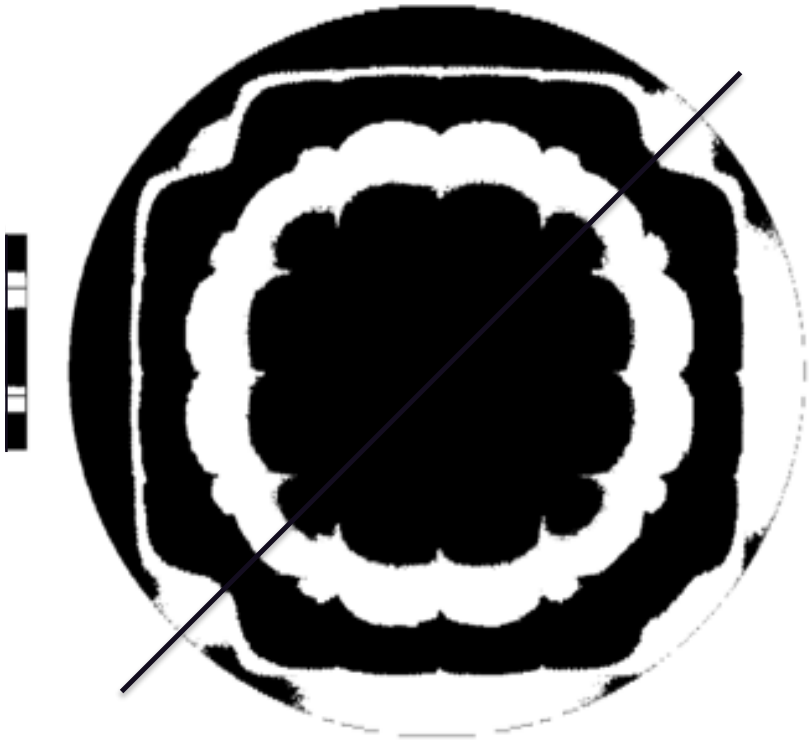

Figure 2-25. A contrast plot emphasizing the asymmetry of the flux values.

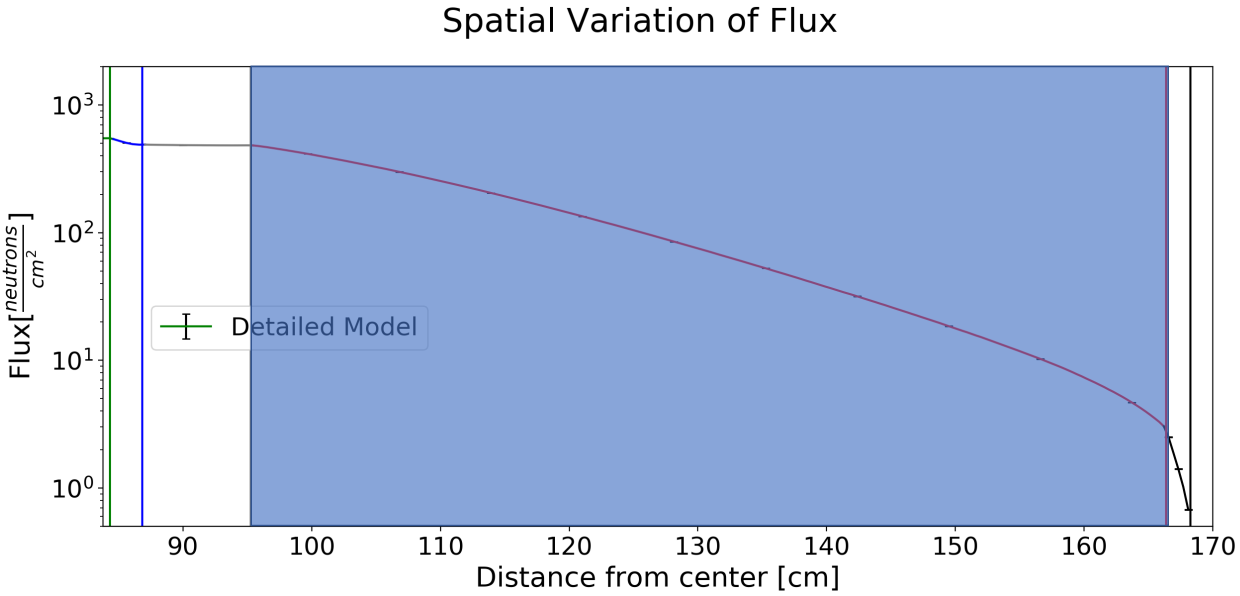

Figure 2-26. The overpack accounts for about half of the reduction to the neutron flux. The purpose of investigating this region is to determine which physical processes are responsible for the attenuation.

CHAPTER 3
THEORY

The behavior of any nuclear system is governed by the distribution of radioactive particles within the system. In the case of a system containing neutrons, the distribution of neutrons can be found by solving the neutron transport equation (NTE). The NTE is also referred to as the Boltzmann transport equation because of its similarity to Boltzmann's equation governing the kinetic theory of gas [40]. Finding an analytic solution of the NTE for even the simplest geometries is a challenging task, since the equation is an integro-differential equation defined over a seven variable phase space. However, the application of assumptions and approximations to the energy and directional dependence of the neutron flux lead to tractable equations. The NTE is derived before applying assumptions and simplifications to reduce the NTE into two, distinct tractable approximations; known as (1) the diffusion approximation and (2) the multigroup discrete ordinates equations.

Before deriving the NTE, it is important to define terms which will be used. The neutron angular density,

$$N(\boldsymbol{r}, \hat{\boldsymbol{\Omega}}, E, t), \tag{3-1}$$

describes the expected number of neutrons in the region of phase space defined by a neutron's position vector $\boldsymbol{r}$, direction of travel $\hat{\boldsymbol{\Omega}}$, and kinetic energy E at time t. It follows that the expected number of neutrons at time t in a volume element $\mathrm{d}V$ having energies in $\mathrm{d}E$ about E and directions within a narrow beam $\mathrm{d}\hat{\boldsymbol{\Omega}}$ about $\hat{\boldsymbol{\Omega}}$ can be described by

$$N(\boldsymbol{r}, \hat{\boldsymbol{\Omega}}, E, t)\,\mathrm{d}V\,\mathrm{d}\hat{\boldsymbol{\Omega}}\,\mathrm{d}E. \tag{3-2}$$

The angular flux is defined as the product of speed v and the number of neutrons,

$$\boldsymbol{\varphi}(\boldsymbol{r}, \hat{\boldsymbol{\Omega}}, E, t) = vN(\boldsymbol{r}, \hat{\boldsymbol{\Omega}}, E, t). \tag{3-3}$$

Using the angular flux, the reaction rate is defined as

$$R_x(\boldsymbol{r}, \hat{\boldsymbol{\Omega}}, E, t) = \Sigma_x(\boldsymbol{r}, \hat{\boldsymbol{\Omega}}, E, t)\boldsymbol{\varphi}(\boldsymbol{r}, \hat{\boldsymbol{\Omega}}, E, t) \tag{3-4}$$

where $R_x(\boldsymbol{r}, \hat{\boldsymbol{\Omega}}, E, t)$ is the frequency of interactions between neutrons and surrounding materials. The parameter $\Sigma_x(\boldsymbol{r}, \hat{\boldsymbol{\Omega}}, E, t)$ is called the macroscopic cross section for reaction "x" (e.g., total reaction cross section, absorption cross section, scattering cross section). The macroscopic cross section describes the probability of an interaction occurring per unit length as a function of incoming neutron energy. The cross section dependence on t and $\hat{\boldsymbol{\Omega}}$ are treated by assuming the composition of the material slowly changes in time and nuclear reactions are invariant to incoming neutron angle respectively.

3.1 Derivation of the Boltzmann Transport Equation for Neutrons by Derivatives

The NTE can be derived by "following" a group of neutrons, referred to as a packet, through a material and describe how neutrons are gained or lost in time [39]. Neutrons with energy E are lost from the packet as a result of a collision over the distance $v\Delta t$, whereas neutrons that do not interact over the distance $v\Delta t$ remain in the packet. The probability of a neutron being removed from the packet over the distance $v\Delta t$ can then be written as

$$\begin{matrix}\text{Probability of a neutron} \\ \text{being removed from the packet}\end{matrix} \equiv \Sigma_t(\boldsymbol{r}, E)v\Delta t, \tag{3-5}$$

and the probability of a neutron remaining in the packet over the distance $v\Delta t$ is defined as

$$\begin{matrix}\text{Probability of a neutron} \\ \text{remaining in the packet}\end{matrix} \equiv 1 - \Sigma_t(\boldsymbol{r}, E)v\Delta t. \tag{3-6}$$

Using 3-6, the number of neutrons remaining in the packet after traveling a small distance of $v\Delta t$ is

$$\begin{matrix}\text{Number of neutrons} \\ \text{remaining in packet}\end{matrix} \equiv N(\boldsymbol{r}, \hat{\boldsymbol{\Omega}}, E, t)[1 - \Sigma_t(\boldsymbol{r}, E)v\Delta t]\,\mathrm{d}V\,\mathrm{d}\hat{\boldsymbol{\Omega}}\,\mathrm{d}E. \tag{3-7}$$

Eqn. 3-7 adjusts the neutron population accounting for neutrons which left the packet through interactions, however, neutrons can enter the packet through two mechanisms: 1) internal neutron source or 2) by scattering from one packet into another. The number of neutrons which enter the packet from an internal neutron source is given by

$$\begin{pmatrix}\text{Number of neutrons entering}\\ \text{packet from internal sources}\end{pmatrix} \equiv S(\boldsymbol{r},\hat{\boldsymbol{\Omega}},E,t)\,\mathrm{d}V\,\mathrm{d}\hat{\boldsymbol{\Omega}}\,\mathrm{d}E\Delta t. \tag{3-8}$$

Neutrons can also enter the packet through scattering interactions, called inscattering. An inscattering reaction occurs when a neutron belonging to the packet described by a volume element $\mathrm{d}V$ with energies in $\mathrm{d}E'$ about E' and directions within $\mathrm{d}\hat{\boldsymbol{\Omega}}'$ about $\hat{\boldsymbol{\Omega}}'$ undergoes a scattering event leaving the neutron traveling in $\mathrm{d}\hat{\boldsymbol{\Omega}}$ about $\hat{\boldsymbol{\Omega}}$ with energy in $\mathrm{d}E$ about E, adding this neutron to the packet $(\boldsymbol{r},\hat{\boldsymbol{\Omega}},E,t)$. The probability of neutrons with energy E' and direction $\hat{\boldsymbol{\Omega}}'$ which scatter into the energy $E+\mathrm{d}E$ with direction in $\hat{\boldsymbol{\Omega}}+\mathrm{d}\hat{\boldsymbol{\Omega}}$ can be written as:

$$\begin{pmatrix}\text{Probability of neutrons entering}\\ \text{packet due to inscattering}\end{pmatrix} \equiv \Sigma_s(\boldsymbol{r},\hat{\boldsymbol{\Omega}}'\rightarrow\hat{\boldsymbol{\Omega}},E'\rightarrow E,t)vN(\boldsymbol{r},\hat{\boldsymbol{\Omega}}',E',t). \tag{3-9}$$

Integrating definition 3-9 over all initial energies $\mathrm{d}E'$ and initial directions $\mathrm{d}\hat{\boldsymbol{\Omega}}'$ yields the number of neutrons that enter the packet due to inscattering,

$$\begin{pmatrix}\text{Number of neutrons entering}\\ \text{packet due to inscattering}\end{pmatrix} \equiv \left[\int_{4\pi}\mathrm{d}\hat{\boldsymbol{\Omega}}\int_0^\infty \mathrm{d}E\Sigma_s(\boldsymbol{r},\hat{\boldsymbol{\Omega}}'\rightarrow\hat{\boldsymbol{\Omega}},E'\rightarrow E,t)vN(\boldsymbol{r},\hat{\boldsymbol{\Omega}}',E',t)\right]\mathrm{d}V\,\mathrm{d}\hat{\boldsymbol{\Omega}}\,\mathrm{d}E\Delta t. \tag{3-10}$$

The neutron density at $\boldsymbol{r}+\hat{\boldsymbol{\Omega}}v\Delta t$ at time $t+\Delta t$ is found by adding 3-7, 3-8, and 3-10 and before dividing the sum by $\mathrm{d}V\,\mathrm{d}\hat{\boldsymbol{\Omega}}\,\mathrm{d}E$:

$$\begin{aligned}N(\boldsymbol{r}+\hat{\boldsymbol{\Omega}}v\Delta t,\hat{\boldsymbol{\Omega}},E,t+\Delta t) = \\ N(\boldsymbol{r},\hat{\boldsymbol{\Omega}},E,t)(1-\Sigma_t v\Delta t) \\ +\left[\int_{4\pi}\mathrm{d}\hat{\boldsymbol{\Omega}}'\int_0^\infty \mathrm{d}E'\Sigma_s(\boldsymbol{r},\hat{\boldsymbol{\Omega}}'\rightarrow\hat{\boldsymbol{\Omega}},E'\rightarrow E,t)N(\boldsymbol{r},\hat{\boldsymbol{\Omega}}',E',t)\right]\Delta t + S(\boldsymbol{r},\hat{\boldsymbol{\Omega}},E,t)\Delta t.\end{aligned} \tag{3-11}$$

Dividing Eqn. 3-11 and taking the limit as $\Delta t \to 0$ yields the result, after rearranging terms,

$$\lim_{\Delta t \to 0}\left[\frac{N(\boldsymbol{r}+\hat{\boldsymbol{\Omega}}v\Delta t,\hat{\boldsymbol{\Omega}},E,t+\Delta t)-N(\boldsymbol{r},\hat{\boldsymbol{\Omega}},E,t)}{\Delta t}\right]+\Sigma_t vN(\boldsymbol{r},\hat{\boldsymbol{\Omega}},E,t) \tag{3-12}$$
$$=\int_{4\pi}\mathrm{d}\hat{\boldsymbol{\Omega}}'\int_0^\infty \mathrm{d}E'\Sigma_s(\boldsymbol{r},\hat{\boldsymbol{\Omega}}'\to\hat{\boldsymbol{\Omega}},E'\to E,t)N(\boldsymbol{r},\hat{\boldsymbol{\Omega}}',E',t)+S(\boldsymbol{r},\hat{\boldsymbol{\Omega}},E,t).$$

Simplifying the first term requires adding and subtracting $N(\boldsymbol{r},\hat{\boldsymbol{\Omega}},E,t+\Delta t)$ to the second term in the numerator of the fraction in Eqn. 3-12 and simplifying the expressions individually. Adding $N(\boldsymbol{r},\hat{\boldsymbol{\Omega}},E,t+\Delta t)$ to the second term in the numerator gives

$$\lim_{\Delta t \to 0}\left[\frac{N(\boldsymbol{r},\hat{\boldsymbol{\Omega}},E,t+\Delta t)-N(\boldsymbol{r},\hat{\boldsymbol{\Omega}},E,t)}{\Delta t}\right]=\frac{\partial N}{\partial t}. \tag{3-13}$$

Subtracting $N(\boldsymbol{r},\hat{\boldsymbol{\Omega}},E,t+\Delta t)$ from the first term in the numerator leads to a less trivial expression, but it is more readily derived when decomposed in Cartesian coordinates as

$$\lim_{\Delta t \to 0}\frac{N(\boldsymbol{r}+\hat{\boldsymbol{\Omega}}v\Delta t,\hat{\boldsymbol{\Omega}},E,t)-N(\boldsymbol{r},\hat{\boldsymbol{\Omega}}E,t+\Delta t)}{\Delta t}=$$
$$\lim_{\Delta t \to 0}\frac{N(x+\Omega_x v\Delta t,y+\Omega_y v\Delta t,z+\Omega_z v\Delta t,\hat{\boldsymbol{\Omega}},E,t))-N(x,y,z,\hat{\boldsymbol{\Omega}},E,t)}{\Delta t}, \tag{3-14}$$

where $\boldsymbol{r}$ and $\hat{\boldsymbol{\Omega}}$ have components $x,\ y,\ z$ and $\Omega_x,\ \Omega_y,\ \Omega_z$ respectively. The infinitesmal $\hat{\boldsymbol{\Omega}}v\Delta t$ is equivalent to Δx. Equation 3-14 is then solved using the chain rule.

$$\lim_{\Delta t \to 0}\frac{N(x+\Delta x,y+\Delta y,z+\Delta z)-N(x,y,z)}{\Delta t}=$$
$$\frac{\Delta N}{\Delta x}\frac{\Delta x}{\Delta t}+\frac{\Delta N}{\Delta y}\frac{\Delta y}{\Delta t}+\frac{\Delta N}{\Delta z}\frac{\Delta z}{\Delta t}=$$
$$v\Omega_x\frac{\partial N}{\partial x}+v\Omega_y\frac{\partial N}{\partial y}+v\Omega_z\frac{\partial N}{\partial z}=v\hat{\boldsymbol{\Omega}}\cdot\boldsymbol{\nabla}N \tag{3-15}$$

Inserting the results of Eqn. 3-13 and Eqn. 3-15 into Eqn. 3-12, and using the definition

$$\varphi(\boldsymbol{r},\hat{\boldsymbol{\Omega}},E,t)\equiv N(\boldsymbol{r},\hat{\boldsymbol{\Omega}},E,t)v \tag{3-16}$$

yields the NTE,

$$\frac{1}{v}\frac{\partial\varphi}{\partial t} + \hat{\boldsymbol{\Omega}}\cdot\boldsymbol{\nabla}\varphi + \Sigma_t\varphi(\boldsymbol{r},\hat{\boldsymbol{\Omega}},E,t) = \int_{4\pi}\mathrm{d}\hat{\boldsymbol{\Omega}}'\int_0^\infty \mathrm{d}E'\Sigma_s(\boldsymbol{r},\hat{\boldsymbol{\Omega}}',E',t)\varphi(\boldsymbol{r},\hat{\boldsymbol{\Omega}}',E',t) + S(\boldsymbol{r},\hat{\boldsymbol{\Omega}},E,t). \tag{3-17}$$

In the previous discussion, internal neutron sources are handled in a general manner. As an aside, a brief discussion of internal neutron sources is provided. A dimensional analysis provides insight into how source terms are defined in the NTE. Since the NTE describes the number of neutrons in a volume at a point in time, then the units must be $\frac{neutrons}{Length^3 Time}$, or in cgs units $\frac{neutrons}{cm^3 s}$. This is easily confirmed by checking the units of one term in Eqn. 3-17. Analyzing the dimensions of the interaction term,

$$\Sigma_t\varphi(\boldsymbol{r},\hat{\boldsymbol{\Omega}},E,t) \equiv \left[\frac{1}{Length}\right]\left[\frac{neutrons}{Length^2 Time}\right] = \left[\frac{neutrons}{Length^3 Time}\right], \tag{3-18}$$

which confirms the previous statement. Therefore, any source term must have these same units.

Internal neutron sources do not depend on the neutron flux. Instead, neutrons are released from a nucleus left in an unstable energy state, typically a result of another nuclear reaction (e.g., fission). Occasionally, neutrons are released as a mechanism for a nucleus to relax to a more favorable energy state.

Writing an internal neutron source term to use in Eqn. 3-17 requires finding the number of neutrons emitted per unit volume per unit time. Chapter 2 discussed using ORIGEN to find the neutron source distribution used in MCNP. ORIGEN outputs the neutron source density from decaying nuclei and the output is compatible with Eqn. 3-8.

3.2 Cylindrical to Planar Coordinate Shift

The cylindrical shape of the spent fuel cask immediately lends to a cylindrical geometry for the mathematical models. However, given the large extent of the cask, it is expected that there exists a point along the radius of the cask where cylindrical geometry can be relaxed to a planar geometry with negligible effect to the neutron flux. This point

can be found through a dimensional analysis by developing non-dimensional forms for both the radial and planar diffusion equations.

Non-dimensional analysis is a process where an equation is rewritten in a manner such that there are no units in the problem (i.e., all parameters and variables in an expression are redefined using ratios rather than dimensional quantities). A comparison can be made between the non-dimensional forms of the 1-D cylindrical diffusion approximation and 1-D planar diffusion approximation to determine the location where planar geometry is appropriate.

Starting with the geometry-independent diffusion equation,

$$-D\boldsymbol{\nabla}\frac{\mathrm{d}^2\phi}{\mathrm{d}x^2} + \Sigma_a\phi = S. \tag{3-82}$$

where the second derivative has been written using the gradient, D is the diffusion coefficient, ϕ is the scalar flux, Σ_a is macroscopic absorption cross section, and S is the source term. The monoenergetic, steady-state, 1-D planar diffusion approximation:

$$-D\frac{\mathrm{d}^2\phi}{\mathrm{d}x^2} + \Sigma_a\phi = S. \tag{3-82}$$

Diving the equation by $-D$ and defining $L^{-2} \equiv \frac{\Sigma_a}{D}$,

$$\frac{\mathrm{d}^2\phi}{\mathrm{d}x^2} - \frac{1}{L^2}\phi + \frac{S}{D} = 0. \tag{3-19}$$

Non-dimensionalizing x,

$$\tilde{x} = \frac{x}{L}, \tag{3-20}$$

where $\tilde{x}$ is the non-dimensionalized form of x. The first derivative becomes

$$\mathrm{d}x = L\,\mathrm{d}\tilde{x} \tag{3-21}$$

in non-dimensional form.

The second order differential of x, $\mathrm{d}x^2$, becomes

$$\mathrm{d}x^2 = L^2 d\,\mathrm{d}\tilde{x}^2. \tag{3-22}$$

Eqn. 3-82 then becomes

$$\frac{1}{L^2}\frac{\mathrm{d}^2\phi}{\mathrm{d}x^2} - \frac{1}{L^2}\phi + \frac{S}{D} = 0, \tag{3-23}$$

or,

$$\frac{\mathrm{d}^2\phi}{\mathrm{d}\tilde{x}^2} - \phi + \frac{L^2 S}{D} = 0. \tag{3-24}$$

Note: $\frac{L^2 S}{D}$ has units of $Length^{-2}Time^{-1}$, which are the same units as ϕ. So,

$$\tilde{\phi} = \frac{\phi}{L^2 S/D}, \tag{3-25}$$

or,

$$\phi = \tilde{\phi}\frac{L^2 S}{D}, \tag{3-26}$$

where $\tilde{\phi}$ is the non-dimensionalized form of ϕ. The second differential of ϕ becomes

$$d^2\phi = \frac{L^2 S}{D} d^2\tilde{\phi}. \tag{3-27}$$

Using $\tilde{\phi}$, Eqn. 3-24 is written as

$$\frac{L^2 S}{D}\frac{\mathrm{d}^2\tilde{\phi}}{\mathrm{d}\tilde{x}^2} - \frac{L^2 S}{D}\tilde{\phi} + \frac{L^2 S}{D} = 0, \tag{3-28}$$

or,

$$\frac{\mathrm{d}^2\tilde{\phi}}{\mathrm{d}\tilde{x}^2} - \tilde{\phi} + 1 = 0. \tag{3-29}$$

The 1-D planar diffusion approximation is now expressed in a non-dimensional form.

Expressing the gradient in Eqn. 3-82 in 1-D cylindrical coordinates yields

$$\frac{1}{r}\frac{\mathrm{d}}{\mathrm{d}r}\left(r\frac{\mathrm{d}\phi}{\mathrm{d}r}\right) - \frac{1}{L^2}\phi + \frac{S}{D} = 0, \tag{3-30}$$

or,

$$\frac{\mathrm{d}^2\phi}{\mathrm{d}r^2} + \frac{1}{r}\frac{\mathrm{d}\phi}{\mathrm{d}r} - \frac{1}{L^2}\phi + \frac{S}{D} = 0. \tag{3-31}$$

Let

$$\tilde{r} = \frac{r}{L}, \tag{3-32}$$

and,

$$\tilde{\phi} = \frac{\phi D}{L^2 S} \tag{3-33}$$

Using the non-dimensionalized variables defined in Eqns. 3-32 and 3-33, Eqn. 3-31 can be rewritten as

$$\frac{\mathrm{d}^2\tilde{\phi}}{\mathrm{d}\tilde{r}^2} + \frac{1}{\tilde{r}}\frac{\mathrm{d}\tilde{\phi}}{\mathrm{d}\tilde{r}} - \tilde{\phi} + 1 = 0. \tag{3-34}$$

Then, the curvilinear form of the diffusion equation is

$$\frac{\mathrm{d}^2\tilde{\phi}}{\mathrm{d}\tilde{r}^2} + \frac{k}{\tilde{r}}\frac{\mathrm{d}\tilde{\phi}}{\mathrm{d}\tilde{r}} - \tilde{\phi} + 1 = 0, \tag{3-35}$$

where $k = 0$ for planar geometries and $k = 1$ for cylindrical geometries. Further, plotting the variable $\frac{k}{\tilde{r}}$ for $k = 1$ will show the location where accounting for cylindrical geometries becomes negligible. Figure 3-1 shows the result from the previous dimensional analysis using material properties of the fuel materials. The black vertical line in Fig. 3-1 shows the location where the value of $1/\tilde{r}$ (since $k = 1$ in cylindrical) is 1.411, or 10% of its initial value (14.112). The location of the vertical black line shows where the cylindrical and planar models agree within 90%, and is located at 10. 260 cm. After 10.260 cm materials can be approximated using planar equations. Meaning, the flux in the fuel region will need to be approximated using a cylindrical diffusion equation, but the MPC, concrete annulus, and carbon steel shell can be approximated in a planar geometry.

3.3 Reduction of NTE

Upon inspection of Eqn. 3-17, there are four derivatives on the left-hand side of the equation (one in time and three spatial derivatives) and three integrals on the right-hand side of the equation (one in energy and two in direction). Equations containing both integrals and derivatives are called integro-differential equations and are among the hardest forms of problems to solve. Further, the NTE is a function of seven variables;

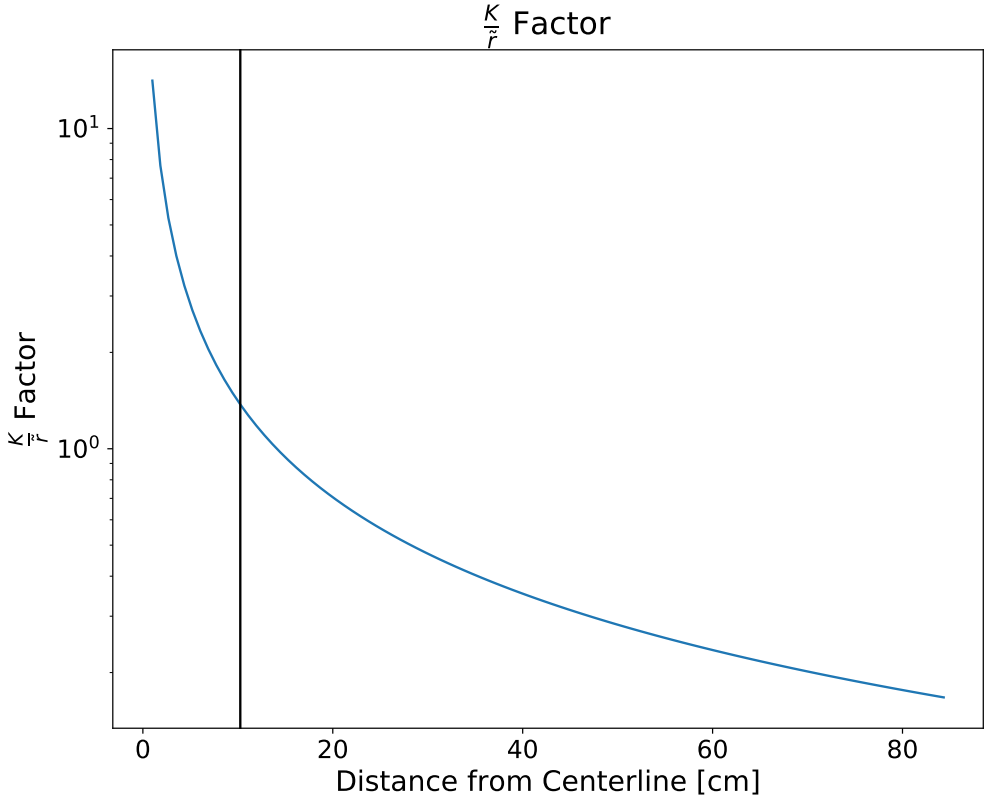

Figure 3-1. As the factor $\frac{k}{\tilde{r}}$ decreases, the planar solutions better approximate cylindrical solutions in the homogenous fuel material. The location of the black vertical line shows the point where the factor $\frac{k}{\tilde{r}}$ is 10% of its initial value at r =10.260 cm.

three spatial, two direction, one energy, and one time. In its current form, the NTE has no complete analytic solution. Therefore, assumptions and approximations are applied to reduce Eqn. 3-17 into a tractable form. The following sections will discuss how the multigroup discrete ordinates equation and the 1-D cylindrical diffusion approximation are derived from the NTE.

3.3.1 Treatment of Time Dependence

The time dependence is contained in the first term in Eqn. 3-17. Assuming the neutron flux is unchanging or slowly changing in time will simplify the time-derivative to zero. This is a fair assumption in the context of the cask since the time between neutron

interactions is much smaller than the time over which the neutron flux is evolving [41]. In this assumption φ is taken to be independent of time, and

$$\frac{\partial \varphi}{\partial t} = 0. \tag{3-36}$$

Then Eqn. 3-17 becomes the steady-state NTE,

$$\hat{\boldsymbol{\Omega}} \cdot \boldsymbol{\nabla} \varphi(\boldsymbol{r}, \hat{\boldsymbol{\Omega}}, E) + \Sigma_t(\boldsymbol{r}, E)\varphi(\boldsymbol{r}, \hat{\boldsymbol{\Omega}}, E) = \int_{4\pi} \mathrm{d}\hat{\boldsymbol{\Omega}}' \int_0^\infty \mathrm{d}E' \Sigma_s(E' \to E, \hat{\boldsymbol{\Omega}}' \to \hat{\boldsymbol{\Omega}}) \varphi'(\boldsymbol{r}, \hat{\boldsymbol{\Omega}}', E')) + S(\boldsymbol{r}, E, \hat{\boldsymbol{\Omega}}). \tag{3-37}$$

Even after eliminating the partial derivative in time, Eqn. 3-17 is still not tractable due to the three spatial derivatives and three integrals. Therefore, further reduction is necessary.

3.3.2 Reduction to 1-D Planar

The hight of the cask (approximately 570 cm) is much greater than the MFP of neutrons in the homogenous fuel, MPC, concrete, and carbon steel which have values less 10 cm, Figs. 2-10, 2-11, 2-15, and 2-18. Meaning neutrons in the materials do not effectively "see" the upper and lower boundaries of the spent fuel cask and the materials can be treated as infinite, or rather, having one spatial dimension.

Reducing the problem from three spatial dimensions to one spatial dimension eliminates two of the three spatial derivatives and one of the two direction derivatives. As an aside, the components of the direction vector $\hat{\boldsymbol{\Omega}}$ are ϕ and θ components. ϕ is the azimuthal angle and θ is the polar angle. It is common to define the variable μ in terms of θ as

$$\mu \equiv \cos\theta, \tag{3-38}$$

where μ is defined over the range [-1, 1] and ϕ is defined over the range [0, 2π]. Integrating Eqn. 3-37 over y, z, and ϕ reduces the dimensionality of the problem as

$$\int_{-\infty}^{\infty} \mathrm{d}y \int_{-\infty}^{\infty} \mathrm{d}z \int_{0}^{2\pi} \mathrm{d}\phi \hat{\boldsymbol{\Omega}} \cdot \boldsymbol{\nabla} \varphi(\boldsymbol{r}, \hat{\boldsymbol{\Omega}}, E) + \Sigma_t(\boldsymbol{r}, E)\varphi(\boldsymbol{r}, \hat{\boldsymbol{\Omega}}, E) - \tag{3-39}$$

$$\int_{4\pi} \mathrm{d}\hat{\boldsymbol{\Omega}}' \int_{0}^{\infty} \mathrm{d}E' \Sigma_s(E' \rightarrow E, \hat{\boldsymbol{\Omega}}' \rightarrow \hat{\boldsymbol{\Omega}}) \varphi'(\boldsymbol{r}, \hat{\boldsymbol{\Omega}}', E') + s(\boldsymbol{r}, E, \hat{\boldsymbol{\Omega}}). \tag{3-40}$$

$$\tag{3-41}$$

Solving the integrals yields:

$$\mu \frac{\partial}{\partial x} \varphi(x, E, \mu) + \Sigma_t(x, E)\varphi(x, E, \mu) = \tag{3-42}$$

$$2\pi \int_{0}^{\infty} \int_{-1}^{1} \Sigma_s(x, E', \mu' \rightarrow E, \mu) \varphi(x, E', \mu') \, \mathrm{d}\mu' \, \mathrm{d}E' + S(x, E, \mu).$$

Eqn. 3-42 is the steady-state 1-D planar form of the NTE. While this equation appears much simpler to solve, the derivative on the left-hand side and two integrals on the right-hand side indicate the equation is still an integro-differential equation and further simplification is required to arrive at a tractable form. There are two common reductions to Eqn. 3-42, 1) the multigroup discrete ordinates approximation and 2) the diffusion approximation. The following sections apply each of these approximations to the NTE in order to arrive at two tractable forms of the NTE which will be used in the remainder of this work.

3.4 Multigroup Discrete Ordinates Approximation

The multigroup discrete ordinates equations handle the two integrals on the right-hand side of Eqn. 3-42 by treating the integral over energy as integrals over energy ranges and approximating the integral over μ by evaluating the neutron flux at discrete angles within the full range of [-1, 1]. The final result is a set of coupled, first-order ordinary differential equations that are analytically tractable.

3.4.1 Treatment of Energy Dependence

The first step in developing multigroup equations is to divide the neutron energy range of interest into a finite number of energy groups, E_g, where $g = 1, 2, ..., G$. The order of the energy group number is such that energy decreases as the group number increases, (e.g., $E_g > E_{g+1}$) [39]. Energy groups are typically chosen such that the total cross section shows little variation within a group. This is done in order for the group averaged cross section to best represent the energy-dependent cross section values of that group.

Integrating Eqn. 3-42 over g yields

$$\underbrace{\int_g \mu \frac{\partial}{\partial x}\varphi(x,E,\mu)\,\mathrm{d}E}_{(1)} + \underbrace{\int_g \Sigma_t(x,E)\varphi(x,E,\mu)\,\mathrm{d}E}_{(2)} = \tag{3-43}$$

$$\underbrace{\int_g 2\pi \int_0^\infty \int_{-1}^1 \Sigma_s(x;E',\mu' \to E,\mu)\varphi(x,E',\mu')\,\mathrm{d}\mu'\,\mathrm{d}E'\,\mathrm{d}E}_{(3)} + \underbrace{\int_g S(x,E,\mu)\,\mathrm{d}E}_{(4)},$$

where each term will be discussed individually. Before continuing, it is important to define the the group flux and group cross sections as:

$$\varphi_g(x,\mu) \equiv \int_{E_g}^{E_{g-1}} \varphi(x,E,\mu)\,\mathrm{d}E = \int_g \varphi(x,E,\mu)\,\mathrm{d}E, \tag{3-44}$$

$$\Sigma_{t,g}(x,\mu) \equiv \frac{\int_g \Sigma_t(x,E,\mu)\varphi(x,E,\mu)\,\mathrm{d}E}{\varphi_g(x,E,\mu)}, \tag{3-45}$$

$$\Sigma_{s,g'\to g}(x,\mu) \equiv \frac{\int_{g'} \varphi(x,E',\mu) \int_g \int_{-1}^1 \Sigma_s(x;E',\mu' \to E,\mu)\,\mathrm{d}\mu'\,\mathrm{d}E\,\mathrm{d}E'}{\varphi_{g'}(x,E',\mu)}. \tag{3-46}$$

$\varphi_g(x,\mu)$ is the group averaged flux, $\Sigma_{t,g}(x,\mu)$ is the group averaged cross section, and $\Sigma_{s,g'\to g}(x,\mu)$ is the group to group, or transfer, cross section.

Definitions 3-44 - 3-46 are used to rewrite Eqn. 3-43 term by term. The first term of Eqn. 3-43 is rewritten in terms of the group flux, 3-44 as

$$\int_g \mu \frac{\partial}{\partial x}\varphi(x,E,\mu)\,\mathrm{d}E = \mu \frac{\partial}{\partial x}\varphi_g(x,\mu). \tag{3-47}$$

Rewriting the second term in Eqn. 3-43 using the total group cross section, Eqn. 3-45, yields

$$\int_g \Sigma_t(x,E,\mu)\varphi(x,E,\mu)\,\mathrm{d}E = \Sigma_{t,g}(x,\mu)\varphi_g(x,\mu). \tag{3-48}$$

The third term in Eqn. 3-43 requires a bit more work. If the integral of $\mathrm{d}E'$ is taken over each individual energy group rather than over 0 to ∞, then

$$\int_0^\infty \mathrm{d}E' = \sum_{g'=1}^{G}\int_{E_{g'}}^{E_{g'-1}} \mathrm{d}E' = \sum_{g'=1}^{G}\int_{g'} \mathrm{d}E', \tag{3-49}$$

and the third term can be expressed using group constants, Eqn. 3-50.

$$\int_{g'} \varphi(xE',\mu)\int_g \Sigma(x;E',\mu'\rightarrow E,\mu)\,\mathrm{d}E\,\mathrm{d}E' = \sum_{g'=1}^{G}\Sigma_{g'\rightarrow g}(x,\mu)\varphi_{g'}(x,\mu) \tag{3-50}$$

Finally, the fourth term is the group source term, Eqn. 3-51. The group source term describes an arbitrary internal source of neutrons with energy in group g.

$$\int_g S(x,E,\mu)\,\mathrm{d}E \equiv S_g(x,\mu). \tag{3-51}$$

Using the redefined terms, Eqns. 3-47 - 3-51, Eqn. 3-43 becomes a set of equations characterizing the flux in each energy group:

$$\mu\frac{\partial\varphi_g}{\partial x} + \Sigma_{t,g}\varphi_g = 2\pi\sum_{g'=1}^{G}\int_{-1}^{1}\Sigma_{s,g'\rightarrow g}\varphi_{g'} + S_g, \qquad g = 1,2,...,G. \tag{3-52}$$

3.4.2 Treatment of Directional Dependence

Equation 3-52 is a set of monoenergetic NTEs where each equation defines the flux for the energy group g. Therefore, if a method for handling the directional dependence can be found for a single equation in the set of equations, the same method can be extended to all equations in Eqn. 3-52. The discrete ordinates method can be used to handle the integral over μ. Figures 2-9, 2-13, 2-17, and 2-20 show the angular distribution of the neutron flux in each material. The neutron flux is isotropic within 7% at locations interior to the

outer surface of the concrete annulus. A relatively isotropic neutron flux through the fuel region, MPC, and part of the concrete annulus acts as an indicator that scattering can be assumed to be isotropic. Therefore, assuming isotropic scattering, the inscattering term reduces to

$$2\pi \sum_{g'=1}^{G} \int_{-1}^{1} \Sigma_{s,g'\to g} \varphi_{g'} \, \mathrm{d}\mu' = \frac{1}{2} \sum_{g'=1}^{G} \Sigma_{s,g'\to g} \int_{-1}^{1} \varphi_{g'} \, \mathrm{d}\mu', \tag{3-53}$$

and Eqn. 3-52 reduces to

$$\mu \frac{\partial \varphi_g}{\partial x} + \Sigma_{t,g} \varphi_g = \frac{1}{2} \sum_{g'=1}^{G} \Sigma_{s,g'\to g} \int_{-1}^{1} \varphi_{g'} + S_g, \qquad g = 1, 2, ..., G. \tag{3-54}$$

Discrete ordinates treats directional dependence by evaluating the integral over μ at a unique set of directions, $\{\mu_i\}$. Evaluating the integral in Eqn. 3-54 at each value of μ_i leads to a weighted sum of neutron fluxes, Eqn. 3-55.

$$\int_{-1}^{1} \varphi_{g'} = \sum_{j=1}^{N} \omega_j \phi_{g'}(x, \mu_j) \tag{3-55}$$

Evaluating Eqn. 3-54 along the set of direction vectors $\{\mu_i\}$, using Eqn. 3-55, results in the multigroup discrete ordinates equations:

$$\mu_i \frac{\mathrm{d}\phi_i^g}{\mathrm{d}x} + \Sigma_t^g \phi_i^g = \frac{1}{2} \sum_{j=1}^{N} \omega_j \sum_{g'=1}^{G} \Sigma_{s,g'\to g} \phi_j^{g'} + S_i^g, \qquad g = 1, 2, ..., G; i = 1, 2, ..., N, \tag{3-56}$$

where ω_j are weights used in the multigroup discrete ordinates equation. The weights are equal to one in a two direction formulation of the discrete ordinates equation [42].

Section 2.2 identified the multigroup discrete ordinates approximation using two energy groups and two directional angles for multiple materials in the cask. Therefore, a set of equations are derived from Eqn. 3-56 using two energy groups ($g = 1, 2$) and two directions ($i = 1, 2$). Iterating over both indices one at a time leads to the following set of

equations:

$g = 1, i = 1$

$$\mu_1 \frac{\mathrm{d}\phi_1^1}{\mathrm{d}x} + \Sigma_t^1 \phi_1^1 = \frac{1}{2}\left(\Sigma_s^{1\to1}\omega_1\phi_1^1 + \Sigma_s^{1\to1}\omega_2\phi_2^1 + \Sigma_s^{2\to1}\omega_1\phi_1^2 + \Sigma_s^{2\to1}\omega_2\phi_2^2\right) + S_1^1; \quad \text{(3-57)}$$

$g = 1, i = 2$

$$\mu_2 \frac{\mathrm{d}\phi_2^1}{\mathrm{d}x} + \Sigma_t^1 \phi_2^1 = \frac{1}{2}\left(\Sigma_s^{1\to1}\omega_1\phi_1^1 + \Sigma_s^{1\to1}\omega_2\phi_2^1 + \Sigma_s^{2\to1}\omega_1\phi_1^2 + \Sigma_s^{2\to1}\omega_2\phi_2^2\right) + S_2^1; \quad \text{(3-58)}$$

$g = 2, i = 1$

$$\mu_1 \frac{\mathrm{d}\phi_1^2}{\mathrm{d}x} + \Sigma_t^2 \phi_1^2 = \frac{1}{2}\left(\Sigma_s^{1\to2}\omega_1\phi_1^1 + \Sigma_s^{1\to2}\omega_2\phi_2^1 + \Sigma_s^{2\to2}\omega_1\phi_1^2 + \Sigma_s^{2\to2}\omega_2\phi_2^2\right) + S_1^2; \quad \text{(3-59)}$$

$g = 2, i = 2$

$$\mu_2 \frac{\mathrm{d}\phi_2^2}{\mathrm{d}x} + \Sigma_t^2 \phi_2^2 = \frac{1}{2}\left(\Sigma_s^{1\to2}\omega_1\phi_1^1 + \Sigma_s^{1\to2}\omega_2\phi_2^1 + \Sigma_s^{2\to2}\omega_1\phi_1^2 + \Sigma_s^{2\to2}\omega_2\phi_2^2\right) + S_2^2. \quad \text{(3-60)}$$

Further, the materials in the cask are assumed to be at temperatures where upscattering in negligible. Duderstadt and Hamilton say upscattering effects are can be neglected above $10kT$, where k is Boltzmann's constant, $8.617x10^{-5}$ eV K^{-1}, and T is the temperature in Kelvin. From the Final Safety Analysis of the HI-STORM 100 spent fuel cask, the maximum allowable temperature of the fuel cladding is 673 K [36]. Then, upscattering effects can be neglected for neutron energies above 0.580 eV. Chapter 2 identified 1 keV as the fast group threshold, which is much much greater than 0.580 eV. Therefore, upscattering is assumed to be negligible. Moreover, there are assumed to be no internal neutron sources within the MPC, concrete, and carbon steel shell. These assumptions are

used to reduce Eqns. 3-57-3-60 to:

$$g = 1, i = 1$$

$$\mu_1 \frac{\mathrm{d}\phi_1^1}{\mathrm{d}x} + \Sigma_t^1 \phi_1^1 = \frac{1}{2}\left(\Sigma_s^{1\to 1}\omega_1\phi_1^1 + \Sigma_s^{1\to 1}\omega_2\phi_2^1\right); \tag{3-61}$$

$$g = 1, i = 2$$

$$\mu_2 \frac{\mathrm{d}\phi_2^1}{\mathrm{d}x} + \Sigma_t^1 \phi_2^1 = \frac{1}{2}\left(\Sigma_s^{1\to 1}\omega_1\phi_1^1 + \Sigma_s^{1\to 1}\omega_2\phi_2^1\right); \tag{3-62}$$

$$g = 2, i = 1$$

$$\mu_1 \frac{\mathrm{d}\phi_1^2}{\mathrm{d}x} + \Sigma_t^2 \phi_1^2 = \frac{1}{2}\left(\Sigma_s^{1\to 2}\omega_1\phi_1^1 + \Sigma_s^{1\to 2}\omega_2\phi_2^1 + \Sigma_s^{2\to 2}\omega_1\phi_1^2 + \Sigma_s^{2\to 2}\omega_2\phi_2^2\right); \tag{3-63}$$

$$g = 2, i = 2$$

$$\mu_2 \frac{\mathrm{d}\phi_2^2}{\mathrm{d}x} + \Sigma_t^2 \phi_2^2 = \frac{1}{2}\left(\Sigma_s^{1\to 2}\omega_1\phi_1^1 + \Sigma_s^{1\to 2}\omega_2\phi_2^1 + \Sigma_s^{2\to 2}\omega_1\phi_1^2 + \Sigma_s^{2\to 2}\omega_2\phi_2^2\right). \tag{3-64}$$

3.5 Reduction to Diffusion Approximation

The diffusion approximation is an alternative reduction of the NTE. There are several methods for deriving the diffusion approximation, however, this derivation uses Legendre polynomial expansions to account for angular dependence in the equation [43]. The NTE can be simplified through the use of spherical harmonics, which in 1-D, reduce to Legendre polynomials to expand the angular flux and source terms while assuming an isotropic angular differential cross section. The 1-D planar, monoenergetic, NTE with isotropic scattering is

$$\mu \frac{\partial}{\partial x}\varphi(x,\mu) + \Sigma_t(x)\varphi(x,\mu) = \frac{1}{2}\int_{-1}^{1} \Sigma_s(x,\mu' \to \mu)\varphi(x,\mu')\,\mathrm{d}\mu' + S(x,\mu) \tag{3-65}$$

Expanding the angular flux with Legendre polynomials separates the directional and spatial components of the angular flux. Legendre polynomials exhibit an orthogonality property, Eqn. 3-66, and a "3-term recursion" relationship, Eqn. 3-67, which are used in deriving the diffusion approximation, where $P_{l/m}(\mu)$ are the Legendre polynomials of order

l or m respectively and δ_{lm} is the Kronecker delta, equal to 1 when $m = l$ and 0 otherwise [43].

$$\int_{-1}^{1} d\mu P_l(\mu) P_m(\mu) = \frac{2}{2l+1}\delta_{lm} \tag{3-66}$$

$$(2l+1)\mu P_l(\mu) = (l+1)P_{l+1}(\mu) + (l)P_{l-1}(\mu) \tag{3-67}$$

Expanding the angular flux in Eqn. 3-65 yields:

$$\mu\frac{\partial}{\partial x}\left[\sum_{l}^{\infty}\frac{2l+1}{2}\phi_l(x)P_l(\mu)\right] + \Sigma_t\sum_{l}^{\infty}\frac{2l+1}{2}\phi_l(x)P_l(\mu) = \tag{3-68}$$
$$\frac{1}{2}\int_{-1}^{1} d\mu'\Sigma_s(x,\mu_0)\sum_{l}^{\infty}\frac{2l+1}{2}\phi_l(x)P_l(\mu') + S(x,\mu).$$

Requiring the projections of Eqn. 3-68 against Legendre polynomials of degree m (e.g., P_m) to be equal to 0 leads to

$$\int_{-1}^{1} d\mu\mu\frac{\partial}{\partial x}\left[\sum_{l=0}^{1}\frac{2l+1}{2}\phi_l(x)P_l(\mu)P_m(\mu)\right] + \int_{-1}^{1} d\mu\Sigma_t\sum_{l=0}^{1}\frac{2l+1}{2}\phi_l(x)P_l(\mu)P_m(\mu) = \tag{3-69}$$
$$\frac{1}{2}\int_{-1}^{1} d\mu P_m(\mu)\int_{-1}^{1} d\mu'\Sigma_s(x,\mu_0)\sum_{l=0}^{1}\frac{2l+1}{2}\phi_l(x)P_l(\mu') + \int_{-1}^{1} d\mu S(x,\mu)P_m(\mu).$$

The summation is truncated at $l = 1$ since the first two terms are all that is necessary for finding the diffusion approximation.

Using the recurrence relationship, Eqn. 3-67, in the first term of Eqn. 3-69 yields

$$\sum_{l=0}^{1}\frac{\partial\phi_l(x)}{\partial x}\left[\int_{-1}^{1} d\mu\frac{l+1}{2}P_{l+1}(\mu)P_m(\mu) + \int_{-1}^{1} d\mu\frac{l}{2}P_{l-1}(\mu)P_m(\mu)\right]. \tag{3-70}$$

Applying the orthogonality gives,

$$\frac{(m-1)+1}{2}\frac{2}{2m+1}\frac{\partial\phi_{m-1}(x)}{\partial x} + \frac{m+1}{2}\frac{2}{2m+1}\frac{\partial\phi_{m+1}(x)}{\partial x}, \tag{3-71}$$

or,

$$\frac{m}{2m+1}\frac{\partial\phi_{m-1}(x)}{\partial x} + \frac{m+1}{2m+1}\frac{\partial\phi_{m+1}(x)}{\partial x}. \tag{3-72}$$

The second term in Eqn. 3-69 is also solved using the orthogonality property as,

$$\Sigma_t \sum_{l=0}^{1} \frac{2l+1}{2} \phi_l(x) \int_{-1}^{1} d\mu P_l(\mu) P_m(\mu) \tag{3-73}$$

such that,

$$\Sigma_t \sum_{l=0}^{1} \frac{2l+1}{2} \phi_m(x) \frac{2}{2m+1}, \tag{3-74}$$

or,

$$\Sigma_t \phi_m(x). \tag{3-75}$$

Solving the third term of Eqn. 3-69 involves calculating the values for $P_{l/m}(\mu)$ for $l, m = 0, 1$, which are $P_0(\mu) = 1$ and $P_1(\mu) = \mu$. Note each integral evaluates to 0 when either l or m is odd. Alternatively, the scattering term evaluates to $2\phi_m$ when l and m are 0.

$$\frac{1}{2}\Sigma_s(x, \mu_0) \sum_{l=0}^{1} \frac{2l+1}{2} \int_{-1}^{1} d\mu' \phi_l(x) P_l(\mu') \int_{-1}^{1} d\mu P_m(\mu) = \begin{cases} 2\phi_0; \ l \ and \ m = 0 \\ 0; \ else. \end{cases} \tag{3-76}$$

And the final term in Eqn. 3-69 is simply redefined as:

$$S_m \equiv \int_{-1}^{1} d\mu S(x, \hat{\mathbf{\Omega}}) P_m(\mu). \tag{3-77}$$

For an isotropic source, $S_m = 0$ for $m > 0$.

Combining the terms leads to the final set of P_1 equations, Eqns. 3-78 and 3-79.

$$\frac{\partial \phi_1}{\partial x} + \Sigma_t \phi_0 = \Sigma_s \phi_0 + S_0 \tag{3-78}$$

$$\frac{1}{3}\frac{\partial \phi_0}{\partial x} + \frac{2}{5}\frac{\partial \phi_2}{\partial x} + \Sigma_t \phi_1 = S_1. \tag{3-79}$$

If this set of equations were solved for ϕ_0, the result would be the diffusion approximation. Unfortunately, there are three unknowns (ϕ_0, ϕ_1, and ϕ_2) and two equations. In fact, this set of equations will always have more unknown variables than equations. Therefore, a

closure condition is needed to truncate the set of equations by setting $\phi_n = 0$ for $n \geq 2$. Eqn. 3-79 then becomes

$$\phi_1 = \frac{-1}{3\Sigma_t}\frac{\partial \phi_0}{\partial x} \tag{3-80}$$

which is Fick's Law [43].

Substituting Fick's Law in Eqn. 3-78 for ϕ_1

$$\frac{\partial}{\partial x}\left[\frac{-1}{3\Sigma_t}\frac{\partial \phi_0}{\partial x}\right] + \Sigma_t \phi_0 = \Sigma_s \phi_0 + S_0, \tag{3-81}$$

which simplifies to the 1-D, mono-energetic, steady state diffusion approximation:

$$-D\frac{\partial^2 \phi_0}{\partial x^2} + \Sigma_a \phi_0 = S_0, \tag{3-82}$$

where D, the diffusion coeffificent is defined as

$$D \equiv \frac{-1}{3\Sigma_t}, \tag{3-83}$$

when D is independent of x. The second derivative, $\frac{\partial^2}{\partial x^2}$, results from expressing the Laplacian operator in a planar coordinates systems where the coordinate-independent diffusion approximation is

$$-D\boldsymbol{\nabla}^2 \phi_0 + \Sigma_a \phi_0 = S_0, \tag{3-84}$$

from Duderstadt & Hamilton [41]. Given the cylindrical geometry of the cask, the diffusion equation is expected to be applied in a cylindrical coordinate system. Equation 3-85 is the 1-D cylindrical, steady-state monoenergetic diffusion equation where the Laplacian has been expressed in cylindrical coordinates.

$$-D\frac{1}{r}\frac{\mathrm{d}}{\mathrm{d}r}\left(r\frac{\mathrm{d}\phi_0}{\mathrm{d}r}\right) + \Sigma_a \phi_0 = S_0 \tag{3-85}$$

CHAPTER 4
ANALYSIS OF SUB-PROBLEMS

This chapter analyzes each sub-problem in depth according to the results assessment methodology using the mathematical models identified in Sec. 2 and derived in Sec. 3. Through the explanation of the causes of each feature, confidence is gained in the correctness of the detailed MCNP simulation.

4.1 Discussion of Fuel Region Sub-problems

4.1.1 Flat Region

Chapter 2 identified the analytic model choice for each material region. However, differential equations only yield unique solutions when coupled with boundary conditions. Therefore, a discussion identifying appropriate boundary conditions in each material is provided. The fuel region has a unique geometry-induced feature at the center of the cylindrical fuel region where the radius is 0. The geometry at the center of the cask suggests the central symmetry boundary condition which limits the solution to a finite value at the centerline of the cask, where $r = 0$, as

$$\lim_{r \to 0} \phi(r) < \infty. \tag{4-1}$$

Further, at the exiting surface of the fuel region, an approximate non-reentrant boundary condition associated with Eqn. 3-85 is

$$\phi(r_b + d) = 0, \tag{4-2}$$

where r_b is the vector of positions comprising the outer surface S of V, and d is an "extrapolation distance" given by

$$d = 2.13D. \tag{4-3}$$

Equation 4-2 is intended to qualitatively reproduce the neutron flux behavior at the outer surface of a non-reentrant convex body, as otherwise observed from more general neutron transport scenarios [44].

Table 4-1. Summary of cross section data in the homogenized fuel.

Parameter	Values
S	20.1430 $\frac{neutrons}{cm^3 s}$
Σ_c	0.01756 $\frac{1}{cm}$
Σ_f	0.00260 $\frac{1}{cm}$
Σ_s	0.02981 $\frac{1}{cm}$
$\bar{\nu}$	2.6475 $neutrons$
r_b	84.34 cm

Table 4-1 summarizes the input parameter values which are used in Eqn. 4-5. These values are calculated using the NJOY cross section processing code, where the cross section data is a composition of the isotopes in the fuel region by weight fraction, made in a similar manner to the homogenous fuel composition [45].

Initially, the flatness of the first feature, Fig. 2-21, suggests that a reduction in fine structure detail can be used to adequately represent a substantial portion the fuel region. Each fuel pin is approximately 1 cm in diameter, yet the neutron flux spatial distribution does not show variations at the centimeter level. Fluctuations in the neutron flux spatial distribution at the centimeter level would require any simplified models to also preserve geometric structures at the centimeter level, but the absence of these fluctuations implies that geometric reductions are possible. Therefore, an MCNP model is developed with a homogenized fuel in the MPC.

For the purpose of clarity, this fuel composition is called "fully homogenized" since it incorporates all the materials inside the MPC. The fully homogenized fuel composition is determined by calculating the mass fractions of each material in the MPC (the stainless steel basket, the neutron absorbing pads, the helium backfill, and the fuel rods). Finally, the density of the fully homogenized fuel is calculated based on the mass fraction of each material to account for the various densities of materials in the MPC (10.44 $\frac{g}{cm^3}$ for a single fuel rod vs. 2.31 $\frac{g}{cm^3}$ for the fully homogenized fuel). The entire interior volume of the MPC is filled with the fully homogenized fuel material. Figure 4-1 is a cross section

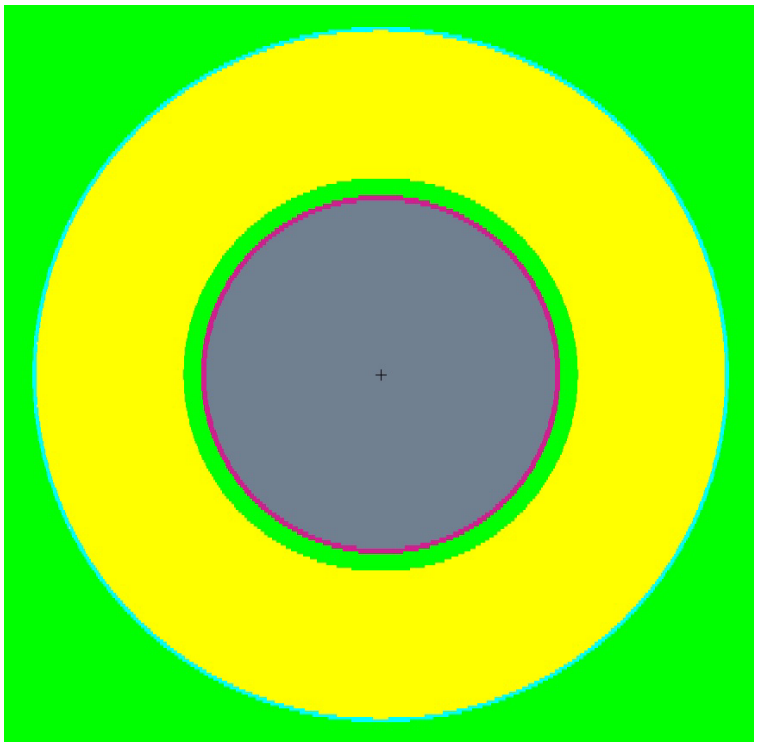

Figure 4-1. The homogeneous model. The gray circle is the fully homogenized fuel which fills the entire volume interior to the MPC.

view of the corresponding MCNP model using the fully homogenized fuel material. This model is referred to as the "homogenous model".

Figure 4-2 shows the homogeneous model neutron flux spatial distribution through the fuel region of the MPC as calculated using MCNP, together with the complementary result from the detailed model. The inset graph shows the relative error between the analog model and the detailed model determined by

$$relative\ error(r) = \frac{\phi(r)_{analog} - \phi(r)_{detailed}}{\phi(r)_{detailed}}, \tag{4-4}$$

where $\phi(r)_{analog}$ is the neutron flux value at location r for the analog model (i.e., homogenous model, helium model, analytic model) and $\phi(r)_{detailed}$ is the neutron flux value at location r given by the MCNP detailed model. From Eqn. 4-4, the homogenous model over predicts the neutron flux spatial distribution by 20-25% through the fuel region. Even though the reduced model overpredicts the detailed flux, the shape of the

neutron flux spatial distribution predicted in both models shows a steady decrease across the inner 65 cm. The relative flatness of the two fluxes is evidence that the inclusion of geometric details is less important than the material properties within the MPC. To further corroborate this notion, Fig. 4-2 also includes results from an analytic model: the dotted line appearing in this figure is a result from monoenergetic, 1-D cylindrical diffusion theory, Eqn. 3-82, which is derived in Sec. 3.5. In this analytic setting, the monoenergetic scalar neutron flux across a 1-D cylindrical region with constant material properties is given by

$$\phi(r) = \frac{S}{DB^2}\left(1 - \frac{I_0(Br)}{I_0(B\tilde{r})}\right); \qquad B \equiv \sqrt{\frac{\Sigma_a - \bar{\nu}\Sigma_f}{D}}. \tag{4-5}$$

where α is the intrinsic neutron source, B is indicated in terms of the macroscopic total absorption cross section Σ_a, macroscopic fission cross section Σ_f, and mean number of neutrons per fission $\bar{\nu}$, and diffusion coefficient D, I_0 is the modified Bessel function of the first kind, and $\tilde{r}$ is the extrapolated radius of the fuel region. The cross section values in Eqn. 4-5 are representative of the homogenous fuel. The spatial curvature of the scalar flux appearing in Eq. 4-5 is controlled principally by the material buckling B; as the value of B increases (resulting when absorption physics is dominant over scattering physics) the neutron flux spatial distribution calculated in Eq. 4-5 produces a flat distribution in r - as in the fuel region of both the detailed and helium computational models. This result is discussed further in conjunction with the sensitivity discussion corresponding to the diffusion approximation in Sec. 7.1.1. The flatness of the diffusion model is proof that the flatness seen in the MCNP models is controlled by material properties (e.g., cross sections) rather than from geometric details (e.g., physical extent of each fuel rod). If the physical extent of the fuel rods were to control the shape of the neutron flux, the results of neutron flux in the detailed model would likely show oscillatory behavior at the 1 cm level, since the fuel rods have diameters of approximately 1 cm. Moreover, the neutron flux would show local maximum values at locations coincident with each fuel rod and local minimums

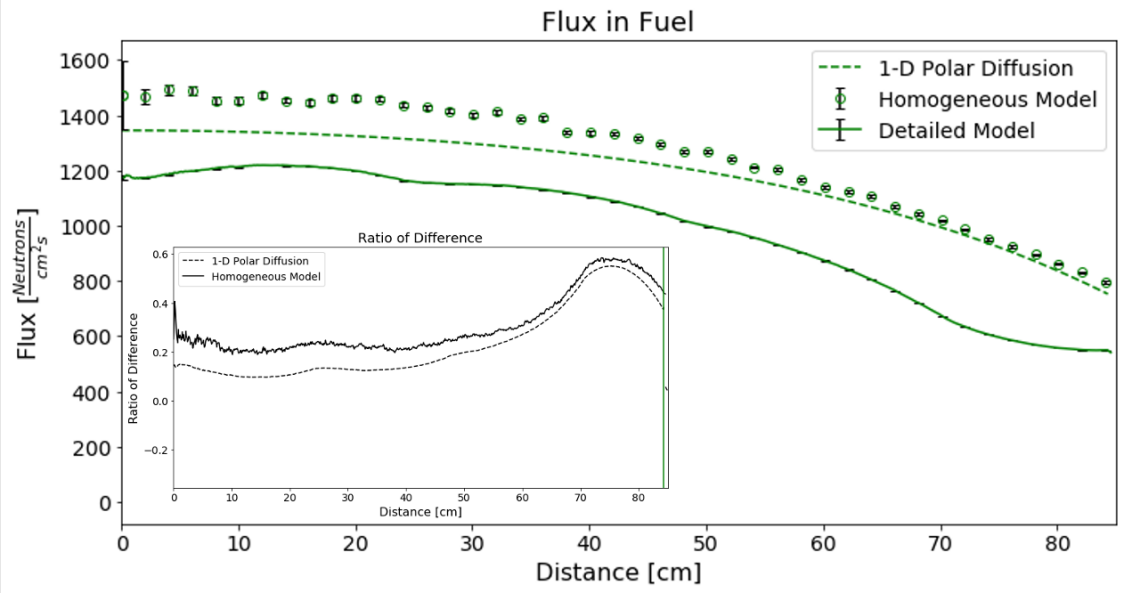

Figure 4-2. The results of the simulated neutron flux spatial distribution from the homogenous model (circles) is similarly flat to the neutron flux spatial distribution of the detailed model (solid line). The flux calculated using the diffusion approximation (dotted line) is also plotted against the two MCNP models. The diffusion approximation also shows the flatness of the neutron flux spatial distribution.

at locations between fuel rods. However, this behavior is not observed in Fig. 4-2. Instead, the flatness of the neutron flux observed in the detailed model is shared by the diffusion solution, Eqn. 4-5, where the geometric details have been homogenized but material properties are preserved in the development of Eqn. 3-85. While the diffusion model captures the essential physics giving rise to the flat flux region, it does not adequately capture the abrupt level off within the fuel region for $r > 65$ cm.

4.1.2 Abrupt Level-off Region

In order to better capture the physics which describes the second feature (Fig. 2-22), a second model is developed. The purpose of this model is to capture the physics associated with the neutron flux spatial distribution suddenly flattening before exiting the MPC. Intuitively, since geometric attenuation is minimal and the MFP for neutrons (approximately 70,000 cm at 1 MeV) is much greater than the thickness of the region between the fuel basket and MPC wall (approximately 10 cm), a free streaming (i.e.,

constant flux) approximation is likely to be valid there. Figure 3-1 confirms that geometric attenuation is minimal at these locations, in fact geometry accounts for a difference of 0.115% between neutron flux values calculated in planar and cylindrical geometries. To further corroborate this notion, the homogeneous model is modified to add an annulus of helium around a fuel region which is reduced in radius in a manner which preserves the volume of the original 32 fuel cells. This model is referred to as the "helium model". Fig. 4-3 shows the difference between the homogenous and helium models. The composition of the fuel region is changed to account for the helium now present in the annulus. The new homogenized fuel composition, called the partially homogenized fuel composition, is made using the mass fractions of materials in the 32 fuel cells (the stainless steel fuel basket, the neutron absorbing pads, the helium interior to the fuel cells, the fuel rods) and the density of the material is adjusted to account for the reduced amount of helium (2.95 $\frac{g}{cm^3}$).

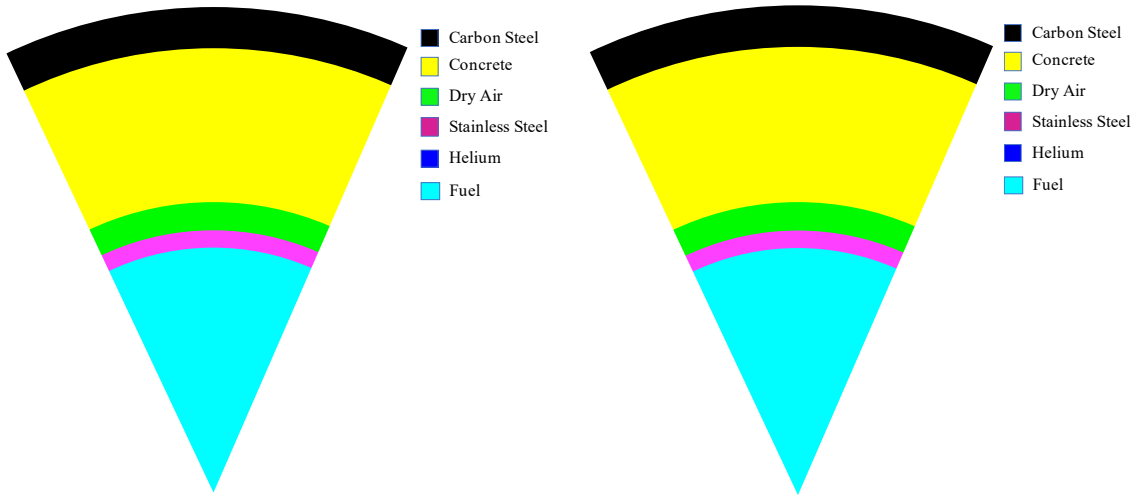

(a) (b)

Figure 4-3. A) Section views of the homogeneous model, B) Helium model. The helium model includes an annulus of helium gas, ∼10 cm thick, added around the homogenized fuel to allow streaming at the edge of the fuel region. Not to scale.

Given the fuel composition of the helium model, these input parameters are evaluated using the nuclear data processing NJOY code [45], where the necessary calculations proceed by weighting the cross section values against the neutron source energy spectrum

Table 4-2. Summary of cross section data in the homogenized fuel of the helium model.

Parameter	Values
S	20.1430 $\frac{neutrons}{cm^3 s}$
Σ_c	0.02264 $\frac{1}{cm}$
Σ_f	0.00335 $\frac{1}{cm}$
Σ_s	0.03842 $\frac{1}{cm}$
$\bar{\nu}$	2.6475 $neutrons$
r_b	74.68 cm

(Fig. 2-6). Otherwise, the nominal input parameter r_b^0 is the radius of the homogenized fuel material, $r = 74.68$ cm. Table 4-2 provides a summary of input parameter values calculated for the homogeneous fuel associated with the helium model. These values are used in the analytic model, the 1-D cylindrical diffusion approximation (Eqn. 4-5), where the fuel composition and geometry have been modified to account for the added helium annulus. That is, Eqn. 4-5 models the neutron flux in the fuel (0 cm−74.68 cm), where the cross section values have been recalculated to account for the new fuel material (matching the fuel material from the helium model). The flux is considered constant from 74.68 cm to 84.34 cm. Holding the flux constant is equivalent to free-streaming in a planar geometry, as curvilinear effects are determined to be negligible between 74.68 cm to 84.34 cm from Fig. 3-1.

Figure 4-4 shows the results of the simulated flux, using MCNP, in the helium model as compared to the detailed model. The fuel region, containing the partially homogenized fuel material, has a smaller radius and the analytic solution is held constant for $r > \tilde{r}$. The increased density of the fuel in the helium model increases the total neutron absorption and thus lowers the amplitude of the neutron flux spatial distribution. The flux flattens out over the last 20 cm, which is a result of adding the non-interacting helium annulus. Again, the effect of geometric attenuation in a cylindrical geometry is not observed, as curvilinear effects are minimized. Fig. 3-1 shows that curvilinear effects account for a 0.115% discrepancy between 1-D planar and 1-D cylindrical geometries. As a result, the helium model better demonstrates that the flatness of the detailed and helium models and

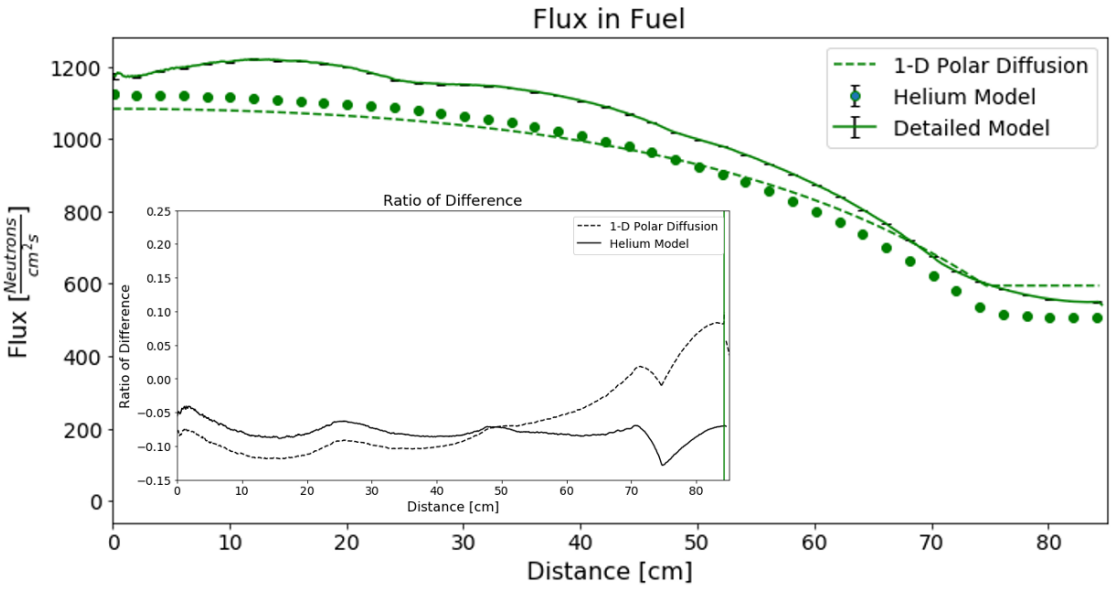

Figure 4-4. The neutron flux spatial distribution simulated by the helium model (circles) captures the neutron flux spatial distribution flattening out in the detailed model (solid line) over the 20 cm region before exiting the fuel region. The diffusion approximation (dotted line) also captures the flux flattening near 65 cm from the cask centerline after adding a helium annulus for neutron streaming.

the diffusion (including a free-streaming) model match, with the exception of the three depressions present in the detailed models. These results show neutrons streaming through the helium region exterior to the fuel cells before exiting into the MPC even though the helium model and the analytic model do not capture the small depressions.

4.1.3 Inter-bundle Depressions

To this point, the simulation results assessment has shown that explanation of causes for the first two features, the flat region and abrupt level-off regions, does not necessitate simulation of geometric details at the individual fuel pin level. However, the physics associated with the three small depressions in the detailed model (seen in Fig. 2-23) has not been explained. Intuition suggests it seems necessary that some level of geometric detail needs to be added back into the reduced complexity simulations to identify the cause of the final two features.

The scalar flux depressions depicted in Fig. 2-23 represent the third feature and are presumed to be caused by the neutron absorbing pads that are present between fuel bundles, located at $-71.62 < r < -71.41$ cm, $-47.61 < r < -47.40$ cm, $-23.61 < r < -23.40$ cm, $0.40 < r < 0.61$ cm, $24.40 < r < 24.61$ cm, $48.41 < r < 48.62$ cm, where r is the distance from the cask centerline. These pads contain ^{10}B, which has a propensity for absorbing thermal neutrons. To corroborate this notion, reintegrating the stainless steel basket structure and neutron absorbing pads is expected to capture the depressions not found in the previous models. Again, comparing the MFP of neutrons in stainless steel 304, the neutron absorbing pads, and fuel rods in Fig. 4-5 shows the MFP is dominated by the absorbing component at a level of approximately 10 cm (or less, depending on the energy of the incident neutrons). These MFP's are similar to the physical thickness of the stainless steel (0.4 cm thick), neutron absorbing pads (0.207 cm thick), and fuel in the MPC (21.42 cm thick). Where, the MFP of 1 MeV neutrons, neutrons with energies near the maximum neutron source energy of 2.71 MeV, is approximately 10 cm in the fuel, 3 cm in the neutron absorbing pads, and 0.5 cm in the stainless steel. Therefore, the neutrons present within the fuel region will likely undergo an appreciable number of interactions in the stainless steel and neutron absorbing materials. However, the neutron flux is expected to decrease in the steel and neutron absorbing pads, as, no neutrons are being generated in these materials in the MCNP models (the MCNP models only simulate neutrons and other types of radiation are neglected, such as α particles generating neutrons through (α,n) reactions).

Another MCNP model is developed to describe the cause of the depressions, Fig. 4-6. This multi-layered model is called the "1-D basket model" and represents a single row of fuel cells from the detailed model with one difference: the volume attributed to fuel materials. In this model, the interior volume of each fuel cell contains a cell homogenized fuel composition with helium on both sides and neutron absorbing pad to the left. The cell homogenized fuel composition is determined using the mass fraction of materials which

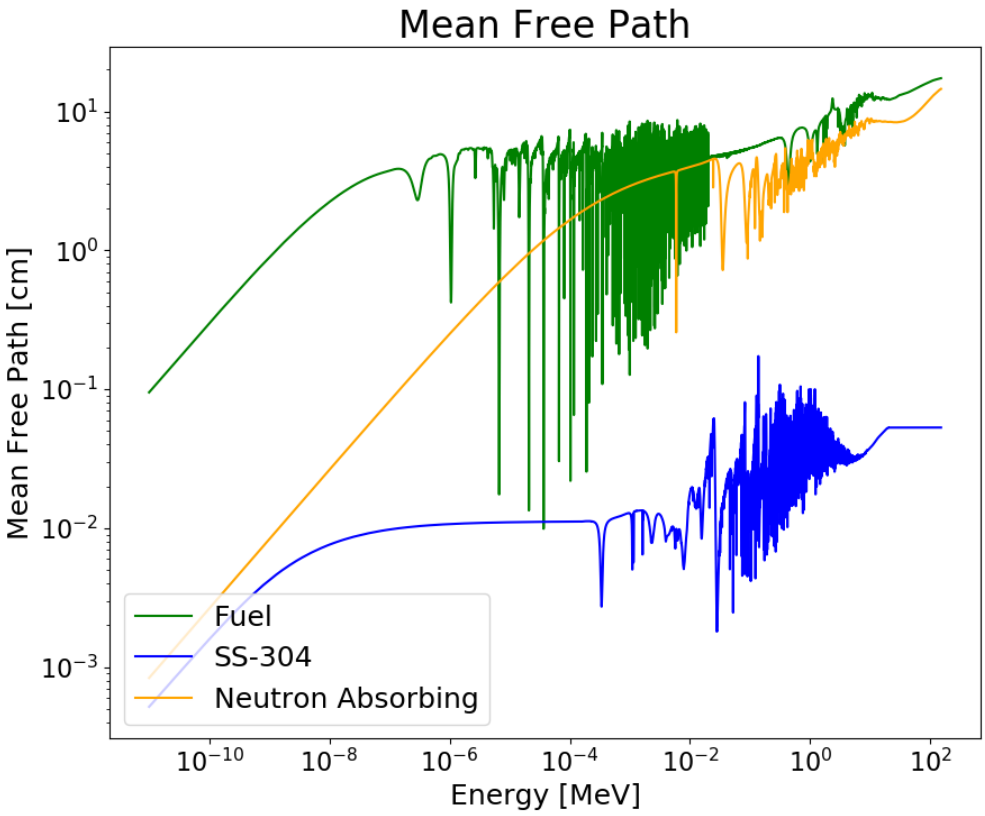

Figure 4-5. The mean free paths for stainless steel 304 (blue), neutron absorbing pad material (orange), and fuel pin material (green). These three mean free paths are similar to the physical thicknesses of each material implying that the steel and neutron absorbing pads need to be included in MCNP simulations as discrete materials instead of being incorporated into the homogenized fuel.

comprise the 264 fuel rods and helium between the fuel rods in each cell. The volume of the cell homogenized fuel material is defined to be equal to the volume of a single fuel bundle.

The simulated neutron flux spatial distribution through the 1-D basket model is shown in Fig. 4-7. The simplified basket model has six small depressions present in the flux around ±25 cm, ±50 cm, ±75 cm. These depressions correspond to a 1-2% local reduction in the flux, which is similar in location and magnitude to the depressions present in the simulated neutron flux spatial distribution in the detailed model. The depressions in the neutron flux spatial distribution occur within the stainless steel and neutron absorbing

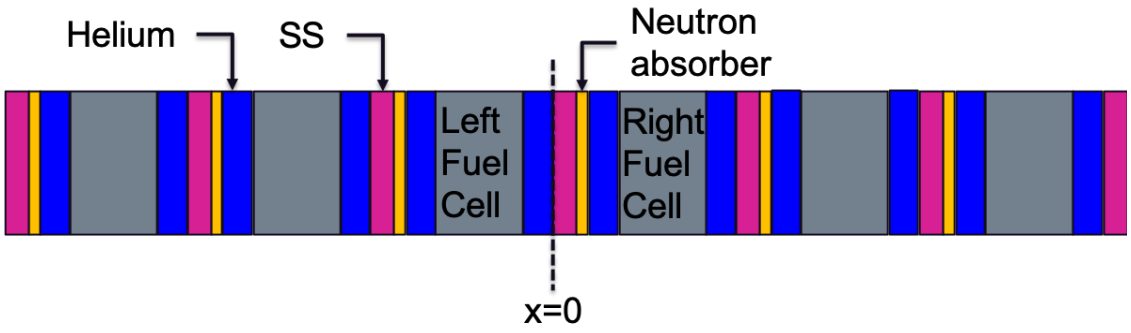

Figure 4-6. The 1-D basket model used to identify the cause of the small depressions. The model is repeating layers of stainless steel (pink), neutron absorbing pads (orange), helium (blue), and cell homogenized fuel (gray).

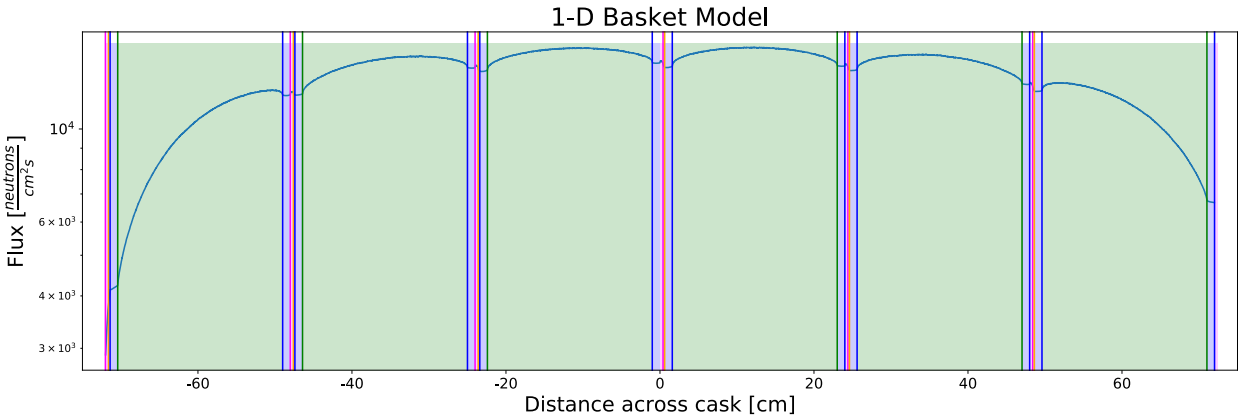

Figure 4-7. The neutron flux spatial distribution simulated from the 1-D basket model. The colors are representative of each material: stainless steel 304 (pink), neutron absorbing pad (orange), helium (blue), and cell homogenized fuel (green). There are depressions present in the flux which occur within the stainless steel and neutron absorbing pads.

pad materials. The flux increases in the fuel as neutrons are born from spontaneous fission decays and (α, n) reactions. The combination of the absorption events in the neutron absorbing pads and source events in the fuel cause the depressions observed in the neutron flux spatial distribution.

4.1.4 Azimuthally Asymmetric Flux

The final feature, the flux asymmetry (seen in Fig. 2-24), is also explained using the 1-D basket model. The detailed model shows a higher flux leaving the bottom right of section of the cask as compared to the top left section of the cask. This discrepancy is

seen at the leftmost and rightmost exiting surfaces in Fig. 4-7. The leftmost face has a lower exiting flux value than the value observed at the rightmost face. Figure 4-8 shows the top-down view of the MPC where the approximate locations of the neutron absorbing pads highlighted with blue lines. From this perspective, pads are located at the top and left side surfaces of each fuel cell. The asymmetric placement of the pads are likely the cause of the azimuthally asymmetric neutron flux. Figure 4-6 is a 1-D representation of Fig. 4-8 and shows the reason for the asymmetry: a neutron born in the left fuel cell and traveling left will pass through three neutron absorbing pads before exiting the left face, which is the same number of neutron absorbing pads that same neutron would have to pass through if it were traveling right. Conversely, if a neutron is born in the right fuel cell and traveling to the left, it passes through four neutron absorbing pads. However, if that same neutron were to travel right, it only potentially encounters two neutron absorbing pads. The number of neutron absorbing pads a neutron potentially encounters is not the same based on the the location of neutron generation and direction of travel because of the placement of neutron absorbing pads in the MPC. The asymmetric loading of these pads directly affects the neutron flux spatial distribution exiting the spent fuel cask.

To further corroborate this notion, the detailed model was adjusted, replacing the stainless steel structure and neutron absorbing pads with vacuum, shown in Fig. 4-9. This modification makes the detailed model fully symmetrical. Figure 4-10 compares the ratio of the neutron flux spatial distribution averaged over the top left section and the flux averaged over the bottom right section from the detailed model where one simulation replaced neutron absorbing pads with vacuum and the original detailed model. The maximum deviation of the ratios of neutron flux spatial densities is 0.1% as a result of replacing non-fuel structure in the MPC with vacuum, confirming the results from the basket model. In contrast, the maximum deviation of these same ratios in the original detailed model is nearly 10%.

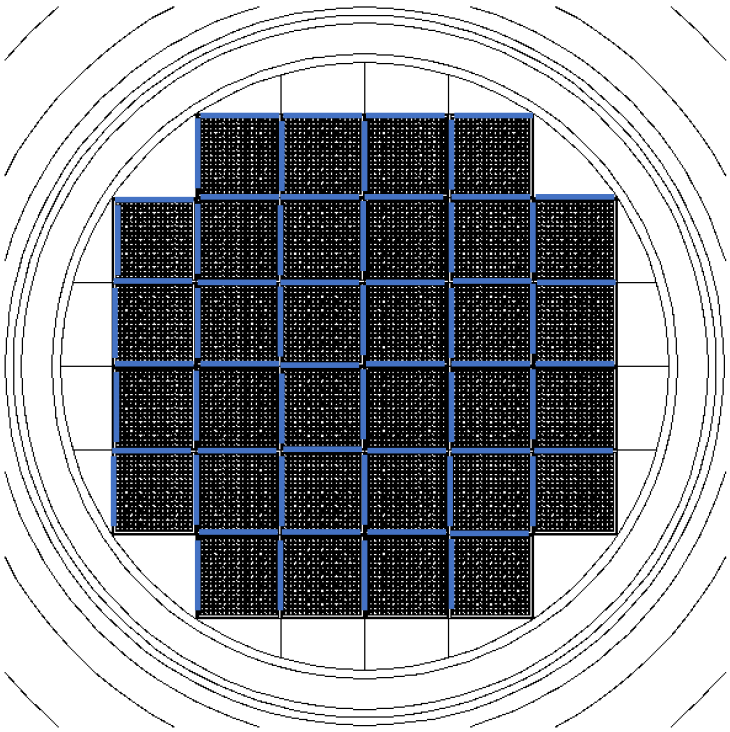

Figure 4-8. The approximate location of the neutron absorbing pads are shown in the MPC. From the perspective shown, the pads are placed at the top and left sides of each cell which may result in the asymmetric neutron flux.

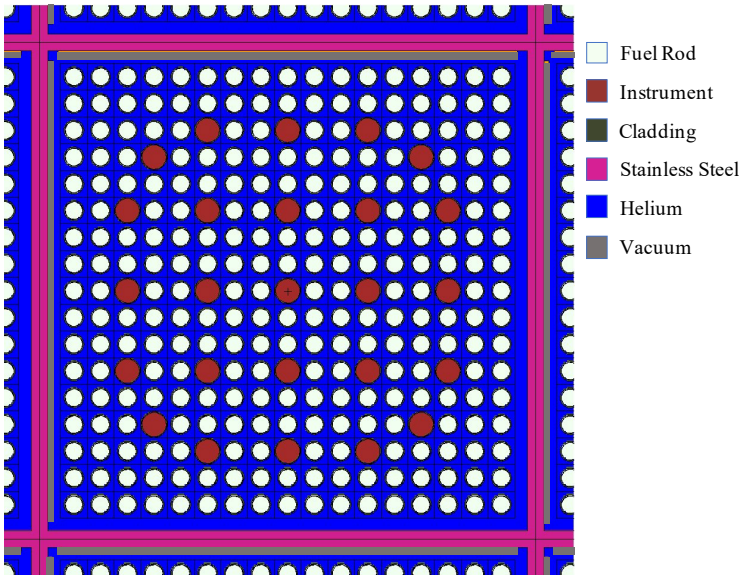

Figure 4-9. A zoomed in top-down view of a single fuel cell where the neutron absorbing pads have been replaced with vacuum.

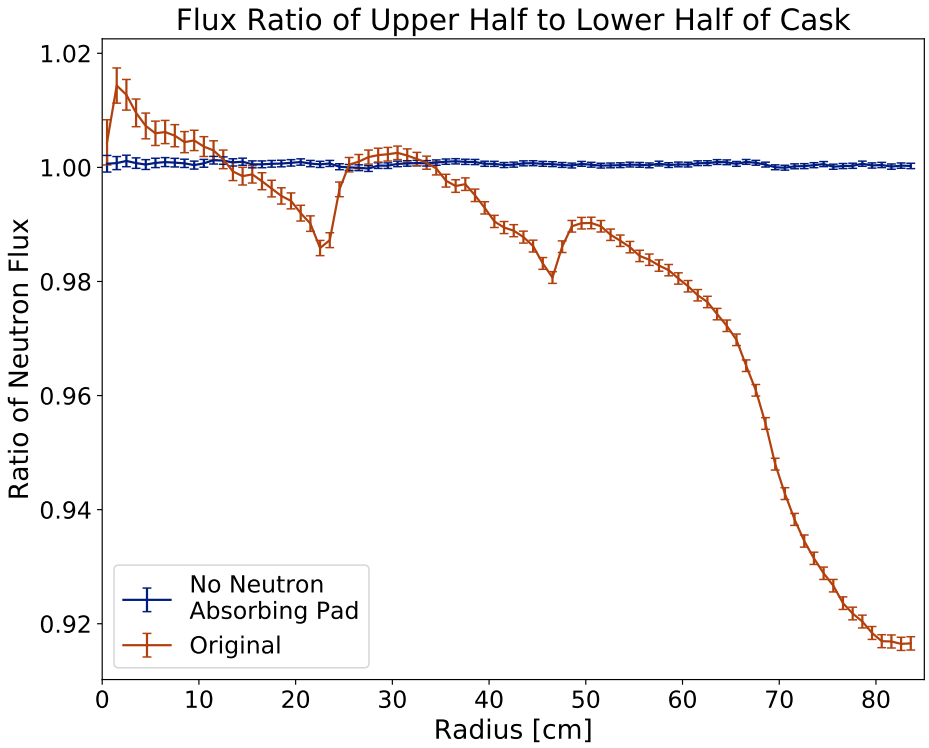

Figure 4-10. The ratio of the neutron flux spatial distribution in the upper left section of the fuel region to the neutron flux spatial distribution in the lower right section of the fuel region. This ratio is nearly 1 over the entirety of the fuel region, confirming the assumption that removing the neutron absorbing pads removes the previously identified depressions.

4.1.5 Alternate Fuel Region Modeling

Previous findings have shown that geometric structures finer than the stainless steel baskets, neutron absorbing pads, and helium annulus result in less than 15% error in the neutron flux, from Fig. 4-4. Therefore, an alternate reduced-fidelity computation model is developed which preserves the stainless steel fuel basket and neutron absorbing pads but homogenizes the fuel pins within each cell. The "cruciform model" is developed to ensure no important physics are neglected in the reduced-order modeling and analysis process. This model uses the cell homogenized fuel definition in each of the 32 original fuel cells. In doing so, the stainless steel fuel basket and neutron absorbing pads are retained

and discrete from the homogenized fuel. The helium surrounding the 32 fuel cells is also retained.

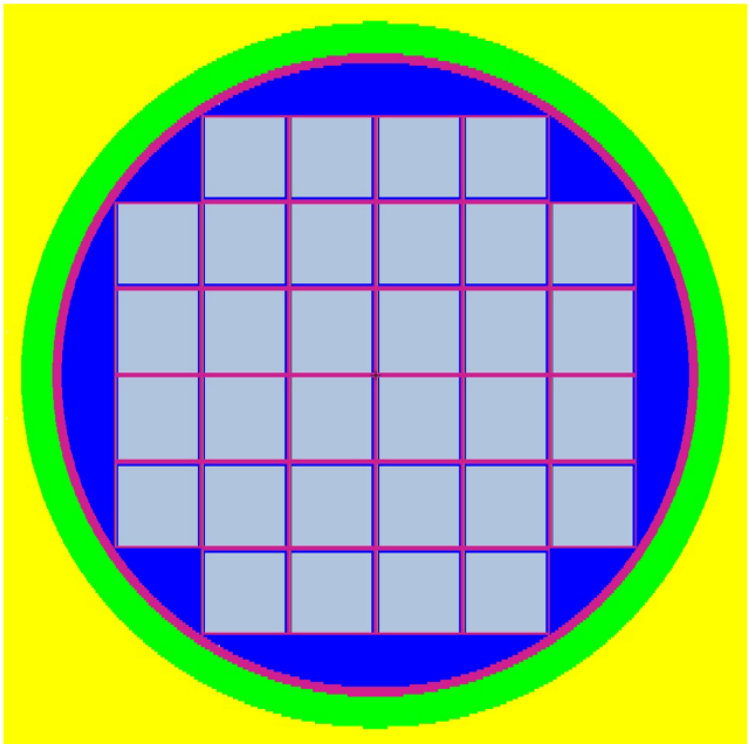

Figure 4-11. The cruciform model. The gray squares are cell homogenized fuel, the stainless steel fuel basket and MPC are pink, the helium annulus is blue, the air exterior to the MPC is green, and concrete is yellow. The neutron absorbing pads (orange) are present in this diagram, but are too thin to be seen here.

The neutron spatial flux distribution simulated by the cruciform model is shown in Fig. 4-12. These results underpredict the flux from the detailed model by 5-7% through the entire fuel region, including in the helium annulus. Moreover, these results can also be interpreted as the cruciform model accounting for the physics relevant to the detailed model's spatial neutron flux distribution at a level greater than 90%. That is, further fine detail additions to the cruciform model will "close the gap" with respect to the detailed model at a sub-10% level.

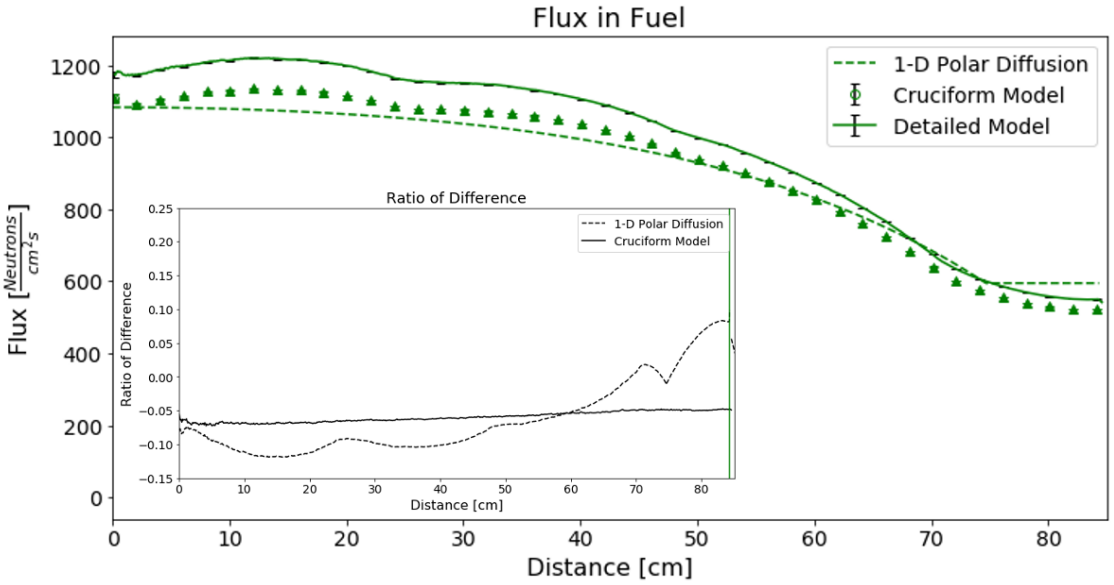

Figure 4-12. The neutron flux spatial distribution of the cruciform model (triangles) capture the flatness of, the leveling off of, and the depressions in the neutron flux spatial distribution seen in the detailed model (solid).

4.2 Discussion of MPC and Overpack Sub-problems

4.2.1 Flux in Concrete

Eqns. 3-61-3-64 are a general set of coupled differential equations which are applied to the MPC, concrete, and the carbon steel shell, which motivates discussion of handling boundary conditions to find unique solutions for each material region. Previously, the air region is decided to be treated as a free-streaming region. Therefore, the concrete region is thought of as sandwiched between the MPC and the carbon steel shell and the neutron flux is chosen to be continuous at both interfaces, between the MPC and concrete and between the concrete and carbon steel shell. The boundary conditions for the right-moving fluxes are taken at the interface of the MPC and concrete, where the boundary conditions for the left-moving fluxes are taken at the interface between concrete and the carbon steel shell.

The boundary conditions are chosen in this manner in order to account for information at the inner and outer radius values of the MPC and overpack. At the outmost radius of the over, there is assumed to be no incoming flux, or, the left-moving fluxes are zero at

this point since neutrons that leave the cask are unlikely to backscatter back into the cask given the large MFP of neutrons in air. To account for this boundary condition, the boundary conditions for the left-moving flux values are taken at the outer thicknesses of each material. The right-moving fluxes are determined from the fuel region. Neutrons are born in the fuel region and, at a macroscopic level, travel outward due to diffusion. Then, these neutrons provide information concerning the right-moving flux through the cask radius, motivating the choice of taking the boundary condition for each right-moving flux at the interior radius of each material. Using the previously described notion, the boundary conditions for a continuous flux in concrete are written as

$$\phi^1_{mpc,1}(r = 86.84\ cm) = \phi^1_{conc,1}(r = 95.25\ cm), \tag{4-6}$$

$$\phi^1_{conc,2}(r = 166.37\ cm) = \phi^1_{cs,2}(r = 166.37\ cm), \tag{4-7}$$

$$\phi^2_{mpc,1}(r = 86.84\ cm) = \phi^2_{conc,1}(r = 95.25\ cm), \tag{4-8}$$

$$\phi^2_{conc,2}(r = 166.37\ cm) = \phi^2_{cs,2}(r = 166.37\ cm), \tag{4-9}$$

where $\phi^g_{mpc,i}$ is the i direction g group neutron flux in the MPC, $\phi^g_{conc,i}$ is the i direction g group neutron flux in concrete, and $\phi^g_{cs,i}$ is the i direction g group neutron flux in the carbon steel shell. Figure 4-13 show the results of the neutron flux calculated by solving Eqns. 3-57-3-60 with the identified boundary conditions, Eqns. 4-6-4-9.

Table 4-3 provides the nominal parameter values used in Eqns. 3-61-3-64 to calculate the neutron flux in the concrete annulus. The input parameters in Tab. 4-3 are determined using NJOY [45] using the energy cutoff value of 1 keV. This value is chosen based on Fig. 2-15, where a 1 keV threshold contains all resonances in the total cross section to the fast group. Energy group boundaries are chosen with the intent of keeping the cross section value as uniform as possible within an energy group [41]. Further, choosing 1 keV as the energy group cutoff means the partial neutron fluxes are continuous between the MPC and concrete annulus.

Table 4-3. Summary of parameter data in the concrete annulus.

Parameter	Values
S^0	0 $\frac{neutrons}{cm^3 s}$
μ_1^0	0.5773502691 *unitless*
μ_2^0	-0.5773502691 *unitless*
$\Sigma_a^{0,1}$	0.00155 $\frac{1}{cm}$
$\Sigma_a^{0,2}$	0.0041 $\frac{1}{cm}$
$\Sigma_s^{0,1\rightarrow1}$	0.28144 $\frac{1}{cm}$
$\Sigma_s^{0,1\rightarrow2}$	0.01456 $\frac{1}{cm}$
$\Sigma_s^{0,2\rightarrow1}$	0 $\frac{1}{cm}$
$\Sigma_s^{0,2\rightarrow2}$	0.37215 $\frac{1}{cm}$
$r_{concrete,inner}$	95.25 *cm*
$r_{concrete,outer}$	166.37 *cm*
concrete thickness	71.12 *cm*

The hydrogen content in concrete is responsible for thermalizing the neutron flux and attenuating neutrons. Figure 4-13 compares the neutron flux from the detailed model (solid line), the E_2S_2 analytic solution (red dashed), the fast energy group E_2S_2 solution (blue dotted), the thermal energy group E_2S_2 solution (brown dotted), and the MCNP helium model (dotted). In concrete, the neutron flux experiences a shift in energies as a result of downscattering occurring on hydrogen atoms. The analytic solutions confirm the observed shift in energies. The fast flux (the blue dotted line) decreases exponentially through the concrete regions. Observing the fast group flux equations, Eqns. 3-61 and 3-62, show no source terms appear in these equations. That is, neutrons in the fast group are only preserved through in-scattering interactions or lost through down-scattering interactions, causing the fast flux to be reduced through the concrete region. In the case of concrete these interactions are mainly scattering since the scattering ratio ($\frac{\Sigma_s}{\Sigma_t}$) in the fast region for concrete is 99.5%. A high scattering ratio at fast neutron energies breeds thermal neutrons. Similarly, observing the thermal flux equations, Eqns. 3-63 and 3-64, show the only source term comes from downscattering of fast neutrons, resulting in the initial increase of the thermal neutron flux shown in the first 10 cm of Fig. 4-13. As the fast neutron population decreases, the rate at which neutrons are thermalized decreases as well, which when combined with loss terms, causes the populations of both the fast

and thermal neutron fluxes to decrease as a function of thickness. Both the analog MCNP model and the analytic model capture the physics of the detailed model within 10%, with the exception of the last 6 cm of the analytic model.

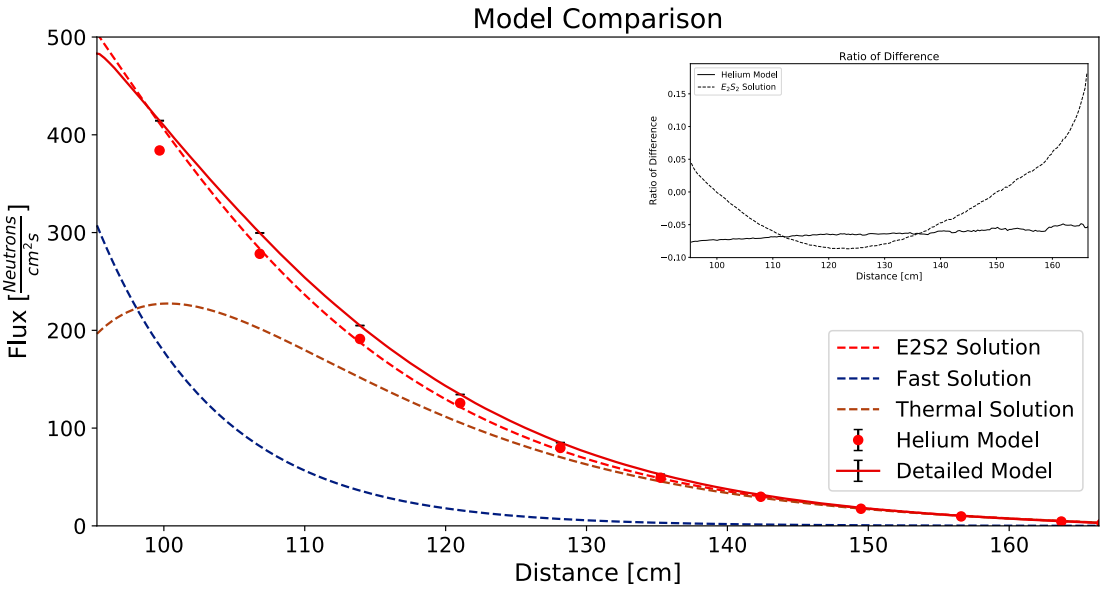

Figure 4-13. The neutron flux spatial distribution of the analytic E_2S_2 model (dashed line), helium model (circles), and detailed model (solid lines). The fast and thermal portions of the E_2S_2 solutions are shown in the blue and brown dotted lines respectively. The inset graphs shows the error between the analog models and detailed model.

The reason the analytic model shows higher disagreement with the detailed model in the outer 6 cm is a result of the boundary conditions. The E_2S_2 equations are solved using a continuous flux boundary condition at both surfaces of the model. While considering the neutron flux as continuous is a physically consistent boundary condition, higher order effects (e.g., continuity of derivatives) are not being considered. Further, the outermost boundary condition assumes that no neutrons will re-enter the cask after leaving. A non-reentrant boundary condition, while nearly physically consistent, will still act as source of error to materials within the cask, since error at the outermost boundary will be propagated through the cask. Further discussion concerning the effects of the boundary conditions is provided in Chpt. 7.

4.2.2 Flux in MPC and Carbon Steel Shell

The MPC and carbon steel shell are the final material regions left to discuss. However, solving Eqns. 3-57-3-60 in these materials requires knowledge of boundary conditions. The boundary conditions corresponding to the MPC are discussed first.

In the MPC, the right-moving flux is considered continuous from the fuel region. Unfortunately, this value is not directly available and some data needs to be taken from MCNP. The analytic flux leaving the fuel is considered monoenergetic and isotropic, however, the flux in the remain cask is treated with two energy groups and two directions. Fig. 2-9b shows 57.290% of the neutrons are traveling rightward at the surface of the MPC and the remaining neutrons are moving leftward. Further, Fig. 2-8h shows 81.493% of the neutrons have energies above 1 keV, which is considered the "fast" energy group for this work. Using these two results, the right-moving partial fluxes can be determined from the value of the monoenergetic isotropic neutron flux leaving the fuel as

$$\phi^1_{mpc,1}\left(r = 84.34cm\right) = (0.5729 * 0.81493)\phi_{fuel}\left(r = 84.34cm\right), \tag{4-10}$$

$$\phi^2_{mpc,1}\left(r = 84.34cm\right) = (0.5729 * 0.18507)\phi_{fuel}\left(r = 84.34cm\right), \tag{4-11}$$

where $\phi^1_{mpc,1}$ and $\phi^2_{mpc,1}$ are the fast and thermal right-moving fluxes respectfully at the interface between the fuel and MPC. The remaining two boundary conditions are taken from the exiting surface of the MPC at 86.84 cm. In order to have a continuous flux at this point, the left-moving fluxes in the MPC must be equal to the corresponding fluxes from the concrete (since the air annulus is a free-streaming region). Therefore, the remaining two boundary conditions are chosen to be

$$\phi^1_{mpc,2}\left(r = 86.84\ cm\right) = \phi^1_{concrete,2}\left(r = 95.25\ cm\right), \tag{4-12}$$

$$\phi^2_{mpc,2}\left(r = 86.84\ cm\right) = \phi^2_{concrete,2}\left(r = 95.25\ cm\right).. \tag{4-13}$$

Table 4-4 also includes values for μ_1 and μ_2. These parameters are chosen by the evaluator and have few constraints (e.g., μ cannot be chosen to equal zero) [42]. Further,

Table 4-4. Summary of parameter data in the MPC.

Parameter	Values
S^0	0 $\frac{neutrons}{cm^3 s}$
μ_1^0	0.5773502691
μ_2^0	-0.5773502691
$\Sigma_a^{0,1}$	0.01912 $\frac{1}{cm}$
$\Sigma_a^{0,2}$	0.13941 $\frac{1}{cm}$
$\Sigma_s^{0,1\rightarrow 1}$	0.54681 $\frac{1}{cm}$
$\Sigma_s^{0,1\rightarrow 2}$	0.00281 $\frac{1}{cm}$
$\Sigma_s^{0,2\rightarrow 1}$	0 $\frac{1}{cm}$
$\Sigma_s^{0,2\rightarrow 2}$	0.89962 $\frac{1}{cm}$
$r_{mpc,inner}$	84.34 cm
$r_{mpc,outer}$	86.84 cm
MPC thickness	2.5 cm

the directions are typically chosen as opposites ($\mu_{N+1-n} = \mu_n$ for $n = 1, 2, \ldots, (N/2)$), and are typically picked according to Gaussian quadrature rules [42].

Eqns. 3-61-3-64 are solved using the boundary conditions (Eqns. 4-10-4-13) to yield analytic expressions in the MPC which are plotted in Fig. 4-14. Figure 4-14 compares the neutron flux from the detailed model (solid blue), the E_2S_2 model solution (dotted blue line), and the analog helium model (circles). The fast and thermal components of the E_2S_2 solution are displayed as the dark blue and brown lines respectively. Even though the thickness of the stainless steel is a similar to the MFP, some of the fast neutrons undergo scattering interactions and thermalize which results in an increase in the thermal flux. The error between the analog models and the detailed model is less than 10%. In fact, the analytic model agrees with the detailed model within 5%, which is better than the helium model, as the Eqns. 3-61 - 3-64 allow for anisotropies in the direction flux where the diffusion approximation, Eqn. 3-85, assumes an isotropic flux. Moreover, there are fewer interactions occurring in the MPC, caused by the thickness of the MPC (2.5 cm) being similar to the MFP of fast neutrons in the MPC (approximately 3 cm). Figure 4-14 shows the flux is flat as compared to the other materials, which further corroborates the concept that only a fraction of the neutrons are undergoing interactions in the MPC. Therefore, less physics is occurring in the MPC as a result of fewer neutron interactions taking place.

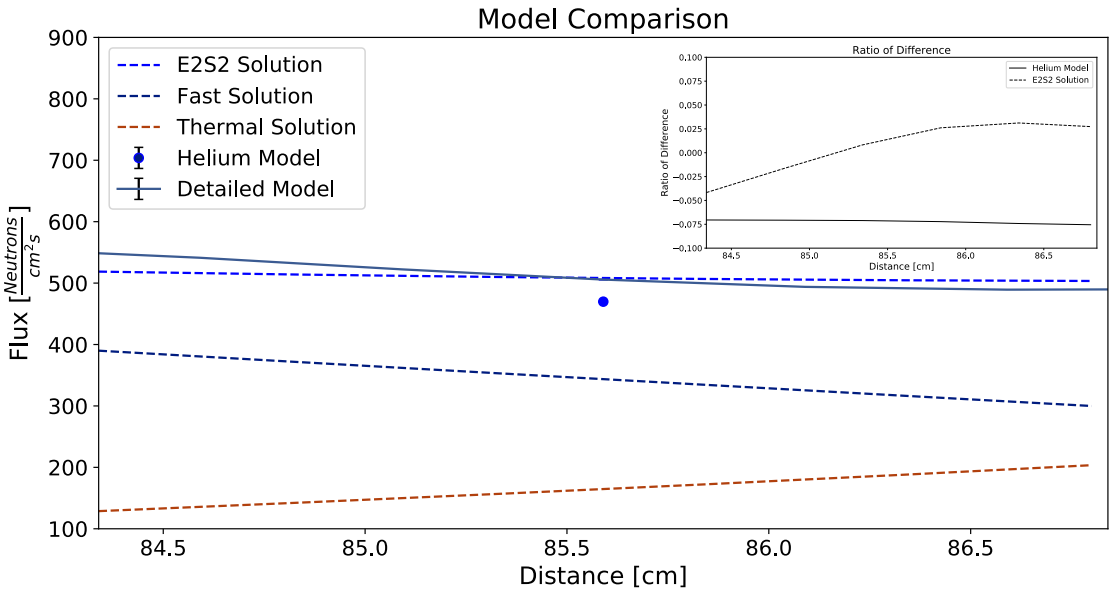

Figure 4-14. The neutron flux spatial distribution of the analytic E_2S_2 model (dashed line), helium model (circles), and detailed model (solid lines). The fast and thermal portions of the E_2S_2 solutions are shown in the blue and brown dotted lines respectively. The inset graphs shows the error between the analog models and detailed model.

Finally, the flux in the carbon steel shell needs to be determined, by first discussing the boundary conditions chosen in order to solve Eqns. 3-57-3-60. The flux at the interface between the concrete and the carbon steel shell is assumed to be continuous and the boundary conditions are written as

$$\phi^1_{conc,1}(r = 166.37\ cm) = \phi^1_{cs,1}(r = 166.37\ cm), \tag{4-14}$$

$$\phi^2_{conc,1}(r = 166.37\ cm) = \phi^2_{cs,1}(r = 166.37\ cm), \tag{4-15}$$

where the right-moving flux values are defined in a consistent manner as those in Sec. 6.2.3. The left-moving flux is assumed to be non-reenterant, meaning a neutron will not return to the cask after it has exited. This is a fair assumption as the large MFP of neutrons in air means neutrons are unlikely to backscatter into the cask once they have entered the environment. Mathematically, a non-reenterant boundary condition is

Table 4-5. Summary of parameter data in the carbon steel shell.

Parameter	Values
S^0	0 $\frac{neutrons}{cm^3 s}$
μ_1^0	0.5773502691 *unitless*
μ_2^0	-0.5773502691 *unitless*
$\Sigma_a^{0,1}$	0.02016 $\frac{1}{cm}$
$\Sigma_a^{0,2}$	0.11740 $\frac{1}{cm}$
$\Sigma_s^{0,1\rightarrow1}$	0.45573 $\frac{1}{cm}$
$\Sigma_s^{0,1\rightarrow2}$	0.00276 $\frac{1}{cm}$
$\Sigma_s^{0,2\rightarrow1}$	0 $\frac{1}{cm}$
$\Sigma_s^{0,2\rightarrow2}$	0.94474 $\frac{1}{cm}$
$r_{carbonsteel,inner}$	166.370 *cm*
$r_{carbonsteel,outer}$	168.275 *cm*
carbon steel shell thickness	1.905 *cm*

expressed as

$$\phi_{cs,2}^1(r = 168.275\ cm) = 0, \tag{4-16}$$

$$\phi_{cs,2}^2(r = 168.275\ cm) = 0.. \tag{4-17}$$

Table 4-5 provides the parameters used in the solution to Eqns. 3-61-3-64 to calculate the neutron flux in the carbon steel shell, with the corresponding boundary conditions, Eqns. 3-61-3-64. The values for the input parameters are calculated using NJOY [45] with an energy cutoff at 1keV. Once again, this energy cutoff value is chosen to isolate resonance structure in the total cross section to the fast group only, and the resonances are absent in the thermal group, Fig. 2-18. Further, choosing 1 keV as the threshold value between the fast and thermal groups matches the threshold value chosen in the concrete region, meaning the partial fluxes have matching energy groups.

Figure 4-15 shows the neutron flux in the carbon steel shell. The flux in the carbon steel shell is almost entirely thermal since the concrete has already thermalized the neutron flux. The analytic model captures this behavior, unfortunately, the analytic model does not capture an increase in the source neutrons in the carbon steel which is observed in the detailed model. Section 7.1.4 describes the causes for this discrepancy further. However, the analytic model agrees within 10-40% over the thickness of the carbon steel.

The higher degree of error is attributed to the small scale of the neutron flux. In fact, the flux at the exiting surface of the cask is 0.68 $\frac{1}{cm^2 s}$ as predicted by the detailed model and 0.91 $\frac{1}{cm^2 s}$ as predicted with the E_2S_2 solution. The error increases through the carbon steel region. A result of the analytic models under predicting loss terms in the carbon steel shell. Figure 4-15 corroborates this result as the total flux does not share the inflection point occurring at 167.132 cm in the detailed model. The inflection point occurs as neutron leakage increases throughout the carbon steel shell, as indicated in by the 29% increase in right moving flux shown in Figs. 2-20a and 2-20b. Further, Fig. 4-15 shows the initial value of the thermal flux at 166.37 cm is larger than the total neutron flux simulated in the detailed MCNP model. The analytic thermal neutron flux is chosen to be continuous with the thermal neutron flux leaving the concrete region at this location and over-predicting the exiting neutron flux from the concrete annulus causes over-predictions in the carbon steel shell flux as well. The effects of boundary conditions are discussed further in Chpt. 7.

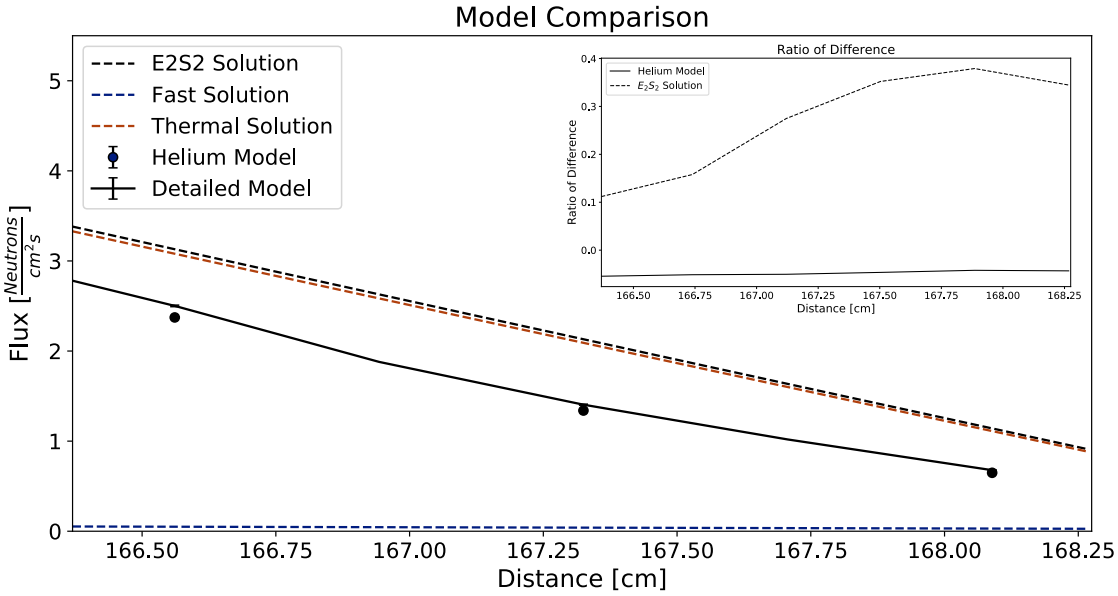

Figure 4-15. The neutron flux spatial distribution of the analytic E_2S_2 model (dashed line), helium model (circles), and detailed model (solid lines). The fast and thermal portions of the E_2S_2 solutions are shown in the blue and brown dotted lines respectively. The inset graphs shows the error between the analog models and detailed model.

4.3 Summary

Using reduced complexity analytic and computational models to analyze the simulation results of a high-fidelity computational model allows for the quantification of effects of any assumptions invoked when developing the latter model. Ensuring important physics are preserved in the course of conducting simulations increases the likelihood of correct results. This work exemplified this notion through a process referred to as "simulation results assessment." As a demonstration, this work included post-simulation analysis of a detailed MCNP model of a HI STORM 100 spent nuclear fuel cask. A series of reduced analytic and computational models were developed and used to identify the physics which causes features in the neutron flux spatial distribution as calculated by the detailed model. In the HI-STORM 100 model, the stainless steel basket, neutron absorbing pads, and helium annulus around the fuel cells are important physical components that need to be preserved in modeling. Retaining the individual fuel pin structure was found to be less important than broadly capturing the lumped material properties inside the individual fuel cells. These results were corroborated using the cruciform model, which appears to capture the physics relevant to the neutron flux spatial distribution in the detailed model beyond the 90% level. The major features of the neutron flux spatial distribution simulated by the detailed model are expected to be correct since the this model preserves material fuel properties and the geometric structure of the neutron absorbing pads and helium annulus.

CHAPTER 5
SENSITIVITY ANALYSIS OF THE DETAILED CASK

The former analysis in Chpts. 2 and 4 help to justify the appropriateness, in terms of characterizing essential physics that give rise to notable features, of the previously used analytic models. Chapter 4 concluded the degree to which each mathematical model captures the physics of its detailed counterpart. Extending the analysis in Chpt. 4 with a complementary sensitivity analysis proves informative as a guide in interpreting, understanding, and rigorizing results of computational studies. Further, the previous analysis justifies using the mathematical models as the focus of an analytic sensitivity analysis. In a similar approach to Chpt. 2, the sensitivity coefficients (SC's) pertaining to cross section values in the detailed cask model are calculated using MCNP and the results are analyzed in order to form the basis of discussion for Chpt. 7. Further, the shortcomings of computational sensitivity analysis are introduced for further discussion.

5.1 Calculating Sensitivity Coefficients with MCNP

SC's are unitless values calculated from sensitivity information and are used to determine the the "importance" of each input parameter (e.g., cross sections). Input parameters with larger SC's have a larger impact on the the system response. The sign of a SC is also important, as the signs indicate the direction of change in the response value given a change in an input parameter parameter value. Meaning, if the SC has a negative value for a given input parameter, increasing the value of that parameter will cause the value of the response to decrease. On the other hand, if the SC has a positive value, increasing the associated input parameter value will cause an increase in the response value. These values can be compared against each other and between models not only to stratify the importance of each value, but also to identify trends occurring in the model. SC's are calculated differently based on whether the model is computational or analytic. Discussion concerning calculations of SC's from analytic models occurs in Chpt. 6. However, in order to discuss trends in the SC's pertaining to cross section values used

in the detailed models, the process for determining SC's from MCNP models is discussed now.

MCNP has the capability to perform a sensitivity study using the PERT card. From the MCNP manual, the PERT card "uses first and second order differential operator techniques" using a Taylor series expansion, which allows "perturbations in cell material density, composition, or reaction cross-section data" [20]. For the purpose of this work, MCNP perturbs cross section data through perturbing the material mass density and, therefore, the macroscopic cross section values. Favorite describes the process for using MCNP to efficiently calculate SC's [46]. In MCNP, SC's are calculated from the results of the Taylor series expansion of the neutron flux. Therefore, taking the second-order Taylor series expansion of the neutron flux as

$$\phi(\sigma_x) = \phi(\sigma_{x,0}) + \left.\frac{\mathrm{d}\phi}{\mathrm{d}\sigma_x}\right|_{\sigma_{x,0}} \Delta\sigma_x + \frac{1}{2}\left.\frac{\mathrm{d}^2\phi}{\mathrm{d}\sigma_x^2}\right|_{\sigma_{x,0}} (\Delta\sigma_x)^2, \tag{5-1}$$

where $\sigma_{x,0}$ is the unperturbed cross section value, $\phi(\sigma_{x,0})$ is the neutron flux evaluated with respect to the nominal value cross sections, and $\Delta\sigma_x \equiv \sigma_x - \sigma_{x,0}$.

The first- and second-order expansion terms are defined as

$$\Delta\phi_1 \equiv \left.\frac{\mathrm{d}\phi}{\mathrm{d}\sigma_x}\right|_{\sigma_{x,0}} \Delta\sigma_x \tag{5-2}$$

and

$$\Delta\phi_2 \equiv \frac{1}{2}\left.\frac{\mathrm{d}^2\phi}{\mathrm{d}\sigma_x^2}\right|_{\sigma_{x,0}} (\Delta\sigma_x)^2 \tag{5-3}$$

respectively. Larger perturbations applied to the cross section values lead to larger changes in the response functions, therefore it is important to define the relative cross section change, p_x, as

$$p_x \equiv \frac{\Delta\sigma_x}{\sigma_{x,0}}, \tag{5-4}$$

where p_x is used to normalize the amount of response change to the amount of perturbation. Further, Eqns. 5-2 and 5-3 can be re-written in terms of p_x after applying the chain rule

as

$$\Delta\phi_1 = \left.\frac{\mathrm{d}\phi}{\mathrm{d}p_x}\right|_{p_x=0} p_x, \tag{5-5}$$

and

$$\Delta\phi_2 = \frac{1}{2}\left.\frac{\mathrm{d}^2\phi}{\mathrm{d}p_x^2}\right|_{p_x=0} p_x^2 \tag{5-6}$$

respectively.

MCNP's perturbation feature estimates the derivatives in Eqns. 5-5 and 5-6 [46]. Equations 5-7 and 5-8 are the two values with corresponding error values, $s_{\Delta\phi_1}$ and $s_{\Delta\phi_2}$ for $\Delta\phi_1$ and $\Delta\phi_2$ respectively, that are output by MCNP when using PERT cards. The value ϕ_n is defined as $\phi(\sigma_{x,n}) \equiv \phi_n$ for notational convenience.

$$\Delta\phi_1(p_{x,r}) \pm s_{\Delta\phi_1} \tag{5-7}$$

$$\Delta\phi_2(p_{x,r}) \pm s_{\Delta\phi_2} \tag{5-8}$$

The values $\Delta\phi_1(p_{x,r})$ and $\Delta\phi_2(p_{x,r})$ are used to determine the SC's. The first-order SC to the cross section value σ_x is defined as

$$S_{\phi,\sigma_x} = \frac{\phi_1}{\phi_0}, \tag{5-9}$$

where ϕ_1 is calculated as

$$\phi_1 = \frac{\Delta\phi_1(p_{x,r})}{p_{x,r}}. \tag{5-10}$$

And ϕ_0 is the unperturbed neutron flux. The uncertainty values corresponding to S_{ϕ,σ_x} are determined by

$$s^2_{S_{\phi,\sigma_x}} = S^2_{\phi,\sigma_x}\left[\left(\frac{s_{\phi_0}}{\phi_0}\right)^2 + \left(\frac{s_{\phi_1}}{\phi_1}\right)^2\right], \tag{5-11}$$

where s_{ϕ_0} is the standard deviation of the unperturbed response given by MCNP and s_{ϕ_1} is calculated as

$$s_{\phi_1} = \frac{s_{\Delta\phi_1}}{|p_x|}. \tag{5-12}$$

The notation of the SC's is similar to notation used for the internal source terms in Eqn. 4-5. However, the two can be distinguished from the subscript (ϕ, σ_x) appearing on the SC's, and used consistently through this effort. Further, the SC's pertaining to the cross sections, Σ_a and Σ_s, are considered for study using MCNP in this program of study, as these values show up as input parameters in Eqn. 4-5 for the fuel region and in the solutions of Eqns. 3-61-3-64 for the MPC, concrete, and carbon steel shell. Equation 4-5 and the solutions to Eqns. 3-61-3-64 contain more input parameters, which will be identified in Chpt. 6, however, these parameters are not compatible with MCNP's PERT capabilities.

The SC's are calculated along the radius of the cask, making them functions of radial distance only. That is, the angular and energy dependence of the SC's is integrated out and radial dependence remains. This handling of the SC's is chosen to reflect the handling of the neutron flux in Chpts. 2 and 4.

5.2 Sensitivity Coefficients in the Detailed Model

5.2.1 Fuel Region

Probably the most impactful shortcoming of using MCNP to determine SC's occurs in the fuel region of the spent fuel cask. In order to perturb cross section values in MCNP, the simulation geometry needs to be modified with a SURFACE card at the location where a simulated measurement is made. That is, the geometry must be changed to accept what sometimes is a "non-physical" surface. Unfortunately, this may not be possible in a given geometry, such as in the fuel containing region of the spent fuel cell. Adding cylindrical surfaces through the fuel lattice precludes a realistic source sampling distribution from being defined across the fuel rods. This prevents the possibility of finding SC's in the fuel containing region of the detailed model. However, development of reduced models allows for comparison between the helium model and the analytic model, Eqn. 3-85, which will be discussed in Chps. 7 and 8.

However, Chpt. 4 motivated the use of the reduced-fidelity MCNP helium model, which serves as a surrogate model in the fuel region. Figure 5-1 shows the SC's pertaining to Σ_f, Σ_c, and Σ_s in the fuel region of the helium model, where Σ_c is the capture cross section defined as $\Sigma_a = \Sigma_c + \Sigma_f$. The SC of Σ_f is positive since fission acts to create neutrons and, therefore, increase the neutron flux (Fig. 5-1). This SC has a linear shape, owing to the homogenous distribution of fissionable material in the cask. Further, any negative slope is a result of the increasing importance of loss mechanisms, as a spent fuel cask is designed to attenuate radiation. That is, spent fuel casks are designed to reduce the neutron flux. Meaning, neutron source terms will have a decreasing effect on the flux through the fuel region in an attempt to attenuate radiation through the cask.

The value of S_{ϕ,Σ_s} is negative, shown in Fig. 5-1. In the range 0 cm-60 cm, S_{ϕ,Σ_s} is flat since neutrons are indirectly lost through thermalization leading to absorption. From 60 cm to 74.68 cm, S_{ϕ,Σ_s} increases in the negative direction owing to leakage in the fuel region. Leakage mechanisms increase near the material boundary which is the reason S_{ϕ,Σ_s} increases in magnitude near the boundary at 74.68 cm.

Figure 5-1 also shows the value of the SC for Σ_c. This value is negative for the entire fuel region, as capture is purely a loss term. S_{ϕ,Σ_c} decreases in magnitude over the fuel region. From 15 cm to 60 cm, both S_{ϕ,Σ_c} and S_{ϕ,Σ_s} decrease in magnitude, alluding to a relationship between the two values when thermalization resulting in capture is the main loss term. From 60 cm to 74.68 cm, neutron loss through leakage is occurring and the SC of Σ_c continues to decrease near the boundary as S_{ϕ,Σ_s} increases in magnitude.

Figure 5-2 shows the absolute values of the SC's in order to make stratifying the parameters by importance more obvious. Through the entire fuel region in the helium model, Σ_f is the least important term, reinforcing the importance of loss physics in a shielding problem. From 0 cm to approximately 70 cm, Σ_s is the second most important parameter and Σ_a is the most important. However, these two parameters switch importance from 70 cm to 74.68 cm as leakage becomes the dominant loss mechanism.

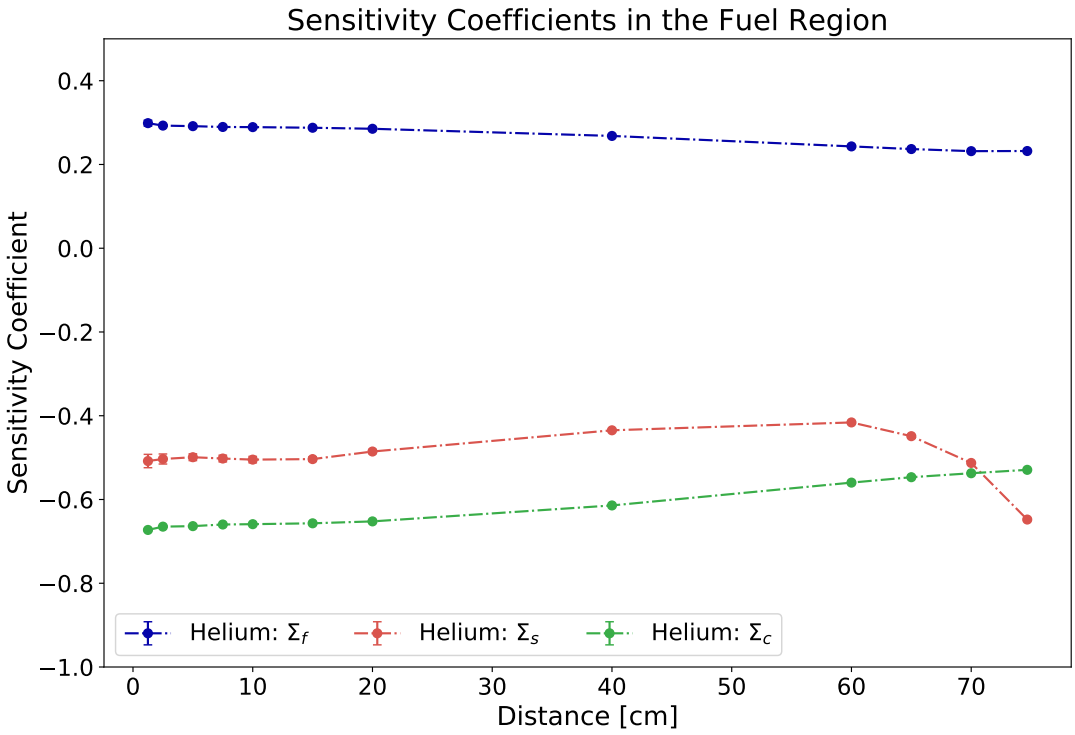

Figure 5-1. SC's corresponding with Σ_f (blue), Σ_s (red), and Σ_c (green) calculated using MCNP in the fuel region of the helium model.

5.2.2 Multipurpose Canister

Figure 5-3 shows the SC's corresponding to Σ_s and Σ_a as the red and green lines respectively. The SC pertaining to Σ_s initially have a positive value at the inner surface of the MPC (84.34 cm from the centerline), before going negative near 85.59 cm. While the values are positive, scattering is acting to preserve the flux value, likely through downscattering which decreases the energy of neutrons but, alone, does not reduce the magnitude of the flux. Once the coefficients become negative, scattering acts as a loss term by causing neutrons to leak through the outer surface of the MPC (86.84 cm).

The SC corresponding to the absorption cross section is entirely negative. Negative sensitivity values indicate that the flux and Σ_a are inversely related. That is, as the absorption cross section increases, the flux decreases. The magnitude of the SC increases from 84.34 cm to 86.34 cm, before decreasing in the remainder of the MPC.

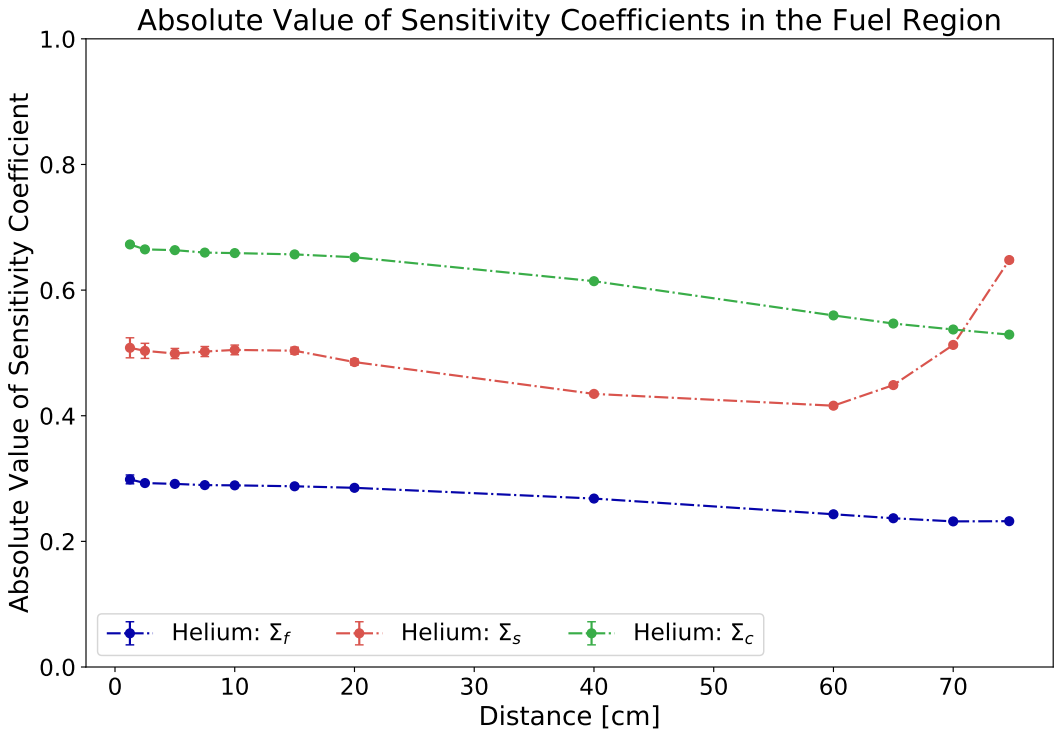

Figure 5-2. The absolute values of the SC's corresponding with Σ_f (blue), Σ_s (red), and Σ_c (green) calculated using MCNP in the fuel region of the helium model.

Figure 5-4 shows the absolute value of the SC's in the MPC. Plotting the absolute values of the SC's makes it easier to identify which parameters are most important at each location within the MPC. For approximately the first 0.5 cm, the scattering cross section is the most sensitive parameter. However, absorption becomes the most sensitive parameter as neutrons move further into the MPC.

5.2.3 Air Region

There is an annulus of air between the MPC and the concrete annulus. Chapter 2 considered the air region as a free-streaming region where the neutron flux was assumed to not interact in the material. Further analysis of the SC's in the air region corroborate the previous assumption as treating the air region as void. Figure 5-5 shows the SC's of Σ_s and Σ_a in the air. From this figure, it is shown that the magnitude of the SC's are much smaller (at least two orders of magnitude smaller than the SC's in the other

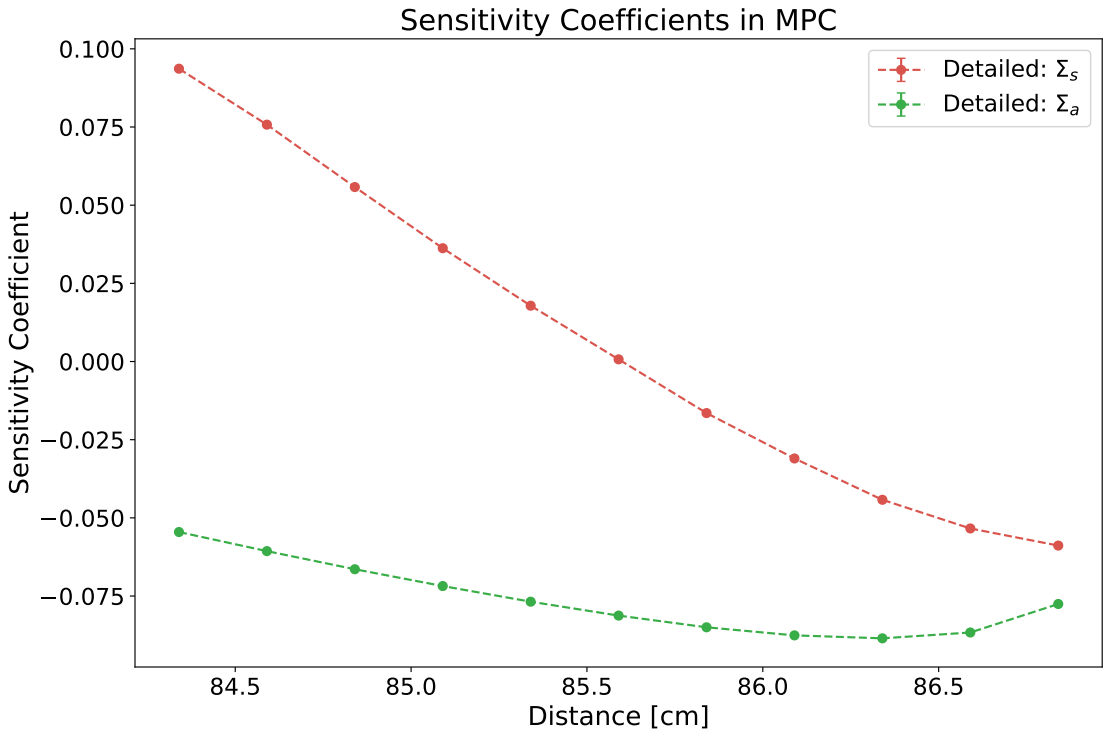

Figure 5-3. SC's corresponding with Σ_s (red) and Σ_a (green) calculated using MCNP in the MPC.

materials, shown in Figs. 5-3, 5-6, and 5-8) and, therefore, further sensitivity analysis in the air region can be neglected. That is, the small SC's in the air mean the neutron flux is relatively insensitive to perturbations in material properties in air.

5.2.4 Concrete Annulus

Chapter 2 determined that approximately half of the neutron flux is attenuated in the concrete and the high hydrogen content in this material caused a shift in the neutron energy spectrum. Presumably, the scattering cross section is essential in driving physics within the concrete. Figure 5-6 shows the SC pertaining to the scattering cross section is initially positive, similar to other materials, before becoming negative near 99.75 cm. The negative SC pertaining to the scattering cross section indicates that neutrons are mainly removed through scattering and neutrons are caught in thermal equilibrium in the concrete as absorption is unlikely in concrete. Near the outer radius of the concrete

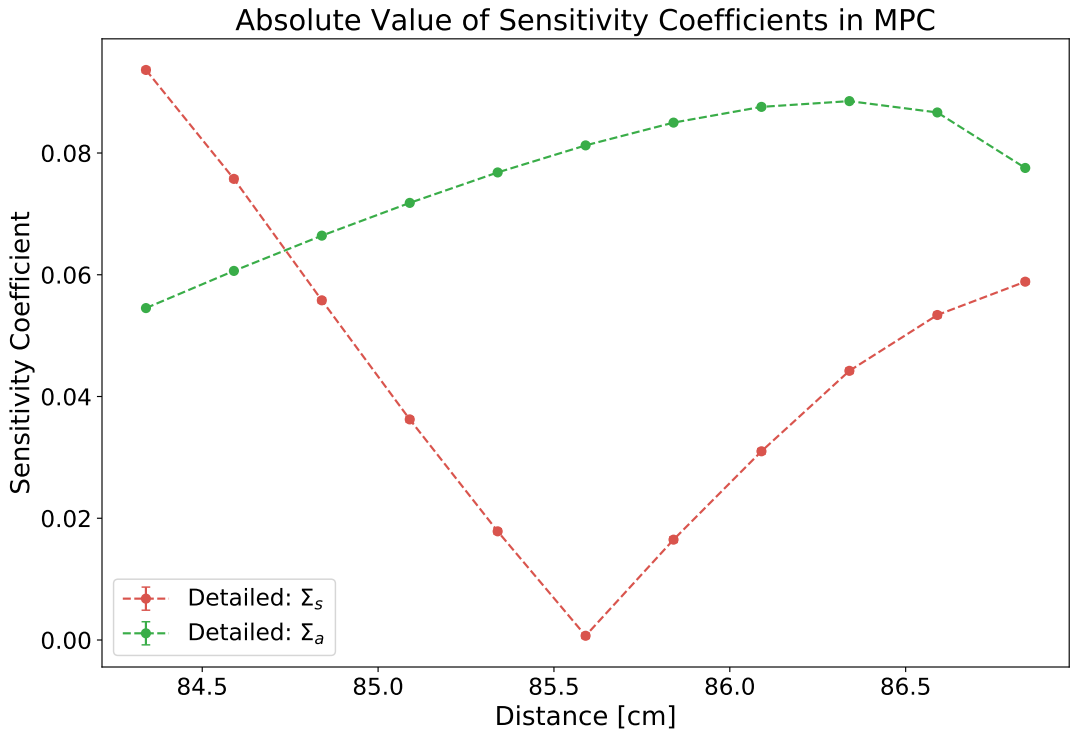

Figure 5-4. The absolute values of the SC's pertaining to Σ_s (red) and Σ_a (green).

(162.75 cm), leakage causes the SC pertaining to the scattering cross section to increase. At this location, the neutron flux is peaked in an outward direction as seen in Fig 2-17. This provides further evidence that scattering is driving 1) attenuation and 2) leakage in the outer radii values of the concrete.

The SC pertaining to the absorption cross section is negative showing that absorption, while less likely to occur than scattering, causes losses in the neutron flux. The increasing slope across the annulus thickness shows how losses due to absorption increase as the magnitude of the thermal flux increases making absorption more likely. At 162.75 cm, the SC pertaining to the absorption cross section decreases in magnitude. This behavior is inversely related to the behavior observed in the SC pertaining to Σ_s alluding to a relationship between increased leakage and decreasing absorption importance.

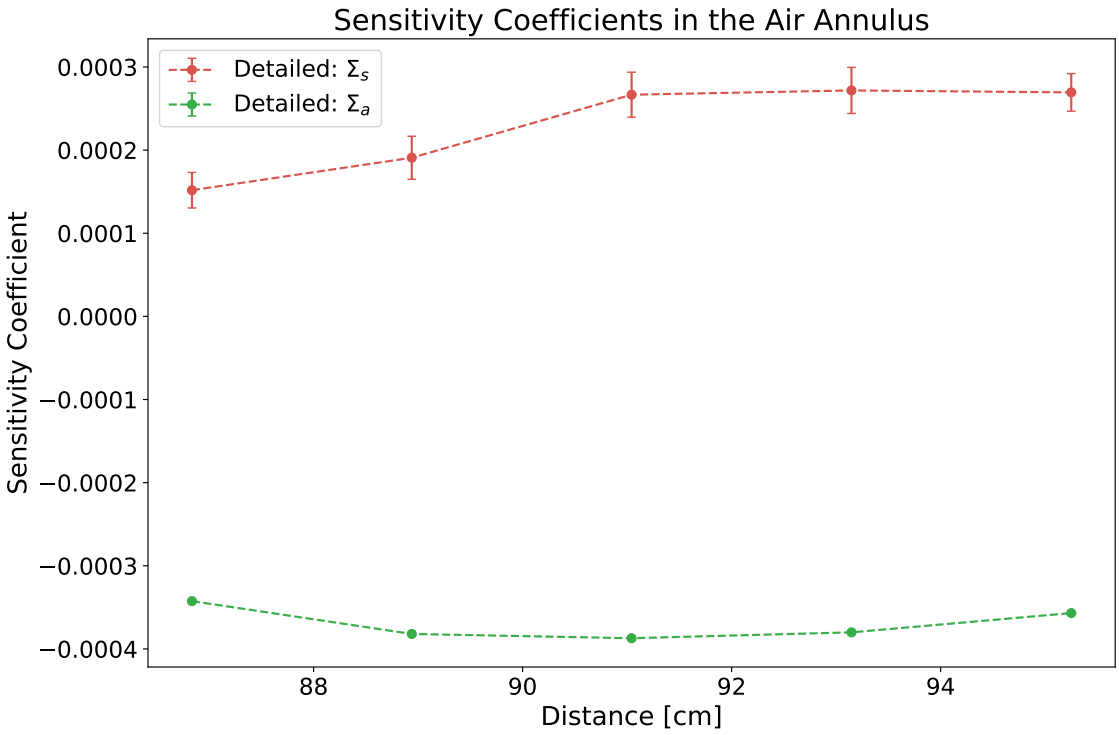

Figure 5-5. The SC's corresponding to Σ_s (red) and Σ_a (green) are two orders of magnitude lower than the other SC's in the other materials. Therefore, an analytic sensitivity analysis for this region can be neglected.

Figure 5-7 shows the absolute values of the SC's in the concrete. Scattering is the most important parameter from approximately 104.25 cm to the outer radius of the concrete at 166.37 cm, which is expected since neutron attenuation in concrete is mainly caused through scattering interactions (as indicated by the larger magnitude of the SC pertaining to Σ_s as compared to those of Σ_a).

5.2.5 Carbon Steel Shell

Figure 5-8 shows the SC's of Σ_s and Σ_a throughout the carbon steel shell. Once again the values of the SC pertaining to Σ_s are initially positive before going negative near 167.51 cm. The forward peaked flux shown in Figs. 2-20a and 2-20b indicates that an increase in neutron leakage is reflected in the increasing negative magnitude of the SC corresponding to Σ_s.

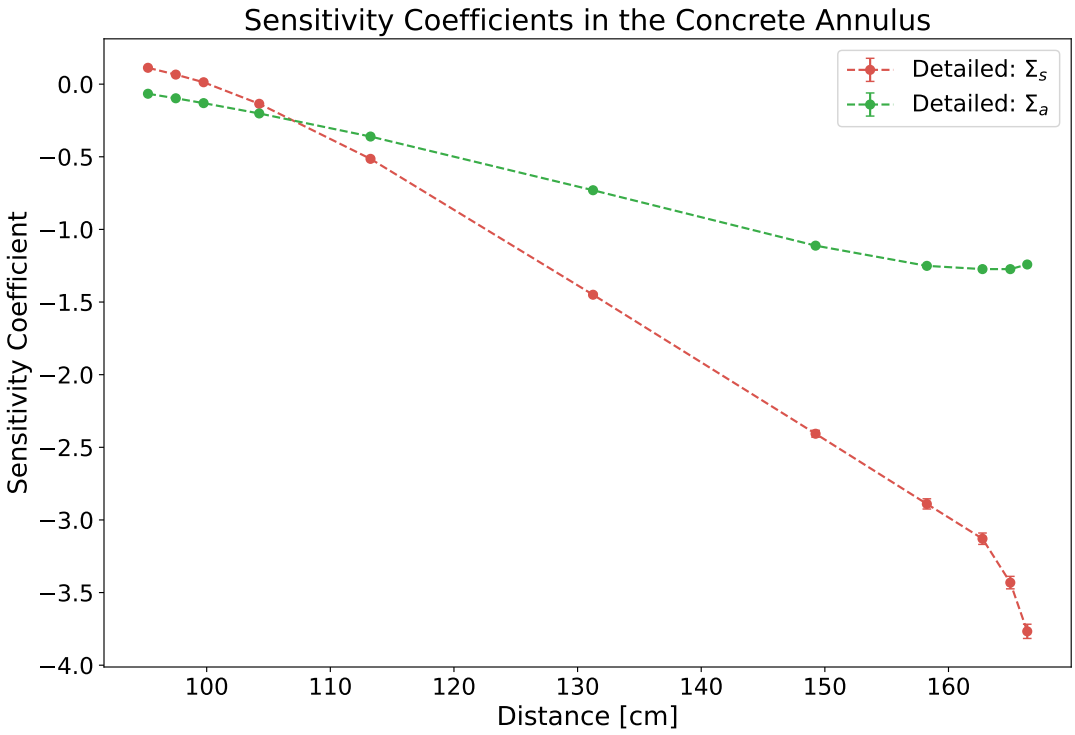

Figure 5-6. The largely negative SC's of Σ_s (red) and Σ_a (green) corroborate the concept that scattering and absorption act as loss mechanisms through the concrete.

The SC pertaining to Σ_a is once again negative since absorption causes neutron loss. There is an inflection point in the SC corresponding to Σ_a near 167.51 cm, the same location where the SC of Σ_s becomes negative. This is another instance where the two sets of SC's are inversely related.

Figure 5-9 again shows the absolute value of the SC's in order to stratify the importance of the parameters. Over the entire carbon steel shell region, the detailed model is more sensitive to the absorption cross section. This indicates that while the carbon steel is a high scattering material, absorption is still highly important.

There are some trends that are seen across all materials, with the exception of the SC's in air. First, the SC pertaining to the total scattering cross section has initially positive values before going negative, shown in Figs. 5-3, 5-6, and 5-8. Figures 2-9, 2-13, 2-17, and 2-20 show that the flux is outward peaked through the entire spent fuel cask

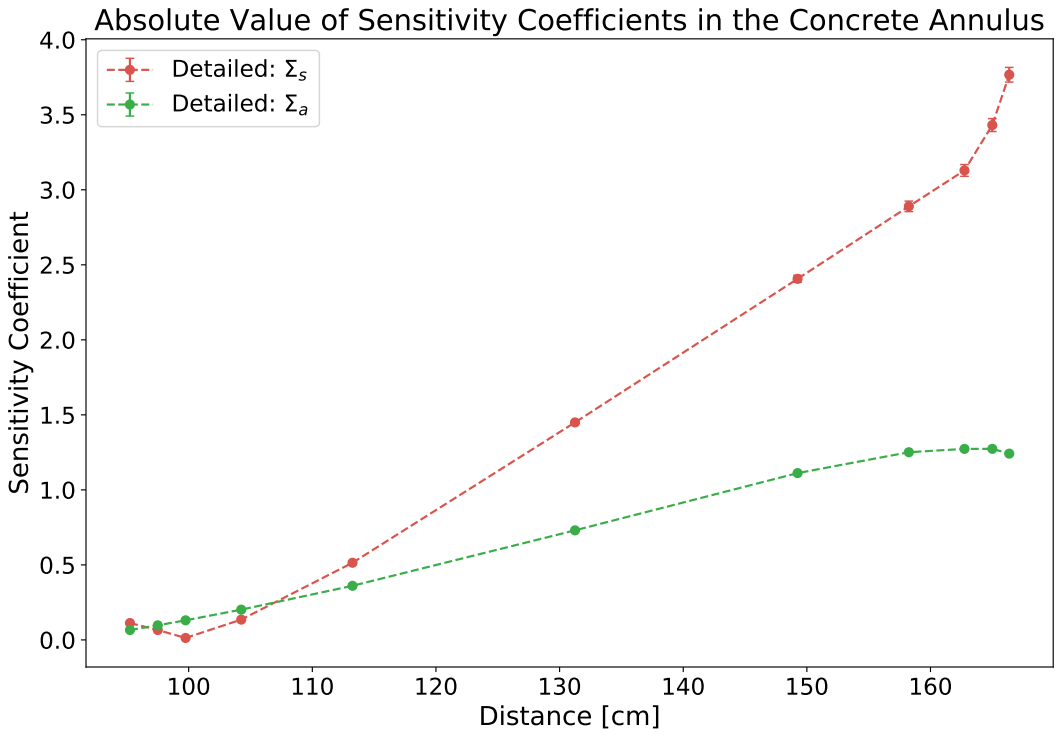

Figure 5-7. The absolute values of the SC's of Σ_a (green) and Σ_s (red) which confirms that the model is more sensitive to the scattering cross section than the absorption cross section for nearly the entirety of the concrete annulus.

and becomes more outwardly peaked further from the centerline. The result is that leakage is less likely at inner boundaries and more likely near outer boundaries, which generally indicates that scattering leads to a flux preservation effect at inner radii values and loss effects at outer radii values. Another trend seen across all the materials is the SC corresponding to the absorption cross section is always negative since absorption (in the absence of fission) is a loss mechanism.

5.3 Shortcomings of Computational Sensitivity Analysis

While computational tools, such as MCNP, provide for extensive sensitivity analysis capabilities, an analytic sensitivity analysis is capable of investigating sensitivities to parameters which are not readily available for investigation with MCNP. One such parameter has been previously identified in Sec. 5.2.1. In cases where the geometry

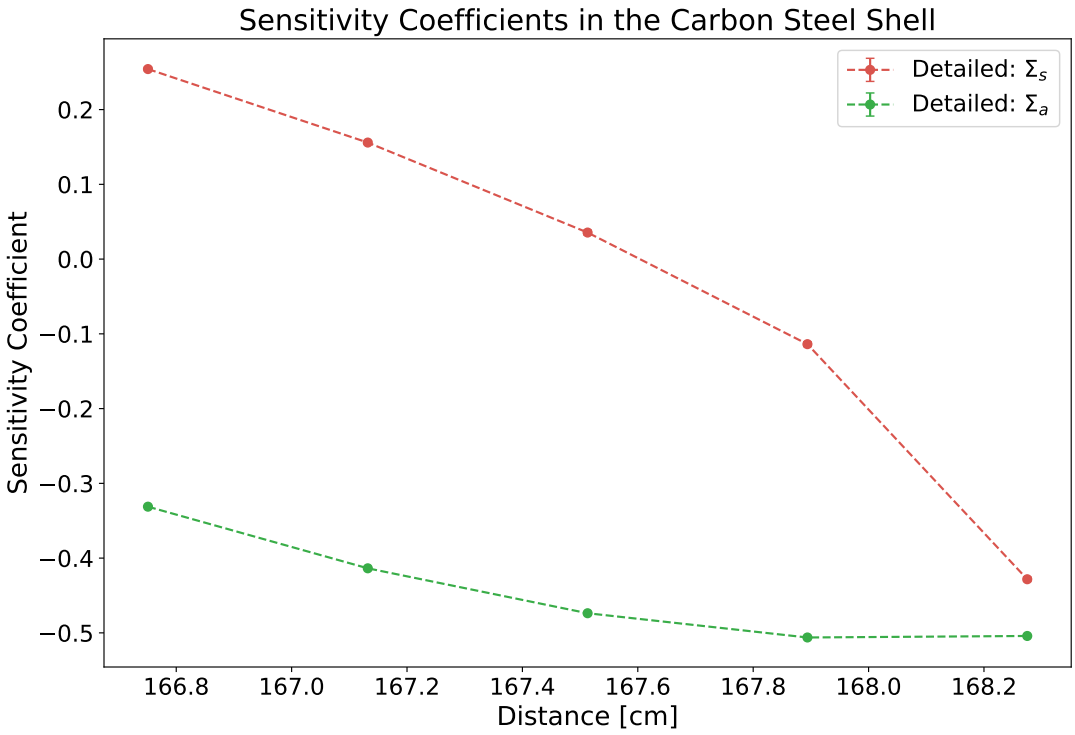

Figure 5-8. SC's with respect to Σ_s (red) and Σ_a (green) in the carbon steel shell. The values of the SC pertaining to Σ_s experience a sign change 167.513 cm which represents a change in the scattering physics. When the values are positive, scattering is acting to preserve the flux. However, when the values are negative, scattering is a loss term caused by neutrons leaking from the steel. Absorption is always negative since absorption results in neutron losses.

precludes modification, it may not be possible to perform a sensitivity analysis. Further, parameters such as source (S) and radius (r_b) from Eqn. 3-85 require running many simulations to manually determine sensitivity information, but are readily available through an analytic methodology, as will be seen in Chpt. 6. The goal of the following chapters is to further identify and understand the physics occurring in the cask and to rigorize the results of the previous sensitivity analysis of the detailed cask.

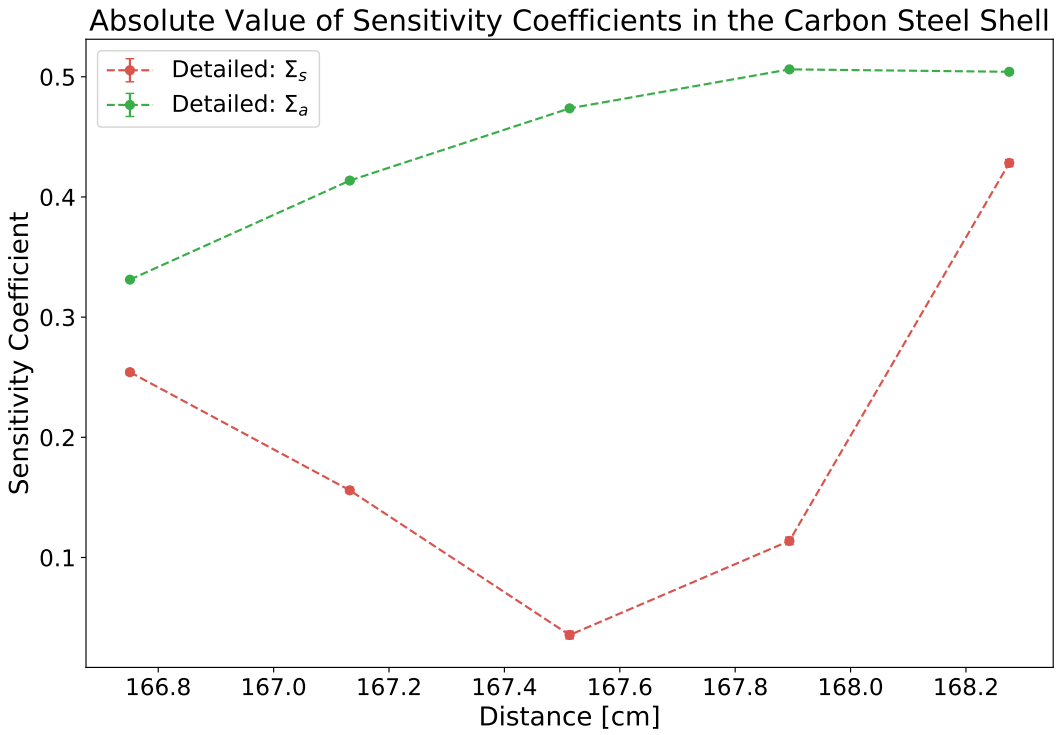

Figure 5-9. Observing the absolute values of the SC's corresponding to Σ_s in red and Σ_a in green show that the neutron flux is most sensitive to the absorption cross section. The slope of the SC pertaining to Σ_a decreases at the same location where the slope for the SC for Σ_S increase, at 167.51 cm, alluding to a relationship between absorption and leakage loss mechanics.

CHAPTER 6
SENSITIVITY THEORY OF REDUCED PHYSICS MODELS

6.1 Local Sensitivity Analysis Primer

Saltelli, Chan, and Scott define sensitivity analysis as the study of "relationships between information flowing in and out of a model [47]." That is, sensitivity analysis investigates how perturbations in input parameter values influence a system's response, where input parameters are data values passed by the user or calculated by a model and are used in the calculation of output variables. The most common input parameters appearing in nuclear engineering models are cross sections, which are derived from material properties supplied by a model or code user. In order to better understand the general process of sensitivity analysis, Oblow and Pin provide a short description of the procedure [48]. To begin, consider the set of linear equations

$$\boldsymbol{R} = \boldsymbol{F}(\boldsymbol{y}, \boldsymbol{\alpha}), \tag{6-1}$$

where

$\boldsymbol{R}$ is a vector of the system responses,

$\boldsymbol{F}$ is a vector of the model equations (e.g., vector containing the diffusion equation),

$\boldsymbol{y}$ is the state vector (e.g., vector of ϕ values),

$\boldsymbol{\alpha}$ is the vector of the system input parameters,

where the vector $\boldsymbol{F}$ can also represent nonlinear model equations, however, the following discussion is limited to linear equations for the purpose of this work.

Local sensitivity information describes first-order sensitivities, that is, the sensitivity information is related to the first derivative of $\boldsymbol{R}$, (e.g. , $\frac{\partial \boldsymbol{R}}{\partial \boldsymbol{\alpha}}$). Further, the first derivative describes the ratio of change in a system's response caused by changing the value of a input parameter [49]. Hence, taking the derivative of Eqn. 6-1 over each input parameter,

$\boldsymbol{\alpha_i}$, independently yields

$$\frac{\mathrm{d}R}{\mathrm{d}\alpha_i} = \frac{\partial \boldsymbol{F}}{\partial \boldsymbol{y}} \frac{\mathrm{d}\boldsymbol{y}}{\mathrm{d}\alpha_i}. \tag{6-2}$$

Since $\boldsymbol{F}$ contains the analytic models described by the user, the value $\frac{\partial \boldsymbol{F}}{\partial \boldsymbol{y}}$ can be calculated directly. Simplifying the final derivative in Eqn. 6-2 requires using the chain rule on Eqn. 6-1 to arrive at

$$\frac{\mathrm{d}\boldsymbol{y}}{\mathrm{d}\alpha_i} = \frac{\partial \boldsymbol{F}}{\partial \boldsymbol{y}} \frac{\mathrm{d}\boldsymbol{y}}{\mathrm{d}\alpha_i} + \frac{\partial \boldsymbol{F}}{\partial \boldsymbol{\alpha}} \frac{\mathrm{d}\boldsymbol{\alpha}}{\mathrm{d}\alpha_i}. \tag{6-3}$$

Re-expressing Eqn. 6-2, using Eqn. 6-3, yields the sought after sensitivity information $\frac{\mathrm{d}\boldsymbol{R}}{\mathrm{d}\boldsymbol{\alpha}}$. However, this approach can be algebraically involved since it requires solving the set of equations $\boldsymbol{F}$ for each input parameter variation.

In response to this problem, Cacuci developed a method for determining sensitivity information for all input parameters simultaneously, given the function $\boldsymbol{F}$ has a solution [13]. Cacuci utilizes the G-derivative, a form of the directional derivative, to find the differential value corresponding to each input parameter simultaneously. The G-derivative can be applied to find sensitivity information various ways, two separate methods will be described here: 1) applying the G-derivative directly to analytical expression of the neutron flux and 2) applying the G-derivative to the governing differential equations and boundary conditions.

In the former method, the unperturbed response value (the value of the response function where all input parameters are unperturbed) is defined as

$$\boldsymbol{R}(\boldsymbol{e}^{\,0}), \tag{6-4}$$

where $\boldsymbol{e}^{\,0} = (\boldsymbol{y}^{\,0}, \boldsymbol{\alpha}^{\,0})$ and the superscript 0 denotes the nominal, or unperturbed, value. If, moreover, the vector $\boldsymbol{h}_\alpha$ contains the perturbation values for M number of input parameters as

$$\boldsymbol{h}_\alpha \equiv (\delta\alpha_1, \delta\alpha_2, \ldots, \delta\alpha_M). \tag{6-5}$$

Sensitivity information of the response function caused by the variations $\boldsymbol{h}_\alpha$ is found by taking the G-derivative, $\delta\boldsymbol{R}(\boldsymbol{e}^0;\boldsymbol{h})$, of the response function, where $\boldsymbol{h}$ is the concatenation of the perturbed input parameter values and the perturbed state values;

$$\boldsymbol{h} \equiv (\boldsymbol{h}_y, \boldsymbol{h}_\alpha). \tag{6-6}$$

Taking the G-derivative of the response thus yields

$$\delta\boldsymbol{R}(\boldsymbol{e}^0;\boldsymbol{h}) \equiv \frac{\mathrm{d}}{\mathrm{d}\epsilon}\left[\boldsymbol{R}(\boldsymbol{e}^0+\epsilon\boldsymbol{h})\right]\Big|_{\epsilon=0} = \lim_{\epsilon\to 0}\frac{\boldsymbol{R}(\boldsymbol{e}^0+\epsilon\boldsymbol{h})-\boldsymbol{R}(\boldsymbol{e}^0)}{\epsilon}, \tag{6-7}$$

where ϵ is interpreted as an infinitesimal deviation from the nominal value of a given input parameter, and the rightmost expression is the definition of the G-derivative. In general, the evaluated result of Eqn. 6-7 can be written as

$$\delta R\left(\boldsymbol{e}^0;\boldsymbol{h}\right) = \sum_i^M \eta_i \delta\alpha_i, \tag{6-8}$$

where η_i contains sensitivity information for the input parameter α_i. The values of η_i are used to calculate the sought after SC's, which provide a relative comparison between input parameters. The SC's are thus calculated using $\delta\boldsymbol{R}$ as

$$S_{y,\alpha_i} = \frac{\delta R}{\delta\alpha_i}\frac{\alpha_i}{R(e^0)} = \eta_i\frac{\alpha_i}{R(e^0)}, \tag{6-9}$$

where S_{y,α_i} is the SC for input parameter α_i [50]. The SC's are comparable to the SC's determined from the computation results using Eqn. 5-9, as described in Sec. 5.1.

The second method of finding sensitivity information involves taking the G-derivative of the governing ordinary differential equation (ODE) and its boundary conditions. Applying the G-derivative to the governing equations and respective boundary conditions leads to what Cacuci named the Forward Sensitivity Equations (FSE) [13]. The boundary condition to Eqn. 6-1 is defined as

$$\left[\boldsymbol{B}\left(\boldsymbol{\alpha}^0\right)\boldsymbol{y}^0 - \boldsymbol{A}\left(\boldsymbol{\alpha}^0\right)\right]_{\partial\boldsymbol{\Omega}} = \boldsymbol{0}, \qquad \boldsymbol{x}\in\partial\boldsymbol{\Omega}, \tag{6-10}$$

where $\boldsymbol{A}$ is the inhomogeneous terms of the boundary conditions and $\boldsymbol{B}$ is an operator. Together $\boldsymbol{A}$ and $\boldsymbol{B}$ work to define the boundary condition within the boundary $\partial\boldsymbol{\Omega}$, and $\boldsymbol{x}$ is the position vector. Then, the sensitivity information, $\delta\boldsymbol{R}\left(\boldsymbol{e}^0;\boldsymbol{h}\right)$, is found by taking the G-derivatives of Eqns. 6-1 and 6-10 which yield

$$\boldsymbol{F}\left(\boldsymbol{\alpha}^0\right)\boldsymbol{h}_y + \left[\boldsymbol{F}'\left(\boldsymbol{\alpha}^0\right)\boldsymbol{y}^0\right]\boldsymbol{h}_\alpha - \delta\boldsymbol{Q}\left(\boldsymbol{\alpha}^0;\boldsymbol{h}_\alpha\right) = \boldsymbol{0} \tag{6-11}$$

and

$$\left\{\boldsymbol{B}\left(\boldsymbol{\alpha}^0\right)\boldsymbol{h}_y + \left[\boldsymbol{B}'_\alpha\left(\boldsymbol{\alpha}^0\right)\boldsymbol{y}^0\right]\boldsymbol{h}_\alpha - \delta\boldsymbol{A}\left(\boldsymbol{\alpha}^0;\boldsymbol{h}_\alpha\right)\right\}_{\partial\boldsymbol{\Omega}} = \boldsymbol{0}, \tag{6-12}$$

respectively, where $\boldsymbol{F}'\left(\boldsymbol{\alpha}^0\right)$ and $\boldsymbol{B}'_\alpha\left(\boldsymbol{\alpha}^0\right)$ are the partial G-derivatives of $\boldsymbol{F}$ and $\boldsymbol{B}$ at $\boldsymbol{\alpha}^0$ respectively, and $\delta\boldsymbol{Q}$ and $\delta\boldsymbol{A}$ are the inhomogeneous terms of the equation and boundary conditions respectively. Eqns. 6-11 and 6-12 together are called the FSE and solving these equations for $\boldsymbol{h}_y$ yields the sensitivity information. SC's are calculated using the results of $\boldsymbol{h}_y$.

As in Chpt. 5, the SC's are used to determine which input parameters cause the largest changes to the neutron flux. The magnitude of the SC's in each material are used to stratify the parameters based on importance. Further, the sign on the SC identifies how the response will change given a perturbation to an input parameter. That is, the neutron flux and input parameter change in the same direction when the SC value is positive. If the SC value is negative, then the neutron flux and the input parameters experience changes in opposite directions. Meaning, a positive perturbation to an input parameter leads to a negative change in the neutron flux.

The remainder of this chapter calculates the SC's for input parameters relating to nuclear data in the solution to Eqn. 4-5, the solution to the 1-D cylindrical diffusion equation, in the fuel region and Eqn. 3-56, the multigroup discrete ordinates equations, in the remainder of the spent fuel cask.

6.2 Local Sensitivity Analysis of Representative Spent Fuel Cask Model

6.2.1 Fuel Region

Section 3 introduced the diffusion approximation which uses experimental data in the form of cross sections to predict the neutron flux through the fuel region of the cask. Taking the solution to Eqn. 3-82 with the boundary conditions given in Eqns. 4-1 and 4-2 is

$$\phi^0(r) = \frac{S^0}{D^0(B^0)^2}\left(1 - \frac{I_0(B^0 r)}{I_0(B^0 \tilde{r}^{\,0})}\right); \qquad B^0 \equiv \sqrt{\frac{\Sigma_a^0 - \bar{\nu}^0 \Sigma_f^0}{D^0}}. \tag{3-85}$$

where S^0 is the intrinsic neutron source, I_0 is the modified Bessel function of the first kind, and $\tilde{r}^{\,0}$ is the extrapolated radius of the fuel region equivalent to $r_b^0 + d^0$. The superscript 0 denotes the nominal value of each input parameter or response function.

Identifying the unperturbed input parameters from Eqn. 3-85 as

$$\boldsymbol{\alpha}^{\,0} \equiv \left(S^0, D^0, B^0, \tilde{r}^0\right), \tag{6-13}$$

and the perturbation vector, $\boldsymbol{h}_\alpha$ as

$$\boldsymbol{h}_\alpha \equiv (\delta S, \delta D, \delta B, \delta \tilde{r}), \tag{6-14}$$

the vector $\boldsymbol{h}_y$ becomes

$$\boldsymbol{h}_y \equiv (\delta \phi). \tag{6-15}$$

Then, the vector of nominal input parameters and response functions is defined as

$$\boldsymbol{e}^{\,0} \equiv \left(\phi^0(r), \boldsymbol{\alpha}_0\right), \tag{6-16}$$

where the response function is

$$R(\boldsymbol{e}^{\,0}) = \phi^0(r). \tag{6-17}$$

Finally, determining the sensitivities for each input parameter using Eqns. 6-13-6-17 in Eqn. 6-7 is equivalent to replacing each input parameter in Eqn. 3-85 with

$$\alpha_i^0 \rightarrow \left(\alpha_i^0 + \epsilon \delta \alpha_i\right). \tag{6-18}$$

Using Eqn. 6-18 to expand the input parameters in Eqn. 3-85 gives

$$\delta R\left(\boldsymbol{e}^{\,0};\boldsymbol{h}\right)=\frac{\mathrm{d}}{\mathrm{d}\epsilon}\left[\frac{\left(S^{0}+\epsilon\delta S\right)}{\left(D^{0}+\epsilon\delta D\right)\left(\left(B^{0}+\epsilon\delta B\right)\right)^{2}}\left(1-\frac{I_{0}(\left(B^{0}+\epsilon\delta B\right)r)}{I_{0}(\left(B^{0}+\epsilon\delta B\right)\left(\tilde{r}^{\,0}+\epsilon\delta\tilde{r}\right))}\right)\right]\Bigg|_{\epsilon=0}. \tag{6-19}$$

Evaluating Eqn. 6-19 yields

$$\delta R\left(\boldsymbol{e}^{\,0};\boldsymbol{h}\right)=\eta_{fuel,1}\left(r\right)\delta S+\eta_{fuel,2}\left(r\right)\delta D+\eta_{fuel,3}\left(r\right)\delta B+\eta_{fuel,4}\left(r\right)\delta\tilde{r}, \tag{6-20}$$

where the r-dependent functions appearing in Eqn. 6-20 are defined by

$$\eta_{fuel,1}\equiv\frac{1-\frac{I_{0}\left(B^{0}r\right)}{I_{0}\left(B^{0}\tilde{r}^{0}\right)}}{\left(B^{0}\right)^{2}D^{0}}, \tag{6-21}$$

$$\eta_{fuel,2}\equiv\frac{-S^{0}}{\left(B^{0}\right)^{2}\left(D^{0}\right)^{2}}\left(1-\frac{I_{0}\left(B^{0}r\right)}{I_{0}\left(B^{0}\tilde{r}^{0}\right)}\right), \tag{6-22}$$

$$\eta_{fuel,3}\equiv\frac{-2S^{0}\left(1-\frac{I_{0}\left(B^{0}r\right)}{I_{0}\left(B^{0}\tilde{r}^{0}\right)}\right)}{\left(B^{0}\right)^{3}D^{0}}-\frac{S^{0}rI_{1}\left(B^{0}r\right)}{\left(B^{0}\right)^{2}D^{0}I_{0}\left(B^{0}\tilde{r}^{0}\right)}+\frac{S^{0}\tilde{r}^{0}I_{0}\left(B^{0}r\right)I_{1}\left(B^{0}\tilde{r}^{0}\right)}{\left(B^{0}\right)^{2}D^{0}\left(I_{0}\left(B^{0}\tilde{r}^{0}\right)\right)^{2}}, \tag{6-23}$$

$$\eta_{fuel,4}\equiv\frac{S^{0}I_{0}\left(B^{0}r\right)I_{1}\left(B^{0}\tilde{r}^{0}\right)}{B^{0}D^{0}\left(I_{0}\left(B^{0}\tilde{r}^{0}\right)\right)^{2}},[3pt] \tag{6-24}$$

and the associated SC's are summarized as

$$S_{\phi_{fuel},S}=\eta_{fuel,1}\frac{S^{0}}{\phi(r)}, \tag{6-25}$$

$$S_{\phi_{fuel},D}=\eta_{fuel,2}\frac{D^{0}}{\phi(r)}, \tag{6-26}$$

$$S_{\phi_{fuel},B}=\eta_{fuel,3}\frac{B^{0}}{\phi(r)}, \tag{6-27}$$

$$S_{\phi_{fuel},\tilde{r}}=\eta_{fuel,4}\frac{\tilde{r}^{0}}{\phi(r)}. \tag{6-28}$$

Equation 3-85 indicates that some of the input parameters appearing within the equation may be defined in terms of other, more fundamental input parameters, such as how Σ_{a}^{0} appears in the definition of B^{0} as well as in D^{0}. In practice, the values for D^{0}, B^{0}, and $\tilde{r}^{0}$ are calculated from experimental data or geometry (in the case of $\tilde{r}^{0}$). Therefore, it is necessary to express each of the above input parameters according to their individual

definitions using Eqns. 6-29 - 6-31:

$$D^0 \equiv \frac{1}{3(\Sigma_s^0 + \Sigma_c^0 + \Sigma_f^0)}, \tag{6-29}$$

$$B^0 \equiv \sqrt{\frac{\Sigma_a^0 - \bar{\nu}^0 \Sigma_f^0}{D^0}} = \sqrt{\frac{\Sigma_c^0 + \Sigma_f^0(1-\bar{\nu}^0)}{\frac{1}{3(\Sigma_s^0+\Sigma_c^0+\Sigma_f^0)}}}, \tag{6-30}$$

$$\tilde{r}^{\,0} \equiv r_b^0 + \frac{0.710}{(\Sigma_s^0 + \Sigma_c^0 + \Sigma_f^0)}, \tag{6-31}$$

where Σ_c^0 is the nominal capture cross section and r_b^0 is the nominal cask fuel region outer radius, and the nominal total absorption cross section is redefined using $\Sigma_a^0 \equiv \Sigma_c^0 + \Sigma_f^0$. Fundamental SC results written in terms of the parameters Σ_s, Σ_c, Σ_f, and r_b are then determined by applying the G-derivative to each of Eqns. 6-29-6-31 and substituting the results into their respective places in Eqn. 6-21 - 6-24.

Redefining the SC's for B, D, and $\tilde{r}$ in terms of those for Σ_c, Σ_s, $\bar{\nu}$, Σ_f, and r_b is a straightforward process similar to how the coefficients were found for B, D, and $\tilde{r}$ above. Taking the G-derivative of each of Eqns. 6-29-6-31, each equation is expressible in the terms $\delta\Sigma_c$, $\delta\Sigma_s$, $\delta\bar{\nu}$, $\delta\Sigma_f$, and δr_b. These definitions are then used in the SC's summarized in Eqn. 6-25 - 6-28 to yield the final expressions.

Applying Eqn. 6-7 to Eqns. 6-29-6-31 using the following definitions for $\boldsymbol{e}^{\,0}$ and $\boldsymbol{h}$,

$$\boldsymbol{e}^{\,0} \equiv \left(\phi^0, \Sigma_c^0, \Sigma_s^0, \bar{\nu}^0, \Sigma_f^0, r_b^0\right) \tag{6-32}$$

$$\boldsymbol{h} \equiv (\delta\phi, \delta\Sigma_c, \delta\Sigma_s, \delta\bar{\nu}, \delta\Sigma_f, \delta r_b) \tag{6-33}$$

yields

$$\delta D(\boldsymbol{e}^{\,0}; \boldsymbol{h}\}) = \frac{\mathrm{d}}{\mathrm{d}\epsilon}\left[\frac{1}{3\left((\Sigma_s^0 + \epsilon\delta\Sigma_s) + (\Sigma_c^0 + \epsilon\delta\Sigma_c) + \left(\Sigma_f^0 + \epsilon\delta\Sigma_f\right)\right)}\right]\Bigg|_{\epsilon=0}, \tag{6-34}$$

$$\delta B(\boldsymbol{e}^{\,0}; \boldsymbol{h}\}) = \frac{\mathrm{d}}{\mathrm{d}\epsilon}\left[\sqrt{\frac{(\Sigma_c^0 + \epsilon\delta\Sigma_c) + \left(\Sigma_f^0 + \epsilon\delta\Sigma_f\right)(1 - (\bar{\nu}^0 + \epsilon\delta\bar{\nu}))}{\frac{1}{3\left((\Sigma_s^0+\epsilon\delta\Sigma_s)+(\Sigma_c^0+\epsilon\delta\Sigma_c)+\left(\Sigma_f^0+\epsilon\delta\Sigma_f\right)\right)}}}\right]\Bigg|_{\epsilon=0}, \tag{6-35}$$

$$\delta\tilde{r}(\boldsymbol{e}^{\,0}; \boldsymbol{h}\}) = \frac{\mathrm{d}}{\mathrm{d}\epsilon}\left[\left(r_b^0 + \epsilon\delta r_b\right) + \frac{0.7104}{(\Sigma_s^0 + \epsilon\delta\Sigma_s) + (\Sigma_c^0 + \epsilon\delta\Sigma_c) + \left(\Sigma_f^0 + \epsilon\delta\Sigma_f\right)}\right]\Bigg|_{\epsilon=0}. \tag{6-36}$$

Evaluating Eqns. 6-34-6-36 determines the variations δB, δD, and $\delta\tilde{r}$ as

$$\delta B = \frac{\delta\Sigma_s\sqrt{3}(-\bar{\nu}^0\Sigma_f^0+\Sigma_c^0+\Sigma_f^0)}{2\sqrt{(-\bar{\nu}^0\Sigma_f^0+\Sigma_c^0+\Sigma_f^0)(\Sigma_c^0+\Sigma_f^0+\Sigma_s^0)}}- \frac{\delta\bar{\nu}\sqrt{3}\Sigma_f^0(\Sigma_c^0+\Sigma_f^0+\Sigma_s^0)}{2\sqrt{(-\bar{\nu}^0\Sigma_f^0+\Sigma_c^0+\Sigma_f^0)(\Sigma_c^0+\Sigma_f^0+\Sigma_s^0)}}+\frac{\delta\Sigma_c\sqrt{3}(-\bar{\nu}^0\Sigma_f^0+2\Sigma_c^0+2\Sigma_f^0+\Sigma_s^0)}{2\sqrt{(-\bar{\nu}^0\Sigma_f^0+\Sigma_c^0+\Sigma_f^0)(\Sigma_c^0+\Sigma_f^0+\Sigma_s^0)}}+ \frac{\delta\Sigma_f\sqrt{3}(-\bar{\nu}^0(\Sigma_c^0+\Sigma_f^0+\Sigma_s^0)-\bar{\nu}^0\Sigma_f^0+2\Sigma_c^0+2\Sigma_f^0+\Sigma_s^0)}{2\sqrt{(-\bar{\nu}^0\Sigma_f^0+\Sigma_c^0+\Sigma_f^0)(\Sigma_c^0+\Sigma_f^0+\Sigma_s^0)}}, \tag{6-37}$$

$$\delta D = \frac{\delta\Sigma_c+\delta\Sigma_s+\delta\Sigma_f}{3\left(\Sigma_c^0+\Sigma_s^0+\Sigma_f^0\right)^2} \tag{6-38}$$

$$\delta\tilde{r} = \frac{0.7104\delta r_b}{\Sigma_c^0+\Sigma_f^0+\Sigma_s^0}-\frac{0.7104 r_b^0(\delta\Sigma_c+\delta\Sigma_f+\delta\Sigma_s)}{(\Sigma_c^0+\Sigma_f^0+\Sigma_s^0)^2}. \tag{6-39}$$

These values are then substituted into Eqn. 6-20 in order to determine the SC's. Chapter 7 provides the SC's with discussion. The theory for determining the SC's in MPC is provided next.

6.2.2 MPC

Chapter 2 identified the same mathematical model, the multigroup discrete ordinates equations (Eqns. 3-61-3-64), for use in the MPC and the overpack (concrete and carbon steel shell). Rather than calculating the SC's directly from the solutions to Eqns. 3-61-3-64, the coefficients can be found through solving the FSE (Eqns. 6-11 and 6-12) for the general form of the multigroup discrete ordinates equations, Eqn. 3-56, which have been reproduced below for convenience.

$$\mu_i\frac{\mathrm{d}\phi_i^g}{\mathrm{d}x}+\Sigma_t^g\phi_i^g=\frac{1}{2}\sum_{j=1}^{N}\omega_j\sum_{g'=1}^{G}\Sigma_{s,g'\to g}\phi_j^{g'}+S_i^g, \qquad g=1,2,...,G; i=1,2,...,N. \tag{3-56}$$

The vector $\boldsymbol{\alpha}^0$ is

$$\boldsymbol{\alpha}^0 \equiv \left(\mu_i, \Sigma_t^g, \Sigma_{s,g'\to g}, \boldsymbol{A}\right), \tag{6-40}$$

where $\boldsymbol{A}$ is included to show the sensitivity information pertaining to the boundary condition values.

Using the FSE requires identifying the operator $\boldsymbol{F}\left(\boldsymbol{\alpha}^0\right)$ as

$$\boldsymbol{F}\left(\boldsymbol{\alpha}^0\right) = \mu_i \frac{\mathrm{d}}{\mathrm{d}x} - \left(\frac{1}{2}\sum_{j=1}^{N}\omega_j \sum_{g'=1}^{G}\Sigma_{s,g'\to g} - \Sigma_t^g\right), \tag{6-41}$$

and the quantity $\left[\boldsymbol{F}'\left(\boldsymbol{\alpha}^0\right)\boldsymbol{y}^0\right]\boldsymbol{h}_\alpha$ as

$$\left[\boldsymbol{F}'\left(\boldsymbol{\alpha}^0\right)\boldsymbol{y}^0\right]\boldsymbol{h}_\alpha = \delta\mu_i \frac{\mathrm{d}\phi_i^g}{\mathrm{d}x} - \left(\frac{1}{2}\sum_{j=1}^{N}\omega_j \sum_{g'=1}^{G}\delta\Sigma_{s,g'\to g}\right)\phi_i^g + \delta\Sigma_t^g\phi_i^g. \tag{6-42}$$

For Eqn. 3-56, $\boldsymbol{h}_\alpha$ is defined as $\boldsymbol{h}_\alpha \equiv (\delta\mu, \delta\Sigma_t^g, \delta\Sigma_{s,g'\to g}, \boldsymbol{A})$, where $\boldsymbol{A}$ represents the inhomogeneous boundary conditions for each material. The vector $\boldsymbol{h}_y$ is then defined as $\boldsymbol{h}_y \equiv (\delta\phi_i^g)$ where $g = 1, 2, \ldots, G$ and $i = 1, 2, \ldots, N$ for both $\boldsymbol{h}_\alpha$ and $\boldsymbol{h}_y$. Equation 6-11 when no internal sources are present becomes

$$\mu_i \frac{\mathrm{d}}{\mathrm{d}x} - \left(\frac{1}{2}\sum_{j=1}^{N}\omega_j \sum_{g'=1}^{G}\Sigma_{s,g'\to g} - \Sigma_t^g\right) + \delta\mu_i \frac{\mathrm{d}\phi_i^g}{\mathrm{d}x} - \left(\frac{1}{2}\sum_{j=1}^{N}\omega_j \sum_{g'=1}^{G}\delta\Sigma_{s,g'\to g}\right)\phi_i^g + \delta\Sigma_t^g\phi_i^g = 0, \tag{6-43}$$

when setting higher order terms to zero. Equation 6-43 is a general expression that can be used in any scenario where sensitivity information of the multigroup discrete ordinates equations is required, including in the other materials of the overpack. Similarly to solving other systems of ODE's, unique solutions are found when solving an ODE with the appropriate boundary conditions. This same principle applies to solving Eqn. 6-43, where Eqn. 6-12 is used to make the required boundary conditions. Each material will have its own set of boundary conditions leading to unique sensitivity information.

The boundary conditions in the MPC are provided in Eqns. 4-10-4-13. Using these boundary conditions in Eqn. 6-12 will give the boundary conditions required to solve Eqn. 6-43. For ease, the boundary conditions represented by Eqns. 4-10-4-11 are written in

matrix form as

$$\begin{pmatrix} \phi^1_{mpc,1}\left(r = 84.34\ cm\right) \\ \phi^1_{mpc,2}\left(r = 86.84\ cm\right) \\ \phi^2_{mpc,1}\left(r = 84.34\ cm\right) \\ \phi^2_{mpc,2}\left(r = 86.84\ cm\right) \end{pmatrix} = \begin{pmatrix} (0.5729 * 0.81493)\phi_{fuel}\left(r = 84.34\ cm\right) \\ (0.5729 * 0.18507)\phi_{fuel}\left(r = 84.34\ cm\right) \\ \phi^1_{concrete,2}\left(r = 95.25\ cm\right) \\ \phi^2_{concrete,2}\left(r = 95.25\ cm\right) \end{pmatrix}. \tag{6-44}$$

The first term in Eqn. 6-12, $\boldsymbol{B}\left(\boldsymbol{\alpha}^0\right) h_y$, is simply

$$\begin{pmatrix} \delta\phi^1_{mpc_0,1}\left(r = 84.34\ cm\right) \\ \delta\phi^1_{mpc_0,2}\left(r = 86.84\ cm\right) \\ \delta\phi^2_{mpc_0,1}\left(r = 84.34\ cm\right) \\ \delta\phi^2_{mpc_0,2}\left(r = 86.84\ cm\right) \end{pmatrix}, \tag{6-45}$$

as there are no operators in the boundary conditions. The second term in Eqn. 6-12, $\left[\boldsymbol{B}'_\alpha\left(\boldsymbol{\alpha}^0\right)\boldsymbol{y}^0\right]\boldsymbol{h}_\alpha$, is identically zero, since the boundary conditions contain no input parameters so the G-derivative evaluates to zero. The final term in Eqn. 6-12, $\delta\boldsymbol{A}\left(\boldsymbol{\alpha}^0;\boldsymbol{h}_\alpha\right)$, accounts for inhomogeneities in the boundary conditions and is equivalent to

$$\begin{pmatrix} (0.5729 * 0.81493)\delta\phi_{fuel}\left(r = 84.34\ cm\right) \\ (0.5729 * 0.18507)\delta\phi_{fuel}\left(r = 84.34\ cm\right) \\ \delta\phi^1_{concrete,2}\left(r = 95.25\ cm\right) \\ \delta\phi^2_{concrete,2}\left(r = 95.25\ cm\right) \end{pmatrix}. \tag{6-46}$$

Therefore, the final expression for the boundary conditions in the MPC is

$$\begin{pmatrix} \delta\phi^1_{mpc,1}\left(r = 84.34\ cm\right) \\ \delta\phi^1_{mpc,2}\left(r = 86.84\ cm\right) \\ \delta\phi^2_{mpc,1}\left(r = 84.34\ cm\right) \\ \delta\phi^2_{mpc,2}\left(r = 86.84\ cm\right) \end{pmatrix} = \begin{pmatrix} (0.5729 * 0.81493)\delta\phi_{fuel}\left(r = 84.34\ cm\right) \\ (0.5729 * 0.18507)\delta\phi_{fuel}\left(r = 84.34\ cm\right) \\ \delta\phi^1_{concrete,2}\left(r = 95.25\ cm\right) \\ \delta\phi^2_{concrete,2}\left(r = 95.25\ cm\right) \end{pmatrix}. \tag{6-47}$$

Solving Eqn. 6-43 with the boundary conditions in Eqn. 6-47 for

$$\boldsymbol{\delta\phi_{mpc}} \equiv \begin{pmatrix} \delta\phi^1_{mpc,1} \\ \delta\phi^1_{mpc,2} \\ \delta\phi^2_{mpc,1} \\ \delta\phi^2_{mpc,2} \end{pmatrix} \tag{6-48}$$

will yield the sought after sensitivity information need to determine the SC's. While the equations are linear and inhomogeneous, and thus in principle possess an analytical solution, this solution is notationally cumbersome, enough so that its explicit reproduction is of little value. For this reason, the results of the numerical analysis in the MPC and overpack are provided graphically and discussed in Chpt. 7.

6.2.3 Concrete

The multigroup discrete ordinates equations, Eqn. 3-56, are chosen as the analytic model representing the neutron distribution in the concrete annulus. Since this model is the same as in the MPC, Eqn. 6-43 will yield the appropriate sensitivity information in the concrete. However, a new set of boundary conditions needs to be determined.

Equations 4-6-4-9 are used to find the terms in Eqn. 6-12. The first term in Eqn. 6-12 becomes

$$\boldsymbol{B}\left(\boldsymbol{\alpha}^0\right)\boldsymbol{h}_y \equiv \begin{pmatrix} \delta\phi^1_{conc,1}(r = 95.25\ cm) \\ \delta\phi^1_{conc,2}(r = 166.37\ cm) \\ \delta\phi^2_{conc,1}(r = 95.25\ cm) \\ \delta\phi^2_{conc,2}(r = 166.37\ cm) \end{pmatrix}, \tag{6-49}$$

where $\delta\phi^g_{conc,i}$ is the perturbed value of the i direction g energy group neutron flux in concrete. Similar to the analysis in the MPC, the second term in Eqn. 6-12, $\left[\boldsymbol{B}'_\alpha\left(\boldsymbol{\alpha}^0\right)\boldsymbol{y}^0\right]\boldsymbol{h}_\alpha$, evaluates to zero as there are no input parameters appearing in the boundary condition equations, Eqn. 4-6-4-9. The final term in Eqn. 6-12, $\delta\boldsymbol{A}\left(\boldsymbol{\alpha}^0;\boldsymbol{h}_\alpha\right)$, is equivalent to the

inhomogeneous quantities in the boundary conditions as shown in Eqns. 6-50.

$$\delta \boldsymbol{A}\left(\boldsymbol{\alpha}^0; \boldsymbol{h}_\alpha\right) \equiv \begin{pmatrix} \delta\phi^1_{mpc,1}(r = 86.84\ cm) \\ \delta\phi^1_{cs,2}(r = 166.37\ cm) \\ \delta\phi^2_{mpc,1}(r = 86.84\ cm) \\ \delta\phi^2_{cs,2}(r = 166.37\ cm) \end{pmatrix}, \tag{6-50}$$

where $\delta\phi^g_{mpc,i}$ is the perturbed neutron flux of the i direction g energy group neutron flux in the MPC and $\delta\phi^g_{cs,i}$ is the perturbed flux of the i direction g energy group neutron flux in the carbon steel shell. Finally, the boundary conditions for use with Eqn. 6-43 in the concrete annulus are

$$\begin{pmatrix} \delta\phi^1_{conc,1}(r = 95.25\ cm) \\ \delta\phi^1_{conc,2}(r = 166.37\ cm) \\ \delta\phi^2_{conc,1}(r = 95.25\ cm) \\ \delta\phi^2_{conc,2}(r = 166.37\ cm) \end{pmatrix} = \begin{pmatrix} \delta\phi^1_{mpc,1}(r = 86.84\ cm) \\ \delta\phi^1_{cs,2}(r = 166.37\ cm) \\ \delta\phi^2_{mpc,1}(r = 86.84\ cm) \\ \delta\phi^2_{cs,2}(r = 166.37\ cm) \end{pmatrix}. \tag{6-51}$$

The final solution to Eqn. 6-43 with the boundary conditions given by Eqn. 6-51 is provided graphically in Chpt. 7. Determining the system of equations in the carbon steel is the final remaining analysis.

6.2.4 Carbon Steel Shell

The carbon steel shell is the final material requiring analysis. Once again, Eqn. 6-43 is the foundational system of differential equations describing the sensitivity information in the carbon steel shell, since the multigroup discrete ordinates equations, Eqn. 3-56, are chosen as the representative analytic model. Solving Eqn. 6-43 requires calulating appropriate boundary conditions.

Using the boundary conditions in the carbon steel, Eqns. 4-14-4-17, the non-zero terms of Eqn. 6-12 can be found as

$$\boldsymbol{B}\left(\boldsymbol{\alpha}^0\right)\boldsymbol{h}_y \equiv \begin{pmatrix} \delta\phi^1_{cs,1}(r=166.37\ cm) \\ \delta\phi^1_{cs,2}(r=168.275\ cm) \\ \delta\phi^2_{cs,1}(r=166.37\ cm) \\ \delta\phi^2_{cs,2}(r=168.275\ cm) \end{pmatrix}, \tag{6-52}$$

and

$$\delta\boldsymbol{A}\left(\boldsymbol{\alpha}^0;\boldsymbol{h}_\alpha\right) \equiv \begin{pmatrix} \delta\phi^1_{conc,1}(r=166.37\ cm) \\ 0 \\ \delta\phi^2_{conc,1}(r=166.37\ cm) \\ 0 \end{pmatrix}. \tag{6-53}$$

There are two zeros appearing in Eqn. 6-53 since the boundary condition is assumed to be exactly zero with no error for these boundary conditions. Further, the second term in Eqn. 6-12, $\left[\boldsymbol{B}'_\alpha\left(\boldsymbol{\alpha}^0\right)\boldsymbol{y}^0\right]\boldsymbol{h}_\alpha$, evaluates to zero since there are no input parameters appearing in the boundary condition equations, Eqns. 4-14-4-17. The final expression for the boundary conditions corresponding to Eqn. 6-43 are expressed as

$$\begin{pmatrix} \delta\phi^1_{cs,1}(r=166.37\ cm) \\ \delta\phi^1_{cs,2}(r=168.275\ cm) \\ \delta\phi^2_{cs,1}(r=166.37\ cm) \\ \delta\phi^2_{cs,2}(r=168.275\ cm) \end{pmatrix} = \begin{pmatrix} \delta\phi^1_{conc,1}(r=166.37\ cm) \\ 0 \\ \delta\phi^2_{conc,1}(r=166.37\ cm) \\ 0 \end{pmatrix}. \tag{6-54}$$

The solution to the system of ODE's given by Eqn. 6-43 with the boundary conditions Eqn. 6-54 is provided, graphically, in Chapter 7. Chapter 7 also compares the sensitivity analysis results of the helium model, the detailed model, and the analytic models to identify salient physics and rigorize simulation analysis.

CHAPTER 7
DISCUSSION OF SENSITIVITY ANALYSIS

The purpose of this chapter is to show the numerical results from the sensitivity analysis of the analytic models conducted in Chpt. 6. From the sensitivity analysis results, discussion of the physical phenomena causing the features in the SC curves in each material region is provided. Finally, the results of the analytic sensitivity analysis are compared to the corresponding results from the MCNP sensitivity analysis.

7.1 Results of Analytic Sensitivity Study

7.1.1 Sensitivity Analysis of the Fuel Region

The representative homogeneous fuel composition employed in the helium model may be used to determine an associated set of nominal input parameters S^0, Σ_c^0, Σ_s^0, $\bar{\nu}^0$, and Σ_f^0 for use with the analytical results appearing in Sec. 6.2.1, featuring an associated quantification of their relevance to the detailed model. The nominal values of the input parameters is summarized in Tab. 4-2

Figure 7-1 depicts the sensitivity coefficients $S_{\phi,i}$ associated with the elemental parameters $i = S$, Σ_c, Σ_s, $\bar{\nu}$, Σ_f, and r_b appearing within the analytical model given by Eqn. 4-5, as calculated using Eqs. 6-21-6-24, 6-25-6-28, and 6-37-6-39 and the data appearing in Table 4-2. Several trends are immediately evident from Fig. 7-1:

- The sensitivity coefficient associated with the intrinsic neutron source term S is identically one since the source term itself appears simply as a scalar multiplier within Eqn. 4-5.
- The sensitivity coefficient associated with the capture cross section Σ_c is negative throughout the entire homogenous fuel region. This phenomenon indicates that as the capture cross section increases, the neutron flux decreases. This behavior is physically plausible since capture is a pure loss mechanism (i.e., as more neutrons are lost to capture, the value of the neutron flux becomes smaller). S_{ϕ,Σ_c} has an inflection point and increases in value near $r = 73$ cm from the centerline, since loss terms are forcing the flux to meet to the boundary value in Eqn. 4-2.
- The sensitivity coefficient of r_b exhibits the most dramatic change across the radius of the cask. In fact, the value increases to 5.051 at $r = 74.68$ cm. Perturbing r_b is effectually perturbing the location of the boundary value, Eqn. 4-2. For this reason,

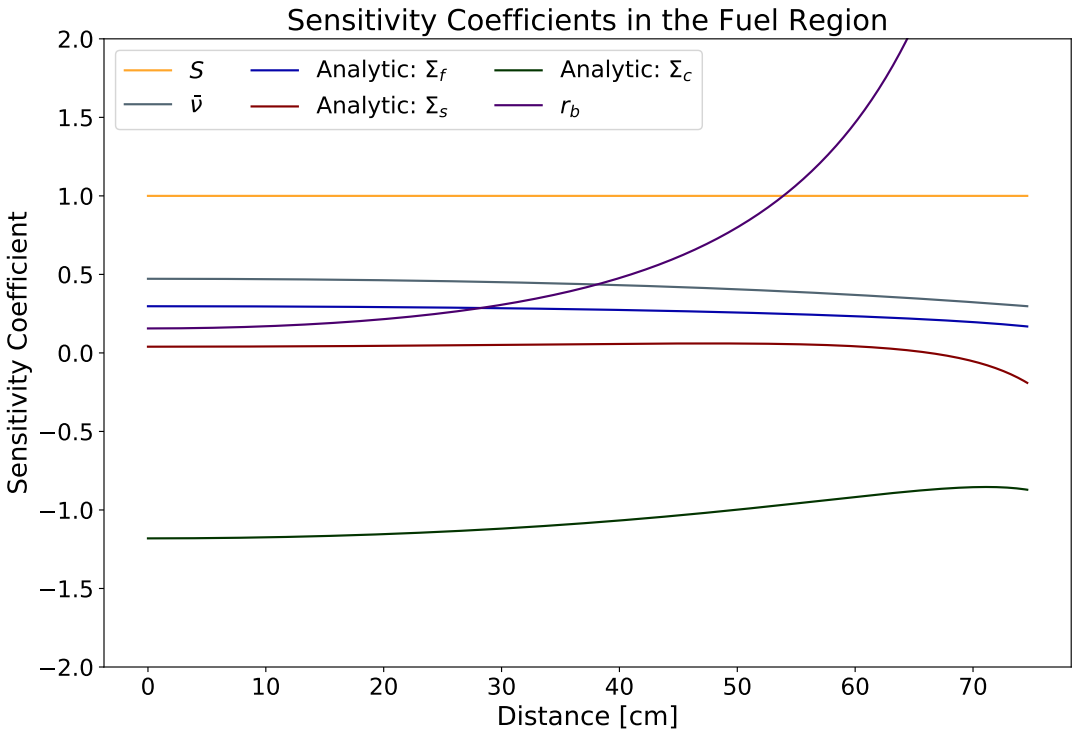

Figure 7-1. Analytical sensitivity coefficients as a function of the cylindrical radius in the homogenized fuel region.

S_{c,r_b} increases drastically from $r = 40$ cm to $r = 74.78$ cm since boundary values are imperative in constructing unique solutions. This also explains why the value is less than 0.04 for the first 40 cm, as the flux at these values is less affected by the boundary value at $r = 74.68$ cm and more affected by the boundary value at the centerline, Eqn. 4-1. Finally, the values are positive since increasing the radius value would force the flux to remain at higher values through the radius of the fuel. The boundary condition at $r = 74.68$ cm effectively sets the value of the flux at this location. Therefore, by furthering the location of this boundary condition (and increasing the thickness of the fuel region), the neutron flux in the fuel region must remain at higher values throughout the homogenized fuel region in order to satisfy the boundary condition. The opposite is true if the fuel radius thickness is lessened, as the neutron flux would have to be attenuated more quickly in order to meet the boundary condition at the perturbed location.

- Figure 7-1 shows that positive perturbations in $\bar{\nu}$ cause uniformly positive perturbations in the neutron flux. This trend is physically plausible since increasing the number of neutrons generated through fission events will increase the flux value throughout a multiplying material. Along these same lines, the sensitivity coefficient for the fission cross section Σ_f is also uniformly positive since increasing the

likelihood of fission will in turn increase the number of neutrons in the homogeneous fuel material (i.e., as the number of neutrons available for transport increases, the flux increases). Moreover, while there appears to be a strong correlation between $S_{\phi,\bar{\nu}}$ and S_{ϕ,Σ_f} as appearing in Fig. 7-1, the two coefficients are not identical since Σ_f appears decoupled from $\bar{\nu}$ as part of its inclusion in the definition of D given by Eqn. 4-5.

- Otherwise, the sensitivity coefficients associated with Σ_f, $\bar{\nu}$, Σ_s, and Σ_c all have a similar shape: they are nearly flat for a majority of the cask's radial extent, before trending toward zero near the outer surface of the cask. This phenomenon is a consequence of all these terms appearing within the definition of B as given by Eqn. 4-5, which in turn controls the shape of the analytical neutron flux. The relationship between these input parameters demonstrates how the structure of the neutron flux is related to the structure of the sensitivity coefficients, since the G-derivative is a linear operator.

- The sensitivity coefficient associated with the scattering cross section Σ_s exhibits the most non-trivial behavior; it is positive and increasing for $r < 66.84$ cm, positive and decreasing for 66.84 cm $< r <$ 70.93 cm, and negative for $r >$ 70.93 cm to the cask outer radius. In turn, these features are indicative of the relative importance of a variety of gain and loss mechanisms occurring within Eqn. 4-5. In particular, for $r <$ 70.93 cm neutron scattering serves a gain mechanism: it acts to spatially redistribute but otherwise preserve the neutron flux within the monoenergetic diffusion model (i.e., in the absence of thermalization). For $r >$ 70.93 cm, neutron scattering is a loss mechanism: scattering in proximity to the outer boundary of the fuel region serves to increase leakage processes. The inflection point occurring at $r =$ 66.84 cm is then indicative of the spatial location where the role of neutron scattering begins to transition: its presence owes to the approximate non-reentrant boundary value given by Eqn. 4-2, which is intended to include leakage mechanics within the analytical diffusion model. That is, if the neutron flux was instead terminated at the physical extent of the fuel region, the analytical model would predict no neutron leakage and rather a zero neutron flux there. In this case, S_{ϕ,Σ_s} would then be uniformly positive, which is clearly a non-physical result in the neighborhood of the cask outer boundary.

To further understand and better rank the importance of the various competing physical phenomenologies included in Eqn. 4-5, Fig. 7-2 depicts the absolute value of each sensitivity coefficient plotted in Fig. 7-1. Several additional trends are immediately evident from Fig. 7-2:

- For a majority of the cask radius, Σ_c is the most important input parameter; however, its importance drops near the cask outer radius as a result of the increase in S_{ϕ,Σ_s} caused by leakage.

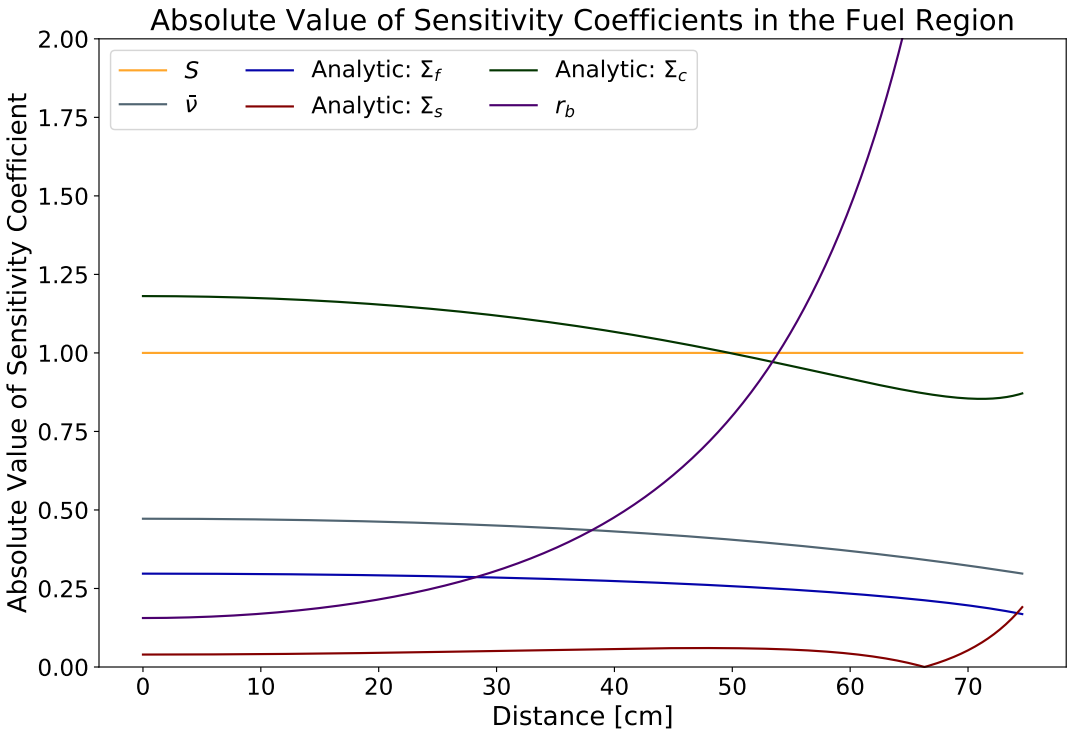

Figure 7-2. The absolute values of the sensitivity coefficients depicted in Fig. 7-1.

- For a majority of the cask radius, S is the second most important input parameter; however, near $r = 50$ cm, S_{c,r_b} quickly becomes the most important parameter and $S_{\phi,S}$ is briefly the most important parameter before becoming the second the important parameter near $r = 54$ cm.

- Initially in the cask radius, $\bar{\nu}$ and Σ_f are the third and fourth most sensitive parameters, respectively. However, the sharp increase in S_{ϕ,r_b} relegates $\bar{\nu}$ and Σ_f to the fourth and fifth most important parameters near $r = 38.098$ cm and $r = 28.283$ cm.

- Initially in the cask, r_b is the fifth most important parameter until approximately $r = 28.283$ cm where S, c, r_b increase and overtakes Σ_f before becoming the most important parameter in the system near 54 cm.

- For a majority of the cask radius, Σ_s is the least important input parameter; however, it becomes the fourth most important parameter near the cask outer radius.

These importance trends manifest in Figs. 7-1 and 7-2 due principally to the r-dependent interplay between the capture and leakage loss mechanisms present in

Eqn. 4-5. For example, capture is the dominant loss mechanism near the cask centerline, as shown in Fig. 7-1 a neutron initially located there is most likely to undergo many interactions before escaping from the cask outer surface. Conversely, leakage becomes an increasingly important loss mechanism near the cask outer radius, the importance of which is observed to eventually exceed that of capture. This physical interplay noticeably manifests in the behavior of S_{ϕ,Σ_s} and S_{ϕ,Σ_c} as depicted in Figs. 7-1 and 7-2: for example, at the point where S_{ϕ,Σ_s} changes sign, S_{ϕ,Σ_c} changes slope. Further, the capture loss mechanism is more important than any source term, with the exception of the internal neutron source term S near $r = 70$ cm, as the cask is a subcritical system by design. The geometry and materials of the cask are chosen in order to limit the neutron flux, and thereby, increasing the loss mechanisms. In fact, the importance of loss mechanisms is a common theme observed in each of the remaining materials of the spent fuel cask.

The previous discussion analyzes the SC's of input parameters in the analytic model. Further comparison of the SC's between the detailed and analytic model in the fuel region identifies essential physics in the detailed model. Figure 7-3 shows the comparison between the SC's calculated from the helium model in MCNP and the analytic SC's. The SC's from the detailed model are not included in the analysis of the fuel region, as limitations of MCNP's perturbation capabilities preclude sensitivity analysis in this region. Further, only the analytic SC's which have comparable computational values are displayed. The inset graph shows the relative error between the analytic model and the helium model using

$$relative\ error(r) = \frac{S(r)_{\phi,\alpha_i,analog} - S(r)_{\phi,\alpha_i,reference}}{S(r)_{\phi,\alpha_i,reference}}, \tag{7-1}$$

where $S(r)_{\phi,\alpha_i,analog}$ is the SC pertaining to the input parameter α_i from the analog model and $S(r)_{\phi,\alpha_i,reference}$ is the SC pertaining to the input parameter α_i from the reference model. In the fuel region, the helium model is the reference model, since limitations of MCNP's sensitivity analysis capabilities precluded analysis of the detailed model in the

fuel region, and Eqn. 4-5 is the analog model. [1] Referencing Fig. 7-3, a comparison of the SC's calculated using the analytic model, Eqn. 4-5, and from the helium model yields:

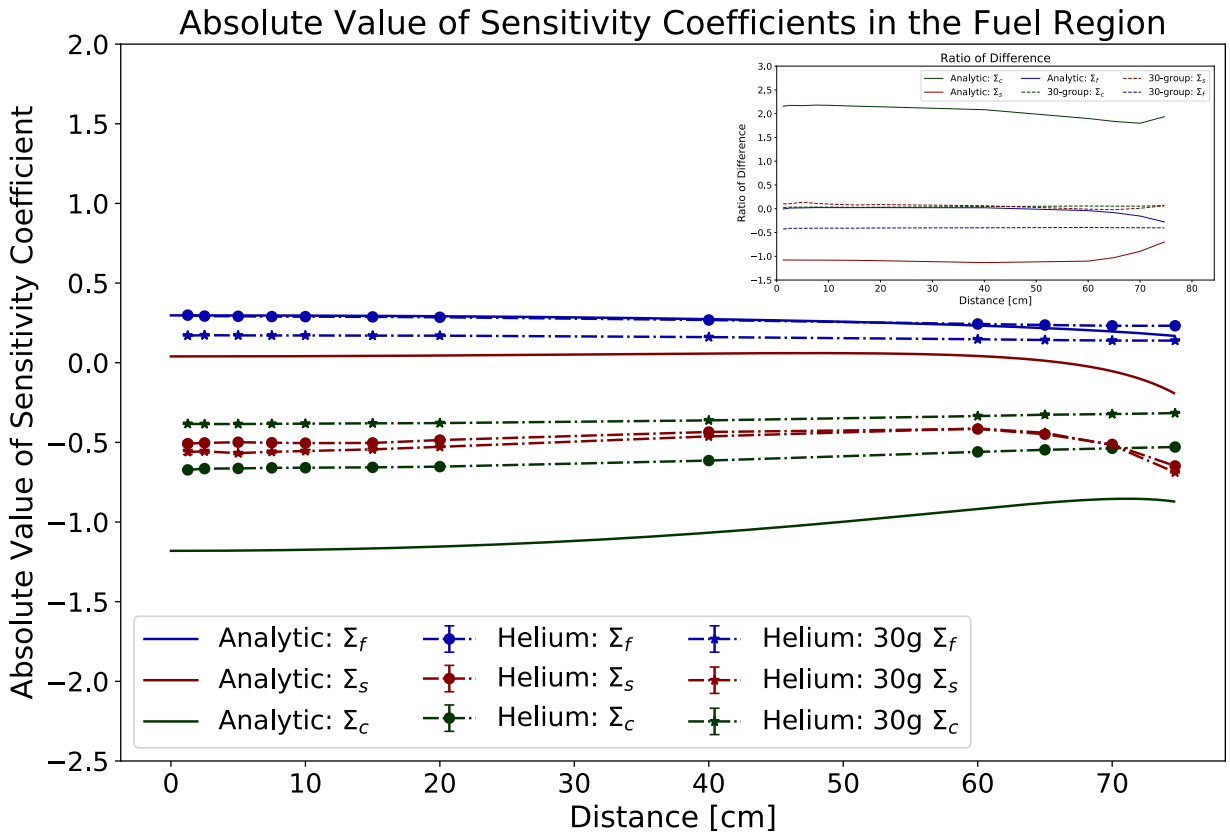

Figure 7-3. A comparison between the SC's from the helium model (dot dashed), the 30-group helium model (dot dashed with star markers),and the analytic model (solid). The inset plot shows the relative error between the SC's calculated with the analytic and helium models.

[1] The SC's for S and r_b are not directly computable from MCNP using the PERT card. MCNP results are given in units of *per source neutron*, therefore the value of $S_{\phi,S}$ is likely 1 as there is a linear relationship between the internal source strength and MCNP simulated neutron flux. However, discussion of the computational SC's is limited to values that are entirely computationally attainable, and $S_{\phi,S}$ is not. Determining the values of S_{ϕ,r_b} through computational means would require running multiple simulations where r_b, the fuel radius, is changed in each simulation, as geometry perturbations are precluded from MCNP's perturbation capabilities. Finally, perturbations in $\bar{\nu}$ are not compatible with MCNP perturbation capabilities, and therefore, cannot be computationally determined.

- The analytic and computational values of S_{ϕ,Σ_f} agree within 5% throughout the fuel region. Near $r = 60$ cm, the value of the analytic SC's pertaining to the fission cross section begins to decrease where the computational values of S_{ϕ,Σ_f} remain flat. Here is the first example of the effect of boundary values. The analytic model in the fuel region requires a boundary value at $r = 78.788$ cm (the extrapolated radius of the fuel). The flux is chosen to vanish at the extrapolated boundary value. Therefore, the value of the analytic S_{ϕ,Σ_f} decreases reflecting the decreasing flux value approaching the boundary value location. The computational model does not share this boundary value, and the computational values of S_{ϕ,Σ_f} do not decrease as a result.

- Figure 7-3 shows there is considerable disagreement between the analytically calculated values of S_{ϕ,Σ_s} and their computational counterparts. There are clear benefits when the two models agree; in this scenario, a code user understands the physics at the level of the analytic models. However, the scenario when the two models do not agree still provides insight into the problem leading to a more rigorous analysis of a simulation. The inset graph in Fig. 7-3 shows the relative error between the two models is nearly constant over the the first 50 cm of the fuel region for each of the parameters. The analytic values of S_{ϕ,Σ_s} are positive due to the choice of a monoenergetic analytic model. That is, choosing a monoenergetic model prevents thermalization which, in turn, does not capture the how the probability of absorption increases as neutrons thermalize, Fig. 7-4a. As a result, neutron scattering can only act as a loss term through leakage, which will not occur until a neutron is significantly close to a boundary. The computational models use continuous energy cross section data which captures thermalization and indirectly leads to neutron loss through capture of thermal neutrons, in addition to the aforementioned leakage process, yielding a negative SC value. Further, the two models have similar shapes, flat before breaking downward. This behavior occurs in the analytic models because of the boundary value at the extrapolated radius. The SC's pertaining to loss terms increase in value at the boundary value since the neutron flux is being forced to zero. However, the computational model does not have boundary values at this location. Instead, the neutron flux is decreasing because the flux is directed outward (from Fig. 2-9b) confirming that neutrons are leaking from the fuel region. Therefore, increasing the scattering cross section will increase the chance that a neutron leaks from the fuel region. Even though the two models do not agree, understanding the causes for the disagreement are as important in understanding the problem as having matching results.

- Finally, the values of S_{ϕ,Σ_c} for analytic and computational models disagree as shown by the inset graph in Fig. 7-3. However, both curves are negative, since absorption is a loss term. The values of the analytically determined S_{ϕ,Σ_c} initially show a reduction around $r = 60$ cm, near the location where S_{ϕ,Σ_s} goes negative ($r = 66.842$ cm). From this, a relationship is again seen between the loss terms, Σ_c and Σ_s. The computationally computed values of S_{ϕ,Σ_c} do not show a drastic reduction at the same location, since scattering is always a loss term in the computational

models. That is, there is no location where scattering physics changes from a preservation term to a loss term, therefore, there is no drastic change in S_{ϕ,Σ_c} in the computational model. Another difference between the two models occurs near the boundary of the fuel region, at $r = 73$ cm where the analytically calculated values of S_{ϕ,Σ_c} has an inflection point. This inflection point results from the boundary value forcing the flux to zero, resulting in larger negative values for S_{ϕ,Σ_c} and S_{ϕ,Σ_s}. The computational model does not have this inflection point since the flux is not forced to zero at this location in the helium model.

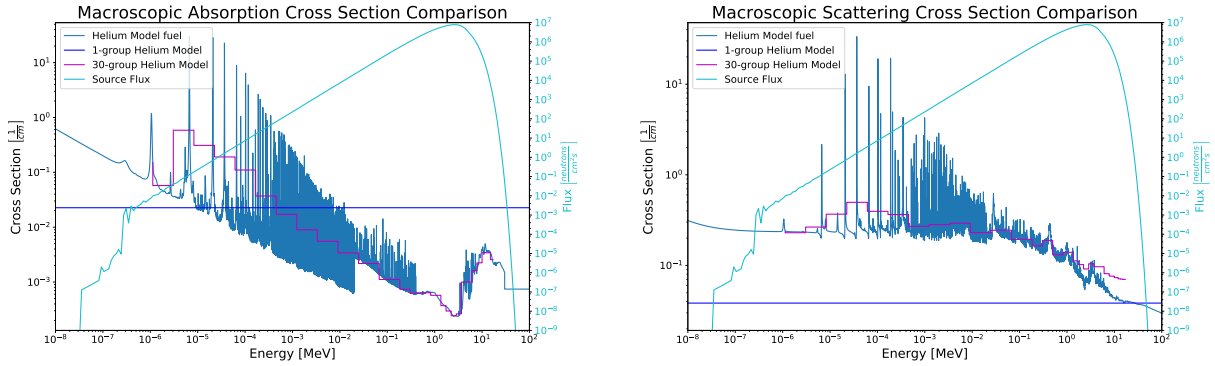

(a) (b)

Figure 7-4. A) The absorption cross section and B) the scattering cross section in the homogenous fuel material used in the helium model. The dark blue line is the continuous energy cross section, the royal blue line is the monoenergetic cross section value used in the analytic model, the purple line is the 30-group cross section data. The source spectrum (light blue) is shown for reference, as the source spectrum is used in NJOY as a weight function to make the monoenergetic cross section value.

The disagreement between the SC's from the helium model and analytic models is a result of oversimplifying the continuous energy cross section data when using only two energy groups. In an effort to investigate the effect of better representing the continuous cross section data by increasing the number of energy groups, a 30-group instantiation of the helium model is developed in MCNP, using the pre-loaded multigroup formulations included in that code [20], the 30-group absorption and scattering cross section values are provided in Fig. 7-4a. The sensitivity coefficients of the 30-group MCNP modes are calculated using Eqn. 5-9, in a similar manner as the SC's from the continuous energy MCNP models. Further, while the cross section data is energy dependent in the 30-group

MCNP models, the simulated neutron flux values are integrated over energy, similarly to the neutron flux values of the continuous energy MCNP models. Figure 7-3 shows the results from the 30-group sensitivity analysis. The SC's from the 30-group model for Σ_a and Σ_s better agree with the corresponding SC's from the helium model than the SC's from the analytic and detailed models. However, the SC's pertaining to Σ_f from the 30-group model show more disagreement than from the analytic model. This conclusion shows that 30 energy groups are insufficient to capture the sensitivity information from the detailed model in the fuel region. Further analysis of the remaining materials shows similar results.

7.1.2 Sensitivity Analysis of the MPC

The E_2S_2 equations are chosen to analytically represent the neutron flux in the MPC. These equations, Eqns. 3-57-3-60, are a system of four coupled ODE's representing four partial fluxes, which depend on group-wise cross section data values. Table 4-4 provides a summary of these values in the MPC. These values are calculated using NJOY with the same composition as MPC in the detailed and reduced-fidelity MCNP models, where the energy cutoff between the two groups occurs at 1 keV [45]. The 1 keV energy cutoff value is chosen as at this energy value, a majority of the resonances occurring in the total cross section are contained in the fast energy group while the the thermal energy group has only one resonance. A lower energy cutoff (i.e., 100 eV) could have been chosen to capture all the resonances in the fast group, however, the fast-to-thermal group cross section becomes too low to accurately capture the neutron transfer from the fast group to the the thermal group. This is a result of choosing the fast energy group to be too wide. In a two-energy group model, a neutron is transferred from the fast group to the thermal group in a single interaction. Meaning, a neutron has to lose a sufficient amount of energy in a single scattering event such that the final energy of the scattered neutron is in the thermal energy group. Choosing too wide of an energy group causes the percentage of neutrons capable of transferring energy groups to decrease. Table 4-4 summarizes the

nominal values of the input parameters used in the solution to the set of equations given by Eqns. 3-61-3-64. Further, finding the SC's for the total flux requires first finding the SC's for each partial neutron flux depending on the group-wise cross sections, as the SC's calculated using MCNP are given for the total scattering and total absorption cross sections rather than the group-wise cross sections. The SC's for the cross section values for the total parameters are defined as

$$S_{\phi,\Sigma_a} = S_{\phi,\Sigma_a^1} + S_{\phi,\Sigma_a^2} \tag{7-2}$$

$$S_{\phi,\Sigma_s} = S_{\phi,\Sigma_s^{1\to1}} + S_{\phi,\Sigma_s^{1\to2}} + S_{\phi,\Sigma_s^{2\to1}} + S_{\phi,\Sigma_s^{2\to2}}, \tag{7-3}$$

where the value $S_{\phi,\Sigma_s^{2\to1}}$ is zero since upscattering is assumed to be zero. The SC's corresponding to each parameter in Tab. 4-4 will be discussed.

Figure 7-5 shows the partial and total SC's pertaining to the absorption cross section. The values of S_{ϕ,Σ_a^2} are more important than the corresponding values for S_{ϕ,Σ_a^1}. Table 4-4 shows the value of Σ_a^2 is more than five times larger than Σ_a^1 causing the difference in importance between the two parameters in spite of the thermal flux only accounting for 20-40% of the total flux in the detailed model (see Fig. 2-12). As expected, both the curves of the SC's pertaining to the group-wise cross section values are negative. Probably the most notable feature of the curves is all the curves become less negative at the boundaries. The values of S_{ϕ,Σ_a} increase from $r = 84.34$ cm to $r = 85.84$ cm, near where the values of S_{ϕ,Σ_s} has a zero point.

Neutron losses are related between the Σ_a and Σ_s, since both input parameters act as loss mechanisms. The value of the neutron flux is controlled at both the left ($r = 84.34$ cm) and the right ($r = 86.84$ cm) surfaces due to the boundary conditions. As a result, there exists a certain number of neutrons which will be attenuated in the MPC. At locations where neutrons are being lost to leakage, the importance of absorption must be reduced to account for the increased importance of leaking neutrons. For the remaining

thickness of the MPC, neutron loss physics is shared between absorption and leakage and this relationship is observed.

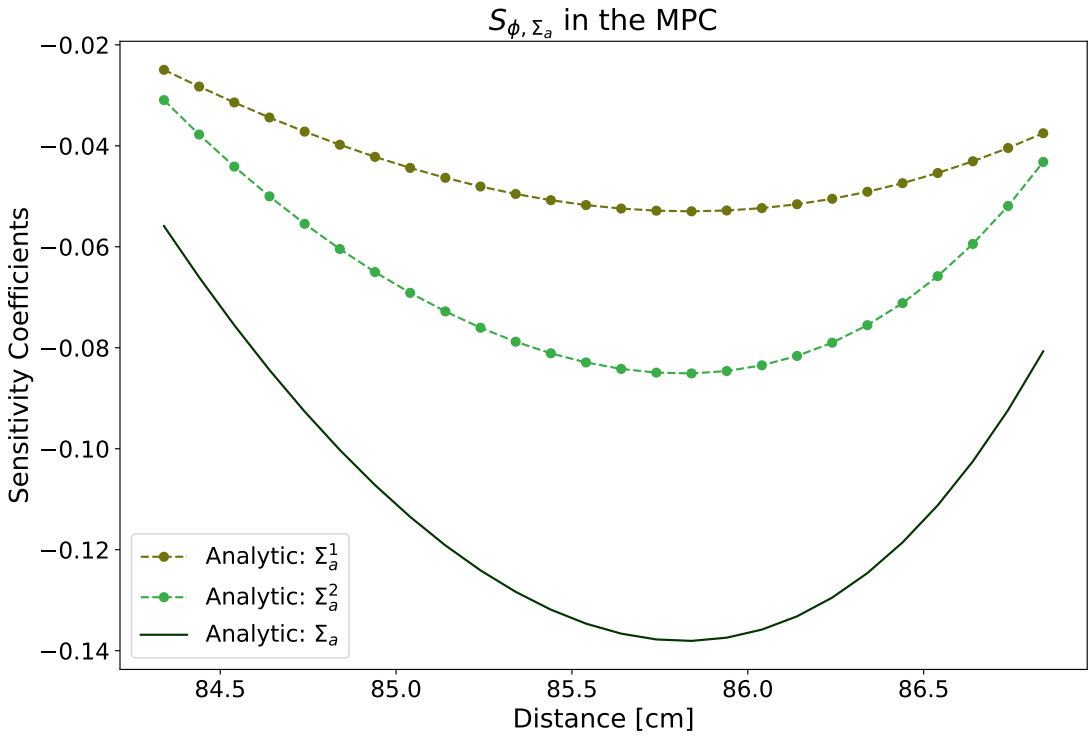

Figure 7-5. The SC's pertaining to Σ_a^1 (dark green dotted), Σ_a^2 (light green dotted), and Σ_a (solid line) in the MPC.

The value of S_{ϕ,Σ_s} is the sum of $S_{\phi,\Sigma_s^{1\to1}}$, $S_{\phi,\Sigma_s^{1\to2}}$, $S_{\phi,\Sigma_s^{2\to2}}$ as shown in Fig. 7-6. This figure shows $\Sigma_s^{0,2\to2}$ is the least important parameter across the thickness of the MPC, since the low energy flux is smaller than the high energy flux in this region. From r = 84.34 cm to nearly r = 85 cm, the most significant partial scattering cross section is the fast in-group scattering cross section, $\Sigma_s^{0,1\to1}$, due to 60-80% of the neutrons belonging to the fast group. As thermal neutrons are bred deeper in the MPC, $S_{\phi,\Sigma_s^{1\to2}}$ becomes the most important partial scattering cross section from r = 84.84 cm to r = 86.09 cm. Beyond this thickness, the fast group in-scattering cross section term becomes most important since the fast group neutrons comprise the majority of the total neutron population and leakage is causing the neutrons in the fast energy group to become most

significant. Also at $r = 86.09$ cm, the SC's corresponding to the total scattering cross section begins to flatten out. This is a result of the continuous flux boundary value as neutrons begin leaking from the MPC.

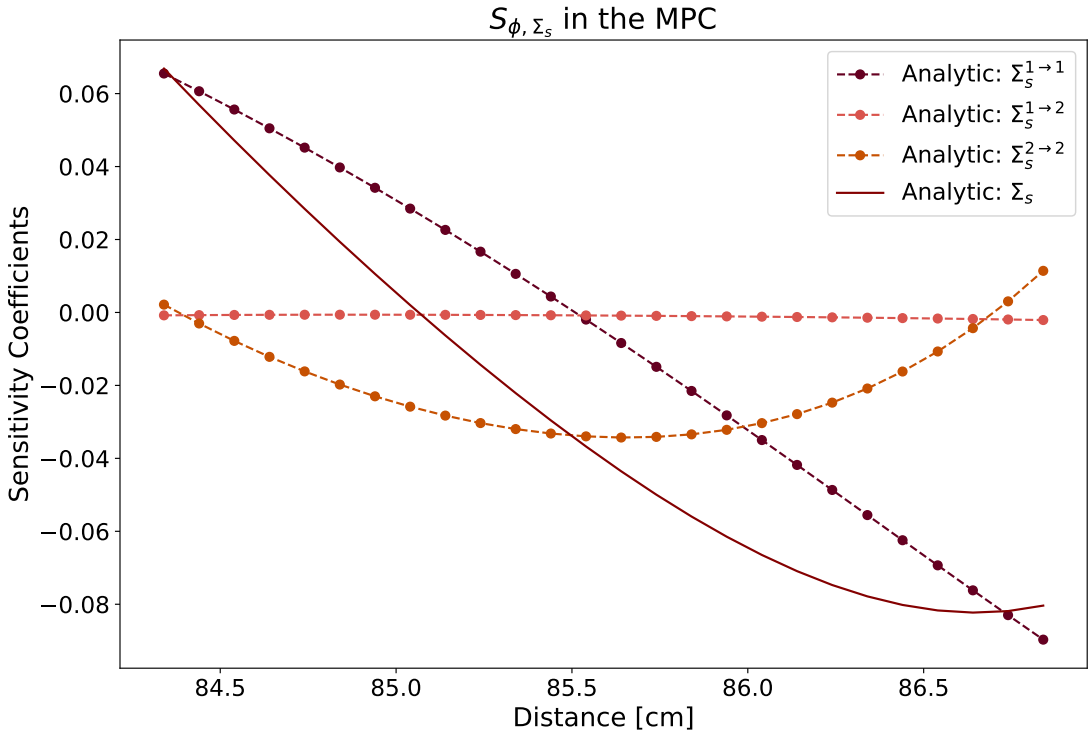

Figure 7-6. The SC's pertaining to the scattering cross sections in the MPC. The values of S_{ϕ,Σ_s} is the sum of the partial sensitivity coefficients $S_{\phi,\Sigma_s^{1\to1}}$, $S_{\phi,\Sigma_s^{1\to2}}$,$S_{\phi,\Sigma_s^{2\to2}}$.

Figure 7-7 shows the sensitivity coefficients pertaining to μ, the directions in which the multigroup discrete ordinates equations are evaluated. The values of μ_1 and μ_2 are included in the sensitivity analysis, since these parameters are chosen and can be set to any angle. The magnitude of the values of the SC's pertaining to μ_1 are larger than the corresponding values pertaining to μ_2, since the right-moving flux has a larger value than the left-moving flux through the entire cask. This behavior is seen in all the remaining materials. The positive values of S_{ϕ,μ_1} mean the flux value will increase as the direction of μ_1 becomes more forward directed. However, choosing μ_2 to be more backward directed would cause a reduction in the total flux. Further analysis of the causes of this behavior is

required, however, it is likely a result of the chosen boundary values and anisotropy in the flux.

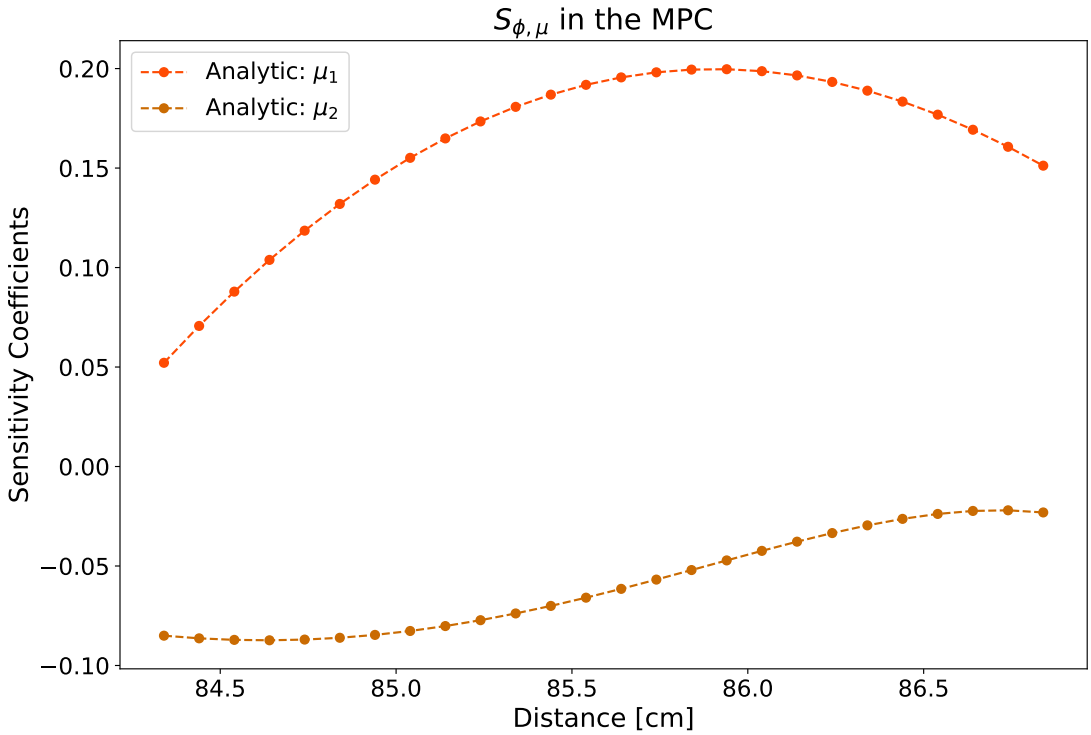

Figure 7-7. The SC's pertaining to the values of μ. The right directed flux (orange) has a SC with a magnitude larger the corresponding values for the left directed flux (brown).

The final parameters to discuss in the analytic models are the boundary values from Eqn. 6-12, $\boldsymbol{A}$, shown in Fig. 7-8. The two most important boundary values at the left surface of the MPC, $r = 84.34$ cm are the two boundary value applied at that location (the boundary values for ϕ_1^1 and ϕ_1^2). These two curves decrease in value through the MPC thickness. At the exiting face ($r = 86.84$ cm), the boundary value for ϕ_2^1 is the most important as the this boundary value is applied at the outer face of the MPC and applies to the fast flux. While the boundary value for ϕ_2^2 is also applied at this location, it is not the second most important boundary value due to the neutron flux population being significantly fast. Figure 7-8 shows that the SC's for the boundary values have

maximum values at the location where the boundary value is applied and decreases away from that location. Further, the values are all positive, meaning, as the boundary value value increases the flux values also increase, a physically intuitive result.

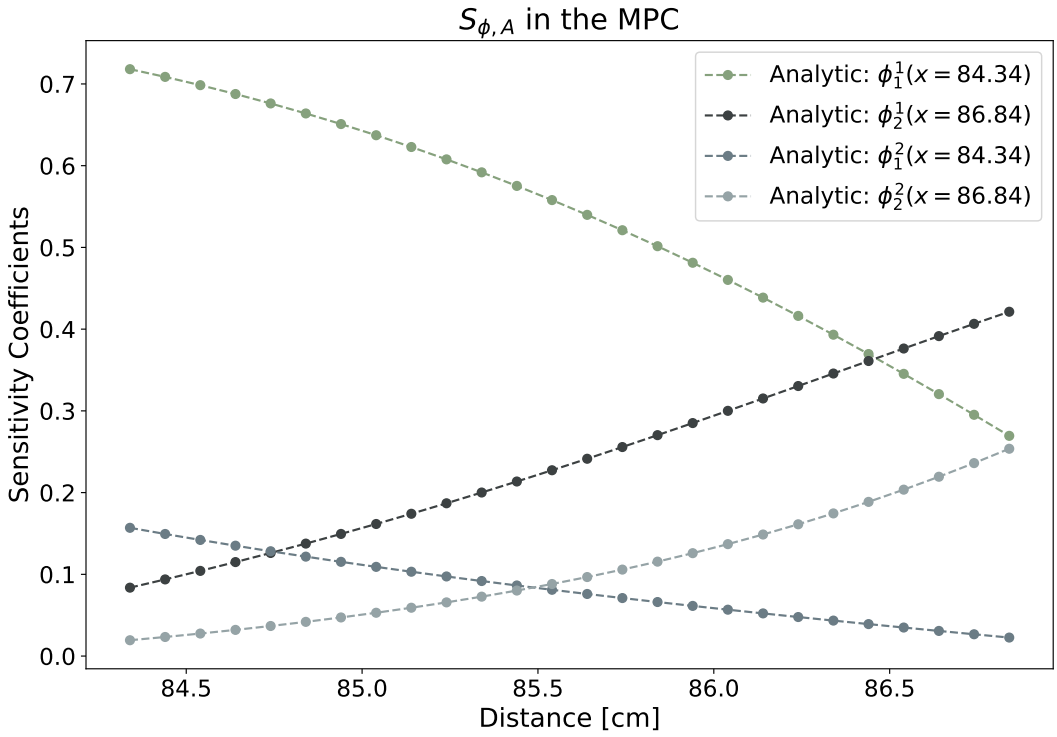

Figure 7-8. The SC's of the boundary values are included in the sensitivity analysis. The flux values for ϕ_1^1 (green-grey) and ϕ_1^2 (dark grey) are given as boundary values at $r = 84.34$ cm, where the flux values for ϕ_2^1 (black) and ϕ_2^2 (light grey) is chosen to be continuous at $r = 86.84$ cm.

The extension of the results assessment methodology in sensitivity metric space requires comparing the SC's from the detailed model, helium model, and analytic model. The only comparable SC's are the cross section values Σ_a and Σ_s [2] . Figure 7-12 compares

[2] The comparison between the SC's from the detailed, helium, and analytic models is limited to Σ_a and Σ_s, since other values included in the analytic sensitivity analysis do not have computational counterparts. μ_1 and μ_2 are analytic constructs and have no counterpart in MCNP. Further, manipulating the thickness of MPC in MCNP can

the values of S_{ϕ,Σ_a} and S_{ϕ,Σ_s} for the detailed model, the helium model, and the E_2S_2 model in the MPC. The inset plot in Fig. 7-12 shows the relative error between the analog models and the detailed model, where the relative error is calculated using Eqn. 7-1 with the reference model being the detailed model. The error values for the analog models' S_{ϕ,Σ_s} drops off the graph at the location where the detailed model's value of S_{ϕ,Σ_s} crosses zero. This is a result of calculating the relative error, since the difference between the model values is divided by the value of the detailed model value. That is, when the detailed model value is nearly zero, the relative error will be large.

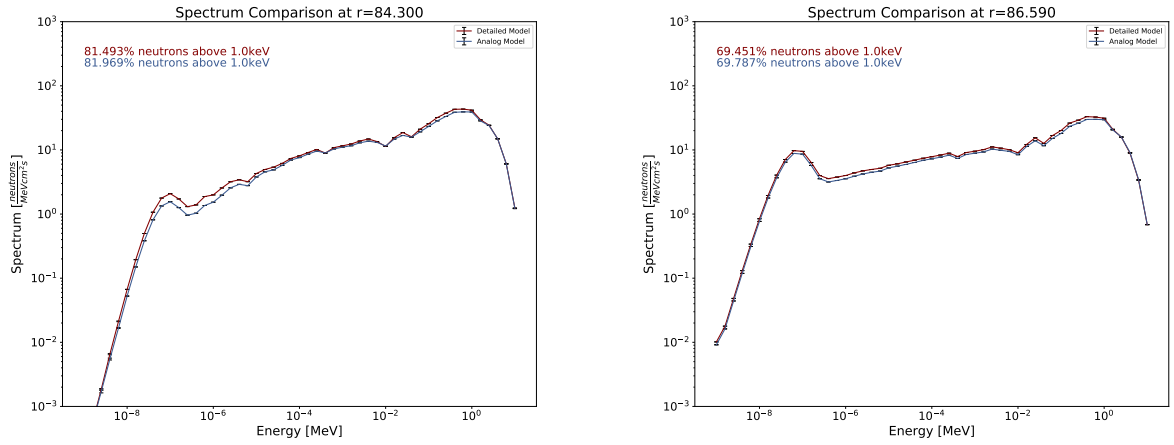

(a) (b)

Figure 7-9. A comparison of the neutron spectrum between the detailed model (red) and helium model (blue) at A) the inner surface of the MPC ($r = 84.340$ cm) and B) near the outer surface of the MPC ($r = 86.590$ cm)

The values for S_{ϕ,Σ_s} of the detailed and helium models are nearly the same through the MPC thickness and the relative error has a maximum value of 6.849% at $r = 85.09$ cm. Overall, it is expected for the SC's of the helium model to be similar to those of the detailed model since there are no assumptions, approximation, or reductions in geometry

only be conducted through running multiple simulations and does not lend itself to direct computational sensitivity analysis using the methods presented in Chpt. 5.

occurring outside of the fuel region in the helium model, making the two MCNP models the same outside of the fuel region. However, there is a noticeable difference in the values of S_{ϕ,Σ_a} between the two MCNP models, as the helium model underpredicts the thermal neutron flux, as seen in Fig. 7-9, especially at the left surface of the MPC (Fig. 7-9a). While the materials and geometry are the same between the MCNP models, the energy spectrum differs between the two causing discrepancies between the sensitivity coefficients. The helium model underpredicts the neutron flux at lower energies, which results in differences appearing in derivative terms (i.e., the SC's).

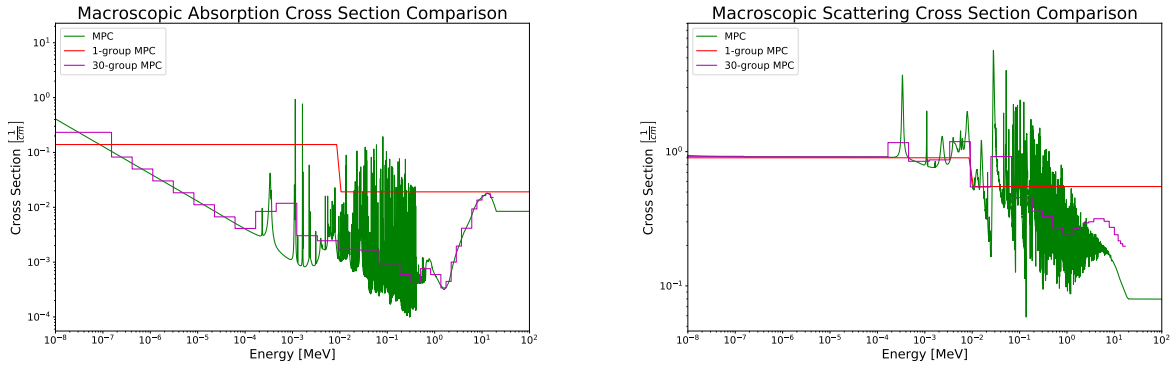

(a) (b)

Figure 7-10. A) The absorption cross section and B) the scattering cross section in the MPC. The dark blue line is the continuous energy cross section, the red line is the two-group cross section value used in the analytic model, the purple line is the 30-group cross section data. Increasing the number of energy groups used to represent the cross section better captures the shape of the continuous energy cross section data.

Further, the analytic model underpredicts the values of S_{ϕ,Σ_s} for positive values of S_{ϕ,Σ_s} and overpredicts the values of S_{ϕ,Σ_s} for negative values of S_{ϕ,Σ_s}. Treating the neutron flux with only two energy groups and two angles artificially preserves the flux between $r =$ 83.34 cm and $r = 85.09$ cm, and over-accounts for leakage between $r = 85.09$ cm and $r =$ 86.84 cm. The implications of these simplifications are further emphasized through the comparison of S_{ϕ,Σ_a}. Using only two energy groups "smoothes" out the various resonances that occur within various cross sections as shown in Fig. 7-10. Similarly to the discussion

in Sec. 7.1.1, a helium model using 30-group cross sections is developed for comparison with the detailed model. Increasing the number of energy groups used to represent the cross sections helps to better capture the continuous energy cross section data, including any resonance structure, shown in Fig. 7-10. The calculated SC's of the 30-group model are included in Fig. 7-12 as the dash-dotted line with star markers. Using 30 energy groups yields SC's which, through inspection, are more representative of the detailed model's values than the 2-group analytic model. This result shows the effect of increasing the energy group number, however it is unlikely a 30-group model sufficiently converges the energy grid, similar to in the fuel region.

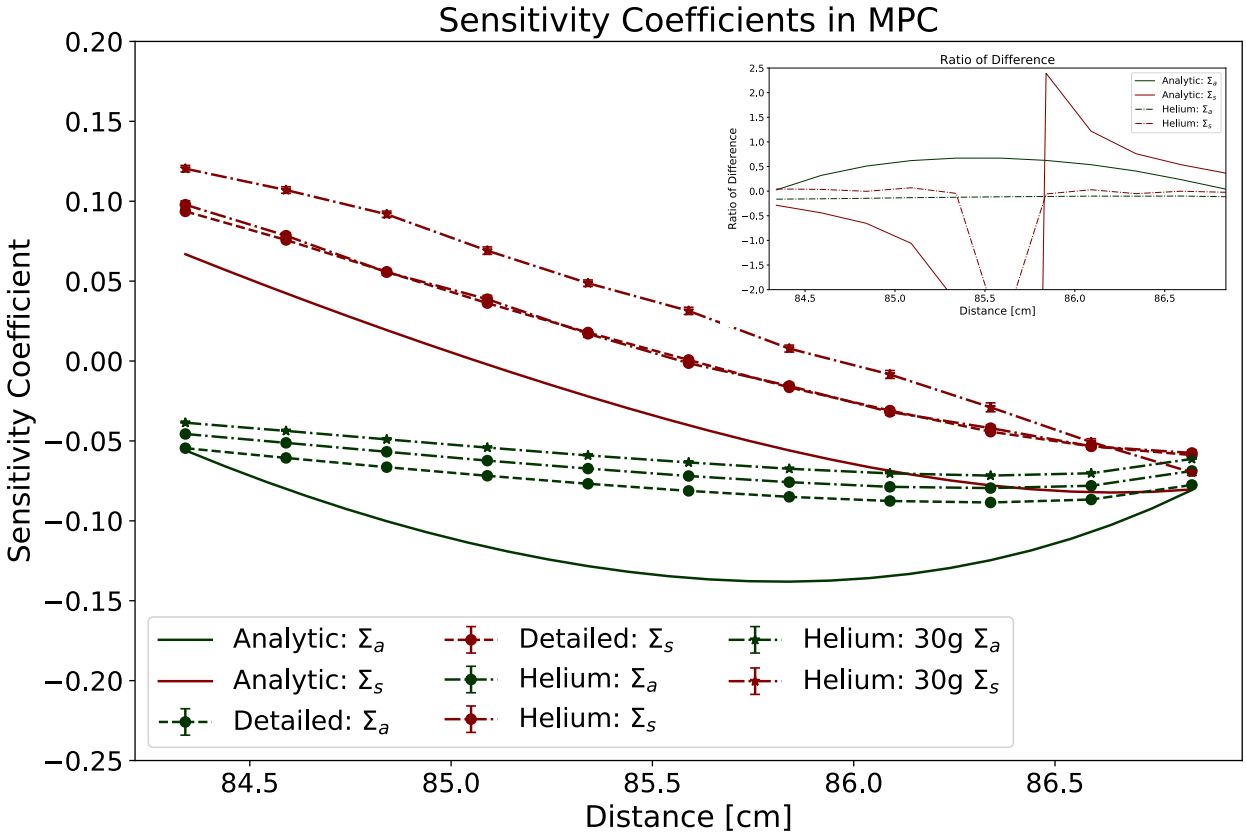

Figure 7-11. A comparison of the SC's from the detailed model (dashed), helium model (dash-dotted), and analytic model (solid). A 30-group model (dash-dot with star markers) is also included to investigate the effect of increasing the energy mesh.

Finally, the SC's in the MPC can be compared to stratify importance. Figure 7-12 shows the absolute values of the various SC's. For the detailed MCNP model, Σ_s is the most important parameter for approximately the first 0.5 cm of the MPC before absorption becomes the most important parameter for the remainder of the cask. Similar behavior is captured with the helium model. The analytic models have a similar behavior, however, Σ_s is the most important parameter for a much smaller distance, $r = 83.34$ cm to $r = 84.44$ cm. The sensitivity analysis proceeds in the concrete annulus.

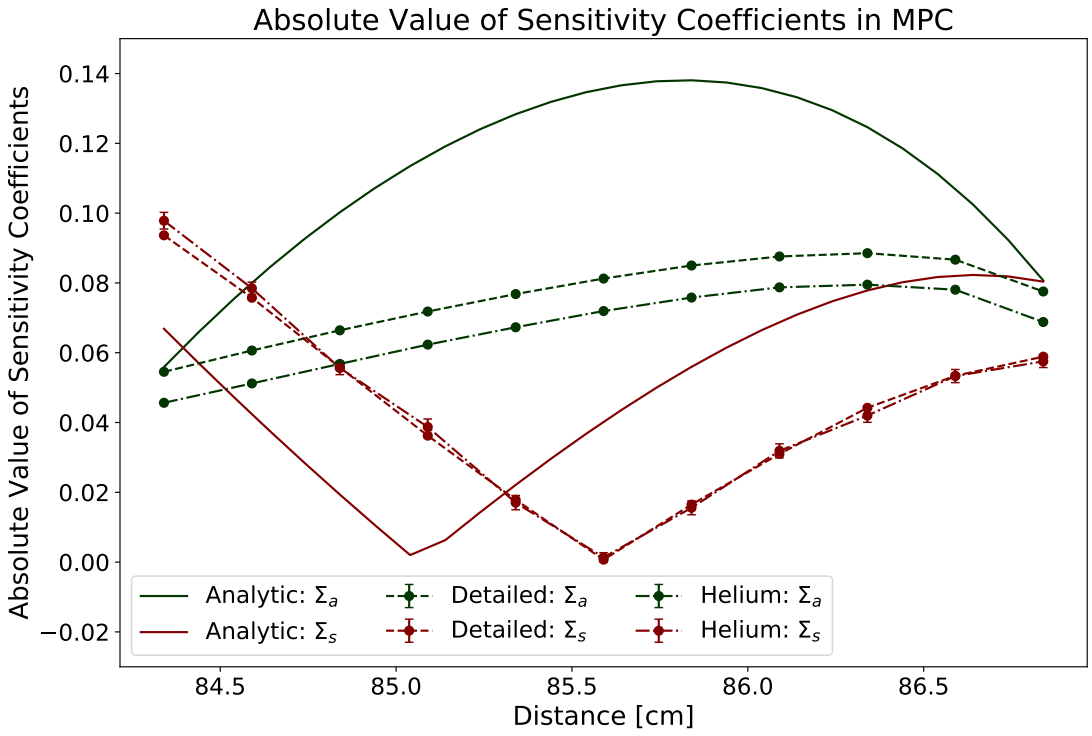

Figure 7-12. The absolute values of the SC's are shown to ease stratification of the parameters in the detailed model (dashed), helium model (dash-dot), and analytic model (solid).

7.1.3 Sensitivity Analysis of the Concrete Annulus

The neutron flux undergoes a shift in energy (show in Figs. 2-16a-2-16h) and sizable reduction, approximately 50%, through the thickness of the concrete annulus (Fig. 2-7). The energy shift indicates scattering physics is driving thermalization, which alludes to a

large importance of scattering physics. The nominal values of the input parameters used to calculate the SC's in the concrete region are provided in Tab. 4-3.

Figure 7-13 shows the values of the SC's for the partial and total absorption cross sections. The contribution to the total SC's from the thermal group cross section is greater than that from the fast energy group, since the value of $\Sigma_a^{0,2}$ is approximately three times larger than $\Sigma_a^{0,1}$, Tab. 4-3. Further, the population of thermal neutrons is increasing through the concrete annulus, which causes the values of S_{ϕ,Σ_a^2} to increase until the edge of the concrete region. Near the edge of the concrete boundary ($r = 166.37$ cm), the values of the SC's for both the thermal and fast group absorption cross sections decrease. A similar behavior is seen in Fig. 7-5 at $r = 86.84$ cm, where the MPC shares a boundary with the concrete. The boundary value at both locations is chosen to have a continuous flux. At locations where a continuous flux boundary value is applied, the SC's pertaining to the cross section data trend toward zero, since the flux is essentially "pinned" to a value at these locations.

The SC's pertaining to the group-wise and total scattering cross sections are shown Fig. 7-14. The negative values of $S_{\phi,\Sigma_s^{1\to1}}$ is indicative of the role that scattering plays in neutron shielding. Concrete has a scattering ratio of 99.452% for fast neutrons, meaning neutrons undergo many scattering events before an absorption event occurs, where the scattering ratio is calculated as $\Sigma_s/(\Sigma_t)$ using cross section values pertaining to the concrete (Tab. 4-3). Therefore, $\Sigma_s^{1\to1}$ acts to prevent forward motion of the neutrons through scattering until a neutron can downscatter and eventually be absorbed. The values of $S_{\phi,\Sigma_s^{1\to2}}$ are negative and increase through the concrete thickness, so, neutrons thermalizing indirectly leads to absorption since the absorption cross section is greater in the thermal energy group, see Tab. 4-3. Figure 2-16 shows the increase in the thermal flux through the concrete region due to the the group-to-group scattering cross section $\Sigma_s^{1\to2}$. This effect is realized in the increasing values of the SC's pertaining to $S_{\phi,\Sigma_s^{1\to2}}$. $S_{\phi,\Sigma_s^{2\to2}}$ is initially positive, since the thermal neutron flux is being preserved for approximately

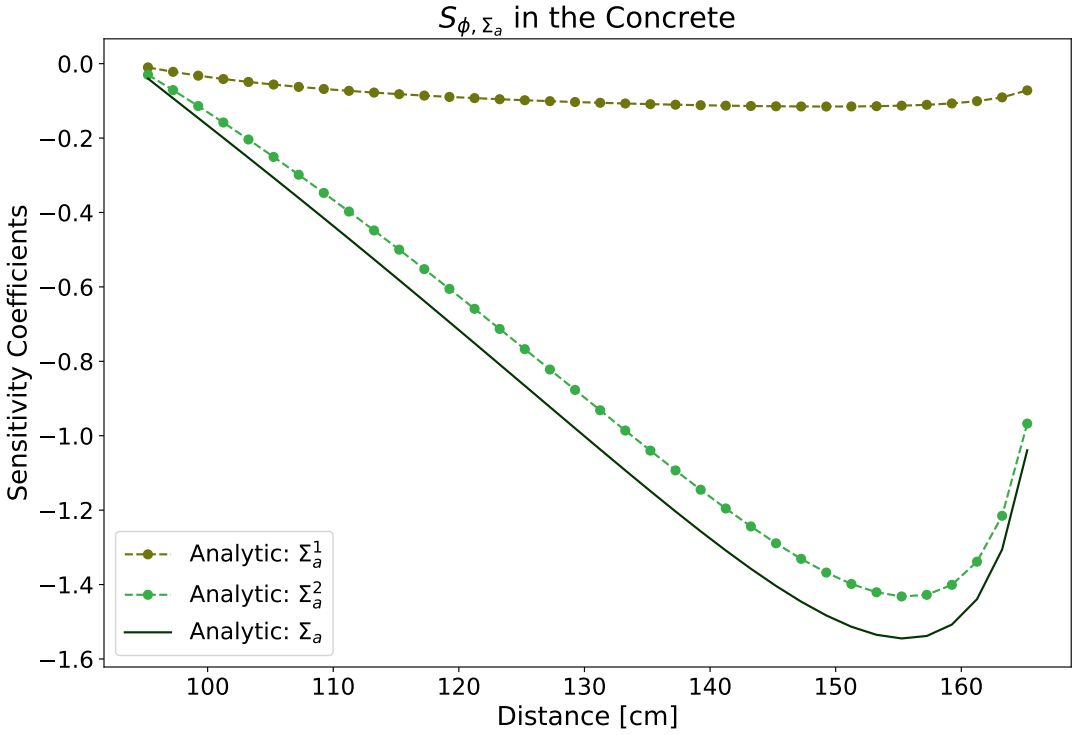

Figure 7-13. The values of S_{ϕ,Σ_a} (solid) in concrete show Σ_a^2 (light green) contributes more to the total sensitivity of the absorption cross section than Σ_a^1 (dark green).

the first 30 cm of the concrete thickness, a result of the high scattering ratio in concrete (98.910% for thermal neutrons). After the first 30 cm, $S_{\phi,\Sigma_s^{2\to 2}}$ has negative values as neutrons are lost indirectly to absorption and directly to leakage. Again, at the right boundary value ($r = 166.37$ cm), the group-wise, and therefore total, SC values trend toward zero due to the continuous boundary value at that location.

Figure 7-15 shows the SC's corresponding to the user-chosen directions μ. The values of the SC's pertaining to μ_1 are greater in magnitude than the same values for μ_2. These two curves have a similar shape which is presumed to be related to applying the same type of boundary value on both edges of the concrete annulus, a continuous flux boundary value. Further investigation of the physics which causes the shape of the curves in Fig. 7-15 is required.

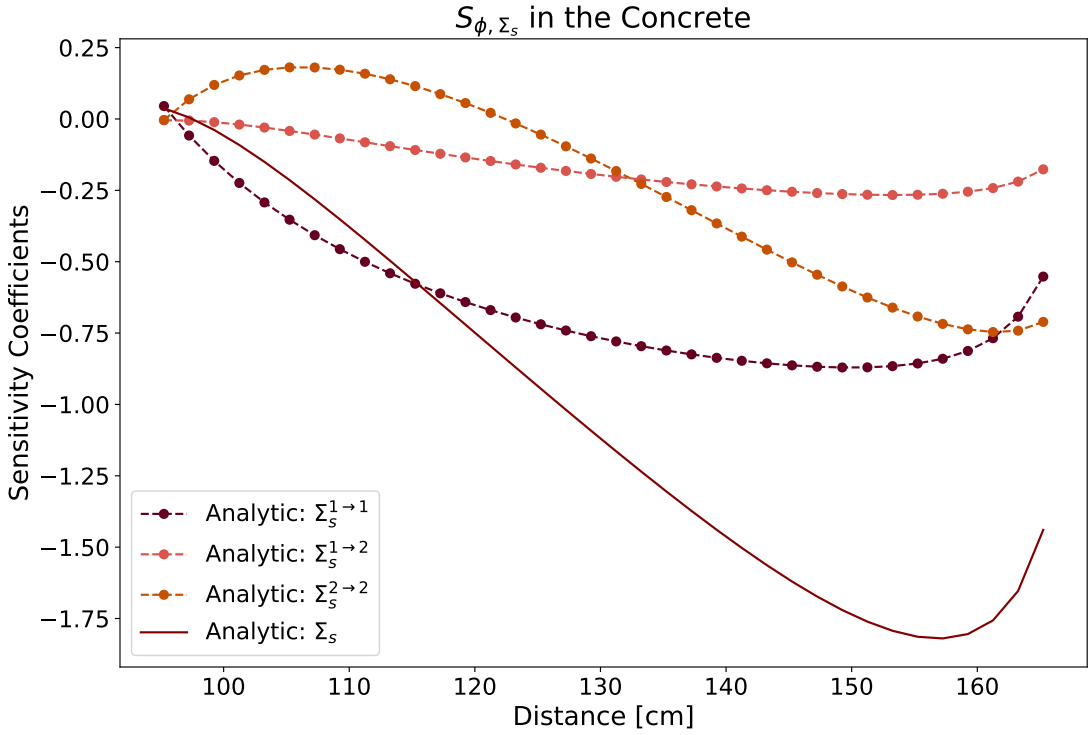

Figure 7-14. The SC's pertaining to the scattering cross section in concrete (solid line). The values of the partial cross section SC's are shown to investigate how the partial fluxes depend on their individual parameters: $S_{\phi,\Sigma_s^{1\to1}}$ (dark red), $S_{\phi,\Sigma_s^{1\to2}}$ (pink), and $S_{\phi,\Sigma_s^{2\to2}}$ (red-orange)

Figure 7-16 shows the SC's pertaining to the boundary value values of Eqns. 3-57-3-60. The boundary values for ϕ_1^1 and ϕ_1^2 both are applied at $r = 95.25$ cm and those for ϕ_2^1 and ϕ_2^2 are applied at $r = 166.37$ cm. At $r = 95.25$ cm, the two most important boundary values are the ones applied at this location, with the boundary value for the fast flux being the more important of the two due to high population of fast neutrons at this location. Moreover, since thermal neutrons are bred from the fast flux, the boundary value for ϕ_1^1 remains the most important boundary value throughout the thickness of the concrete, as changing the number of incoming fast neutrons affects the fast and thermal fluxes. Further, the values of the SC's corresponding to the boundary value for ϕ_1^2

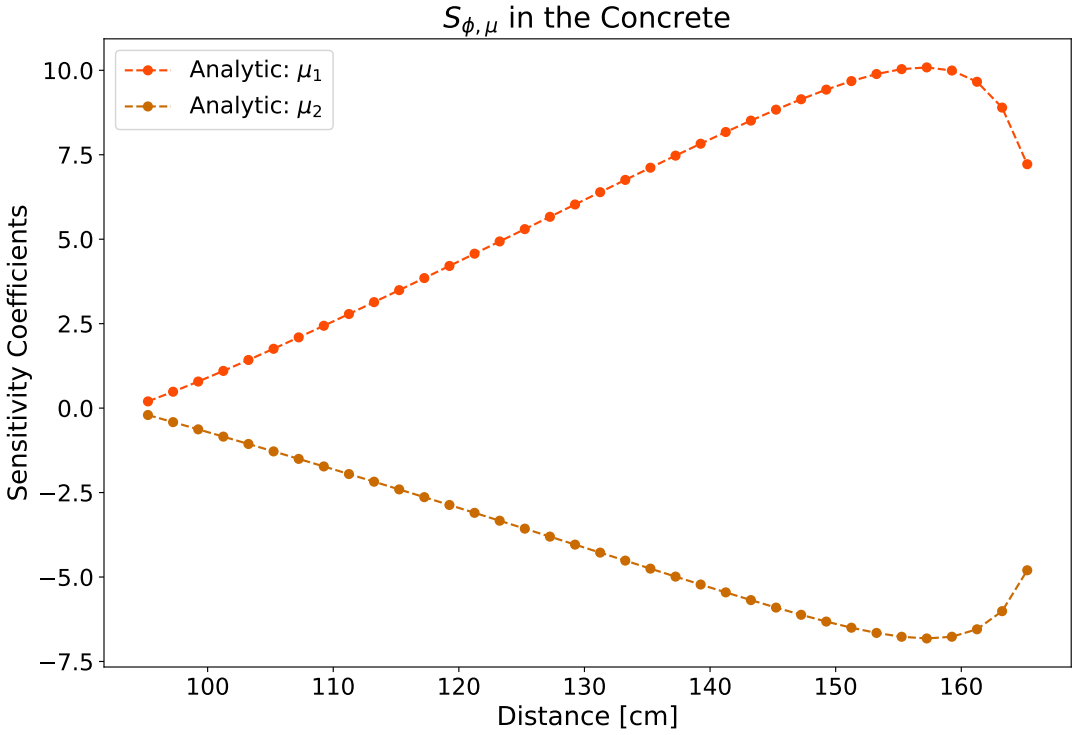

Figure 7-15. The values of the SC's pertaining to μ_1 and μ_2. The values of S_{ϕ,μ_1} (orange) have a larger magnitude than S_{ϕ,μ_2} (brown), signifying more importance being attributed to μ_1 than μ_2.

decreases through the thickness since the population of the thermal flux depends more on downscattering from the fast group than from incoming thermal neutrons.

At the other boundary ($r = 166.37$ cm), the boundary value for ϕ_1^1 is still the most important boundary, owing to dependence between the thermal neutron population and downscattered neutrons from the fast group. However, the second most important parameter is the boundary value for ϕ_2^2, since the thermal flux has a higher population at the exiting surface of the concrete than the fast neutron population at that location. The values of the boundary value of ϕ_2^1 are the least important since the population of fast neutrons entering the concrete at $r = 166.37$ cm is comparatively low (about 0.753% of the total flux).

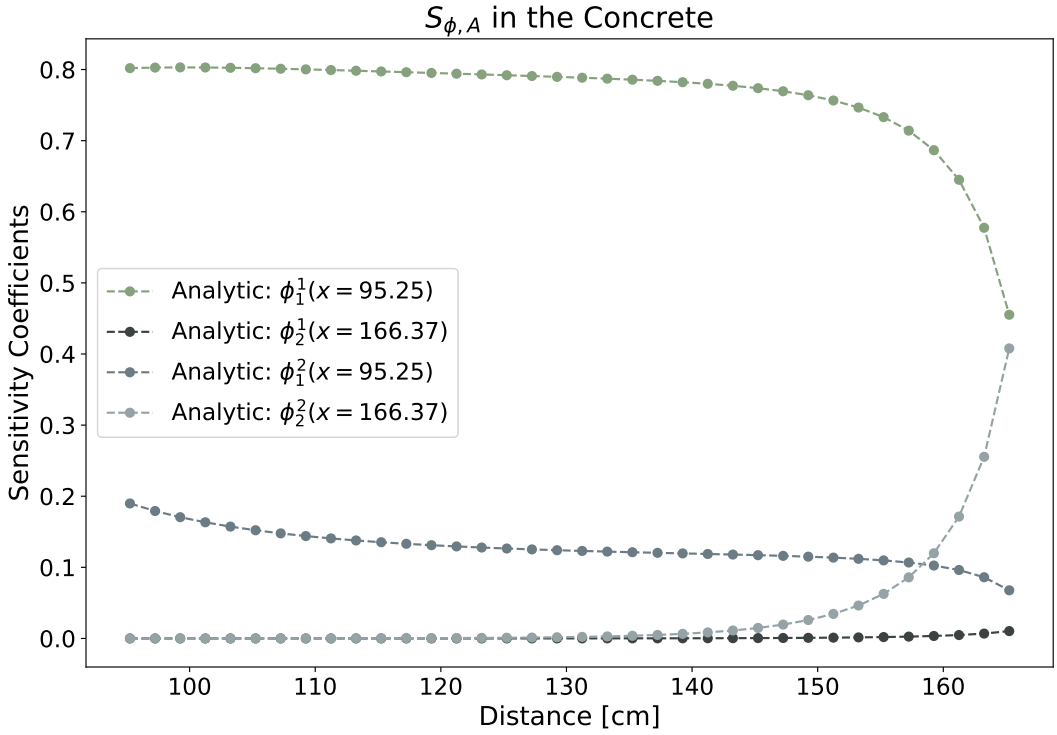

Figure 7-16. Perturbing the boundary values is equivalent to error occurring in the flux values at the material interfaces. These graphs effectively show how deep into the concrete region a specific boundary value affects the neutron flux.

After analyzing the physics driving the behavior in the concrete annulus, it is necessary to compare the SC's from the analytic, helium, and detailed models in the concrete annulus. Figure 7-19 compares the SC's for the detailed, helium, and analytic models. This figure shows better agreement between the computational models than is seen in the MPC. In fact, the values of S_{ϕ,Σ_a} and S_{ϕ,Σ_s} agree within 1.070% and 1.314% respectively over the concrete thickness. The helium and detailed model show better agreement in the concrete than in the MPC since the energy spectra compare more favorably in the concrete than in the MPC, Fig. 7-17. The further neutrons travel away from the fuel region, the more the energy spectra will agree, since the helium and detailed models differ in the fuel region only. For a majority of the concrete region, the analytically calculated values for S_{ϕ,Σ_a} overpredict the sensitivities of the detailed model and the

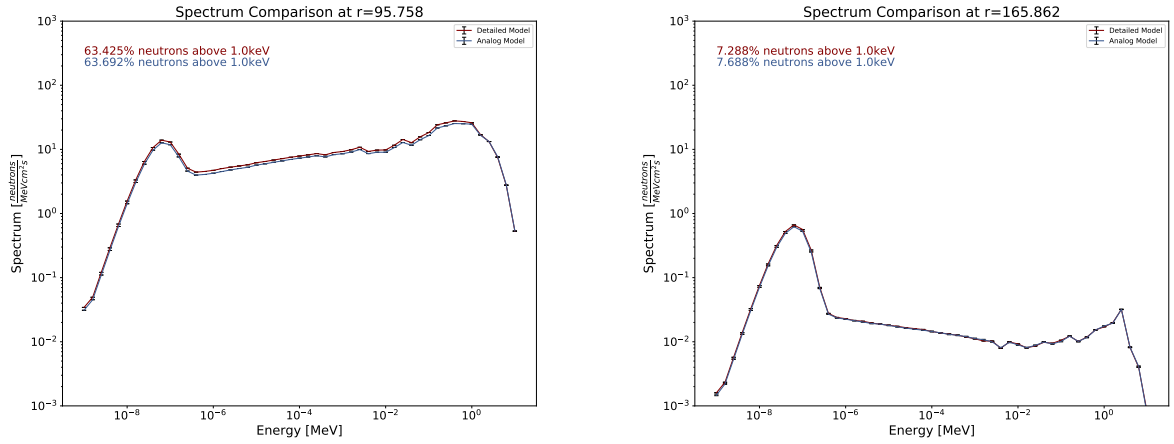

(a) (b)

Figure 7-17. A comparison of the neutron spectrum between the detailed model (red) and helium model (blue) at A) near the inner surface of the concrete annulus (r = 95.758 cm) and B) near the outer surface of the concrete annulus (r = 165.862 cm)

analytically calculated values of S_{ϕ,Σ_s} underpredict those from the detailed model. The discrepancy is a result of using only two energy groups in the analytic model. Similar to the other material regions, a version of the helium model is developed in MCNP using 30 group cross section data rather than continuous energy cross section data, where Fig. 7-18 show the continuous energy, two energy group, and 30 energy group cross section values. Thirty energy groups better capture the structure (i.e., resonances) of the continuous energy cross section data than the two energy group data provided in Tab. 4-3. The results of the sensitivity analysis performed on the 30-group helium model are displayed in Fig. 7-19. The values of the SC's from the 30-group model compare favorably to those from the detailed model, confirming that the previous discrepancies between the SC's from the analytic and detailed models are a result of using too few energy groups.

Both the values of S_{ϕ,Σ_s} and S_{ϕ,Σ_a} from the analytic models decrease in magnitude near the material boundary at r = 166.37 cm. As previously discussed, this phenomenon is a result of applying boundary values and are artifacts of analytic modeling. For this reason, these trends are not seen in the computationally derived SC's. In fact, the SC's

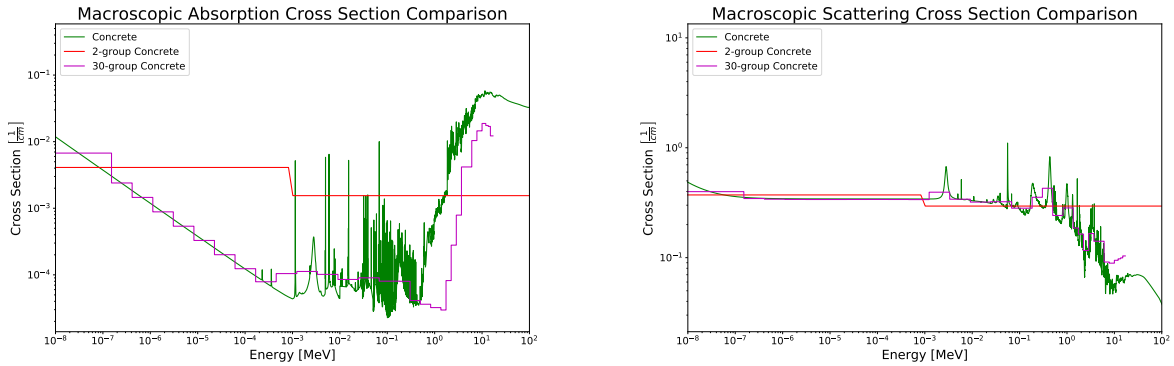

(a) (b)

Figure 7-18. A) The absorption cross section and B) the scattering cross section in the concrete annulus. The dark blue line is the continuous energy cross section, the 30-group cross section values (purple) better capture the shape of the continuous energy cross section values than the 2-group cross section values (red), which are used in the analytic models.

pertaining to the scattering cross section in both the detailed and helium models increase at the boundary. Neutrons at this location are able to "see" the exterior of the cask, as the carbon steel thickness immediately exterior to the concrete region is 1.9 cm and the MFP for thermal neutrons in the carbon steel region is around 1 cm, Fig. 2-18. The values of S_{ϕ,Σ_a} from the computational models flatten out near the boundary of the concrete in response to the increased leakage occurring following the previously identified relationship between the two loss mechanisms.

Figure 7-20 shows the absolute values of the SC's. In the detailed model, Σ_a and Σ_s have similar SC's for the initial 9 cm of the concrete annulus with Σ_a generally being the most important value. However, after 9 cm, Σ_s is the most important parameter due to the amount of scattering which causes thermalization in the detailed model. This same behavior occurs in the analytic model however, Σ_a is the most important parameter for the initial 20 cm. While these two locations are separated by 11 cm, the analytic models capture the general shape of the SC's from the detailed model within 50% relative error between $r = 104.25$ cm and $r = 162.75$ cm.

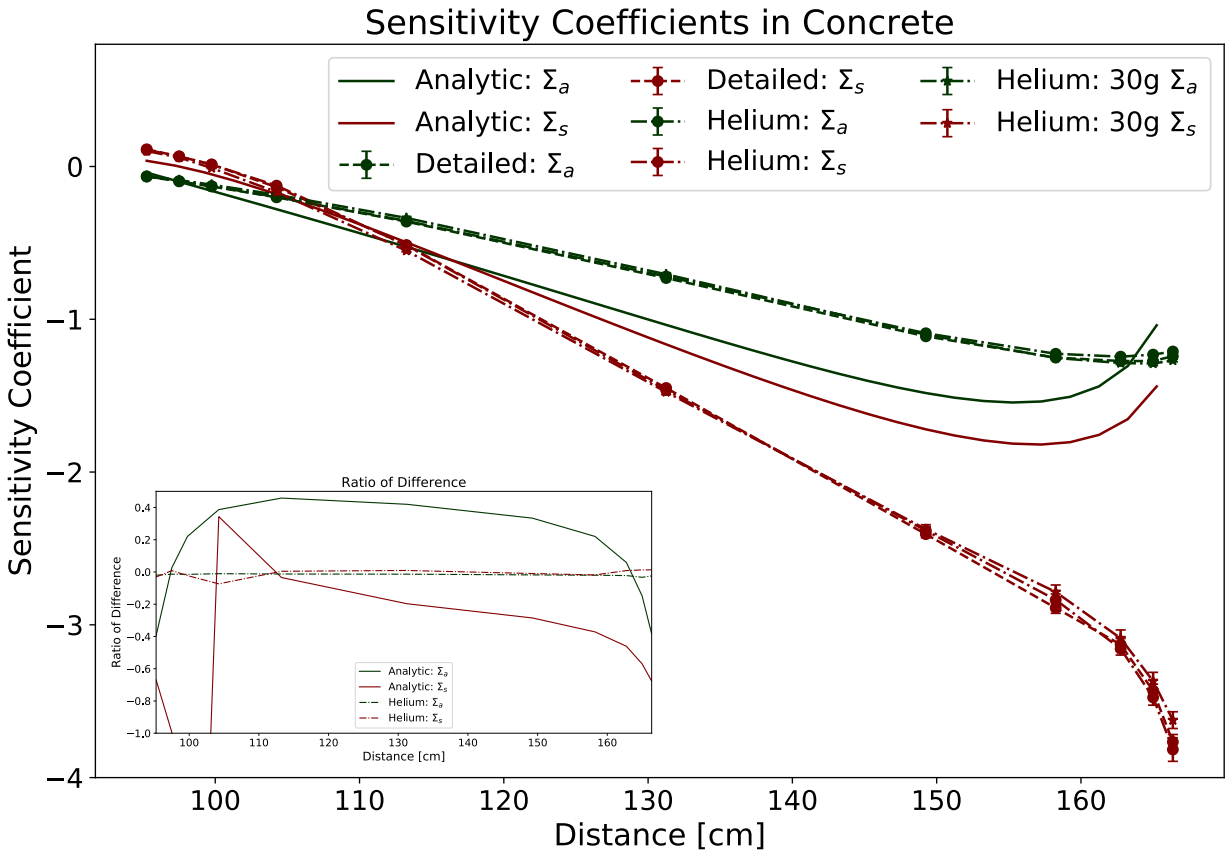

Figure 7-19. The sensitivity coefficients for Σ_a (green) and Σ_s (red) from the detailed, helium, and analytic model. The models agree that the scattering cross section is the most important parameter over most of the concrete annulus due to the amount of thermalization occurring in the concrete.

7.1.4 Sensitivity Analysis of the Carbon Steel

The final material to be analyzed is the carbon steel shell, which is the outermost layer of the cask. The carbon steel shell is thin (1.9 cm) compared to the MFP for thermal neutrons (1 cm, Fig. 2-18), as the neutron flux is predominately thermal in the carbon steel (Figs. 2-19a and 2-19b). Further, there is no energy shift occurring in the shell and the angular distribution is predominately forward peaked, resulting from the the cask being surrounded by a high MFP material (air). The nominal values of the input parameters used to calculate the SC's in the carbon steel shell are given in Tab. 4-5.

Figure 7-21 shows the values of the analytically determined SC's pertaining to the absorption cross section in carbon steel calculated from the solutions to Eqns. 3-61-3-64.

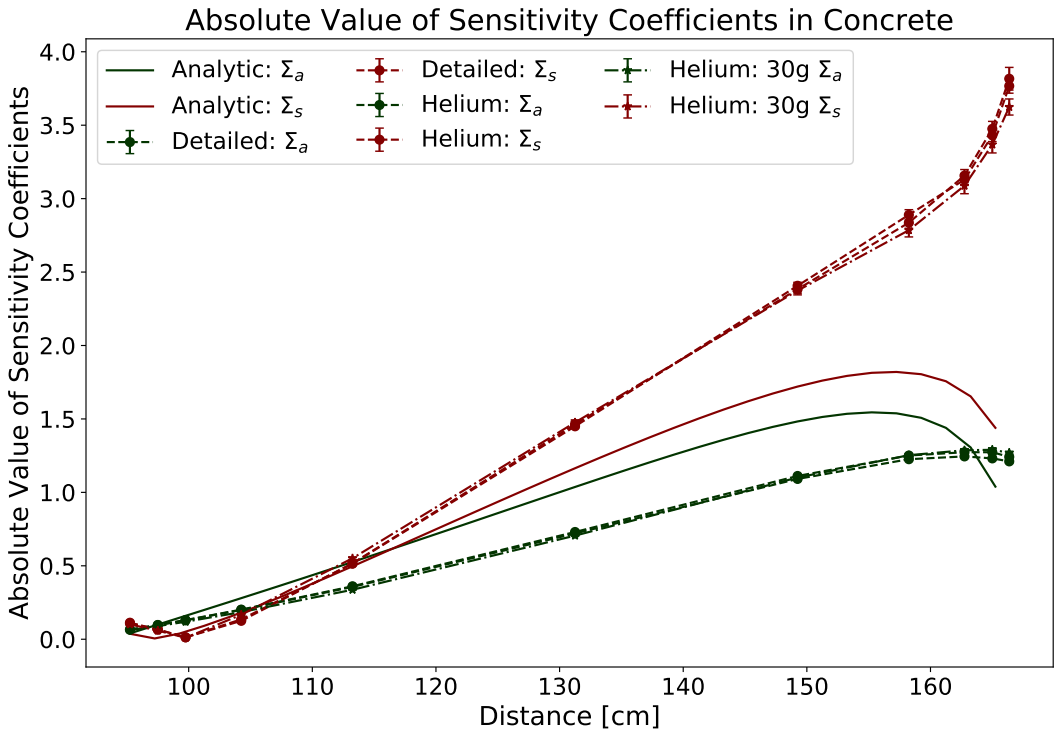

Figure 7-20. The absolute values of the sensitivity coefficients from the detailed model, helium model, and analytic model.

The flux in the carbon steel is mainly thermal and, as a result, the values of S_{ϕ,Σ_a^1} is nearly zero through the thickness of the carbon steel. The values of S_{ϕ,Σ_a^2}, and therefore S_{ϕ,Σ_a}, increase through the cask as thermal neutrons are absorbed through the steel. S_{ϕ,Σ_a} does not decrease in magnitude near the boundary at $r = 168.275$ cm, since the boundary values applied at this location are not continuous flux boundary values. Rather, a non-reentrant condition was applied to the left-moving partial fluxes, ϕ_2^1 and ϕ_2^2. Further, there is no noticeable relationship between the two types of loss mechanisms as a result of these boundary values.

The values of S_{ϕ,Σ_s} initially have positive values for the first 0.5 cm of the carbon steel thickness before having negative values for the remainder of the material thickness, as shown in Fig. 7-22. This behavior has been observed in the analytically calculated values of S_{ϕ,Σ_s} in each previously discussed material. The positive values of $S_{\phi,\Sigma_s^{2\to2}}$ indicate

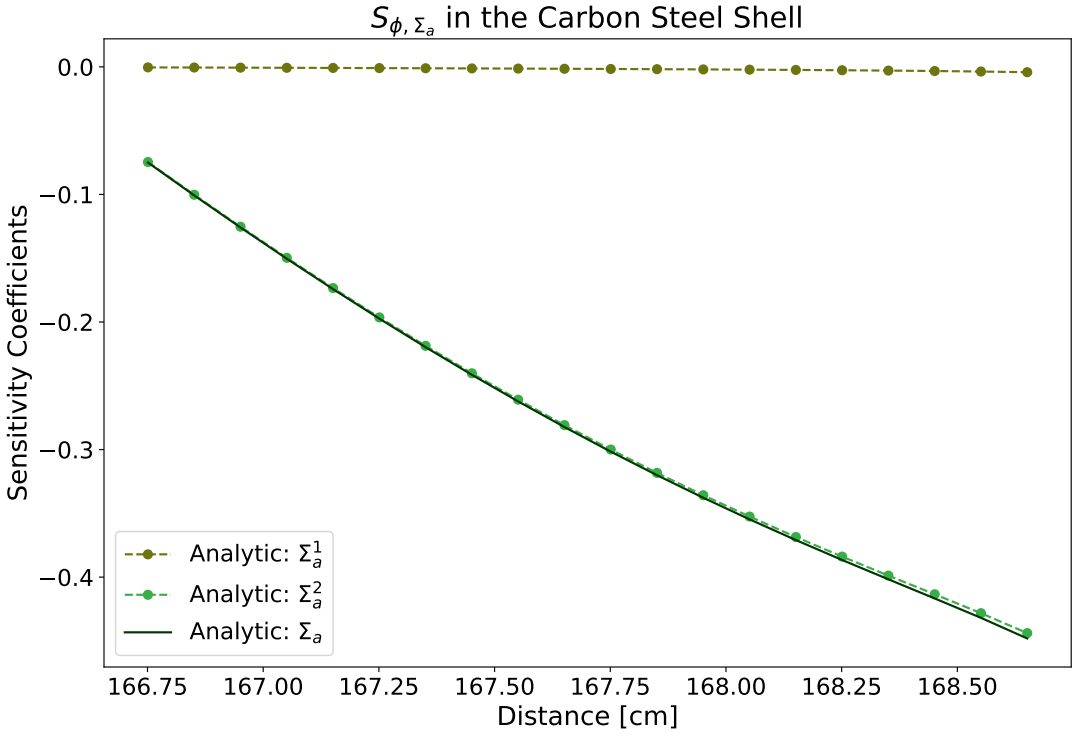

Figure 7-21. S_{ϕ,Σ_a^1} (dark green) essentially has a zero value through the carbon steel shell thickness resulting from the small population of fast neutrons compared to the thermal neutron population. Then, S_{ϕ,Σ_a} (solid) is nearly equivalent to S_{ϕ,Σ_a^2} (light green).

that scattering is acting to preserve the thermal flux for the first 0.5 cm before leakage dominates scattering physics for the remainder of the shell thickness. In the carbon steel shell, the thermal flux accounts for approximately 90% of the total flux. The physics determined by the $\Sigma_s^{1\to1}$ and $\Sigma_s^{1\to2}$ values is proportional to the value of the fast flux, which explains the reason $S_{\phi,\Sigma_s^{1\to1}}$ and $S_{\phi,\Sigma_s^{1\to2}}$ are nearly zero for the entire thickness of the carbon steel. Finally, there is an increase in the magnitude of $S_{\phi,\Sigma_s^{1\to1}}$ and $S_{\phi,\Sigma_s^{2\to2}}$ near the boundary at $r = 168.275$ cm. This occurs as a result of the chosen boundary values. The non-reentrant condition only applies to the left-moving flux equations, Eqns. 3-60 and 3-60. Meaning, the flux values for ϕ_1^1 and ϕ_1^2 are determined entirely by the material properties. The boundary values at $r = 166.37$ cm and the right-moving flux leaks

strongly out of the cask as there is no material present past $r = 168.275$ cm. Since there are no constraints on the right moving flux at $r = 168.275$ cm, there is no relationship between the leakage and absorption loss mechanism, because the flux at $r = 168.275$ cm is not pinned to a value as in the other materials.

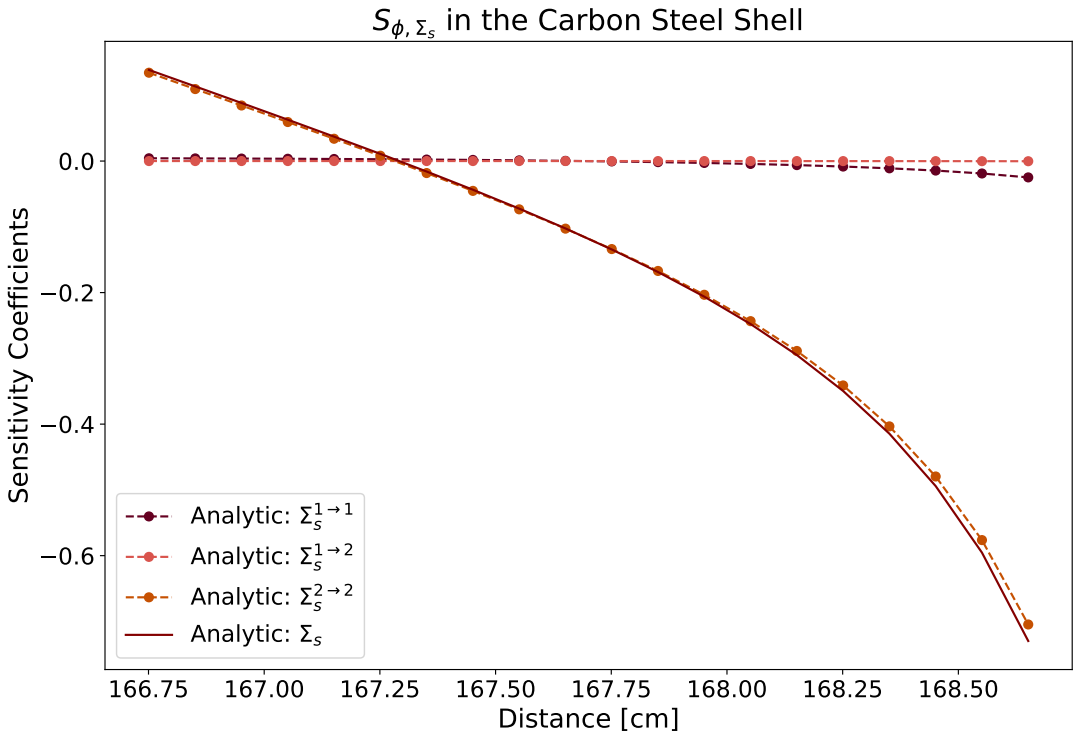

Figure 7-22. The neutron flux in the carbon steel shell is 90% thermal. Meaning, $S_{\phi,\Sigma_s^{2\to2}}$ (red-orange) controls the values of S_{ϕ,Σ_s} (solid). The low populations of fast neutrons leads to nearly zero values of $S_{\phi,\Sigma_s^{1\to1}}$ (dark red) and $S_{\phi,\Sigma_s^{1\to2}}$ (pink).

Figure 7-23 shows S_{ϕ,μ_1} and S_{ϕ,μ_2}. The values of S_{ϕ,μ_1} are greater than S_{ϕ,μ_2}. The boundary values applied to the right-moving flux is a continuous flux condition at the interface between the concrete and carbon steel. Without having a material outside of the carbon steel shell, the values of S_{ϕ,μ_1} increase linearly. The boundary values applied to the left moving flux are different from those applied elsewhere in the cask. The left-directed fluxes have a non-reentrant boundary value applied, which presumably causes the shape of

the curve in Fig. 7-23. Further analysis is required to identify the physics which causes the behavior of S_{ϕ,μ_1} and S_{ϕ,μ_2}.

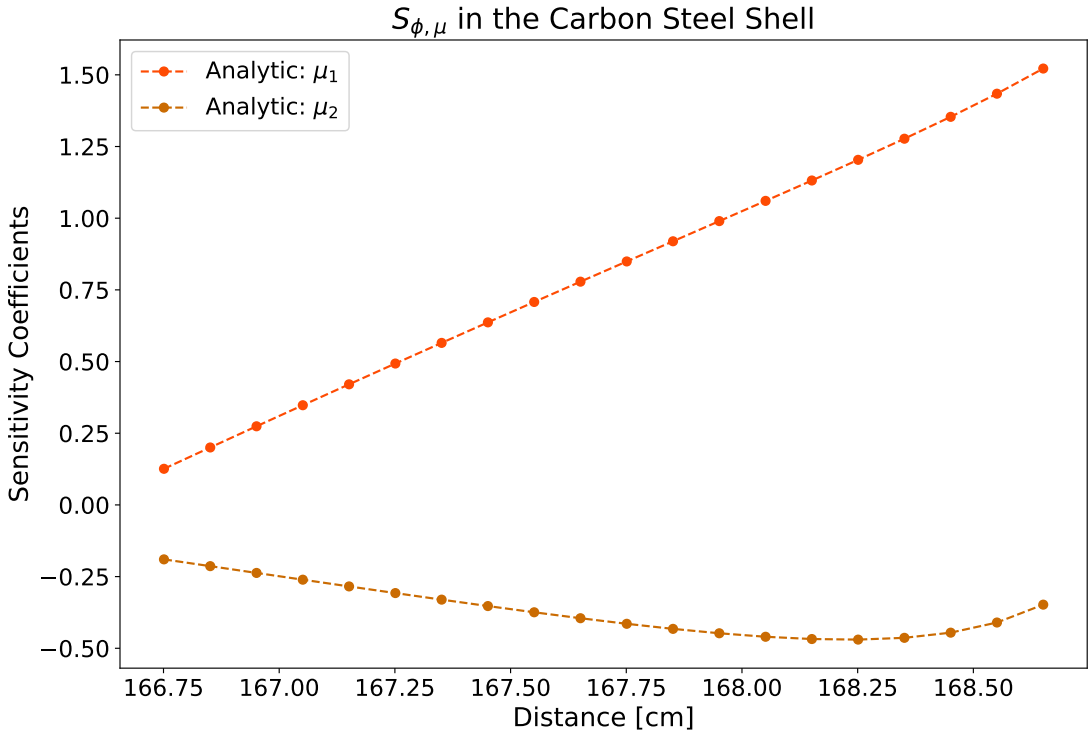

Figure 7-23. The values of the SC's of the directions, μ values. S_{ϕ,μ_1} have higher values than S_{ϕ,μ_2} across the thickness of carbon steel shell.

Figure 7-24 shows the SC's pertaining to the boundary value values. The values of the SC's corresponding to the boundary values of ϕ_2^1 and ϕ_2^2 are identically zero, since the unperturbed value of the left-moving flux at $r = 168.275$ cm is zero (a result from choosing a non-reentrant boundary value). The values of the SC's for ϕ_1^2 are the most important since the thermal flux is approximately 90% of the total flux through the carbon steel and slightly decreases through the carbon steel thickness as the thermal flux decreases. The values of the SC's for the boundary values of ϕ_1^1 slightly increase over the cask thickness are a result of the increase in the contribution of the fast flux to the total flux. Figure 2-19 shows the fast flux accounts for approximately 7% of the total flux entering the carbon steel shell and nearly 15% of the total flux exiting the carbon steel shell in the detailed

model. Initially, this is attributed to a small number of fast neutrons being born through nuclear reactions. However, the slight increase in the SC's of the boundary value for ϕ_1^1 reflects the slight increase in the fast flux, which is determined to be caused by extra absorption occurring in the thermal flux causing a reduction in the total flux. The effect caused by thermal neutrons being preferentially absorbed as compared to fast neutron would increase the ratio of the fast flux to total flux.

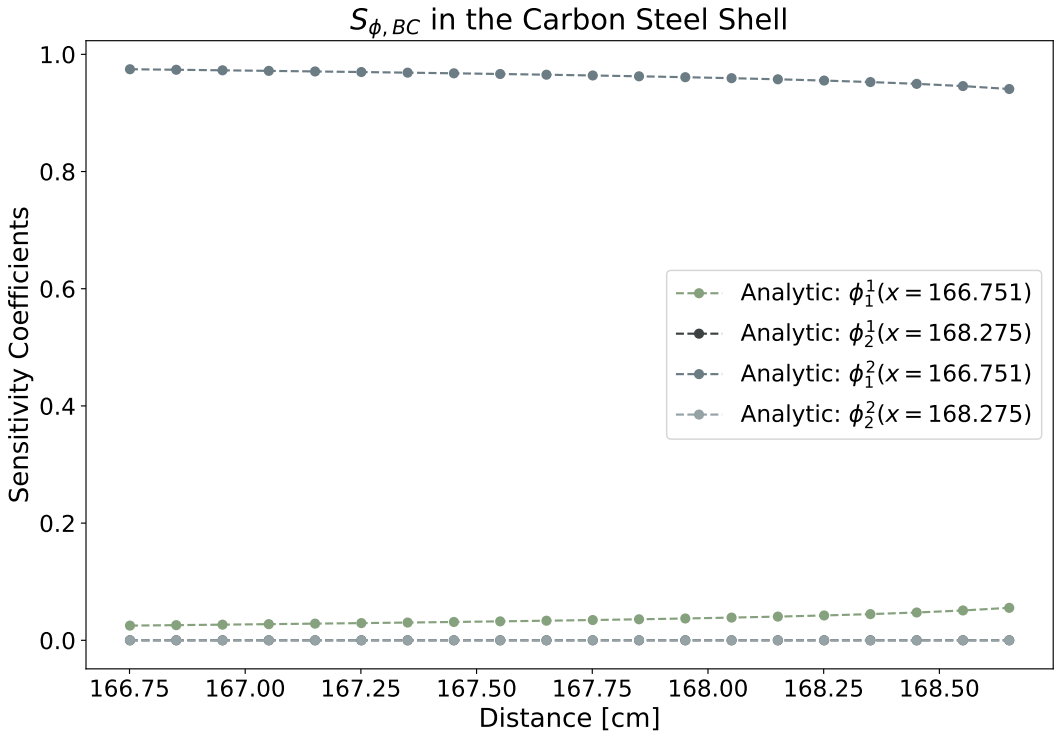

Figure 7-24. The non-reentrant boundary value causes the values of the SC's pertaining to the boundary values for ϕ_2^1 (black) and ϕ_2^2 (light grey) to evaluate to zero. However, the boundary values applied to the right-moving fluxes, ϕ_1^1 (green-grey) and ϕ_1^2 (dark grey), are non-zero and the boundary values have importances related to the intensities of the fast and thermal fluxes respectively.

The previous analysis helped to identify physics occurring in the carbon steel shell using simple analytic models. However, by first identifying how certain physics causes causes changes to the neutron flux, the SC's of the detailed model can be analyzed with

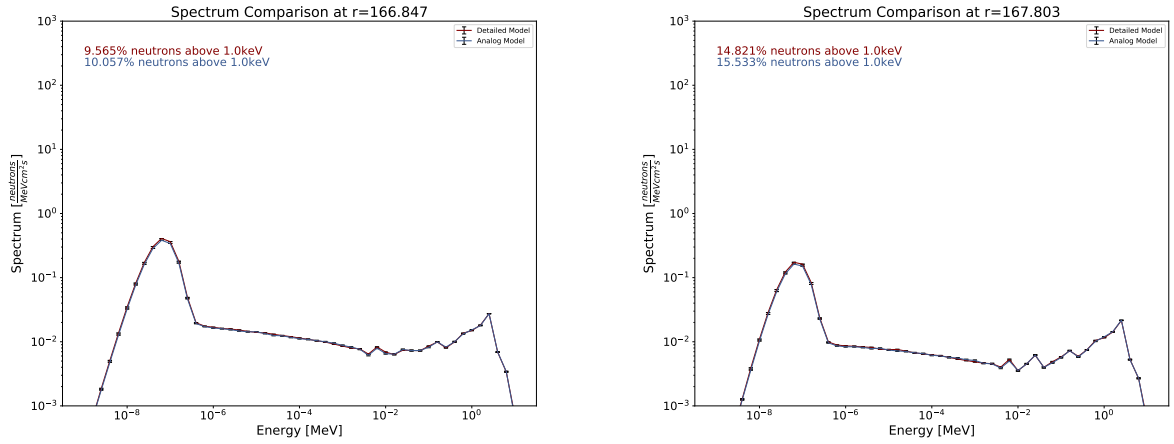

(a) (b)

Figure 7-25. A comparison of the neutron spectrum between the detailed model (red) and helium model (blue) at A) near the inner surface of the carbon steel shell (r = 166.847 cm) and B) near the outer surface of the carbon steel shell (r = 167.803 cm)

more depth through comparison with the analog models. The comparison of the SC's is shown in Fig. 7-27. The helium model is capturing the results form the sensitivity analysis within 6% for S_{ϕ,Σ_s} away from the location of the root of the detailed model's S_{ϕ,Σ_s}, and 2.38% for S_{ϕ,Σ_a}. These discrepancies are attributed to the small differences between the energy spectra of the detailed and helium models, seen in Fig. 7-25. The analytic models underpredict both S_{ϕ,Σ_a} and S_{ϕ,Σ_s} by a maximum of 64.168% and 83.482%, respectfully, away from the root location. The error of S_{ϕ,Σ_s} goes to a value of 618% at the location the root of S_{ϕ,Σ_s} for the detailed model. Again, this is a result of S_{ϕ,Σ_s} from the detailed model being close to zero, leading to high values of relative error. The overall shape of the SC's from the detailed model is captured by the analytic models. The SC's from both the analog and computational models show the values of S_{ϕ,Σ_s} increasing near r = 187.894 cm. This is caused by an increase in neutrons leaking out of the carbon steel shell. The difference between the SC's from the detailed and analytic models is attributed to an unrefined energy mesh, shown through the comparison of the detailed model and previously discussed 30-group model in Fig. 7-27. A comparison of the continuous energy,

two energy group, and 30 energy group models is provided in Fig. 7-26, which shows that the 30-group cross section data better represents the structure of the continuous energy cross section data than when using two energy groups.

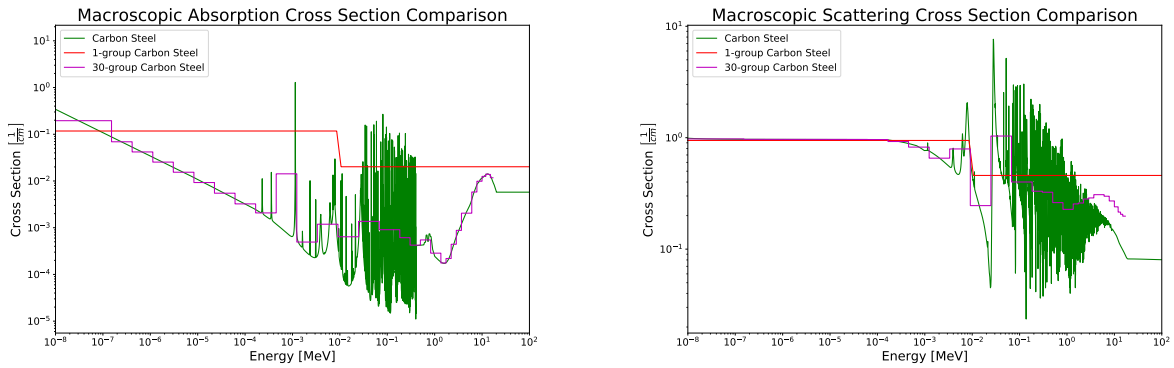

(a) (b)

Figure 7-26. A) The absorption cross section and B) the scattering cross section in the carbon steel shell. The dark blue line is the continuous energy cross section, the 30-group cross section values (purple) better capture the shape of the continuous energy cross section values than the 2-group cross section values (red), which are used in the analytic models.

Figure 7-28 compares the absolute values of the SC's in the carbon steel shell. In the computational models, Σ_s is the most important parameter for nearly the first 0.38 cm before Σ_a becomes the most important parameter. A common theme which occurs in the materials is that Σ_a tends to be the most important parameter even though the materials are mostly scattering, demonstrating that unless a material is almost entirely dominated by scattering, a smaller magnitude parameter may be more important in properly modeling physics. As a result of under-representing the SC's, the analytic results have two intersection points. In the analytic models, Σ_s is the most important parameter from $r = 166.37$ cm to $r = 166.47$ cm and again from $r = 167.97$ cm to $r = 168.275$ cm. From $r = 166.47$ cm to $r = 167.97$ cm, Σ_a is the most important parameter.

7.2 Summary

The previous sensitivity analysis of the detailed and analog models and comparison of the results helps to identify, characterize, and importance rank processes occurring in

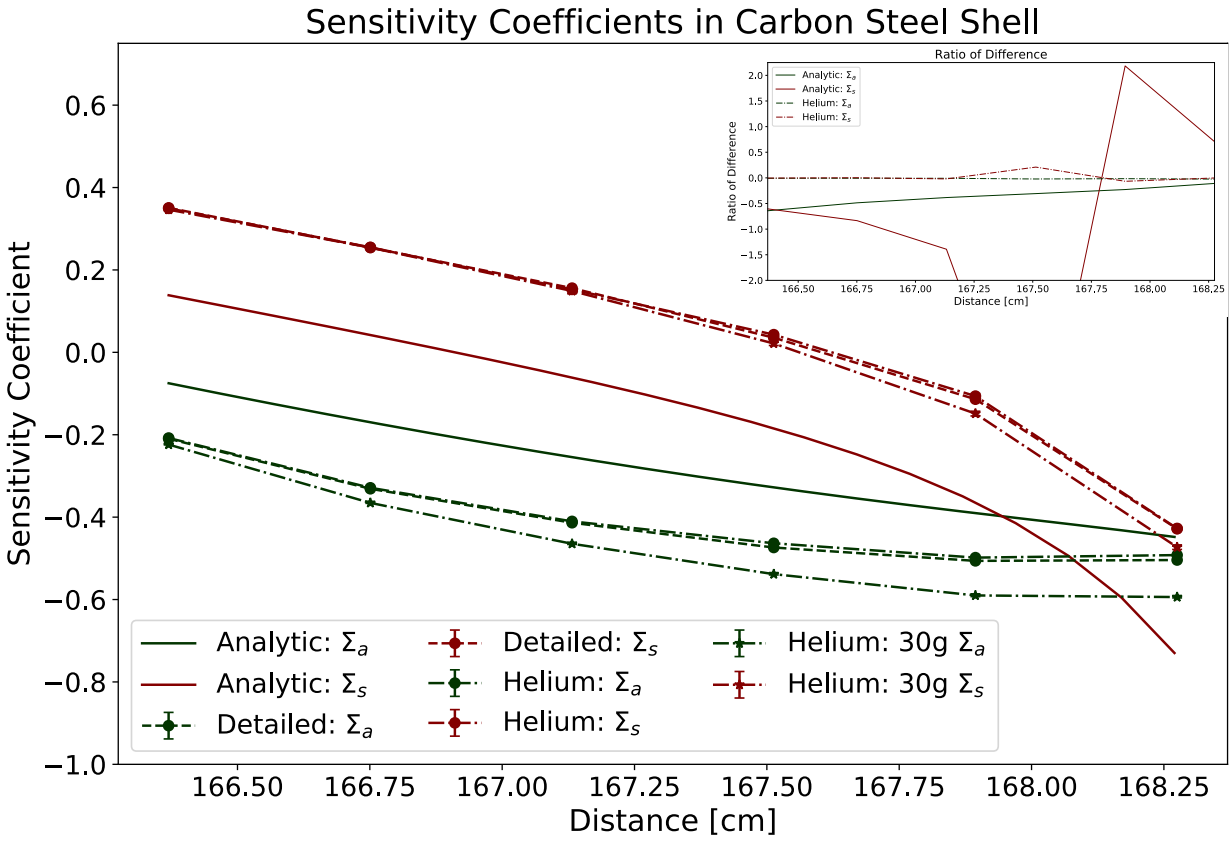

Figure 7-27. A comparison of the SC values between the detailed model (dotted), helium model (dot-dashed), and analytic model (solid). The 30-group model (dot-dashed with star markers) is also shown to see the effects of using a larger number of energy groups.

the spent fuel cask. There are some behaviors that are persistent through the materials analyzed:

- S_{ϕ,Σ_a} calculated in from the analytic models is generally controlled by the energy group where the value of Σ_a is largest.
- S_{ϕ,Σ_s} as determined in the analytic models is controlled by the in-group scattering cross section value where the flux is most intense.
- S_{ϕ,Σ_s} from the analytic models initially has positive values before becoming negative (moving left to right through the material), meaning scattering preserves the flux as it enters a material, before loss physics occurs through leakage and indirect absorption (through thermalization).
- Refining the energy grid better captures the first derivative information of the detailed model, as seen through the SC's from the 30 energy group models generally

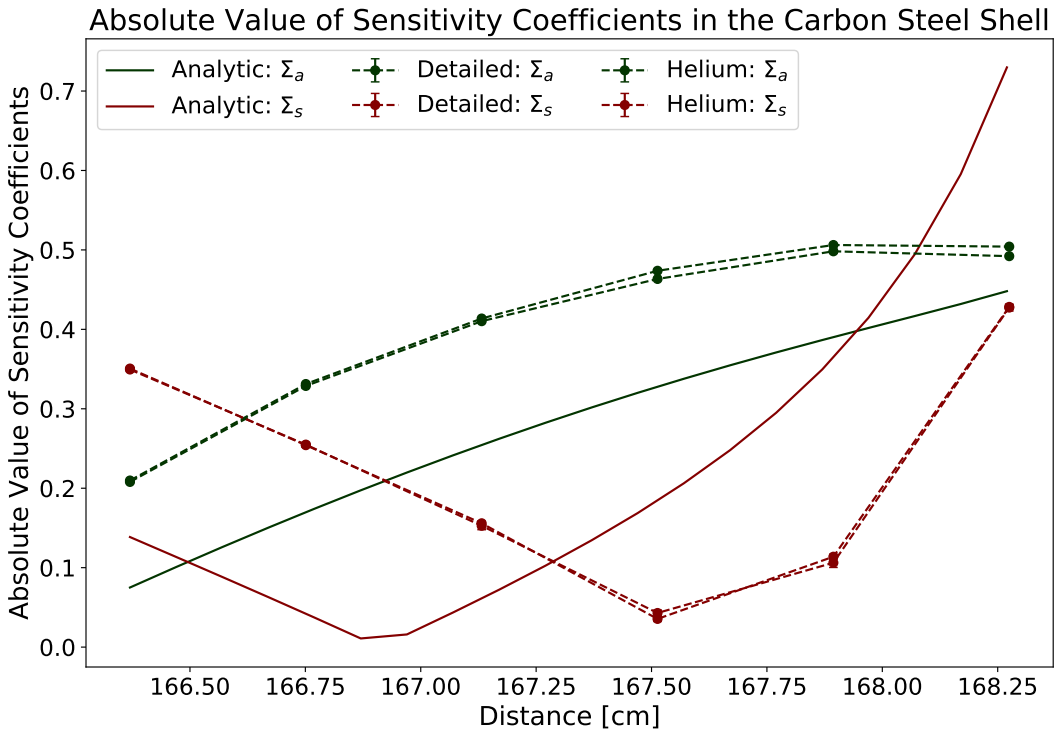

Figure 7-28. The absolute values of the sensitivity coefficients from the detailed model, helium model, and analytic model.

showing better agreement with the SC's of the detailed model than between the SC's of the two energy group model and the detailed model.

- Σ_a generally is the most important cross section value even though the materials are mostly scattering.

Given the previous analysis, future work should include an energy grid refinement study to determine an effective grid number for capturing the sensitivity information to some prescribed level of fidelity.

CHAPTER 8
CONCLUSIONS

Analytical models are useful tools for enhancing traditional analysis from the extensive computational modeling used in nuclear engineering. Using reduced complexity analytic and computational models to analyze the simulation results of a high-fidelity computational model allows for the quantification of effects of any assumptions invoked when developing the latter model. Ensuring important physics are preserved in the course of conducting simulations increases the likelihood of correct results. This work exemplified this notion through a process referred to as "simulation results assessment," or more simply "results assessment." As a demonstration, this work includes post-simulation analysis of a detailed MCNP model of a HI-STORM 100 spent nuclear fuel cask. A series of reduced analytic and computational models are developed and are used to identify the physics which causes features in the neutron flux spatial distribution as calculated by the detailed model. In the HI-STORM 100 model, the stainless steel basket, neutron absorbing pads, and helium annulus around the fuel cells are important physical components that need to be preserved in modeling. Retaining the individual fuel pin structure is found to be less important than broadly capturing the lumped material properties inside the individual fuel cells. These results are corroborated using the cruciform model, which appears to capture the physics relevant to the neutron flux spatial distribution in the detailed model beyond the 90% level. The major features of the neutron flux spatial distribution simulated by the detailed model are expected to be correct since the this model preserves material fuel properties and the geometric structure of the neutron absorbing pads and helium annulus. Further, the multigroup discrete ordinates equations compares to the neutron flux from the detailed model within 15% in the MPC, concrete, and carbon steel shell.

Further, the previous analysis is extended with a results assessment through sensitivity analysis. Performing sensitivity analysis reveals the underlying mathematical

structure inherent to a scenario, leading to an even deeper understanding of the salient physics. Incorporating a study of appropriate analytical models acts as part of a broader program of study which underpins the results from increasingly complicated computational science simulations. Further, the addition of analytically computed sensitivity information proves informative as a guide in interpreting, understanding, and rigorizing results of existing and future computational studies.

In the spirit of established analytical and computational model comparison techniques and outcomes the various analytical results, examples, and commentary provided in Chpts. 4, 6, and 7 represent an example of how an incorporated comparison with analog models and analytic sensitivity analysis studies can be used to set up, precondition, and eventually inform or compare against a complementary computational sensitivity analysis study. Within this conceptual strategy, and against the backdrop of the detailed MCNP computational model of a HI-STORM 100 spent nuclear fuel storage cask, the results appearing herein exemplify a more general recipe justifying the development and execution of local sensitivity analysis formalisms within the context of surrogate analytical models:

1. Establish a high-fidelity computational model, and extract key features of the simulation output.
2. Based on these key features, establish a reduced-fidelity model of the same underlying scenario; preferably this model is amenable to analytical or semi-analytical solution.
3. Compare results from the analytic or semi-analytic study with results from the computational model to verify appropriateness of reduced-fidelity model. Here, comparisons are conducted by determining the relative error between the models.
4. Execute a sensitivity analysis study on the reduced-fidelity model; again, preferably this study will be amenable to analytical or semi-analytical evaluation.

5. Scenario dependent evaluation of the analytical or semi-analytical sensitivity structure requires nominal input parameters; these must also be consistent with the key features extracted from the high-fidelity computational model.
6. Establish scenario-dependent sensitivity trends and input parameter importance ranking to precondition additional high-fidelity computational sensitivity analysis studies.

The aforementioned results assessment methodology is exemplified through the enhanced analysis of the detailed cask MCNP model, which is superficially analyzed in Chapter 2. Chapter 4 uses analytic and reduced-fidelity models to identify which physical processes are influencing the neutron flux at different locations within the fuel cask.

- Developing the homogenous model demonstrates that some of the geometric details are capable of being reduced and the fuel region can be treated as a single, homogenous material. Using a homogeneous material motivates the use of the diffusion approximation, Eqn. 3-85, as the radial thickness of the homogenous fuel is large enough to allow for neutron diffusion. Even though the homogenous model and diffusion approximation capture the general flat shape of the neutron flux from the detailed model, the analog models did not capture a level-off region occurring near the outer edge of the fuel region. Nor did the analog models capture multiple localized depressions in the neutron flux, thus motivating further refinement of these simplified models.

- The insufficiencies in the previous analog models (i.e., the models did not capture the neutron flux leveling-off at the outer radius of the fuel region) lead to the addition of a helium streaming region to the reduced-fidelity MCNP and analytic models. Identifying the necessity of neutron streaming regions in the analogous models indicates the importance of including including a neutron streaming region inside of the fuel region.

- While the helium model and solution to the diffusion approximation, Eqn. 4-5, modified with a streaming region compare more favorably to the detailed model than the homogenous and original diffusion approximation, none of the analog models capture the three small depressions occurring in the neutron flux predicted by the detailed model. Therefore, a 1-D array model is developed in MCNP which investigated the effects of the the stainless steel basket and neutron absorbing pads which are located inside the MPC. Through this analysis, the stainless steel basket and neutron absorbing pads cause the neutron flux to decrease 1-2% at the locations of the stainless steel basket and neutron absorbing pads. Identifying the causes

of the depressions demonstrate the importance of preserving the structure of the stainless steel basket and neutron absorbing pads in the detailed model.

- An asymmetry in the azimuthal neutron flux is identified during the analysis of the detailed model. The asymmetry is a result of the asymmetric loading of neutron absorbing pads in the fuel region. This conclusion further reinforces the importance of accounting for the neutron absorbing pads in the analysis of the spent fuel cask.

- The conclusions of the previous analyses show which geometric details can be homogenized and which need to be retained. That is, individual fuel pins can be homogenized into a single material as long as material properties are accounted for though homogenization. However, the stainless steel basket and neutron absorbing pads need to be retained to accurately model the spent fuel cask. Therefore, the cruciform model is developed to test these conclusions. The cruciform model captures the physics occurring in the fuel region within 7%, and corroborating the results from the previous analyses.

- The multigroup discrete ordinates equations, Eqns. 3-61-3-64, are used to model the neutron flux in the MPC, concrete, and carbon steel shell. In each of these materials, the analytic model in the MPC and concrete have relative error values less than 15% throughout each material. The highest relative error values given by the analytic models outside of the fuel region are seen in the carbon steel shell, a combined effect from the small magnitude of the neutron flux simulated in the detailed model and the analytic models underpredicting neutron loss mechanisms.

Identifying the physical causes which generate features in the simulated neutron flux from the detailed model aids in corroborating these results, an irreplaceable practice when experimental data is lacking. Further, the results assessment methodology acts complementary to existing validation techniques, which rely on experimental data to compare against simulation results. Comparing simulation results with foundational theory reinforces the validity of simulation results.

The results from the detailed model are further rigorized with the addition of results assessment through sensitivity analysis. Chapter 7 conducts a sensitivity analysis on the analytic models which are used throughout the cask. This analysis concludes:

- The sensitivity coefficients of input parameters in the modified diffusion approximation (i.e., Eqn. 4-5 with a neutron free-streaming region applied) show that Σ_a is the most important term in through the fuel region, signifying the importance of loss mechanisms in a sub-critical system.

- Even though the MPC is scattering dominated, 96.638% for fast neutrons and 86.583% for thermal neutrons, Σ_a is the most important input parameter occurring in both the analytic and computational MPC models. Again, using 30 energy groups to model the cross section data yields better agreement between the SC's in the 30-group helium and detailed models than between the two energy group analytic model and detailed model. This is a result of the 30 group cross section data better capturing resonances in the cross section data than the two energy group models, Fig. 7-10.

- The concrete region has a scattering ratio of 99.452% for fast neutrons and 98.910% for thermal neutrons. The high scattering ratios occurring in the concrete annulus leads to the high importance of Σ_s as compared to Σ_a, Fig. 7-19. This is the only material region where scattering has a higher importance than absorption, even though the other materials are also scattering dominated. This result shows how a smaller magnitude parameter may be more important when properly modeling physics.

- The neutron flux in the carbon steel shell has seen a shift in energy, a result of thermalization occurring in the concrete annulus. This leads to increased importance of thermal energy scattering cross section being observed in the carbon steel shell. This effect is best observed in Fig. 7-22, which shows S_{ϕ,Σ_s} in the carbon steel shell. In fact, throughout the MPC, concrete, and carbon steel shell, the SC's pertaining to the total scattering cross section are dominated by the energy group pertaining to the partial flux with the highest magnitude.

- The scattering cross section alone is generally seen to act as a "pass-through" mechanism. That is, scattering does not act to remove neutrons in the manner absorption does, but rather, scattering "pushes" the neutrons through a material, either preserving the flux or causing leakage.

- The group-wise absorption cross section contributing the most importance to the SC of the total absorption cross section is always the thermal group absorption cross section in the MPC, concrete annulus, and carbon steel shell. This occurs because the thermal absorption cross section always has a larger value than the fast neutron absorption cross section. Therefore, SC's pertaining to the absorption cross section are dominated by the group-wise absorption cross section value with the largest value. Further, the absorption cross section generally has higher importance values than the scattering cross section values as the spent fuel cask is a sub-critical system, meaning loss mechanisms have more importance than gain mechanisms in the cask.

- Using a monoenergetic or two energy group model is shown to misrepresent the SC's in each material of the spent fuel cask, as the one and two energy group cross sections underrepresent the fine structure of the cross sections. Therefore, a version of the helium model is developed using 30 energy group cross section data. Using more energy groups better captures the fine structure of the continuous energy cross

section data. Performing a sensitivity analysis on the 30-group helium model shows better agreement between the sensitivity coefficients of the 30-group model and the detailed model than the monoenergetic and two group analytic models and the detailed model. This conclusion reinforces the concept that the analytic models use too few energy groups to reproduce sensitivity information of the detailed model. While the analytic models may require more energy groups to adequately capture the sensitivity information of the detailed model, explaining the reasons for the discrepancies between the analytic models and the detailed model provide insight into how the energy dependence in the cross sections influences the neutron flux.

- There is a relationship between loss mechanisms occurring in the cask (namely leakage and absorption), which is observed in the fuel region, the MPC, the concrete annulus, and the carbon steel shell. As the importance of leakage physics increases, the importance of absorption decreases. Further, this relationship is a result of pinning the neutron flux to a specific value at the interface between each material, through the boundary conditions. Taking the flux to have specific values at the material interfaces means only a specific number of neutrons can be lost inside a single material, and those neutrons must be shared between absorption and leakage. Therefore, as one mechanism causes more neutrons to be lost, the other mechanism decreases in response.

As the fuel cask is a sub-critical system, loss mechanisms are seen to have higher sensitivities than gain mechanisms through the entire cask. Presumably, if this analysis were to be conducted on a critical or super-critical system, the sensitivities of loss mechanisms would be equal to or less than gain mechanisms respectively. The extension of an analytic sensitivity analysis helps identify the causes of physics driving features in the SC's pertaining to Σ_a and Σ_s in the analytic models. From these conclusions, the analysis of the S_{ϕ,Σ_a} and S_{ϕ,Σ_s} (or S_{ϕ,Σ_c}, S_{ϕ,Σ_f}, and S_{ϕ,Σ_s}in the fuel region) from the detailed model. Further, the differences between the SC's pertaining to Σ_a and Σ_s (or Σ_c, Σ_f and Σ_s in the fuel) are attributed to the two energy group model (or monoenergetic model in the fuel region) not representing resonance structure in the cross section data. Therefore, a version of the helium model is developed using 30 energy group cross section data in MCNP, and corresponding SC's are calculated from this model. The 30 energy group data is shown to have better agreement with the continuous energy MCNP models (with the exception of S_{ϕ,Σ_f} in the fuel region), a result of the 30 energy group cross section data better capturing resonance structure appearing in the continuous energy cross section

data. Finally, the analytic sensitivity analysis extends the scope of the sensitivity analysis to input parameters which are not directly computationally available for a computational sensitivity analysis (i.e., S, r_b, and $\bar{\nu}$ using the current capabilities of MCNP).

More broadly, sensitivity analysis results are capable of guiding future research to reduce uncertainty in the most impactful input parameters inherent to a given scenario of interest. Further, by identifying the most impactful parameters a code user can identify if any simplifications were made when developing an input which would affect the results. From these conclusions, a user could either change the input to address any insufficiencies or explain the insufficiencies and identify pathways for improvement. Either decision results in a more thorough examination of the problem, which is ultimately the goal of any scientific study.

Further, the analytical results provided in this work are intended to be informative of complementary studies performed using computational tools. A process exemplified in Chp. 7, perhaps the most meaningful application of this work is the performance of a purely computational, local sensitivity analysis study in the context of both the detailed and helium models, using MNCP. In such an activity, the results of this work serve two principal purposes:

1. The analytical results are used to guide more expensive (in terms of time or resources) computational studies, by identifying input parameters that are either particularly important or rapidly variable at some physical location within a fuel cask geometry or physics model, or somehow otherwise impactful.
2. The analytical results are directly compared to computationally derived, local sensitivity coefficient information, thus further illuminating not only the possible sufficiency and limitations of various analytical models, but also the most important physics occurring within neutron transport simulation of spent fuel cask scenarios.

8.1 Summary of Chapters

Chapters 2,4, 6, and 7 exemplify the results assessment methodology in its application to the HI-STORM 100 spent fuel cask and complimentary analytic models.

Chapter 1 motivates the application of what is termed the "results assessment" methodology to spent fuel casks, and more specifically the HI-STORM 100. While spent fuel casks have been the center of much research within the nuclear sciences and engineering communities, validation activities are limited, as experimental data is sparse. The results assessment methodology is designed to work complimentary to existing validation methods to rigorize analysis of simulations, an imperative task when experimental data is lacking.

Chapter 2 introduces the Holtec Int. HI-STORM 100 spent fuel cask and corresponding computation model (the detailed model). A basic analysis of the computational results from the detailed model is also provided in order to identify analytic models capable of representing the neutron flux in the fuel. Further, an analytic model is chosen and justified in each fuel sub-region. Chapter 2 concludes by identifying each analogous analytic and reduced-fidelity computational models for analysis in Chpt. 4.

Chapter 3 derives the neutron transport equation. The diffusion approximation and multigroup discrete ordinates approximation are developed from the neutron transport equation. Chapter 3 also includes a discussion of geometry reductions and identifies the location where the geometry can be reduced from cylindrical to planar, approximately 10 cm from the cask centerline.

Chapter 4 develops reduced-fidelity computational models for comparison against the detailed and analytic models. Using reduced complexity analytic and computational models to analyze the simulation results of a high-fidelity computational model allows for the quantification of effects of any assumptions invoked when developing the latter model. Ensuring important physics are preserved in the course of conducting simulations increases the likelihood of correct results. This work exemplified this notion through a process

referred to as "simulation results assessment." As a demonstration, Chpt. 4 included post-simulation analysis of a detailed MCNP model of a HI STORM 100 spent nuclear fuel cask. A series of reduced analytic and computational models are developed and used to identify the physics which causes features in the neutron flux spatial distribution as calculated by the detailed model. In the HI-STORM 100 model, the stainless steel basket, neutron absorbing pads, and helium annulus around the fuel cells are important physical components that need to be preserved in modeling. Retaining the individual fuel pin structure was found to be less important than broadly capturing the lumped material properties inside the individual fuel cells. These results were corroborated using the cruciform model, which appears to capture the physics relevant to the neutron flux spatial distribution in the detailed model beyond the 90% level. The major features of the neutron flux spatial distribution simulated by the detailed model are expected to be correct since the this model preserves material fuel properties and the geometric structure of the neutron absorbing pads and helium annulus. Outside of the fuel region, the E_2S_2 model captures the physics occurring in the concrete region of the detailed model within 10%. These same analytic models capture the physics within the detailed model within 5% in the MPC and 40% in the carbon steel shell. The reason for the higher degree of error in the carbon steel is an over-prediction of the thermal flux exiting the concrete annulus.

Chapter 5 introduced the sensitivity analysis discussion of the detailed model. This chapter calculated the SC's pertaining to Σ_a and Σ_s for each material in the detailed model. Through this analysis, the SC's for air proved to be sufficiently low compared to the other SC's and air is neglected from the analysis. Further, in the fuel region, MPC, and carbon steel shell the absorption cross section is determined to be the most important parameter for the majority of each material.

Chapter 6 introduced the local sensitivity analysis and the FSAP method for analytically calculating SC's. The method is then applied to the flux model which is the solution to the diffusion approximation. Then, the FSAP method is applied to the

governing system of multigroup discrete ordinates equations which is applicable is a general result for any material where the multigroup discrete ordinates equations are acceptable. Further, the G-derivative is used to find the equations for the boundary condition of the MPC, concrete annulus, and carbon steel shell.

Chapter 7 analyzed the results from of the analytic sensitivity analysis from Chpt. 6. Analytically determining SC's are shown to be capable of investigating more parameters than are capable in MCNP. Multiple behaviors are found to appear across each material in the cask; 1) the values of S_{ϕ,Σ_a} are shown to be controlled by the group-wise absorption cross section with the highest value (the thermal group cross section), 2) the values of S_{ϕ,Σ_s} is controlled by the in-group scattering cross section matching the group with the highest neutron flux, 3) the values of S_{ϕ,Σ_s} initially have positive values before becoming negative, showing that scattering acts to preserve the flux before leakage and thermalization physics occur, 4) even though the materials are scattering dominated, the SC's pertaining to the absorption cross section tend to be more important that those pertaining to the scattering cross section.

8.2 Recommendations for Future Work

In addition to this necessary program of study, there appears to be a nearly limitless sequence of higher-fidelity analytical fuel cask models in which the G-derivative formalism may be brought to bear. Candidate analytical models along these lines include but are not necessarily limited to multi-group neutron diffusion models, multi-group Pn or Sn neutron transport models, and multi-group integral or integro-differential neutron transport models. Depending on the physical processes of interest, each of these models may be formulated as static or time-dependent, in various representative geometries, and featuring any number of multi-material regions. Again, the ultimate intent of analytical sensitivity analysis studies within any of these formalisms is to enable comparison to complementary computational results.

The results assessment methodology is not limited to spent fuel casks. The proposed methodology is compatible with other areas in nuclear science and engineering, such as radiation detections and shielding, reactor physics modeling (including next-generation reactors), and nuclear medicine. The proposed methodology is appropriate anywhere analytic models can be developed.

From the conclusion in Chpt. 7, an energy group grid refinement study should be conducted to find the minimum number of energy groups required to gain agreement between the SC's of the multigroup analytic and detailed models. Comparing values of the analytically calculated and computationally derived SC's showed an insufficiency in the energy grid refinement. In some materials, the concrete annulus and the carbon steel shell, a 30-group model may be adequate for capturing first derivative information. However, in the fuel region and MPC, a 30 energy group mesh had not sufficiently converged to the asymptotic range. Further, more analysis is required to identify the physics controlling behavior in S_{ϕ,μ_1} and S_{ϕ,μ_2}.

Finally, programs of sensitivity analysis as applied to computational models of spent nuclear fuel casks appears to be an area ripe for further advancement in research and development. This being the case, and in tandem with the aforementioned potential for new, analogous analytical treatments, there also appears to be ample opportunity for the computational evaluation of not only local sensitivity information as pertaining to spent fuel casks, but also the more complete global metrics.

REFERENCES

[1] G. Barenblatt, *Flow, Deformation, and Fracture: Lectures on Fluid Mechanics and the Mechanics of Deformable Solids for Mathematicians and Physicists.* Cambridge University Press, 2014.

[2] "Nuclear Power Summary - News & Notes," DOE, Tech. Rep., April 2019.

[3] R. H. J. JR., "Dry cask inventory assessment," Savanah River National Laboratory, Tech. Rep., 2016.

[4] C. Greulich and et. al., "High energy neutrons transmission analysis of dry cask storage," *Nuc. Inst. and Meth. in Phys. Res. A*, vol. 874, pp. 5–11, 2017.

[5] I. Harkness and et al., "Development of neutron energy spectral signatures for passive monitoring of spent nuclear fuels in dry cask storage," *EPJ Web of Conferences-ANIMMA 2017*, vol. 170, 2018.

[6] I. Harkness and et. al., "Feasibility of fast neutron spectroscopy for safegaurds and verification of spent fuel in dry cask storage," Los Alamos National Laboratory, Tech. Rep. LA-UR-18-29519, 2018.

[7] W. Fickett, "Detonation in miniature," *Am. J. Phys.*, vol. 47, no. 12, pp. 1050–1059, 1979.

[8] "Guide for verification and validation in computational solid mechanics," American Society of Mechanical Engineers, American National Standard ASME V&V 10-2006, 2006.

[9] W. L. Oberkampf and T. G. Trucano, "Verification and validation benchmarks," *Nuc. Eng. and Desn.*, no. 238, pp. 716–743, 2008.

[10] W. L. Oberkampf, T. G. Trucano, and C. Hirsch, "Verification, validation, and predictive capability in computational engineering and physics," *Appl. Mech. Rev.*, vol. 57, no. 5, pp. 345–384, 2004.

[11] T. Sullivan, *Introduction to Uncertainty Quantification.* Springer, 2015.

[12] P. Knupp and K. Salari, *Verification of Computer Codes in Computational Science and Engineering.* Chapman & Hall/CRC, 2003.

[13] D. Cacuci, *Sensitivity and Uncertainty Analysis: Theory.* Chapman & Hall/CRC, 2003, vol. 1.

[14] H. Bode, *Network Analysis and Feedback Amplifier Design.* Van Nostrand-Reinhold, 1945.

[15] M. D. McKay, "Sensitivity analysis," Los Alamos Scientific Laboratory, Tech. Rep. LA-UR-79-982, 1979.

[16] Thiele.H and F.-M. Borst, "Shielding benchmark calculations with scale/mavric and comparison with measurements for the german cask castor haw 20/28 cg," *Nuclear Thechnology*, vol. 168, no. 3, pp. 867–870, 2017.

[17] "Scale: Comprehensive modeling and simulation suite for nuclear safety analysis and design," Oak Ridge National Laboratory, report, 2011.

[18] P. Roache, *Verification and Validation in Computational Science and Engineering*. Hermosa, 1998.

[19] C. Wharton, E. Seabury, A. Caffrey, and P. Winston, "Summary report: Inl cdcis cask scanner testing at doel, belgium," Idaho National Laboratory, Tech. Rep., 2013.

[20] C. Werner and et. al., "Mcnp6.2 release notes," Los Alamos National Laboratory, report LA-UR-18-20808, 2018.

[21] R. Mosteller, "Bibliography of mcnp verification and validation: 2004," Los Alamos National Laboratory, Tech. Rep. LA-UR-04-8965, 2004.

[22] F. B. Brown, "The mcnp6 analytic criticality benchmark suite," Los Alamos National Laboratory, Tech. Rep. LA-UR-16-24255, 2016.

[23] P. Grechanuk and et al., "Semi-analytic benchmarks for mcnp6," *2017 American Nuc. Soc. Annual Meeting*, no. LA-UR-17-20668, 2017.

[24] B. C. Kiedrowski and et al., "Mcnp6 shielding validation suite: Past, present, and future," *2011 American Nuc. Soc. Winter Meeting*, 2011.

[25] F. B. Brown, M. E. Rising, and J. L. Alwin, "Verification of mcnp6.2 for nuclear criticality safety applications," Los Alamos National Laboratory, Tech. Rep. LA-UR-17-23822, 2017.

[26] S. Mashnik, "Validation and verification of mcnp6 against intermideat and high-energy experimental data and results by other codes," Los Alamos National Laboratory, Tech. Rep., 2010.

[27] Y. Chen and et. al., "Surface dose rate calculations of a spent-fuel storage cask by using mavric and its comparison with sas4 and mcnp," *Nuclear Thechnology*, vol. 175, no. 1, pp. 343–350, 2017.

[28] A. Chen, Y. Chen, J. Wang, R. Sheu, Y.-W. Liu, and S. Jiang, "A comparison of dose rate calculations for a spent fuel storage cask by using mcnp and sas4," *Annals of Nuclear Engineering*, vol. 35, pp. 2296–2305, 2008.

[29] C. R. Priest, "Dosimetry, activation, and robotic instrumentation damage modeling of the holtec hi-storm 100 spent nuclear fuel system," Master's thesis, North Carolina State University, MS Thesis 2014.

[30] R. Kelly and et al., "Uncertainty quantification of concrete utilized in dry cask storage," *Rad. Transport and Pro.*, 2013.

[31] Y. Gao and et. al., "Radiation dose rate distributions of spent fuel casks estimated with mavric based on detailed geometry and continuous-energy," *An. of Nuc. Eng.*, no. 117, pp. 84–97, 2018.

[32] H. Yang, C. Liao, and Z. Liu, "Imaging a dry storage cask with cosmic ray muons," Oregon State University, Tech. Rep., 2018.

[33] C. Liao and H. Yang, "Design of a cosmic-ray muon tomography system for dry storage cask imaging," *IEEE*, 2014.

[34] S. Agostinelli and et. al., "Geant4 - a simulation tool kit," *Nucl. Instrum. Meth. A*, vol. 506, pp. 150–303, 2003.

[35] C. A. Miller and et. al., "Verification of dry storage cask loading using monoenergetic photon sources," *Annals of Nuclear Engineering*, vol. 137, 2020.

[36] "Hi-storm fsar," Holtec International, report, 2017.

[37] (2019, Dec). [Online]. Available: https://www.nrc.gov/waste/spent-fuel-storage/dry-cask-storage.html

[38] H. R. Trellue and et. al., "Description of the spent nuclear fuel used in the next generation safegaurds initiative to determine plutonium mass in spent fuel," Los Alamos National Laboratory, report, 2011.

[39] G. I. Bell and S. Galsstone, *Nuclear Reactor Theory*. Von Nostrand Reinhold Company, 1970.

[40] H. Bindra and D. V. Patil, "Radiative or neutron transport modeling using a lattice boltzmann equation framework," *Physical Review E*, vol. 86, 2012.

[41] J. J. Duderstadt and L. J. Hamilton, *Nuclear Reactor Analysis*. John Wiley and Sons, 1876.

[42] E. E. Lewis and J. W. F. Miller, *Computational Methods of Neutron Transport*. American Nuclear Society, Inc., 1993.

[43] A. F. Henry *et al.*, *Nuclear-reactor analysis*. MIT press Cambridge, Massachusetts, 1975, vol. 4.

[44] J. R. Lamarsh and A. J. Baratta, *Introduction to Nuclear Engineering*. Prentice Hall, 2001.

[45] R. MacFarlane and et.al., *The NJOY Nuclear Data Processing System, Version 2016*, Los Alamos National Laboratory, December 2016.

[46] J. Favorite, "Using the mcnp taylor series perturbation feature (efficiently) for shielding problems," *EPJ Web of Conferences-ICRS-13 and RPSD-2016*, no. 153, 2017.

[47] A. Saltelli, K. Chan, and E. M. Scott, *Sensitivity Analysis*. John Wiley & Sons, 2000.

[48] E. M. Oblow and F. G. Pin, "Sensitivity analysis using computer calculus: A nuclear easte isolation application," *Nuc. Science and Eng.*, vol. 94, pp. 46–65, 1986.

[49] *Sensitivity Analysis and Applications to Nuclear Power Plant*, The University fo Tennessee. IEEE IJCNN, 1992.

[50] Y. Qiu, M. Aufiero, K. Wang, and M. Fratoni, "Development of sensitivity analysis capabilities of generalized responses to nuclear data in monte carlo code rmc," *An. of Nuc. Eng.*, no. 97, pp. 142–152, 2016.

BIOGRAPHICAL SKETCH

Tyler Joseph Remedes began his academic career at Colorado School of Mines. He always enjoyed a challenge and chose to pursue a Bachelor of Science degree in engineering physics. While at Mines, he was an undergraduate researcher in Dr. Uwe Griefe's research group where he helped develop, prepare, and test organic neutron scintillation detectors. It was through this experience that he decided to continue his education at the University of Florida. Tyler's time at UF saw research in many areas of nuclear engineering as he explored various realms of nuclear engineering, including nuclear fuels, cosmic radiation shielding, nuclear imaging, and finally neutronics. Tyler spent his first summer at Los Alamos National Laboratory in 2016 where he worked on signal processing for ultra-fast radiation detection. In 2018, Tyler returned to Los Alamos, this time to stay, and worked with Dr. Scott Ramsey and Mr. Joe Schmidt learning about the utility of analytics as applied to neutronics. His time working with Dr. Ramsey and Mr. Schmidt has been a transformative period for Tyler.